MATHEMATICAL AND STOCHASTIC MODELLING OF MOLECULAR COMMUNICATION SYSTEMS FOR ADVANCED DRUG DELIVERY APPLICATIONS

by

Muneer M. Al-Zubi

A dissertation submitted in fulfilment of the requirements for the degree of

Doctor of Philosophy

Faculty of Engineering and Information Technology

University of Technology Sydney

July 2020

Certificate of Original Authorship

I, Muneer Al-Zubi declare that this thesis, is submitted in fulfilment of the requirements for the award of Doctor of Philosophy, in the School of Biomedical Engineering at Faculty of Engineering and Information Technology at the University of Technology Sydney.

This thesis is wholly my own work unless otherwise reference or acknowledged. In addition, I certify that all information sources and literature used are indicated in the thesis.

This document has not been submitted for qualifications at any other academic institution.

This research is supported by the Australian Government Research Training Program.

Signature: Production Note: Signature removed prior to publication.

Date: 06/07/2020

Abstract

Molecular communication (MC) is an emerging nanoscale communication paradigm, biologically inspired by the cellular communications via biochemical molecules in the living organisms. The MC paradigm is highly suitable for modelling and abstraction of the underlying complex processes in the drug delivery systems (DDSs) over wide spatiotemporal scales. Targeted and implantable DDSs are advanced and engineered technologies for effective delivery of anticancer drugs to the cancerous tumors without affecting other healthy parts in the body. This approach offers an efficient alternative or adjunctive therapy to other treatment techniques, such as conventional chemotherapy, thermal ablation, and surgical resection. In-Silico (mathematical and stochastic) models are key tools to understand and quantify the various parameters and processes in the DDSs, including drug transport, release processes, reaction, and other physicochemical interaction processes in the biological microenvironments inside the body. These models play an essential role in the design and development of the DDSs which in order can reduce the animal experiments and can save time and reduce cost.

The focus of my Ph.D. research is to develop novel mathematical and stochastic simulation models using MC paradigm for localized targeted and implantable DDSs over nano- and micrometer scales in complex biological microenvironments. Using the MC paradigm, the drug delivery process is abstracted as a communication mechanism where the drug source acts as a transmitter while the target site (e.g., cancer cell) acts as a receiver and the biological environment through which the molecules get transported acts as a propagation channel. The anticancer drug molecules represent the information carriers that contain the physicochemical properties of the drug. We use system analysis approach using the channel impulse response (CIR) coupled with the signal processing technique (convolution) for modelling the targeted and implantable DDSs in tumor microenvironments (TME). This approach provides more general and flexible models compared to other modelling approaches.

The thesis made original contributions in the following four major aspects:

(1) Generalized mathematical and stochastic simulation models are developed for diffusion-based molecular communications (MC) in complex fluidic microenvironments that include multilayered physical structures, ligand-receptor reaction, anisotropic diffusion, and the effect of reactive obstacles. These generalized models are developed for modelling and design of both the targeted drug delivery systems (TDDS) as well as the molecular communication systems between bio-nanomachines or cells in such complex environments over microscopic scale. (2) The proposed multilayer MC models have been extended for modelling the intravascular TDDS including anticancer drug release from the nanocarriers (NCs) and drug transport across the endothelial barrier of the tumor vasculature in tumor microenvironments. (3) Novel mathematical and stochastic simulation models are developed for modelling the implantable drug delivery system (IDDS) in tumor by predicting and characterizing the release process and drug distribution in the surrounding tumor tissue. (4) Pharmacokinetic /Pharmacodynamics models are developed for modelling the combination therapy using local implantable drug delivery systems in solid tumors following thermal ablation therapy.

Acknowledgments

First and foremost, I would like to express my sincere thanks to my principle supervisor **Prof. Ananda Sanagavarapu** for the continuous support and help in my PhD study and related research, and for his patience, motivation, and huge knowledge. He helped me at all the times of my research and with writing of this thesis. I could not have imagined having a better advisor for my PhD study. Discussions with him helped me to work in this emerging topic besides producing this high-quality dissertation. Without him, the road towards the completion of this research would have been difficult. Also, I would like to thank my co-supervisor **Dr. Steve Ling** for his unceasing encouragement during my PhD study.

I am also grateful to University of Technology Sydney (UTS) for awarding me full prestigious international scholarships to undertake my PhD study.

Dedication

*To **my parents and my family** for their love, endless support and encouragement. I am forever indebted to my parents, who have always kept me in their prayers and taught me the meaning of life. Moreover, this thesis is dedicated to my beloved wife, **Duaa**, who has been a constant source of support and encouragement. Without them, the completion of this work would not have been possible.*

Abbreviations

AUC	Area Under the Curve
CIR	Channel Impulse Response
CT	Computed Tomography
DDD	Drug Delivery Device
DDS	Drug Delivery System
DOX	Doxorubicin
DTI	Diffusion Tensor Imaging
ECS	Extracellular Space
ECM	Extracellular Matrix
EPR	Enhanced Permeability and Retention
FDA	Food and Drug Administration
HT	Hyperthermia
IBP	Intervascular Blood Pressure
IDDS	Implantable Drug Delivery System
IFF	Interstitial Fluid Flow
IFP	Interstitial Fluid Pressure
ISFI	In-Situ Forming Implant
IVF	Interstitial Velocity Field
IVIVC	In Vitro - In Vivo Correlation
MC	Molecular Communication

MCvD	Molecular Communication via Diffusion
MEC	Minimum Effective Concentration
MRI	Magnetic Resonance Imaging
MSD	Mean-Square Displacement
MW	Molecular Weight
NC	Nanocarrier
PTX3	Pentraxin-3
PD	Pharmacodynamic
PK	Pharmacokinetic
PLGA	Poly (Lactic-co-Glycolic Acid)
QS	Quorum Sensing
RDME	Reaction-Diffusion Master Equation
RF	Radio Frequency
RFA	Radiofrequency Ablation
RMSE	Root-Mean Square Error
RN	Receiving Nanomachine
TDDS	Targeted Drug Delivery System
TME	Tumor Microenvironment
TN	Transmitting Nanomachine
TSL	Thermosensitive Liposome

List of Publications

Journals:

1. M. Al-Zubi and A. Sanagavarapu, "Modelling of Implantable Drug Delivery System in Tumor Microenvironment using Molecular Communication Paradigm", *IEEE Access,* vol. 7, pp. 141929-141940, 2019.
2. M. Al-Zubi and A. Sanagavarapu, "Modeling a composite molecular communication channel", *IEEE Transactions on Communications*", vol. 66, pp. 3420-3433, 2018.
3. M. Al-Zubi and A. Sanagavarapu, "Modeling of Ligand-Receptor Protein Interaction in Biodegradable Spherical Bounded Biological Micro-Environments", *IEEE Access,* vol. 6, pp. 25007-25018, 2018.
4. M. Al-Zubi and A. Sanagavarapu, "Implantable Biosensor Interface Platform for Monitoring of Atherosclerosis", *IEEE Sensors Letters*, vol. 4, p. 5500204, 2020.

Conferences:

1. M. Al-Zubi, A. Sanagavarapu, and S. Ling, "Influence of Tissue Anisotropy on Molecular Communication", *IEEE International Engineering in Medicine and Biology Conference* (*EMBC*)*,* Germany*,* pp. 2921-2924, 2019.
2. M. Al-Zubi, A. Sanagavarapu, and S. Ling, "Impact of Reactive Obstacle on Molecular Communication between Nanomachines", *IEEE International Engineering in Medicine and Biology Conference* (*EMBC*)*,* USA*,* pp. 4468-4471, 2018.
3. M. Al-Zubi, A. Sanagavarapu, and S. Ling, "Comparison of Reception Mechanisms for Molecular Communication via Diffusion", *International Conference on Information and Communication Systems (ICICS),* Jordan*,* pp. 203-207, 2018.
4. M. Al-Zubi and A. Sanagavarapu, "Modelling of multilayer biological medium under molecular communication paradigm", *IEEE Life Sciences Conference (LSC)*, Australia, pp. 31-34, 2017.

Table of Contents

List of Figures

List of Tables

CHAPTER 1

Introduction

1.1 Background

The conventional cancer chemotherapy has many drawbacks, such as poor drug bioavailability and toxic side-effects, which causes damage of both the cancer and healthy cells [1]. The targeted and implantable drug delivery systems are effective and safer techniques for delivery of drugs to the target site without affecting other healthy parts in the body [2, 3]. Mathematical and stochastic simulation modelling of the transport and interaction mechanisms in the biological environment from the drug source until the drug reaches the target site inside the body play a key role in the design and development of the DDSs. Moreover, the spatiotemporal drug concentration profile inside the body is essential for predicting the pharmacokinetic (PK) parameters and for optimal design of the DDSs. In general, the models can predict the results for scenarios that cannot be performed experimentally as well as to make new predictions with a minimum number of experimental trials [4]. This will reduce number of the animals used in the experiments and save time and cost.

Molecular communication (MC) paradigm is highly useful in abstracting the molecular transport in terms of telecommunication methodology which is useful for modelling the DDSs [5, 6]. The MC paradigm is an emerging nanoscale communication mechanism, biologically inspired by intracellular and intercellular communications in the living organisms [7, 8]. The molecular communication via diffusion (MCvD) is the most widely used molecular transport mechanism between the biological entities, i.e., natural cells or synthetic nanomachines, using random diffusion of biochemical molecules such as hormones, portions, ions, etc. [9]. Using MC paradigm, drug delivery process can be

abstracted as a communication mechanism where the drug source (e.g., the nanocarrier or the implant) acts as a transmitter while the target site (e.g., a cancer cell) acts as a receiver. Drug molecules represent the information carriers that contain the physicochemical properties of the drug. The biological environment, in which the drug molecules are transported, acts as a propagation channel.

Mathematical and stochastic modelling of the drug delivery systems using MC paradigm provides a clear understanding for drug transport and interaction in the body over a wide range of spatial scales (e.g., large tissue, small tissue, or cell) and temporal scales (e.g., days, hours, or seconds) by adjusting of the model parameters in a flexible manner. However, other approaches such as classic compartmental modelling are limited to study the drug distribution over large spatial and temporal scales [10]. This approach may be an inappropriate for modelling the targeted drug delivery systems (TDDSs) and the implantable drug delivery systems (IDDSs) where the drug distribution and the physicochemical interactions occur over very small spatiotemporal scales. Moreover, since the channel impulse response (CIR) is a crucial function for modelling the MC systems, we can exploit this advantage using system analysis approach via convolution for modelling the DDSs using various drug sources. In contrast to other modelling approaches, system analysis approach via convolution provides general structure models with flexible and faster evaluation of the kinetics using few assumptions that are simple to verify experimentally [11, 12]. Another advantage using this approach is the ability to obtain the input drug release function via deconvolution by knowing the output drug concentration profile.

Synthetic bio-nanomachines (also known as nanocarriers or nanorobots in this thesis), loaded with therapeutic agents (e.g., anticancer drug), can be used as a means of implementing the TDDSs [13]. The TDDS is a promising engineered approach for delivery of anticancer drug to the target site (e.g., cancer cell) in a controlled manner without harming other healthy cells. The rapid developments in bio-nanotechnology pave the way for fabrication nanoscale entities such as synthetic bio-nanomachines (nanocarriers) which can be used for drug delivery applications [14]. Moreover, the IDDS offers an efficient alternative or adjunctive therapy to other treatment techniques, such as thermal ablation and systemic administration, particularly when the conventional therapies fail or cannot be applied [15]. In this approach,

anticancer drug will be locally delivered from a miniaturized implant inside the tumor over a prolonged period of time ranging from days to years. The TDDS and IDDS are attractive and advanced strategies that provide lower toxicity and higher drug bioavailability compared to conventional chemotherapy [2].

The aqueous biological microenvironments through which drug molecules are transported and interacted are extremely complex. These environments have a significant effect on the drug distribution in the body and particularly at the site of action. Therefore, modelling of the drug transport paths as well as understanding the molecular transport process over the time and distance in such complex microenvironments will help in design the targeted and implantable DDSs including the drug sources (e.g., the nanocarriers and the implants). Also, modelling pharmacokinetic and pharmacodynamic processes in such complex environments represent the basis for designing the DDSs. Another important issue in design the TDDSs and IDDSs is developing accurate models for the drug release process from the nanomachines and implants as well as for the interaction process between the drug molecules and the target cells.

1.2 Concept of Molecular Communication

Molecular communication (MC) is the communication mechanism between the syntactic or natural cells inside the body [16]. It is a new communication paradigm in which the information can be exchanged through the chemical molecules. In recent years, MC has received attention of several researchers in biology and engineering around the world. Recently, the IEEE 1906.1 standard is established for nanoscale and molecular communication systems [8]. Molecular communication has many features such as biocompatibility, energy efficiency, and small size [9]. Hence, for communication between nanoscale machines inside the human body, MC is highly suitable. The most significant medical applications of MC are drug delivery systems, disease detection, In-body nanonetworks, health monitoring, and lab-on-a-chip systems [14, 17].

In MC, the information is carried in patterns of molecules, as shown in Figure 1.1. Information molecules may propagate in the biological environments by random Brownian motion, or sometimes they are carried by molecular motors. The information may be encoded

in either the molecular concentration or it may be inscribed directly on the molecules (like DNA). The chemical and physical properties of molecules, as well as their concentration at a given location and at a specific time, are usually very important.

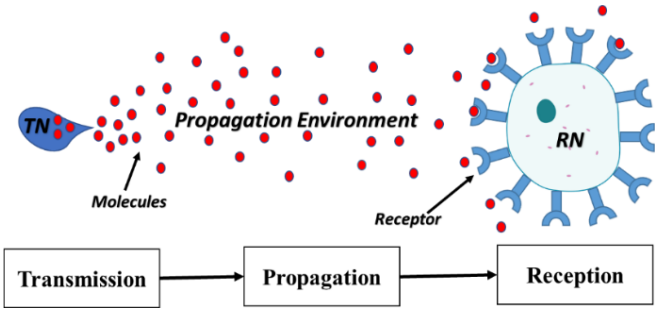

Figure 1.1: Schematic representation of a basic molecular communication via diffusion system.

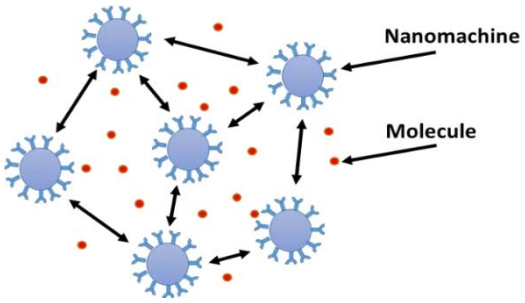

Figure 1.2: Molecular communication between nanomachines in a nanonetwork.

1.2.1 Biological Nanomachines and Nanonetworks

The bio-nanomachines (also known as nanorobots or nanocarriers) are small devices that contain tiny components with sizes range from 1 to 100 nanometers and usually made of either biological or bio-compatible materials [8, 18]. They can perform simple tasks such as computation, actuation, and sensing. The nanomachines usually have sizes range from a macromolecule to biological cell size [8]. As shown in Figure 1.2, a collection of bio-nanomachines form a nanonetwork where they communicate to perform specific complex tasks. An example of biological nanonetwork is quorum sensing (QS) in which the bacterial cells sense concentration of a particular molecule, i.e., an autoinducer, in cooperative manner to determine bacterial cell density inside the environment and then to activate signaling pathways to perform functions such as infection or forming new colony [19].

1.2.2 Transport Mechanisms

Various forms of MC systems have been described based on the type of the transport mechanism, viz., passive transport, e.g., molecular communication via diffusion (MCvD) following purely Brownian motion, or active transport, e.g., bacterium-based communication and molecular motors [9]. Among these, MCvD is very common in nature as it uses a simple transport method for the chemical molecules via an independent random walk process which can be described by Brownian motion. This motion is caused by thermal vibration and collisions with other molecules which alter the trajectory of moving particles [20]. In MCvD, the molecules propagate from the transmitting bio-nanomachine (TN) to the receiving bio-nanomachine (RN) without requiring additional infrastructure or external energy [17, 21]. As an example, the movement of molecules in the extracellular matrix (ECM) can be described by free-diffusion while advection-diffusion model is appropriate for characterizing the cardiovascular system due to blood flow.

1.2.3 Mathematical and Stochastic Modelling Approaches

The diffusion can be mathematically modelled using Fick's laws, which originally proposed by Adolf Fick in 1855 [22]. The Fick's first law of diffusion states that the diffusive flux is related to the concentration and its magnitude proportional to the concentration gradient (i.e., spatial derivative) and the flux travels from region of high concentration to region of low concentration. If the molecules move independently from each other, then the molecular diffusion and the spatiotemporal concentration in a fluidic medium, are mathematically described by Fick's second law of diffusion. The random movement of particles was first observed in 1827 by Robert Brown and thus it is called Brownian motion. In 1905, Albert Einstein developed theory of Brownian motion [23, 24]. He derived the fundamental relation between the diffusion coefficient and the mean-square displacement of the Brownian particles on a microscopic basis. Moreover, he derived an equation which relates the diffusion coefficient to measurable physical quantities. Fick's laws of diffusion and Einstein equations represent the basis for the mathematical and stochastic simulation modelling of the MC and drug delivery systems in this thesis.

1.2.4 Molecular Communication via Diffusion (MCvD)

In general, molecular communication via diffusion (MCvD) system has three main parts [25], viz., transmitter, propagation medium (channel), and receiver, as shown in Figure 1.1. The transmitter may represent a bio-nanomachine, drug delivery device (DDD), biological cell, etc., which emits the molecules in the propagation environment, e.g., blood vessels, extracellular matrix (ECM), tumor microenvironment, etc. The biochemical information can be encoded in the various molecule's properties such as type or concentration of the molecules. Once the TN releases the molecules, they diffuse throughout the environment via random Brownian motion to finally reach and react with the receptor proteins at the target site that act as a receiver. Then, the receiver decodes the information that is encoded in the molecular pattern to take a specific action. A simple example is the quorum sensing (QS) where the bacteria cells communicate to each other to take action such as forming a colony or seeking out larger numbers of their species [8].

1.2.5 Propagation Channel Models

The efficiency and performance of MC systems highly depend on the accurate modelling of the propagation environments (paths) within the body. The path travelled by molecules from a source to a destination, plays a very significant role in predicting an accurate molecular concentration profile at the receiver (the target site). In the communication parlance, the path travelled by the molecules is denoted as 'propagation channel'.

In general, for modelling such complex MC environments, the temporal concentration profile and the channel impulse response (CIR) are required for obtaining the diffusive channel characteristics, optimum system design, and performance analysis [26]. Almost all the cells in the biological in-vivo environments are surrounded by other cells as well as extracellular matrix (ECM), and it is possible that the molecules can diffuse in any arbitrary direction [27]. Thus, the propagation medium should be modelled as a three-dimensional (3-D) space where the information molecules move in both space and time via random diffusion in all directions. However, it is difficult to develop general channel models valid for all MC channels but modelling a specific complex environment can help in providing more accurate and realistic results.

1.2.6 Transmission and Reception Mechanisms

Modelling of transmission and reception mechanisms are essential in designing the bio-nanomachines for medical applications. A single bio-nanomachine can be viewed as a functional unit, which can interact with molecular signals. They can be designed from either natural biological cells or using biocompatible synthetic nano-materials [8]. After the TN releases the molecules, they will reach the RN, e.g., the target cell, and may react with the protein receptors lying on its surface. In nature, the biochemical molecules can reversibly react with the receptor's proteins once they arrive at the receiver membrane. The reaction process between the molecules and the receptors at the target cells have been extensively studied in the biological environments [28, 29]. Indeed, the cell membrane is covered by too many receptors which can capture and recognize different types of the molecules (ligands) [14]. When the ligands bind to the receptors, ligand-receptor complexes will be created. Then, a cascade of triggers will be initiated which in order produces different responses depending on the type of the received ligands. In MC paradigm, the molecular concentration profile and the number of bound receptors, i.e., ligand-receptor complexes, at the target site form the molecular received signals [30].

1.3 Advanced Drug Delivery Systems

The drug delivery systems (DDSs) have been gaining importance in the last few years. The DDS is an engineered approach for the delivery of drug accurately at the site of action to minimize the side effects. Chemotherapy can be delivered to the target site via various administration routs such as oral, intravenous, intraperitoneal, and intramuscular routs. The administration rout of chemotherapy is very important in tumor treatment. For example, some tumor types may response better to chemotherapy when it is locally delivered to the target site (e.g., tumor). Drug delivery to specific sites in the body requires different delivery systems depending on the chosen drug administration routes.

Conventional systemic chemotherapy causes severe side effects because the anticancer drugs target both cancer and healthy cells. Also, the drugs may not reach the target site with enough concentration due to fast clearance in the blood, i.e., bioavailability problem. Therefore, large amounts of drug need to be administered to reach the target site with enough therapeutic

concentration. Development of effective drug delivery mechanisms for the treatment of malignant tumors is important as developing a new drug. The potential activity of drug in the body can be effectively achieved when it is precisely delivered to the site of action. The targeted drug delivery systems (TDDSs) using nanocarriers (NCs) and implantable drug delivery systems (IDDSs) using miniaturized implants offer efficient alternative or adjunctive therapies to other treatment techniques such as radiofrequency ablation (RFA) and systemic chemotherapy [15]. The TDDSs and IDDSs are attractive strategies that use smaller drug doses with providing improved therapeutic efficiency and less toxic side effects compared to systemic chemotherapy [2].

1.3.1 Targeted Drug Delivery Systems using Nanocarriers

The advantage of TDDSs is to improve presence of the therapeutic payloads at the target site which improving the therapeutic efficacy while minimizing the side effects on the other healthy parts in the body. Nanomedicine is the branch of medicine that uses the nanotechnology in making nanoscale materials, e.g., nanocarriers and nanoparticles, for medical applications including drug delivery and diagnosis [31]. Recent advances in bio-nanotechnology have enabled scientists to make drug NCs such as liposomes and nanoparticles, which can be used for targeted delivery of anticancer therapeutics [31]. Encapsulation of drug molecules inside the NCs can improve their bioavailability at the site of action and reduce the toxicity on other healthy parts in the body.

In TDDSs, the NCs can enter the body through intravenous injection and then they swim in the bloodstream to reach the target tissue, e.g., tumor, as shown in Figure 1.3. The NCs utilize the enhanced permeability and retention (EPR) effect, i.e., leaky tumor vasculature, in their extravasation process across the endothelial barrier to the tumor tissue [32]. The nanocarrier-based TDDSs can be classified into active and passive mechanisms [2]. Passively targeted NCs start releasing their therapeutic cargos on-demand using either internal stimuli due to the changes in the local environment (e.g., pH level or temperature), or external stimuli (e.g., ultrasound, heat, or magnetic field), i.e., stimuli-responsive NCs. In active targeting, specific targeting ligands are attached on the surface of NCs which bind to specific overexpressed receptors on the cell surfaces to activate the process of drug release intracellularly or intercellularly. Active targeting is a complementary strategy for increasing

the targeting efficiency and retention of NCs at the target site. Alternatively, the NCs may releases their cargos intravascularly when they reach the tumor vasculature without needing to extravasate from blood vasculature across the endothelial barrier, i.e., this approach is termed intravascular drug release approach [33]. This approach can increase drug bioavailability in the tumor and provide high therapeutic efficacy.

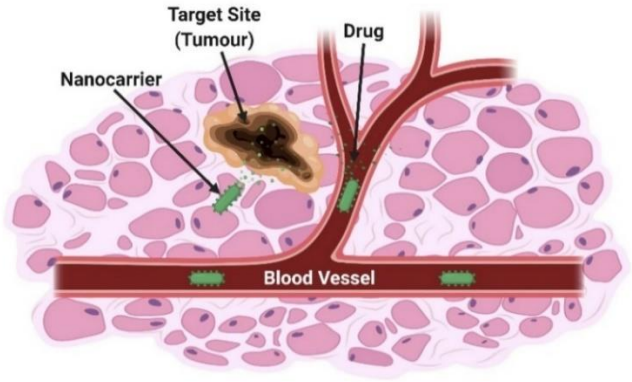

Figure 1.3: Graphical illustration of targeted drug delivery to tumor using nanocarriers.
(This figure is created with BioRender)

Another significant achievement is the nanorobotic technology which is expected to have a wide range of biomedical applications within the near future, particularly for targeted drug delivery [13]. The capability of nanorobots to perform the targeted drug delivery has been established at laboratory scale, e.g., DNA-based nanorobots [34]. In future, MC may provide the communication capability between the nanorobots to release the drugs exactly at the target site in a cooperative manner.

1.3.2 Implantable Drug Delivery Systems

The recent advances in bio-nanotechnology help in design molecular compounds and drug delivery devices to improve the therapeutic outcomes. Despite all the advancements in DDSs, overcoming the biological barriers is the main challenge in drug delivery process. Delivery of anticancer drugs to tumor via systemic administration in bloodstream suffers from a high drug elimination and enzymatic degradation. Also, it results in many side effects as the majority of drugs will accumulate in other parts of the body [3]. Controlled release of anticancer drug using IDDSs, e.g., polymeric implant, is a powerful alternative approach to the systemic drug delivery [35]. In IDDSs, therapeutic agents are locally delivered inside the

tumors over a prolonged period of time as shown in Figure 1.4. The released drug will transport through the surrounding tissue and interact with the molecular and cellular components of the tissue, i.e., elimination via the local capillaries, uptake and binding by the cells, biotransformation, etc. The IDDSs are emerging technologies for delivery of the chemotherapy drugs to tumors when the low bioavailability or high toxicity is a problem. In order to design efficient IDDSs, it is essential to accurately predict the spatiotemporal distribution of the drug in the implant vicinity and the surrounding tissues.

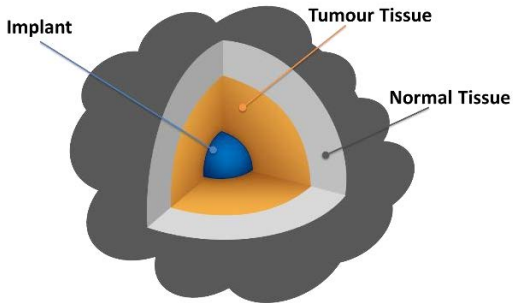

Figure 1.4: Schematic illustration of a drug implant inserted in a tumor.

The IDDSs can be classified into two main categories, namely, passive and active (or dynamic) systems [36]. The passive systems include both nondegradable and biodegradable implants without dynamic mechanisms. However, in the active systems, a positive driving force can be used to modulate drug release using some energy-dependent techniques. In this thesis, we focus on the passive implants which are typically made of biocompatible materials (e.g., polymer) and modulate drug release based on a passive diffusion phenomenon. The drug release profiles from the implants influenced by the following factors: the physicochemical properties of the drug and polymer materials, the shape and size of the implants, and the environmental conditions [37]. The reservoir-based implants and matrix-based implants are the most common nondegradable implants which typically made of polymers. In the polymeric matrix-based implants, drug spreads homogeneously in the matrix material. However, in the reservoir-based implants, the drug release is characterized by the permeability and thickness of a permeable membrane which covers the compact drug core. The nondegradable implants should be extracted after depletion of the drug cargo to avoid the adverse clinical sequelae. On the other hand, the biodegradable implants were

developed to overcome the drawbacks of the non-biodegradable implants. The biodegradable implants are made of biocompatible polymers that can be broken down into safe metabolites and then absorbed or excreted by the body. The previously mentioned IDDSs require a surgical procedure to insert the implants, and in the case of non-biodegradable implants, they need surgical removal. Another attractive and biocompatible IDDS is in-situ forming implants (ISFIs) which depend on a minimally invasive administration procedure via injection and simple manufacturing process [38]. In this system, anticancer drug will be mixed with other biodegradable materials (e.g., PLGA) and then the resulting mixture will be injected into the tissues which can then be transformed into a solid or semi-solid depot in situ via phase separation. Typically, injectable ISFIs have dual-release pattern with a large initial burst release followed by sustained release over a period of hours to weeks [39].

1.3.3 Combination Therapy using Implantable DDS and Thermal Ablation

Thermal ablation is minimally invasive therapy which can be used as an alternative therapy for systemic chemotherapy and surgical interventions for unresectable tumors or when other treatments have high levels of risk [40]. The main challenge in using thermal ablation, e.g., radiofrequency (RFA) or high-intensity focused ultrasound (HIFU) ablation, is the risk of the local recurrence and the residual tumor cells after ablation, particularly in the tumor periphery [39, 41]. Many experimental studies showed high efficiency for using of local IDDSs to kill the residual cancer cells at the periphery of thermally ablated tumors and to prevent tumor recurrence [39, 42]. Combined (or hybrid) treatment using implantable drug delivery and thermal ablation can result in a better therapeutic efficacy by destroying the tumor compared to using a single therapy technique.

1.4 Abstraction of DDSs using Molecular Communication Paradigm

Study of MC is particularly suitable for modelling and abstraction of the drug delivery systems [5, 6]. We exploit MC paradigm for abstracting and modelling of the TDDSs and IDDSs, as shown in Figure 1.5 and Figure 1.6, respectively. In TDDSs, the drug-loaded nanocarriers (NCs) are abstracted as transmitters from the perspective of MC paradigm, which can enter the human body via intravenous injection, see Figure 1.5. After that, drug NCs will move through the bloodstream and some NCs extravasate from the blood vessels

to the surrounding tissues. Drug NCs release their therapeutic payloads either in the blood or in the surrounding tissue, upon reaching the target site. Here, the focus is on modelling drug release from NCs (or nanomachines) as well as drug transport and interaction in the surrounding biological environment when the NCs become close to the target site inside the blood microvessel. However, transport of the NCs through the bloodstream including the various physicochemical processes in the blood were extensively addressed in the literature [5, 26], and it is beyond the scope of this thesis.

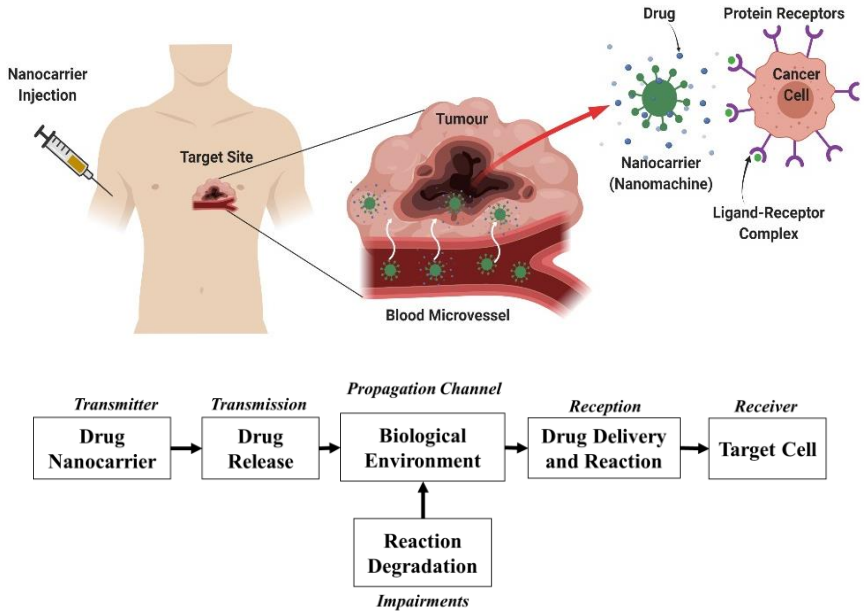

Figure 1.5: Abstraction of nanocarrier-based TDDS using MC paradigm. (This figure is created with BioRender)

The drug release process can be abstracted as a transmission process in MC paradigm. Here, the physicochemical properties of drug molecules represent the information sent by the transmitters. The complex biological environments in which the drug molecules transport act as communication channels that have specific characteristics and structures. After the drug molecules reach the target cell, they will react with the protein receptors on the cell membrane to form the ligand-receptor complexes which can be abstracted as a reception mechanism. Here, the target cells (e.g., cancer cells) act as receivers which can be assumed to have spherical shape [43]. The drug concentration in the vicinity of the cell as well as number of the bound receptors (ligand-receptor complexes) on the cell represents the received signals.

The pharmacokinetic processes which affect amount of the drug that reaches the target cells act as the channel impairments.

Abstraction of the IDDSs using MC paradigm is shown in Figure 1.6. The drug implant acts as a transmitter, which releases drug molecules over a long period of time while drug release process can be abstracted as a transmission mechanism. The drug molecules represent the information carriers that contain the physicochemical properties of drug. The released drug molecules will transport to the surrounding tumor tissue via diffusion and convection processes. Drug molecules suffer from elimination (perfusion) into the blood and lymph microvessels. Also, drug molecules are liable to interact with enzymes, and thus they may degrade to other compounds by altering their chemical structures. Moreover, drug molecules may bind and interact with other molecules and proteins present in the tissue.

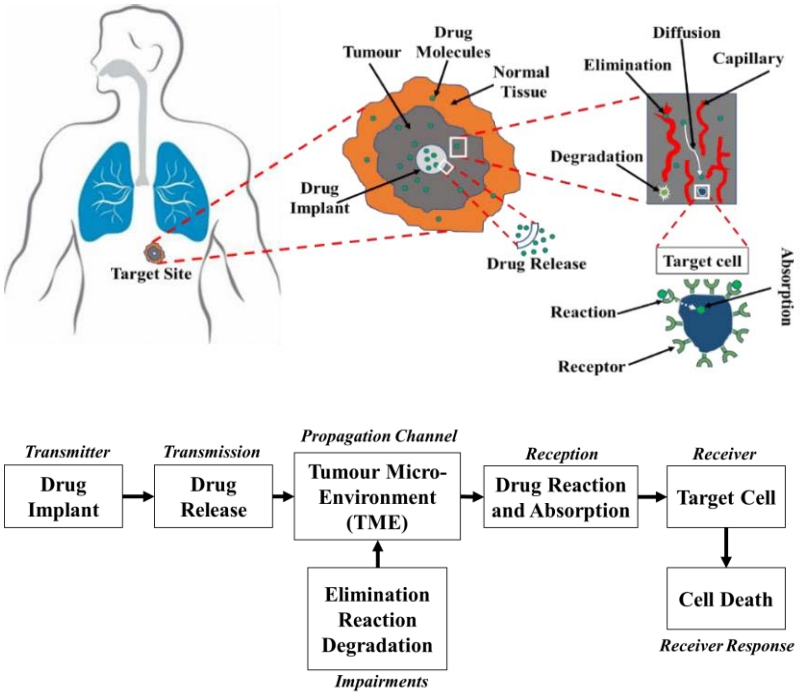

Figure 1.6: Abstraction of IDDS in tumor using MC paradigm.

The tumor microenvironment (TME) together with the diffusion and convection processes, act as a propagation channel from the point view of MC parlance. Furthermore, using MC paradigm, the thermally ablated tumor can be modelled by modifying properties of the communication channel. The processes mentioned above, that affect transport of drug

molecules in the TME represent the channel impairments. Interaction of drug molecules with the cancer cell can be abstracted as a reception mechanism where the cancer cell acts as a receiver. The cell has many types of protein receptors, and each type can capture a specific target ligand. The ligands (molecules) will react and bind with these receptors on the cell to form ligand-receptor complexes. The number of bound receptors on the cell (ligand-receptor complexes) represents the received signal. Then, different reaction processes may be initiated inside the cell which may lead to cell death, that acts as a receiver response in MC framework.

1.5 Research Motivation and Aim

The focus of this thesis is on developing mathematical and stochastic models for the release, transport, and interaction of drug molecules in complex biological microenvironments inside the body using molecular communication paradigm for modelling targeted and implantable drug delivery systems. Movements of the drug molecules from the drug source to the target site depend on the transport mechanisms (e.g., diffusion and convection) as well as on the interaction processes with the cells and other pharmacokinetic processes in the biological environments. The drug molecules will diffuse inside the body, which consists of complex biological environments (also known as channels in MC paradigm). Therefore, temporal distribution of drug at the target site is extremely dependent on the physicochemical properties of the drug and the surrounding biological environment. The understanding and modelling of how drug molecules transport and react with other biological entities, e.g., cells and other molecules, in such complex environments in the body (pharmacokinetics) is essential for optimum design and deployment of sophisticated DDSs. In addition, the death of cancer cells depends on the drug concentration in the vicinity of the cells where a minimum concentration is required to kill the cells. Therefore, study the relationship between the drug concentration and the effect of drug at the site of action (pharmacodynamics) is an integral component in development and design of the DDSs.

Molecular communication (MC) is powerful paradigm for modelling and abstraction of the DDSs to understand the underlying complex processes [5, 6]. Mathematical and stochastic models can help us to predict the spatiotemporal distribution and pharmacokinetic /pharmacodynamic behaviour of drugs in the tissues. The MC paradigm provides clear ways

for understanding of drug transport and interaction in the body over a wide range of spatiotemporal scales in a flexible and comprehensive manner. Moreover, the channel impulse response (CIR) brought in by the MC paradigm would allow exploitation the system analysis approach via convolution for modelling the DDSs with various drug sources. The convolution approach was even used by U.S FDA as a predictive mathematical model describing the relationship between an in-vitro dosage and an in-vivo response, i.e., commonly known as in vitro–in vivo correlation (IVIVC) [44]. These models allow researchers to extrapolate in vivo results from animal models to humans by linking the laboratory experiments with clinical applications [45]. Also, mathematical modelling provides important insight for examining the various biophysical and biochemical features of drug and tissue which significantly affect drug uptake and penetration [12]. These models can be applied to both preclinical and clinical trials to improve drug delivery and development processes. Therefore, they would be of great help in design and optimize various DDSs including the TDDSs and IDDSs which are powerful and efficient techniques for cancer treatment. This will save cost and time as well as reduce the number of animals used in the experiments.

Most of the works in the literature focused on design and analysis of MC from perspective of communication theory for nanoscale communication applications. In spite of the wide range of MC applications [14], few works utilize MC paradigm in modelling and analysis of the DDSs, e.g., [5, 6]. The characteristics of the drug release process from drug source (transmitter), biological environment (propagating channel), drug reaction with the target cells (reception mechanism), and other physicochemical processes, represent the key challenges and play an important role in optimum design of the drug delivery applications using MC paradigm [17]. One of the main challenges associate with the development and deployment of the NCs and the implants for drug delivery inside the body is the complexity of the biological environments. The transport and reaction of drug in the complex biological environments, e.g., multilayer tissues, bounded tissues, tumor tissues, anisotropic tissues, need to be modelled accurately over small spatiotemporal scales. Thus, we can optimize design and operation of the NCs (e.g., liposomes or nanorobots) and the implants for targeted and implantable drug delivery applications.

The propagation channel models play a significant role in predicting the temporal molecular concentration profile accurately at the RN (the target site). There is still a lack of knowledge as to how the molecules exchange and interact with other cells within the complex biological media inside the living organisms. However, design of end-to-end MC models will bring a systems approach for understanding the transport and interaction of the molecules in the body. Therefore, further improvements on the existing MC models are required to provide more accurate results and for optimum design of various biomedical applications such as TDDSs. Several tissues inside the body have multilayer structure with different diffusion properties such as artery wall and the medium of the blood-tissue barrier [46, 47]. The biological in-vivo and in-vitro environments, e.g., the tumor microenvironment [48, 49], are usually small in size and bounded media which have a significant impact on transport and distribution of the diffusive molecules. Therefore, impact of the complexity in structures and characteristics of the biological environments need to be considered in modelling of the drug transport in such environments. Furthermore, modelling of the reaction and reception mechanism at target cells will provide more accurate prediction for the molecular distribution and other responses which may improve the development of the TDDSs. Another important mechanism that should be considered is biotransformation or biodegradation of drug in the biological environments due to various factors such as enzymatic reaction [50].

Many experimental studies for tumor treatment using the IDDSs are available in the literature, but very few mathematical and stochastic models were reported [15]. In fact, more than 85% of human cancers appear as solid tumors. Many experiments showed that using the IDDSs following thermal ablation therapy leads to better therapeutic outcomes in destroying the residual cancer cells and preventing the tumor recurrence [39, 42]. Thus, modelling of the local drug delivery systems using miniaturized implants inside the tumors is highly required, particularly, in thermally ablated tumors. Moreover, we require pharmacodynamics model to examine impact of the anticancer drug on the cancer cells as well as to predict the toxicity on the surrounding healthy tissues.

1.6 Research Contributions

The contributions in this thesis are summarized below which will be explained in detail in the subsequent chapters:

(1) *Mathematical and stochastic simulation models for molecular transport in multilayer (composite) biological microenvironments using molecular communication paradigm.*

In this work, we develop a rigorous mathematical model as well as a novel 3-D stochastic particle-based simulator for molecular transport in composite multilayer biological microenvironments. We derived a generalized closed-form expression for the channel impulse response (CIR) of a MCvD medium having any number of layers (regions). Moreover, in the derived CIR expression, we include the temporal variation of the molecular concentration by taking effects of the different diffusivities and the interface boundary conditions, simultaneously. The steady-state averaging models do not take these into consideration [51, 52]. Even for a two-layer MCvD channel, derivation a closed-form CIR expression including effects of both the time-derivative and interface conditions is significantly more complex than the simple averaging approach proposed in [51]. Finally, the various channel metrices, namely, peak amplitude, peak time, and signal width, are examined using both analytical and stochastic simulation approaches. Furthermore, we developed a novel 3-D stochastic particle-based simulator for a multilayer MCvD media and then we verify the exact analytical results with the simulations for composite molecular channels having various number of layers. The proposed models can be applied to a wide range of applications in multilayer biological media for both microscopic and macroscopic scales such as modelling of the targeted drug delivery using drug-loaded nanocarriers (NCs) across the blood microvessel walls.

(2) *Intravascular Nanocarrier-based targeted drug delivery in tumor microenvironment using the multilayer molecular transport models.*

We utilize the proposed multilayer MCvD models for modelling the intravascular anticancer drug release from drug-loaded nanocarriers (NCs) and drug transport across the endothelial barrier of tumor vasculature into the surrounding tissue in tumor microenvironment (TME). The biological environment between the NCs and the target site is considered as a multilayer (multi-region) medium consists of the lumen, microvessel wall, and tumor tissue. The model

can be applied for different types of drug-loaded NCs such as DOX-loaded thermosensitive liposomes (TSLs). The proposed models are flexible and suitable for NCs with different release rate profiles (e.g., rapid or slow release rates), by fitting the release function to the experimental data. We examine the impact of the release rate and the endothelial barrier permeability on the DOX drug distribution in tumor tissue using TSL nanocarriers with different release rates.

(3) *Modelling of the ligand-receptor protein interaction on the target cells in a 3-D bounded microenvironment using molecular communication*.

We derived the first mathematical formulation for the ligand-receptor protein interaction at the target sites, i.e., the molecular received signal, in 3D bounded diffusive microenvironments. In this model, we derive analytical closed-form expression for the CIR of 3D bounded spherical microenvironment involving point TN and spherical reversible RN. We derive analytical expression for the expected number of bound receptors, i.e., number of ligand-receptor protein complexes, on the target site (or the RN). In this work, a reversible reaction process is used to model the reception mechanism that involves the binding of ligands to the receptor proteins on the receiver surface (the target cell). Moreover, the degradation of the molecules due to enzymes and pH effects in the environment are included. In addition, we develop a comprehensive stochastic particle-based simulator which incorporates both the reversible-reaction reception mechanism and the molecular degradation inside a 3-D bounded microenvironment. Also, influence of the medium boundary on the diffusive molecules is modelled in the proposed stochastic simulator.

(4) *Influence of anisotropy and reactive obstacles on extracellular molecular communication (transport) via diffusion*

In this work, we examine influence of the anisotropy and reactive biological obstacles (e.g., cells), on the molecular communication (transport) via diffusion between a sending cell or nanocarrier (i.e., acts as a TN) and a receiving cell (i.e., acts as a RN) in the extracellular space (ECS). We develop particle-based simulators for the prediction of the received molecules by the RN by considering the impact of the reactive obstacle and the anisotropy in 3-D microenvironments. Impacts of the size and reaction properties of the obstacle on the

received signal are examined. Moreover, we compare the received signal for the case of absence and existence of the obstacle and for both the passive and fully absorptive RNs. Furthermore, we study impact of the anisotropy on molecular communication by comparing the simulation and analytical CIR in an anisotropic diffusive biological microenvironment. Therefore, it is essential to consider impact of the reactive obstacles and anisotropic diffusion in the channel to accurately predict the molecular received signal at the target site. Thus, this work could help in design of the drug delivery and diagnosis systems as well as in the applications of In-Body nanonetworks and the bio-nanomachines inside the biological environments.

(5) *Modeling of implantable drug delivery system in tumor using mathematical and stochastic simulation approach via molecular communication paradigm*.

In this work, we propose novel analytical and stochastic simulation models for anticancer drug delivery into tumors using implantable drug delivery devices. We develop a new mathematical model for drug release and distribution of anticancer DOX drug following insertion of a dual-release implant in a tumor using the MC paradigm coupled with the convolution approach. The implant releases anticancer drug over two phases, namely, burst and sustained releases. Moreover, we model the dynamics of drug release from the implant as well as the distribution and elimination of drug molecules within the tumor tissue. We derived a closed-form expression for the CIR which characterizes the whole channel components. Also, we derived a closed-form analytical expression for anticancer drug concentration profile in the tumor. Moreover, we develop a novel accurate stochastic random walk diffusion simulator for monitoring the spatiotemporal drug concentration profile following insertion the implant in the tumor. The accuracy of the proposed models is verified by comparing our models to the published experimental data in the literature. In contrast to other existing models, the analytical proposed model offers a more general approach for obtaining the spatiotemporal drug concentration profile for any drug release function of the implant based on the convolution with the derived CIR. The proposed models can also be generalized to modelling drug transport in other tissues and using different drugs by incorporating the tissue and drug-specific characteristic parameters. These models offer powerful ways to optimize the design of the implantable drug delivery systems (IDDSs) in tumor and other tissues.

(6) *Mathematical pharmacokinetic/pharmacodynamic (PK/PD) models for combination therapy using implantable anticancer drug delivery after thermal ablation in solid tumors*

We provide comprehensive mathematical pharmacokinetic/pharmacodynamic (PK/PD) models for combination therapy using implantable drug delivery system (IDDS) following thermal ablation inside solid tumors with the help of MC abstraction. Here, the DOX-loaded implant (act as a transmitter) is assumed to be inside ablated and non-ablated solid tumors that surrounded by normal tissues. We provide a specified model for each pharmacokinetic (PK) process, namely, DOX distribution, binding/unbinding of DOX to albumin in the interstitial extracellular space (ECS), cellular influx/efflux of DOX, and elimination of DOX through the blood and lymphatic vessels. Impact of the above-mentioned PK processes are included in the drug transport model for predicting the extracellular and intracellular concentration of both free and bound drugs. Moreover, influence of the interstitial velocity field (IVF) in the tumor and normal tissue are included in this model. Finally, impact of DOX on cancer cells is evaluated using pharmacodynamic (PD) model that depends on the spatiotemporal intracellular concentration of DOX and the characteristics of both anticancer drug and tumor cells. Moreover, the drug toxicity on normal tissue is evaluated in terms of the anticancer drug concentration. Accuracy and validity of our proposed model are verified and compared with the published experimental data as well as with the analytical and stochastic simulation models. To the best of our knowledge, this work is the first comprehensive mathematical PK/PD model that addresses the combination therapy using intratumorally IDDS inside malignant solid tumors with/without thermal ablation under various physicochemical processes simultaneously.

1.7 Thesis Organization

The thesis is organised as follows:

Chapter 1: This chapter presents an introduction to the research topic in this thesis including the concept of MC and its application for modelling the targeted and implantable DDSs. We introduce the research motivations and aims as well as a summary for the various contributions in this thesis.

Chapter 2: In this chapter, we review the related works in two areas covered by this thesis, namely, MC and its applications in targeted and implantable DDSs. We review the various aspects of MCvD, e.g., transmission/reception mechanisms and channel modelling, and the application in modelling the TDDSs and the IDDSs for tumor treatment. We present the limitations on the previous mathematical and stochastic simulation models in this field.

Chapter 3: We propose mathematical and stochastic simulation models for multilayer biological microenvironments using MC paradigm by considering the simultaneous effects of the channel characteristics. Moreover, we employ the proposed multilayer MCvD models for modelling intravascular nanocarrier-based targeted delivery of anticancer drug in TME.

Chapter 4: In this chapter, we derive mathematical and stochastic simulation models for the ligand-receptor protein interaction on the target cell (i.e., act as a RN) in a 3-D bounded microenvironment using MC paradigm. The proposed models examine influence of the various reaction mechanisms on the molecular received signal (i.e., the ligand-receptor protein complexes).

Chapter 5: In this chapter, we examine influence of the anisotropy and reactive biological obstacles (e.g., cells), on the extracellular MCvD transport between a sending cell (or nanocarrier) and a receiving target cell in the extracellular space (ECS).

Chapter 6: In this chapter, we propose novel analytical and stochastic simulation models for the IDDS in tumor using MC paradigm and the system analysis approach via convolution. We predict the spatiotemporal distribution of anticancer DOX after insertion of a dual-release implant in the tumor.

Chapter 7: In this chapter, we develop comprehensive mathematical PK/PD models for the combination therapy using IDDS following thermal ablation inside solid tumors with the help of MC abstraction. Impact of the various PK processes are included in the drug transport model for predicting the extracellular and intracellular concentration of both free and bound drugs. Impact and toxicity of DOX on cancer and normal cells is evaluated using specific PD model.

Chapter 8: This chapter concludes the thesis and presents the scope for future work.

CHAPTER 2

Literature Review

2.1 Introduction

In this chapter, we review the related works in two areas covered by this thesis, namely, molecular communication (MC) and drug delivery systems (DDSs). We review the various aspects of molecular communication via diffusion (MCvD) which are useful for modelling and abstraction of the targeted DDSs, particularly, the channel models and the transmission/reception mechanisms. Moreover, we review the previous related works on modelling of the implantable DDSs for tumor treatment. We present the limitations on the previous mathematical and stochastic simulation works in this field.

2.2 Molecular Communication via Diffusion

In the literature, several passive and active transport mechanisms of MC have been addressed, e.g., MCvD, molecular motors, bacterium-based communication, etc [9]. Among these mechanisms, MCvD is a powerful scheme for transporting information molecules via random diffusion from a transmitting nanomachine (TN(to a receiving nanomachine)RN(without requiring additional infrastructure or external energy [8]. The molecules propagate in the medium (a.k.a. the propagation channel) following Brownian motion [20], and the expected number of received molecules (and the concentration) can be predicted by the channel impulse response (CIR).

Accurate end-to-end MCvD models between the molecular source, e.g., TN, and the destination, e.g., RN, through the biological medium (propagating channel) are essential for optimum design of the MC systems and their applications for the DDSs. Most of the MC models are discussed from the perspective of data communication theory while only a few studies exploit MC paradigm for developing and modelling some applications in medicine

and healthcare as will be discussed in this chapter.

2.2.1 Transmission and Reception Mechanisms

Modelling of transmission and reception mechanisms are essential for design the bio-nanomachines and drug sources for medical applications, e.g., DDSs. The transmission process (e.g., act as drug release process in the DDSs) is the first component in the MC systems. In the literature, the transmission process has been widely restricted to an impulse (or instantaneous) release of the molecules in order to derive the channel impulse response (CIR), e.g., [30]. However, the release process from the real molecular sources, e.g., the drug-loaded nanocarriers (NCs) and implants, need to be modelled as a function of time by fitting the temporal experimental release profiles, e.g., [49]. This allows researchers to use the CIR to obtain the response for the practical molecular sources via convolution approach as will be demonstrated later in other chapters.

In MC, the target site (e.g., the cancer cell) can be modelled as a receiver. Many receiver models for MCvD have been reported in the literature including passive, irreversible, and reversible receivers [9]. The type and complexity of each receiver model depends on the nature of the target site and the expected accuracy of the reception mechanism. Several MCvD models that employ passive receiver in unbounded biological media were studied in the literature, e.g., [53, 54]. The passive receiver is a virtual and simple model, which is usually, assumed to have a capability of counting the molecules without either impeding their diffusion or creating any chemical or physical reactions on its surface. The passive receiver can be useful for predicting the concentration level in the vicinity of the target site, but it cannot model the realistic biological reception and reaction mechanisms at the target site. In an irreversible receiver (either partially or fully absorption model), the molecules irreversibly react with the protein receptors on the receiver surface via an irreversible reaction mechanism. In [55, 56], the authors derived analytical expressions for the number of received molecules by an irreversible receiver in an unbounded propagation environment. In addition, influence of size and density of the absorbing receptors on the received signal has also been examined in [57]. The effect of the molecular degradation on MCvD is analyzed using a fully absorbing receiver model in an unbounded medium [58]. In [59], an equivalent discrete-time model was proposed for MCvD in an unbounded channel using a fully absorbing receiver.

The reaction (binding and unbinding) process that the molecules undergo with the receptor proteins on the target cells have been investigated extensively [28, 60]. One of the examples is binding of the cytokine ligands (CD40L), released by platelets in the bloodstream, with the CD40 receptors on the endothelial cells that cover the blood vessel wall [28, 29]. To accurately model the reception mechanism, a realistic reversible reaction model is required. In [61], steady-state molecular concentration has been derived for a reversible reaction receiver located in an unbounded medium. The reaction-diffusion master equation (RDME) is employed for evaluating the mean and covariance of the output signal for a reversible receiver in an unbounded medium [62]. Extension of this work for a voxelated cubic bounded medium was addressed in [63] where, a first-order reversible reaction is considered inside the receiver rather than on its surface. Improved MCvD models using the reversible reaction mechanism on the receiver surface have been derived in [30, 64]. However, the works mentioned above have mostly been restricted to unbounded media that ignore effect of the medium boundary on the molecular diffusion. Hence, they may not correctly predict the molecular concentration and the bound receptors at the target site (i.e., the RN) in bounded biological media.

2.2.2 Channel Models

Accurate modelling of the diffusive microenvironments in which the molecules diffuse from the source to the destination, plays an important role in predicting of the spatiotemporal molecular concentration profile at the destination, e.g., the target cell. In the communication parlance, the biological microenvironment is denoted as “propagation channel”. The MC channel can be modelled using the channel impulse response (CIR) which is needed to obtain both the channel characteristics and the spatiotemporal concentration profile. The CIR offers a powerful tool for predicting the response for various molecular sources via signal processing technique of convolution.

The propagation channel is an aqueous cellular biological environment inside the human body which may consist of a combination of biological tissues in the form of multilayer structures, e.g., medium of blood-tissue barrier and artery wall [46, 47]. However, simplifying assumptions are usually employed in the literature for modelling the diffusion in such complex environments. The MC propagation media were modelled as a single

homogeneous regions with same diffusion properties, e.g., [58, 65]. Recently, a modelling approach was presented in [51, 52], where a multilayer MCvD channel was replaced by an equivalent homogeneous medium with a single effective diffusion coefficient. However, the effective diffusion coefficient was obtained by averaging the diffusion coefficients of all the layers. This model is valid only under the steady-state condition when the time-derivative of molecular concentration is equal to zero, and the diffusion is restricted to a single direction without including the effect of the multilayer interfaces [22]. Thus, such a simple approximated model could lead to erroneous estimation of the molecular concentration in the composite multilayer biological media.

Moreover, simplified models for unbounded biological media (channels) have been widely employed in the literature for MC systems to simplify the mathematical derivations, e.g., [66]. The biological environments inside any living organism are small bounded media, e.g., stomach, blood vessel, tumor, etc. Moreover, the outer region of tumor is usually needed to be modelled using appropriate boundary condition to reflect impact of the drug elimination through the blood capillaries and the surrounding normal tissue [49]. Also, the biodegradation of the molecules due to enzymes and pH levels is considered in modelling of the biological environments [58]. Recently, in [67-70], the authors derived the CIR for MCvD models using transparent (passive) receivers in spherical and cylindrical bounded media with either fully reflective or fully/partially absorptive boundary. Moreover, a CIR for MCvD is derived using a fully absorbing receiver inside spherical and cylindrical diffusion channels with fully reflective boundary [71, 72]. However, these models use either passive or fully absorbing receiver without modelling the ligand-receptor reversible interaction on the receiver surface which represents the main realistic reception mechanism on the target site. Moreover, all the previously mentioned works did not examine the simultaneous influence of both the interaction process at the RN together with the reaction/elimination at the medium boundary.

Almost all the cells inside in-vivo environments are surrounded by other cells as well as extracellular space (ECS) where the molecules diffuse in any arbitrary direction [27]. In [73], the spatiotemporal dynamics of the molecular transport in ECS was modelled. The physicochemical features of ECS are captured based on parameters such as tortuosity,

volume fraction, and cross section areas of the diffusion paths. In the literature, few works investigate impact of the reactive objects in the biological microenvironment (e.g., ECS) on the distribution of the molecules in the vicinity of the RN (the target site). In [74, 75], the effect of fully absorptive receiver on another in MCvD channel has been addressed. However, the interfering receiver was modelled as a perfect fully absorbing node, which represents a special case of an irreversible receiver (partially absorber). Moreover, some biological tissues inside the body are highly anisotropic having directional diffusion coefficients such as the brain white matter [76]. The mathematical and simulation models can provide a practical alternative method to estimate the molecular distribution and interaction in the various anisotropic tissues within the body by incorporating the experimentally determined parameters. In the literature, anisotropic diffusion was widely studied with the main focus on measuring the transport properties (e.g., diffusion tensor) of various substances and to reveal the microscopic structure and geometry of that tissues such as the ECS in the brain, e.g., [77]. However, mathematical and stochastic modelling of anisotropic biological microenvironments for MC applications is required for accurate prediction of the spatiotemporal distribution of the molecules in such environments, particularly, at the target site.

The previous works in MC area are mostly restricted to idealized and homogeneous environments with lack of the knowledge on how the molecules exchanges and interact with other cells within complex propagation environments. Such complex environments may contain membrane boundaries, barriers, multilayer tissues, reactive cellular obstacles, anisotropic tissues, etc. Therefore, the existing models of the simplified environments may cannot accurately model the realistic propagation environments that construct the human body. Moreover, the transmission mechanism, which may act as a drug release from a NC or an implant and the reception mechanism should be characterised using more realistic models.

2.3 Targeted Drug Delivery Models

The DDSs are engineered approaches for delivery of an appropriate amount of drug at the target site with minimizing the side effects. The recent advances in bio-nanotechnology help in design therapeutic molecular compounds and NCs which can improve the therapeutic

effects such as using DNA-based nanorobots and thermosensitive liposomes (TSL) for targeted drug delivery [34, 78]. In future, the researchers aim to make these nanomachines capable of performing more complex tasks through communications and mutual coordination. Molecular communication framework has the potential for implementing advanced medical solutions such as targeted drug delivery systems (TDDSs). In [14], a literature review was conducted on the potential applications of MC in medicine. Recently, a conceptual model for a molecular-based communication network has been proposed to be used in the circulatory system for drug delivery applications using drug NCs (nanobots) [79]. In [80], a MC model for insulin-glucose system was presented from the theoretical perspective of communication to be used in diagnosis and treatment of insulin resistance.

In the context of drug delivery, the information conveyed by the drug molecules is the therapeutic action. The state-of-the-art of studying the challenges and research opportunities of DDS using MC paradigm was presented in [81, 82]. Particularly, the TDDSs have been considered as one of the most powerful applications of MC paradigm [5, 6]. In [5], MC paradigm was used as an abstraction for modeling particulate DDS inside the body by developing a channel model for propagation of drug molecules through the cardiovascular network. Based on this model, the authors developed in [26], a pharmacokinetic TDDS model for prediction of drug propagation in the blood under physicochemical processes and abnormal health conditions. Engineering of antibody-mediated DDS using MC paradigm and by conveying the information via concentration was proposed in [6]. A leader-follower-based model of mobile MC networks was developed for target detection applications based on mathematical models and laboratory experiments in [83]. In [84], the authors presented a targeted drug delivery model in multiple disease sites based on MC using an enzyme-triggered liposome via self-trigger techniques. However, the previous mathematical models for TDDS mainly focus on modelling the NCs transport through the bloodstream to reach the target site and then release the loaded-drug near the target cells, i.e., extravascular drug release.

In TDDSs, a small amount of the injected NCs can accumulate inside the tumors due to multiple physiological barriers such as the endothelial barrier and the high pressure inside the tumors [32]. Alternatively, using intravascular drug release approach, the NCs can release

the drug intravascularly when they reach the tumor vasculature without needing to extravasate across the endothelial barrier [33, 85]. This approach can increase drug bioavailability in the tumor and provide high therapeutic efficacy. Recently, a nanorobot was developed using DNA origami which can release the therapeutic payload when binds to a specific protein expressed on the endothelial cells inside the tumor microvessels [34]. Moreover, the TSLs can be triggered using external stimuli for intravascular drug release and can be modified into targeted TSL [78]. Therefore, there is a need for modelling the intravascular drug release from NCs and free drug transport and interaction through the surrounding tissue across the vasculature barrier over microscopic scale. This can enhance development and design of the nanocarriers to provide high therapeutic efficacy. In [1], the authors developed a mathematical model to compare the intravascular and extravascular release of DOX from liposomes with the conventional chemotherapy. However, this model was developed based on compartmental approach using first-order ordinary differential equations assuming homogeneous characteristics and identical drug distribution in the tissue. There is a need to develop more precise and flexible mathematical and stochastic models for the intravascular release and transport of anticancer drug from nanocarriers inside the tumor microenvironments considering the different diffusion and dimension characteristics over high spatio-temporal scales.

2.4 Implantable Drug Delivery Models

Drug delivery via systemic administration suffers from high elimination and enzymatic degradation which leads to low drug bioavailability at the target sites. In addition, majority of anticancer drugs accumulate in other parts in the body which lead to many toxic side effects. Local DDSs using implants offers an efficient alternative or adjunctive therapy to other therapies such as systemic administration, thermal ablation, and surgical therapy [15]. The implantable drug delivery systems (IDDSs) are attractive strategies that provide high drug concentration at the site of action with minimizing the toxicity on other healthy parts in the body [86]. Compared to systemic chemotherapy, the IDDSs require less dosage and fewer applications which may result in better therapeutic outcomes. The concept of the IDDSs perhaps dated back to 1938, when Deansby and Parkes studied the effects of subcutaneous implantation of compressed pellets of crystalline estrone in chickens [35]. A polymeric

membrane with controlled drug release is originated by Folkman and Long in 1960 who examined the use of silicone rubber (Silastic®) for prolonged systemic drug administration [87]. Fortunately, the IDDSs have been clinically approved nowadays for cancer treatments, such as Gliadel® degradable polymer implants [88]. Also, poly (lactic-co-glycolic acid) (PLGA) is FDA-approved polymer that attracts much research interest due to its biocompatibility, biodegradability, and sustained-release properties [39]. Moreover, the commercialized products, Atridox® and Eligard®, are FDA approved in-situ forming implants (ISFIs) made of biodegradable and biocompatible synthetic polymers [38].

Many experimental studies for formulation and evaluation of the polymeric implants by examining their release kinetics and therapeutic efficiency were reported in the literature, e.g., [89-91]. The results show that these implants could significantly inhibit the tumor growth and reduce the tumor size. Mathematical models, including pharmacokinetic and pharmacodynamic models, have played a key role in the advancement of DDSs. Most of the drug transport models found in the literature are limited to systemic administration drug delivery approach, e.g., [49, 60]. However, few mathematical models for drug transport in tumors using the IDDSs have been reported in the literature while the other models generally attempt to examine drug release kinetics and polymer degradation [92-94]. A mathematical model for distribution and elimination of drug following the release from a sustained release implant was solved numerically using finite difference technique [95]. In [96, 97], mathematical models were derived for prediction of the drug concentration profile of Carmustine (BiCNU®) based on drug release from polymer implants in rat and rabbit brain tissues assuming constant concentration on the implant surface. In [98], steady-state diffusion and elimination model using biodegradable pellets is proposed assuming constant concentration on the implant surfaces. In [99, 100], the authors provided simple models using finite-element method for prediction of the drug transport and clearance in the brain following drug release from the polymers. In these models, the authors do not examine impact of the release kinetics and transport parameters on the drug distribution. In [101], the authors developed a mathematical model using finite-element software to study delivery of BCNU to brain tumor using systemic administration and local release from polymers. Computational fluid dynamics model for studying transport suitability of different

chemotherapeutic drugs using polymeric wafers in brain tumor was implemented in [102]. A review for simple mathematical models of local distribution of drug in tissue after local release from controlled release devices is presented in [86].These models were solved for transient and steady state but with constant concentration assumption on the polymer/tissue interface.

However, most of the reported models assume that the release function to be either constant or simple decaying function or/and solved for steady state. This assumption is not reasonable for realistic drug implants where the release rate decreases with the time after insertion of the implant in the tissue and sometimes following dual-release profile such as in-situ forming implants. Moreover, the release pattern should be characterized in an optimum way by fitting the release rate function to the experimental release data of the implants. Also, to the best of our knowledge, no stochastic simulation models were proposed for the release and distribution of anticancer drug in tumors using the IDDSs. Stochastic particle-based simulation provides a powerful alternative approach to mathematical and computational modelling, which can also be either used as an alternative modelling approach or as a benchmarking tool for examining the validity and accuracy of the analytical models. Furthermore, system analysis approach via impulse response convolution offers a powerful alternative and general models for drug transport and pharmacokinetics compared to other modelling techniques [103]. This technique can help in obtain the drug concentration profiles for different release pattern via convolution with the impulse response function, also known as the CIR in this thesis. The CIR expresses the drug concentration response of a given tissue as though the drug is immediately released into the tissue. This convolution technique is used by FDA as a mathematical model describes the relationship between in-vitro dosage and its in-vivo response, i.e., in vitro - in vivo correlation (IVIVC) model [44].

The biodegradable implants can be degraded into products which absorbed in the living surrounding tissues [104]. Polymer degradation and erosion processes contribute to drug release kinetics of the implants where some mathematical models addressed these processes [94]. However, it is reasonable to assume that the polymer degradation rate is slow compared to drug diffusion inside the implant [95]. Thus, the size of polymeric implant remains constant over the diffusion duration since the implant releases drug prior to any significant

degradation [105]. The mathematical models that explain mechanisms of controlled release such as drug diffusion within the implants or polymer degradation are outside the scope of this thesis. In this thesis, the impacts of various design factors on the drug release process are combined in the release rate function by fitting the experimental release data from the published works in the literature.

In addition to the above-mentioned limitations, there is a need for mathematical models that can predict the drug biodistribution and pharmacokinetics/pharmacodynamics (PK/PD) using dual-release implants. Some implants can be designed in a controlled way to release a large amount of drug early, i.e., burst release, to rapidly reach the effective therapeutic concentration at the target site while keeping drug concentration within the effective level during the sustained release phase [106]. However, in other dual-release implants such as ISFIs, a large undesirable burst release may cause major toxicity problem and consume the loaded drug in the implants rapidly [107]. Thus, the overall drug release duration will be reduced which in order leads to poor therapeutic efficiency. Minimizing the initial burst become an attractive challenge and one of the key issues in design of the ISFIs [108]. Therefore, pharmacodynamic modelling for impact of the anticancer drug on the surrounding healthy and tumor tissues is necessary for design the implants to get high therapeutic efficiency.

2.5 Combination Therapy for Tumors: Implantable Drug Delivery with Thermal Ablation

Image-guided thermal ablation therapy (e.g., using radiofrequency, focused ultrasound, microwave, or laser) has received significant attention for the treatment of many cancerous tumors [109]. Thermal ablation is minimally invasive technique used as an alternative therapy for systemic chemotherapy and surgical interventions for unresectable tumors or when other therapies have high levels of risk [110]. Radiofrequency ablation (RFA) is one of the most clinical powerful thermal ablation techniques for treatment of small solid tumors (i.e., < 3cm) due to its simplicity, high response rates, and relatively low side effects [110]. However, similar to other thermal ablation techniques, the main challenges of using RFA are the risk of local recurrence and the residual tumor cells after ablation, particularly, in the

tumor periphery [41, 111]. A recurrence rate of 49% to 74% was found following the treatment using RFA [112]. Moreover, it has been shown that the recurrent tumor after RFA has more growth rate and vascular invasion than a tumor without RFA [113]. Combination therapy using local IDDSs following thermal ablation can result in a better therapeutic efficacy by destroying the residual cancer cells in solid tumors and preventing tumor recurrence compared to use a single therapy alone [39, 42]. The results showed that the anticancer drug concentration is significantly higher in ablated tumor tissue compared to the normal tissue [114]. The results revealed that the anticancer drug can reach the region beyond the ablated tissue (residual tumor) which causes high apoptosis rate and low proliferation rate of tumor cells and consequently causes significant tumor shrinkage.

In [106], mathematical model was derived at steady-state for design a dual-release DOX-loaded implant to provide the optimal drug pharmacokinetics at the tumor ablation boundary after RFA. Numerical model was proposed to estimate the DOX drug transport parameters, e.g., diffusivity and elimination rate, following insertion of a dual-release implant in liver tissues with/without RFA [115]. In [116-118], the authors proposed a computational transport model for simulation and prediction transport and pharmacokinetics of DOX after inserting biodegradable implants in liver tumors with/without RFA. However, the models discussed above are derived based on many simplified assumptions such as taking impact of pharmacokinetics (e.g., elimination, cellular uptake/efflux, and binding) as an average equilibrium process via effective rate constant. These models do not characterize and predict the dynamic intracellular concentration of anticancer drug and binding of anticancer drug with proteins in the tissue. Furthermore, the above-mentioned works do not provide any pharmacodynamic model which can be used for evaluating the therapeutic efficacy, i.e., the impact of the anticancer drug on tumor and healthy tissues. To the best of our knowledge, there is no comprehensive model characterizes transport, pharmacokinetic, and pharmacodynamic of the anticancer drug in solid tumor using dual-release implant with or without applying thermal ablation.

2.6 Summary

This chapter presents a review of the literature for mathematical and simulation models of the diffusion-based molecular communication and the drug delivery systems (DDSs). We review the channel models as well as the transmission and reception mechanisms for molecular communication via diffusion. Moreover, the potential applications and models in the literature for molecular communication in modelling of the targeted drug delivery systems are discussed. Also, we review the previous related works on modelling of the implantable DDSs for tumor treatment. Finally, we discussed the literature related to the mathematical and computational models of the combination therapy using anticancer drug implants following thermal ablation in tumors.

Chemotherapy can be delivered to the target site via various administration routs such as oral, intravenous, intraperitoneal, and intramuscular routs. Although, the proposed mathematical and stochastic approaches in this thesis focus on vascular and local administration, they can be extended and modified to be appropriate with other administration routs. Also, the models presented in this thesis are applicable for other therapeutic modalities such as combination therapy.

CHAPTER 3

Modelling of Molecular Communication in Multilayer Biological Microenvironments for Targeted Drug Delivery Application

3.1 Introduction

In molecular communication (MC), the aqueous biological microenvironment acts as a propagation medium (channel). This channel has a significant impact on the molecular received signal, which can be obtained via the channel impulse response (CIR). The mathematical convolution using the CIR is a very useful general approach to derive the response at the target site for any input (e.g., molecular source). According to the mathematical theory of diffusion, any diffusion problem can be solved for either transient or steady state. However, the transient analysis provides more information on the temporal channel characteristic. It is essential to know how the CIR or the molecular concentration profile changes within a short time duration and not just after considerable time (i.e., at steady state). For example, in drug delivery systems (DDSs), it is important to analyze the drug concentration and drug effect on the disease cells overtime to control the drug delivery process. In nature, the biological and cellular environments inside the body may consist of multiple layers (regions) with varying characteristics such as thicknesses and diffusion properties. Some examples of composite multilayer channels are molecular transport through the lipid bilayer of cell membrane [119], transport of drugs across the blood-brain barrier [47], diffusion of oxygen and carbon dioxide through the layers of the respiratory membrane [120], and drug transport across the artery wall [46]. Hence, understanding and modelling of the molecular transport across such complex multilayer microenvironments assume greater

significance potentially for the design of the DDSs. These biological environments cannot be treated as single homogeneous regions but should be characterized using more accurate models by considering the different properties of each layer. In the literature, the diffusive multilayer microenvironments are simplified as homogeneous media with average diffusivity to simplify the mathematical derivation of the CIR [51, 52]. However, such simple models could lead to inaccurate prediction of the molecular concentration in the biological multilayer microenvironments, particularly, over very short time intervals.

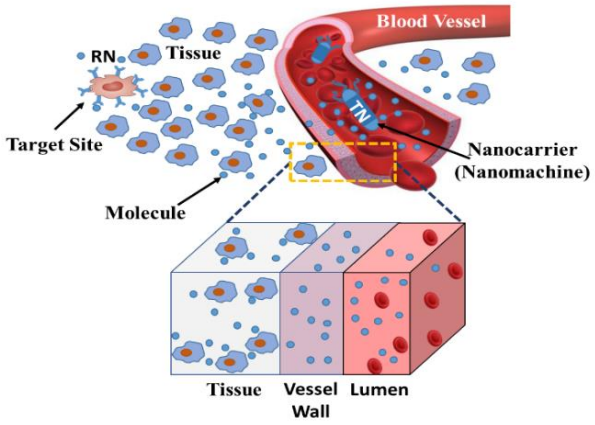

Figure 3.1: Graphical representation of drug release from nanocarriers and drug transport across the blood vessel wall to the target site.

More importantly, in targeted drug delivery systems (TDDSs), the anticancer drug molecules or the nanocarriers (NCs) need to move from the bloodstream across the vascular wall before reaching the target site (e.g., the tumor cells) as shown in Figure 3.1. Therefore, modelling of the diffusion channel between the blood and the surrounding tissues through the vascular barrier, which can be seen as a multilayer environment, is very important for the design and operation of the TDDSs. In this chapter, the convection in the surrounding tissue is neglected because the molecular transport is mainly dominated by diffusion. Moreover, the effect of blood flow on drug transport inside the microvessels is ignored and it will be left for future work.

Molecular communication (MC) paradigm can be used for abstraction and modelling of the TDDSs using drug nanocarriers (or nanomachines). The drug-loaded NC can be abstracted as a transmitter releasing the drug molecules, that act as information (or messages), to the

target sites (e.g., cancer cells) that can be abstracted as the receivers. The biological microenvironment in which drug molecules diffuse acts as a propagation (or communication) channel. Finally, the drug concentration at the target cells represents the received signal. Thus, the drug release process from the source (e.g., NC) and the delivery process at the destination (e.g., target sites) can be abstracted as the transmission and reception mechanisms in MC paradigm, respectively.

In this chapter, we develop a rigorous mathematical model as well as a stochastic particle-based simulator for obtaining a generalized CIR for the molecular transport via diffusion in a 3-D composite multilayer biological microenvironment. In this molecular communication via diffusion (MCvD) model, the channel is considered to have multiple layers (regions) with different thicknesses and diffusion properties. We propose a generalized analytical approach for modelling such a multilayer MCvD channel for arbitrary placement of the transmitting and receiving bio-nanomachines. For example, the transmitting and receiving bio-nanomachines may represent the drug source (e.g., NC) and the target site (e.g., cancer cell), respectively. Using this approach, we derive a generalized closed-form analytical CIR expression for a 3-D diffusive biological medium consisting of multiple layers. In addition, a stochastic particle-based simulator is developed and validated with the derived analytical CIR expression. Various communication metrics, namely, peak amplitude, peak time, and signal width, are derived to evaluate the system performance using both analytical and stochastic simulation approaches. The aim here is to present an analytical benchmark reference solution with which the simulations can be verified and validated. Moreover, to evaluate various system performance metrics which can be used to understand MCvD and molecular transport through multilayer media. Although we focus on the microscale media in this work, the proposed model can be applied to a wide range of applications in multilayer biological media for both microscopic and macroscopic scales. Moreover, we demonstrate the use of the proposed models for predicting the drug concentration in the tumor microenvironment (TME) using intravascular drug delivery from drug-loaded nanocarriers.

The remainder of this chapter is organised as follows. In section 3.2, the structure and components of the multilayer MCvD model are described. We propose the generalized mathematical formulation in section 3.3, and then proceed to derive exact closed-form

analytical CIR expressions for a molecular diffusive channel that is composed of multiple layers. An expression for the average diffusion coefficient of a multilayer MCvD medium at steady-state is given in section 3.4. The performance metrics are discussed in section 3.5. In section 3.6, a comprehensive stochastic simulation framework for 3-D multilayer MCvD channel is presented. In section 3.7, we utilize the proposed models for predicting the drug concentration in TME after releasing the anticancer drug from the NCs. In section 3.8, the analytical results are verified and validated with the stochastic simulation results. Finally, the chapter summary is given in section 3.9.

3.2 System Topology

The system considered here includes a transmitting bio-nanomachine (TN) communicating to a receiving bio-nanomachine (RN) using chemical information molecules in a complex multilayer MC channel, as shown in Figure 3.2.

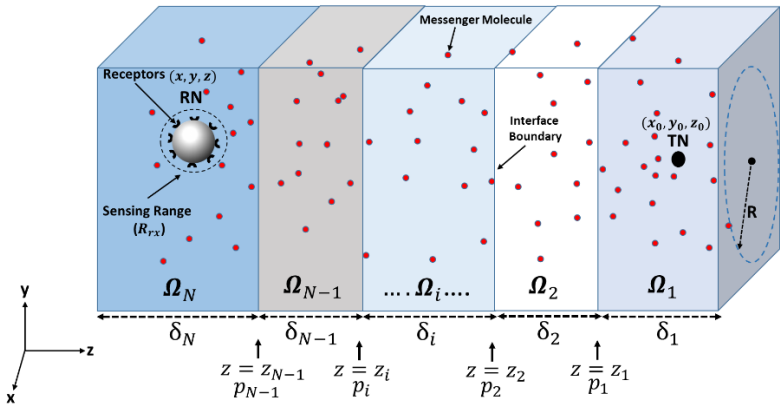

Figure 3.2: An illustration diagram of a general multilayer MCvD propagation channel.

As discussed before, MC paradigm can be used to abstract the release process of drug molecules from a drug source (e.g., injection or nanocarrier) and the drug delivery to a target site (e.g., cancer cells) through a multilayer biological microenvironment inside the body. In this chapter, nanocarriers, nanomachines, or nanorobots are used interchangeably to refer to the same nanodevices. The channel has multiple layers (or regions) with different thicknesses and diffusion properties. The information molecules diffuse independently following Brownian motion in all the directions between the TN and RN within the propagation environment (channel). The information molecules are chemical compounds, e.g., drug

molecules, which are assumed to diffuse independently carrying chemical information from the TN to RN. Here, we consider cylindrical coordinate system (with radius R) to obtain a mathematical solution for the proposed molecular propagation channel where the axis of the cylinder coincides with the z-axis. The channel consists of different layers (Ω_i), and each layer except the first and last layers is assumed to have a finite thickness (δ_i) with different viscosities and/or temperatures resulting in different diffusion coefficients (D_i), and different molecular concentrations, (P_i), for i=1,2,3,…,N. In this model, the medium is assumed to be Newtonian, thus each layer has constant viscosity and consequently constant diffusivity.

There are (N-1) interfaces between the layers which are located at z_j with permeability coefficients p_j, where j=1,2,3,…, N-1. Moreover, we assume that the transmitter nanomachine (TN) is located in the layer-1 (Ω_1) at the position (x_0, y_0, z_0). The TN is assumed to be an instantaneous point-like source which emits 'Q' information molecules into the channel at time t=t_0. The TN size is assumed to be negligible compared to the relative distance between the TN and RN. Furthermore, the receiver nanomachine (RN) is assumed to be a 3-D transparent (passive) sphere with radius R_{rx} and volume V_{rx} which could be located at any arbitrary location (x, y, z) in any layer. It is also assumed that the RN has the capability of counting the received molecules at any time instant, and it does not restrict the movement of the information molecules.

3.3 Mathematical Formulation of Multilayer MC Channel

In this section, we first derive closed-form analytical expressions for the CIR of a 3-D composite multilayer MC channel having multiple layers (or regions) with distinct diffusion properties, as shown in Figure 3.2. The diffusion properties within each layer are assumed to be identical and invariant irrespective of the diffusion direction, i.e., isotropic diffusion. Also, the medium is assumed to be Newtonian with constant viscosity and diffusivity in each layer. The diffusion of molecules in a fluidic medium assuming they move independently from each other is mathematically described by Fick's second law of diffusion which is given by [22] as

$$\frac{\partial P_i\left(r,t;r_0,t_0\right)}{\partial t} = D_i \nabla^2 P_i\left(r,t;r_0,t_0\right) \tag{3.1}$$

where, $P_i(r,t;r_0,t_0)$ is the molecular concentration in the unit of (mol/m^3) for the i^{th} layer at the location r=(x,y,z) and at the time t due to molecules initially emitted at the location r_0=(x_0,y_0,z_0) and at the time t_0, ∇^2 is the Laplacian operator, and D_i is the diffusion coefficient in the i^{th} layer in (m^2/s) given by Stokes-Einstein equation [121] as,

$$D_i = \frac{K_B T_a}{6\pi \eta_i r_m} \tag{3.2}$$

where $K_B = 1.38\times10^{-23}$ (J/K) is the Boltzmann constant, T_a is the medium absolute temperature in (Kelvin), η_i is the dynamic viscosity constant of the i^{th} layer, and r_m is the hydraulic radius of the chemical information molecule.

In the 3-D Cartesian coordinate system, the Laplacian operator can be expressed as follows,

$$\nabla^2 = \frac{\partial^2}{\partial x^2} + \frac{\partial^2}{\partial y^2} + \frac{\partial^2}{\partial z^2} \tag{3.3}$$

We employ a rigorous mathematical technique [122] to derive the CIR for the MC channel with multiple layers. The Laplace domain expression for spatiotemporal distribution of the information molecules, i.e., the concentration, in the i^{th} layer can be expressed as a superposition of two functions as

$$\tilde{P}_i = \tilde{u}_i + \tilde{v}_i \tag{3.4}$$

where, the functions $\tilde{P}_i$, $\tilde{u}_i$, and $\tilde{v}_i$ are the Laplace transforms of the molecular concentration expressions P_i, u_i, and v_i, respectively. Here, we do not show the parameters $(r,t;r_0,t_0)$ to simplify the notation.

The term u_i is the concentration expression at any location $r=(x,y,z)$ in a 3-D unbounded MCvD medium due to instantaneous emission of the information molecules by a point-like TN located at the position $r_0=(x_0,y_0,z_0)$. The molecular concentration u_i is given by [54, 123] as,

$$u_i = \frac{1}{\left(4\pi D_i\left(t-t_0\right)\right)^{\frac{3}{2}}} exp\left(-\frac{\left\|r-r_0\right\|^2}{4D_i\left(t-t_0\right)}\right) \tag{3.5}$$

where the separation distance between the TN and RN is given as

$$d = r - r_0 = \sqrt{R^2 + \left(z - z_0\right)^2} \tag{3.6}$$

The radial distance R is defined as

$$R = \sqrt{\left(x - x_0\right)^2 + \left(y - y_0\right)^2} \tag{3.7}$$

The distribution function (3.5) has been widely used in the literature, which represents the solution of the diffusion equation (3.1) using the following initial and boundary conditions:

$$\lim_{t \to t_0} P\left(r, t; r_0, t_0\right) = \delta\left(r - r_0\right) \tag{3.8}$$

$$\lim_{r \to \pm\infty} P\left(r, t; r_0, t_0\right) = 0, \quad t \geq t_0 \tag{3.9}$$

where $\delta(\cdot)$ is the Dirac delta function.

The parameter $\tilde{v}_i$ is the solution of the diffusion equation (3.11) that vanishes at $t=t_0$ and when it is added to $\tilde{u}_i$, Eq. (3.4) will satisfy the boundary conditions (3.13)-(3.16). Assuming that the diffusion to be symmetrical about the z-axis in a cylindrical coordinate system and is independent of the azimuth angle θ, the diffusion equation [22, Eq. (1.7)] can be expressed as

$$\frac{\partial v}{\partial t} = D\left[\frac{\partial^2 v}{\partial R^2} + \frac{1}{R}\frac{\partial v}{\partial R} + \frac{\partial^2 v}{\partial z^2}\right] \tag{3.10}$$

Now, after extending the diffusion equation (3.10) to N-layers and applying the Laplace transform with respect to t, we get

$$\frac{\partial^2 \tilde{v}_i}{\partial R^2} + \frac{1}{R}\frac{\partial \tilde{v}_i}{\partial R} + \frac{\partial^2 \tilde{v}_i}{\partial z^2} - \lambda_i^2 \tilde{v}_i = 0 \tag{3.11}$$

where, the function $\tilde{v}_i$ is the Laplace transform of the concentration v_i, and the parameter λ_i is defined as

$$\lambda_i^2 = \frac{s}{D_i} \tag{3.12}$$

where the parameter '*s*' is the complex frequency parameter.

The boundary conditions at the interfaces between the layers are extended for *N*-layer medium in the Laplace domain [22, 124]:

$$D_j \frac{\partial \tilde{P}_j}{\partial z} = D_{j+1} \frac{\partial \tilde{P}_{j+1}}{\partial z}, \text{ at } \; z = z_j \tag{3.13}$$

$$D_j \frac{\partial \tilde{P}_j}{\partial z} = p_j \left(\tilde{P}_j - k_j \tilde{P}_{j+1} \right), \text{ at } \; z = z_j \tag{3.14}$$

The boundary condition (3.13) imposes continuity of the flux at the interfaces between the layers. This ensures that there is no accumulation of molecules at the interfaces between the layers assuming their thicknesses are negligible. The boundary condition (3.14) allows for possible changes in the concentration at the interfaces in relation to the permeability coefficients p_j. This change in the molecular concentration is equal to the difference between the concentrations on each side of the interfaces, which is also proportional to the flux. The permeability controls the ability of the diffusing molecules to pass through the interface. As a special case, for a fully permeable interface, i.e., when $p_j \rightarrow \infty$, all the molecules pass without any physical or chemical reactions.

We assume that the concentration will vanish as the first and last layers extend to infinity. This assumption can be represented in the Laplace domain as

$$\lim_{z \to \infty} \tilde{P}_1 = 0 \tag{3.15}$$

$$\lim_{z \to -\infty} \tilde{P}_N = 0 \tag{3.16}$$

Using fully-permeable interfaces between the layers (i.e., $p_j \rightarrow \infty$), the boundary condition (3.14) will be reduced to

$$\tilde{P}_j = k_j \, \tilde{P}_{j+1}, \quad z = z_j \tag{3.17}$$

where, k_j is the ratio of the concentration in the layer Ω_j to that in layer Ω_{j+1} when the final equilibrium is attained [22].

The molecules are instantaneously emitted by the TN at time t_0. Thus, an impulsive signal is used as an initial condition which can be expressed in the Laplace domain as

$$\lim_{t \to t_0} \tilde{P}_i = \begin{cases} \delta\left(r - r_0\right) e^{-s t_0}, & i = 1 \\ 0 \qquad\qquad\quad , & i = 2,3,\ldots,N \end{cases} \tag{3.18}$$

Since the TN is assumed to be located in the first layer, the function $\tilde{u}_i$ vanishes for all the layers except the first layer. Thus, the molecular concentration in each layer can be expressed in the Laplace domain as

$$\tilde{P}_i = \begin{cases} \tilde{u}_i + \tilde{v}_i, & i = 1 \\ \tilde{v}_i \quad , & i = 2,3,\ldots,N \end{cases} \tag{3.19}$$

The function $\tilde{v}_i$ for i^{th} layer can be written as follows [122]:

$$\tilde{v}_i = \int_0^\infty \left[A_i(\xi, s) e^{-g_i z} + B_i(\xi, s) e^{g_i z} \right] J_0(\xi R) \xi d\xi \tag{3.20}$$

where, $A_i(\xi,s)$ and $B_i(\xi,s)$ are weighting functions, $J_0(.)$ is the Bessel function of the first kind of order zero, and

$$g_i = \sqrt{\xi^2 + \lambda_i^2} \tag{3.21}$$

$$\lambda_i = \sqrt{s/D_i} \tag{3.22}$$

The function $\tilde{u}_i$ is obtained by taking the Laplace transform of (3.5) as

$$\tilde{u}_1 = \int_0^\infty \left(4\pi D(t - t_0)\right)^{-\frac{3}{2}} e^{-\frac{R^2 + (z - z_0)^2}{4(t - t_0)D}} e^{-st}\, dt \tag{3.23}$$

Then, using [125, Eq. (29.3.82)], we get

$$\tilde{u}_1 = \frac{exp\left(-\lambda_1 \sqrt{R^2 + (z - z_0)^2}\right) e^{-st_0}}{4\pi D_1 \sqrt{R^2 + (z - z_0)^2}} \tag{3.24}$$

The equation (3.24) can be rewritten as an integral in terms of the Bessel function. We start by substituting $\mu = 0$ and $v = 0.5$ in [126, Eq. (13.47.2)], as follows

$$\int_0^\infty J_0(bt)\left(t^2 + z^2\right)^{-1/4} K_{1/2}\left(a\sqrt{t^2 + z^2}\right) t\, dt = \frac{1}{a^{1/2}} \left(\frac{\sqrt{a^2 + b^2}}{z} \right)^{-1/2} K_{-1/2}\left(z\sqrt{a^2 + b^2}\right) \tag{3.25}$$

where, $K_n(\cdot)$ is the modified Bessel function of second kind of nth order.

Now, using the identity [126, Eq. (3.71.13)] and the fact that both $K_{1/2}(\cdot)$ and $K_{-1/2}(\cdot)$ are equal, we can rewrite (3.25) as follows

$$\int_0^\infty \frac{\sqrt{\pi} e^{-a\sqrt{t^2+c^2}} J_0(bt)}{\left(2a\sqrt{t^2+c^2}\right)^{1/2}\left(t^2+c^2\right)^{1/4}} t\,dt = \frac{1}{a^{1/2}}\left(\frac{\sqrt{a^2+b^2}}{c}\right)^{-1/2}\left(\frac{\pi}{2c\sqrt{a^2+b^2}}\right)^{1/2} e^{-c\sqrt{a^2+b^2}} \tag{3.26}$$

Then, Eq. (3.26) can be rearranged as

$$\int_0^\infty \frac{e^{-a\sqrt{t^2+c^2}}}{\sqrt{t^2+c^2}} J_0(bt)\, t\,dt = \frac{1}{\sqrt{a^2+b^2}} e^{-c\sqrt{a^2+b^2}} \tag{3.27}$$

Substituting $a=|z-z_0|$, $b=R$, $c=\lambda_1$, and $t=\xi$, and then multiplying both sides of Eq. (3.27) by $exp(-st_0)/(4\pi D_1)$, we get

$$\frac{e^{-st_o}}{4\pi D_1}\int_0^\infty J_0(Rt)\frac{e^{-|z-z_0|\sqrt{\xi^2+\lambda_1^2}}}{\sqrt{\xi^2+\lambda_1^2}}\xi\,d\xi = \frac{e^{-st_o}}{4\pi D_1}\frac{e^{-\lambda_1\sqrt{R^2+(z-z_0)^2}}}{\sqrt{R^2+(z-z_0)^2}} \tag{3.28}$$

The term on the right-hand side of Eq. (3.28) is equal to $\tilde{u}_1$ which is given by Eq. (3.24). Thus, it can be expressed as

$$\tilde{u}_1 = \frac{e^{-st_0}}{4\pi D_1}\int_0^\infty \frac{1}{g_1} e^{-g_1|z-z_0|} J_0(\mathrm{R}\xi)\xi d\xi \tag{3.29}$$

In general, for a stratified, N-layer channel, the functions $A_i(\xi,s)$ and $B_i(\xi,s)$ can be found by solving the system of $2(N\text{-}1)$ equations (3.13)-(3.14). Therefore, any increase in the number of the layers will result in a many-fold increase in the derivation complexity of the CIR, unlike the steady-state approximation [51, 52].

In molecular communication, the CIR is defined as the expected number of received molecules by the receiver due to an instantaneous release of the information molecules by the transmitter (e.g., the nanocarrier) [127]. In this model, the receiver is assumed to be a passive observer, and it is common to assume that the receiver is sufficiently far from the transmitter, i.e., $d \gg R_{rx}$. Therefore, the molecular concentration throughout the volume of the passive RN is considered to be uniform and equal to the concentration at the receiver

centre [127]. Thus, the CIR can be expressed as

$$\bar{N}_i = Q\, V_{rx}\, P_i \tag{3.30}$$

where P_i is the molecular concentrations in the i^{th} layer given by the inverse Laplace transform of Eq. (3.19) , and $V_{rx} = (4/3)\pi R_{rx}^3$ is the volume of the spherical receiver.

In case of a single-layer MCvD medium of an infinite extent, given that Q molecules are instantaneously emitted by the TN at time $t=t_0$, the CIR can be given as

$$\bar{N} = Q\, V_{rx}\, u_i \tag{3.31}$$

where u_i is the concentration in an infinite single-layer medium given by Eq. (3.5).

The values of the parameter k_j can be obtained at the equilibrium when the concentrations in the layers do not change with time, i.e., the time derivatives of concentrations vanish.

$$\frac{\partial P_1}{\partial t} = \frac{\partial P_2}{\partial t} = \ldots = \frac{\partial P_N}{\partial t} = 0 \tag{3.32}$$

When the time derivative in (3.1) vanishes at the equilibrium, we can write the following identity in the time domain:

$$D_j \nabla^2 P_j = D_{j+1} \nabla^2 P_{j+1} \tag{3.33}$$

Now, substituting the time domain value of Eq. (3.17), i.e., $P_j = k_j P_{j+1}$, in Eq. (3.33), we get

$$k_j = \frac{D_{j+1}}{D_j} \tag{3.34}$$

Equation (3.34) is an important result that is required for obtaining the final expression of the CIR.

3.3.1 The Channel Impulse Response of Two-Layer MCvD Channel

In this subsection, we obtain exact closed-form expressions for the concentration and the CIR of a two-layer MCvD channel with fully permeable interfaces. For fully permeable interfaces, i.e., very large permeability coefficients, the information molecules pass between the layers (regions) without any physical or chemical reactions. Here, we consider $N=2$ and the layer-

1 (Ω_1) is defined by $z \geq z_1$ with diffusion coefficient D_1 and concentration P_1 while the layer-2 (Ω_2) is defined by $z<z_1$ with diffusion coefficient D_2 and concentration P_2, as shown in Figure 3.3.

Now, the concentration expressions for layer-1 and layer-2 can be evaluated in the Laplace domain by substituting (3.20) and (3.29) in (3.19) as follows:

$$\tilde{P}_1 = \tilde{u}_1 + \tilde{v}_1 = \int_0^\infty \left[\frac{e^{-st_0}}{4\pi D_1} \frac{1}{g_1} e^{-g_1|z-z_0|} + A_1 e^{-g_1 z} + B_1 e^{g_1 z} \right] J_0(\xi R)\, \xi\, d\xi \tag{3.35}$$

$$\tilde{P}_2 = \tilde{v}_1 = \int_0^\infty \left[A_2 e^{-g_2 z} + B_2 e^{g_2 z} \right] J_0(\xi R)\, \xi\, d\xi \tag{3.36}$$

where the variables (ξ, s) are omitted to simplify the notation.

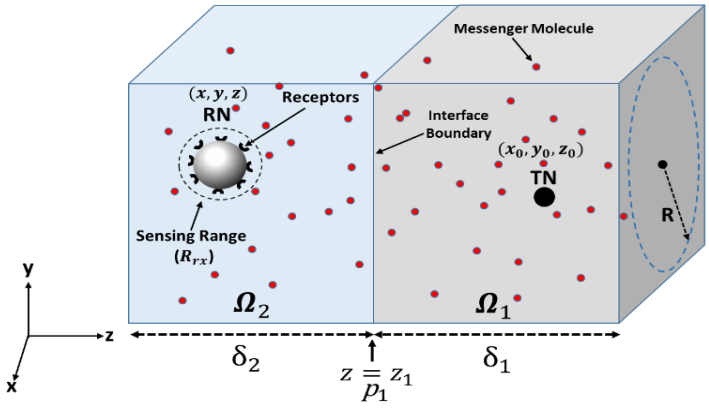

Figure 3.3: An illustration diagram of a two-layer MCvD propagation channel.

Now, we obtain the weighting functions (A_1, A_2, B_1, B_2) for partially permeable interfaces as evaluated in Appendix (A. 1) to get the following expressions:

$$A_2 = B_1 = 0 \tag{3.37}$$

$$A_1 = \frac{k_1 p_1 D_1 g_1 - D_2 g_2 (p_1 - D_1 g_1)}{4\pi D_1 g_1 \left[k_1 p_1 D_1 g_1 + D_2 g_2 (p_1 + D_1 g_1) \right]} e^{g_1(2z_1 - z_0)} e^{-st_0} \tag{3.38}$$

$$B_2 = \frac{2p_1}{4\pi \left[k_1 p_1 D_1 g_1 + D_2 g_2 (p_1 + D_1 g_1) \right]} e^{g_1(z_1 - z_0) - g_2 z_1} e^{-st_0} \tag{3.39}$$

For a fully permeable interface, i.e., $p_1 \to \infty$, Eqs. (3.38)-(3.39) can be evaluated as follows

$$A_1 = \lim_{p_1 \to \infty} \left[\frac{k_1 p_1 D_1 g_1 - D_2 g_2 \left(p_1 - D_1 g_1 \right)}{4\pi D_1 g_1 \left[k_1 p_1 D_1 g_1 + D_2 g_2 (p_1 + D_1 g_1) \right]} e^{g_1 (2z_1 - z_0)} e^{-st_0} \right] \tag{3.40}$$

$$B_2 = \lim_{p_1 \to \infty} \left[\frac{p_1}{2\pi \left[k_1 p_1 D_1 g_1 + D_2 g_2 (p_1 + D_1 g_1) \right]} e^{g_1 (z_1 - z_0) - g_2 z_1} e^{-st_0} \right] \tag{3.41}$$

After evaluating the limits in Eqs. (3.40)-(3.41), we get

$$A_1 = \frac{k_1 D_1 g_1 - D_2 g_2}{4\pi D_1 g_1 \left[k_1 D_1 g_1 + D_2 g_2 \right]} e^{g_1 (2z_1 - z_0)} e^{-st_0} \tag{3.42}$$

$$B_2 = \frac{1}{2\pi \left[k_1 D_1 g_1 + D_2 g_2 \right]} e^{g_1 (z_1 - z_0) - g_2 z_1} e^{-st_0} \tag{3.43}$$

Alternatively, Eqs. (3.42)-(3.43) can be directly obtained by applying the boundary condition (3.17) instead of (3.14). Now, the concentration expression in layer-1 (Ω_1) can be obtained by substituting Eqs. (3.37)and (3.42) in (3.35).

$$\tilde{P}_1 = \tilde{f}_1 + \tilde{f}_2 + \tilde{f}_3 \tag{3.44}$$

where,

$$\tilde{f}_1 = \frac{e^{-st_0}}{4\pi D_1} \int_0^\infty \frac{1}{g_1} e^{-g_1 |z - z_0|} J_0 \left(R\xi \right) \xi d\xi \tag{3.45}$$

$$\tilde{f}_2 = -\frac{e^{-st_0}}{4\pi D_1} \int_0^\infty \frac{1}{g_1} e^{-g_1 (z_0 + z - 2z_1)} J_0 \left(\xi R \right) \xi d\xi \tag{3.46}$$

$$\tilde{f}_3 = \frac{k_1 e^{-st_0}}{2\pi} \int_0^\infty \frac{1}{k_1 D_1 g_1 + D_2 g_2} e^{-g_1 (z_0 + z - 2z_1)} J_0 \left(\xi R \right) \xi d\xi \tag{3.47}$$

The functions $\tilde{f}_1$ and $\tilde{f}_2$ in (3.44) are evaluated in the time domain for $t \geq t_0$ using [125, Eq. (29.3.84)] and with the help of time and complex shifting properties of the Laplace transform.

$$f_1 = \mathcal{L}^{-1} \left[\tilde{f}_1 \right] = \frac{1}{4\pi D_1} \left(\frac{D_1}{\pi (t - t_0)} \right)^{1/2} e^{-\frac{(z - z_0)^2}{4D_1 (t - t_0)}} \int_0^\infty e^{-\xi^2 D_1 (t - t_0)} J_0 \left(R\xi \right) \xi d\xi \tag{3.48}$$

$$f_2 = \mathcal{L}^{-1}\left[\tilde{f}_2\right] = -\frac{1}{4\pi D_1}\left(\frac{D_1}{\pi\left(t-t_0\right)}\right)^{1/2} e^{-\frac{\left(z_0+z-2z_1\right)^2}{4D_1\left(t-t_0\right)}} \int_0^{\infty} e^{-\xi^2 D_1\left(t-t_0\right)} J_0\left(R\xi\right)\xi d \tag{3.49}$$

where, $\mathcal{L}^{-1}(\cdot)$ is the inverse Laplace transform.

Now, the integrals in (3.48) and (3.49) can be evaluated using [125, Eq. (11.4.29)] by making v=0,

$$f_1 = \frac{1}{\left(4\pi D_1\left(t-t_0\right)\right)^{3/2}} exp\left(-\frac{R^2+\left(z-z_0\right)^2}{4D_1\left(t-t_0\right)}\right) \tag{3.50}$$

$$f_2 = -\frac{1}{\left(4\pi D_1\left(t-t_0\right)\right)^{3/2}} exp\left(-\frac{R^2+\left(z_0+z-2z_1\right)^2}{4D_1\left(t-t_0\right)}\right) \tag{3.51}$$

The term $\tilde{f}_3$ in (3.44) can be expressed using [128, Eq. (3.310)] and by substituting the values of g_1 and g_2 from Eqs. (3.21)-(3.22),

$$\tilde{f}_3 = \frac{k_1 e^{-st_0}}{2\pi}\int_0^{\infty}\int_0^{\infty} exp\left(-\left(\xi^2+\frac{s}{D_1}\right)^{1/2}\left(mk_1 D_1 + z_0 + z - 2z_1\right)\right)$$

$$\times exp\left(-\left(\xi^2+\frac{s}{D_2}\right)^{1/2} mD_2\right) J_0\left(\xi R\right)\xi d\xi dm \tag{3.52}$$

The inverse Laplace transform of Eq. (3.52) is evaluated in Appendix (A. 2) as

$$f_3 = \frac{k_1}{8\pi^2\left(D_2 t\right)^{3/2}}\int_0^1 \frac{1}{\left(v-t_0'\right)^{1/2}\left(1-v-t_0'\right)^{1/2}\left(\left(1-v-t_0'\right)+\alpha^2\left(v-t_0'\right)\right)}$$

$$\times exp\left(-\frac{\alpha^2 R'^2}{4\left(\left(1-v-t_0'\right)+\alpha^2\left(v-t_0'\right)\right)}\right)\mathcal{P}_1\left(v\right)dv \tag{3.53}$$

where,

$$\mathcal{P}_1(v)=\frac{-(z_0'+z')(v-t_0')}{V^2}e^{-\frac{(z_0'+z')^2}{4(v-t_0')}}+\frac{\alpha k_1\left(\pi(1-v-t_0')(v-t_0')\right)^{1/2}}{V^{3/2}}\exp\left(\frac{-(z_0'+z')^2}{4V}\right)$$

$$\times\left[1-\frac{(z_0'+z')^2}{2V}\right]erfc\left(\frac{-k_1\alpha(z_0'+z')(1-v-t_0')^{1/2}}{2(v-t_0')^{1/2}V^{1/2}}\right) \tag{3.54}$$

$$V=k_1^2\alpha^2(1-v-t_0')+(v-t_0') \tag{3.55}$$

where, $erfc(\cdot)$ is the complementary error function and the dimensionless parameters $(t_0', R', \alpha, z_0', z')$ are defined in Appendix (A. 2).

By adding Eqs. (3.50), (3.51), and (3.53), we get an expression for molecular concentration in the layer-1 (Ω_1) as

$$P_1=\frac{1}{4(\pi D_1 t(1-t_0'))^{3/2}}\sinh\left(\frac{z_0'z'}{2(1-t_0')}\right)\exp\left(-\frac{R'^2+z_0'^2+z'^2}{4(1-t_0')}\right)+\frac{k_1}{8\pi^2(D_2t)^{3/2}}$$

$$\times\int_0^1\frac{1}{(v-t_0')^{1/2}(1-v-t_0')^{1/2}\left((1-v-t_0')+\alpha^2(v-t_0')\right)}$$

$$\times exp\left(-\frac{\alpha^2R'^2}{4\left((1-v-t_0')+\alpha^2(v-t_0')\right)}\right)\mathcal{P}_1(v)\,dv \tag{3.56}$$

where $\sinh(a)=(e^a-e^{-a})/2$ is the hyperbolic sine function.

Assuming the TN releases the information molecules at the time $t_0=0$, Eq. (3.56) reduces to

$$P_1=\frac{1}{4(\pi D_1 t)^{3/2}}\sinh\left(\frac{z_0'z'}{2}\right)exp\left(-\frac{R'^2+z_0'^2+z'^2}{4}\right)+\frac{k_1}{8\pi^2(D_2t)^{3/2}}$$

$$\times\int_0^1\frac{1}{v^{1/2}(1-v)^{1/2}\left(1-v+\alpha^2v\right)}exp\left(-\frac{\alpha^2R'^2}{4\left(1-v+\alpha^2v\right)}\right)\mathcal{P}_1(v)\,dv \tag{3.57}$$

where $\mathcal{P}_1(v)$ is given in Eq. (3.54) after substituting $t_0'=0$.

The molecular concentration in layer-2 (Ω_2) with a fully permeable interface can be obtained

by substituting Eqs. (3.37) and (3.43) in (3.36) to get

$$\tilde{P}_2 = \int_0^{\infty} \frac{1}{2\pi(k_1 D_1 g_1 + D_2 g_2)} \exp\left(g_1(z_1 - z_0) - g_2 z_1 + g_2 z\right) e^{-st_0} J_0(\xi R)\, \xi d\xi \tag{3.58}$$

The denominator in Eq. (3.58) can be rewritten using the identity [128, Eq. (3.310)], then by substituting the values of g_1 and g_2 from Eqs. (3.21)-(3.22) we get

$$\tilde{P}_2 = \frac{e^{-st_0}}{2\pi} \int_0^{\infty}\int_0^{\infty} \exp\left(-\sqrt{\frac{D_1\xi^2 + s\left(mk_1 D_1 - (z_1 - z_0)\right)}{D_1}} \right) \times exp\left(-\frac{\sqrt{D_2\xi^2 + s}\,(z_1 - z + mD_2)}{D_2} \right) dm\, J_0(\xi R)\, d\xi \tag{3.59}$$

Following a similar procedure to that applied for obtaining the concentration in layer-1 and assuming that the TN releases the information molecules at the time $t_0 = 0$, the expression for molecular concentration in layer-2 (Ω_2) can be expressed as

$$P_2 = \frac{1}{8\pi^2 (tD_2)^{3/2}} \int_0^1 \frac{1}{v^{1/2}(1-v)^{1/2}(1 - v + \alpha^2 v)}\, exp\left(-\frac{\alpha^2 R'^2}{4(1 - v + \alpha^2 v)} \right) \mathcal{P}_2(v)\, dv \tag{3.60}$$

where,

$$\mathcal{P}_2(v) = \frac{k_1^3 \alpha^4 (1-v) z' - v z_0'}{V^2} exp\left(-\frac{z_0'^2 (1-v) + \alpha^2 z'^2 v}{4v(1-v)} \right) + \frac{k_1 \alpha \left(\pi v (1-v)\right)^{1/2}}{V^{3/2}} \times exp\left(-\frac{\left(\alpha^2 k_1 z' + z_0'\right)^2}{4V} \right) \left[1 - \frac{\left(\alpha^2 k_1 z' + z_0'\right)^2}{2V} \right] erfc\left(\frac{\alpha\left(z'v - k_1 z_0'(1-v)\right)}{2v^{1/2}(1-v)^{1/2} V^{1/2}} \right) \tag{3.61}$$

The CIR can be obtained by substituting Eqs. (3.57) and (3.60) in (3.30). The definite integrals in Eqs. (3.57) and (3.60) can be easily evaluated using numerical integration techniques. It is important to note that the derived concentration expressions in a two-layer medium can be reduced to that of an unbounded single-layer medium. This can be verified by substituting $D=D_1=D_2$, $g = g_1 = g_2$, and $k_1=1$ in (3.42)-(3.43) to evaluate the inverse Laplace transform of (3.35)-(3.36). It must be noted that derivation of closed-form

concentration expressions can be significantly more complicated, even for a two-layer medium, than the averaging approach that is proposed in [51]. The challenges arise mainly due to the non-zero time-derivative as well as the interface boundary conditions. However, when the number of layers exceeds two, i.e., for N>2, it is difficult to evaluate a closed-form expression for the inverse Laplace transform. Thus, we need numerical approximations, as will be discussed in the next subsection.

3.3.2 The Channel Impulse Response of Multilayer MCvD Channel (N>2)

In this subsection, a closed-form expression for the concentration and the CIR in multilayer MCvD environment (N>2) is derived. In this case, as explained before, the exact inverse Laplace transform cannot be evaluated, and therefore, we use Zakian's method for numerical inversion [129]. After substituting Eqs. (3.20) and (3.29) in (3.19), we get a general concentration expression in the Laplace domain for any layer as

$$\tilde{P}_i = \int_0^{\infty} \left[\delta_{i1} \frac{e^{-st_0}}{4\pi g_i D_i} e^{-g_i |z-z_0|} + A_i e^{-g_i z} + B_i e^{g_i z} \right] J_0\left(\xi R\right) \xi d\xi \tag{3.62}$$

where δ_{i1} is the Kronecker Delta function given as

$$\delta_{i1} = \begin{cases} 1, & i = 1 \\ 0, & i \neq 1 \end{cases} \tag{3.63}$$

Applying the boundary conditions (3.15)-(3.16) to Eq. (3.62), we get

$$A_N = B_1 = 0 \tag{3.64}$$

Applying the boundary conditions (3.13)-(3.14) to Eq. (3.62), we get

$$\frac{D_j}{g_{j+1} D_{j+1}} \left[\frac{\delta_{j1} e^{-st_0}}{4\pi D_j} e^{-g_j (z_j - z_0)} - g_j \left(A_j e^{-g_j z_j} - B_j e^{g_j z_j} \right) \right] = B_{j+1} e^{g_{j+1} z_j} - A_{j+1} e^{-g_{j+1} z_j} \tag{3.65}$$

$$\delta_{j1} \frac{e^{g_j (z_j - z_0)} e^{-st_0}}{4\pi g_j D_j k_j} + \frac{A_j}{k_j} e^{-g_j z_j} + \frac{B_j}{k_j} e^{g_j z_j} = A_{j+1} e^{-g_{j+1} z_{j+1}} + B_{j+1} e^{g_{j+1} z_{j+1}} \tag{3.66}$$

In general, the functions A_j and B_j can be found by solving the system of 2×N equations (3.65)-(3.66) for *j=1,2,..., N* using mathematical computation software, e.g., MATLAB or

Mathematica. It can be clearly observed here that the derivation becomes more complex as the number of the layers (N) increases.

The inverse Laplace transform of Eq. (3.62) can be obtained using Zakian's method for numerical inversion [129] as

$$P_i = \frac{2}{t}\sum_{m=1}^{5} Re\left\{K(m)\tilde{P}_i(s)\right\} \tag{3.67}$$

where the complex constants, $K(m)$ and $a(m)$, are listed in Table 3.1, and the parameter 's' is defined as follows

$$s = \frac{a(m)}{t} \tag{3.68}$$

Table 3.1: Complex constants for Zakian's method.

m	$a(m)$	$K(m)$
1	12.83767675+1.666063445i	-36902.0821+196990.426i
2	12.22613209+5.012718792i	61277.0252-95408.6255i
3	10.9343031+8.40967312i	-28916.5629+18169.1853i
4	8.77643472+11.9218539i	4655.36114-1.90152864i
5	5.22545336+15.7295290i	-118.741401-141.303691i

After substituting the concentration expression (3.67) in (3.30), we will get the CIR for MC diffusive media having any number of layers which are evaluated numerically using MATLAB. The results in this chapter show that the expression (3.67) provides high prediction accuracy despite the numerical inversion of the Laplace transform.

3.4 Averaging Approximation for Multilayer MCvD Channel at Steady-State

Here, we present an expression for the average diffusion coefficient of a multilayer MCvD medium at steady-state for uni-dimensional diffusion and fully permeable interfaces. This average diffusion coefficient was used in the literature to replace the multilayer medium with an equivalent single-layer medium for the calculation of the CIR [51]. For steady-state condition, the flux remains constant everywhere within the medium and the time-derivative

of the concentration vanishes. Thus, the drop in the total concentration over all the layers is equal to the sum of the drops in each layer as follows

$$\frac{l}{D} = \frac{l_1}{D_1} + \frac{l_2}{D_2} + \ldots + \frac{l_N}{D_N} \tag{3.69}$$

where l is the overall thickness of the medium, l_i is the thickness of i^{th} layer, and D_i is the diffusion coefficient of i^{th} layer. Under the steady-state condition, one can calculate the average diffusion coefficient of a multilayer medium using (3.69) as

$$D_{avg} = \frac{l}{\frac{l_1}{D_1} + \frac{l_2}{D_2} + \ldots + \frac{l_N}{D_N}} = \frac{1}{\sum_{i=1}^{N} \frac{L_i}{D_i}} \tag{3.70}$$

where $L_i = l_i / l$ is the ratio of the i^{th} layer thickness to medium thickness. The average diffusion coefficient (3.70) is widely known in the literature for steady-state diffusion [22], and it is similar to the diffusion coefficient derived in [51]. However, this expression is not suitable to examine the temporal channel characteristics, but it may be useful for measuring the effective (apparent) diffusivity of the multilayer media [22]. Finally, after substituting the average diffusion coefficient (3.70) in the CIR expression of a single-region medium, we get approximated CIR expression for a multilayer medium. However, it must be recognized that this simple CIR expression depends on many assumptions, which may lead to inaccurate predictions, as will be demonstrated later.

3.5 Performance Metrics for Molecular Communication

In this section, we show the procedure of obtaining the performance communication metrics, viz., peak time, peak amplitude, and width of the CIR for a multilayer MCvD channel. In drug delivery systems, these metrics represent very important pharmacokinetic (PK) parameters. The variation of the peak amplitude (N_{peak}) over the separation distance between the TN and the RN, can be interpreted as the channel attenuation. The amplitude attenuation has a significant influence on the molecular received signal. Moreover, the peak time (t_{peak}) measures the delay between transmission and reception of the molecular signals. The molecular signal width is another important metric in molecular communication systems. The width of the molecular received signal can be defined as the time period at which the

signal has a value higher than its half-maximum (i.e., 1/2 N_{peak}).

For unbounded single-layer MCvD channel, the peak time can be derived by finding the time instant at which the time derivative of the CIR (3.31) vanishes, and it is given by [130] as

$$t_{peak} = \frac{d^2}{6D} \tag{3.71}$$

The peak time for a single-layer MCvD channel is proportional to the square of the separation distance between the TN and RN, and it is inversely proportional to the diffusion coefficient. Hence, any increase in the diffusion coefficient will result in faster movement (diffusion) of the molecules, which causes a corresponding decrease in the peak time.

For a single-layer (homogeneous) MCvD channel, the peak amplitude N_{peak} can be obtained by substituting the peak time given in Eq. (3.71) in the CIR (3.31). Thus, we get the following result:

$$N_{peak} = \left(\frac{3}{2\pi e}\right)^{3/2} \frac{QV_{rx}}{d^3} \tag{3.72}$$

The peak amplitude is similar to that derived in [130], but it is scaled by the receiver volume since the expected number of the received molecules at the RN is evaluated. The peak amplitude for a single-layer MCvD channel does not depend on the diffusion coefficient while it is inversely proportional to the third power of the separation distance between TN and RN.

The width of the molecular signal is also inversely proportional to the diffusion coefficient in a single-layer MCvD channel. This means that a larger diffusion coefficient can lead to a narrower signal width. For an unbounded single-layer MCvD channel with impulsive TN and passive RN, the signal width is given by [130].

$$t_w = \frac{0.4501}{D} d^2 \tag{3.73}$$

However, finding closed-form expressions of the communication metrics for a diffusive multilayer medium requires analytical time derivative of the CIR, which could lead to additional mathematical complexity. To avoid this, we find the peak amplitude of Eq. (3.30) numerically for multilayer media and record the corresponding time instant (i.e., peak time)

for various TN-RN separations. Furthermore, the signal width can be numerically evaluated by finding the time instants at which the CIR (3.30) exceed the half-maximum. Then, the signal width is equal to the difference between these time instants. Through this, we realize that the peak amplitude in the multilayer medium depends on the diffusion coefficient, which will be further elaborated later in this chapter.

3.6 Stochastic Simulation Framework

Stochastic simulation can provide accurate results by tracking the random position of each molecule individually within the simulation environment. In this section, we present a comprehensive framework of stochastic particle-based simulation for MCvD in 3-D multilayer channel. The simulator is programmed using MATLAB to validate the analytical expressions. Moreover, this stochastic model can be used as an alternative modelling approach, particularly, when more complexity is added to the system for which it is not easy to find analytical solutions. The total simulation time T_s is divided into many time steps, and each step has a time width Δt. An impulse function is used for modelling the instantaneous emission process of the molecules by the TN, which is located at (x_0, y_0, z_0). Then, the molecules move randomly and independent of each other in all the directions following Brownian motion. The coordinates of the information molecules are tracked and recorded at each time step during the simulation. The random location of each molecule at the time instant $t=i\,\Delta t$ is updated using the following equation [74]:

$$(x_i, y_i, z_i) = (x_{i-1}, y_{i-1}, z_{i-1}) + (\Delta x_i, \Delta y_i, \Delta z_i) \tag{3.74}$$

where $i=1,\ldots,N_t$, N_t is number of the simulation time steps, (x_{i-1}, y_{i-1}, z_{i-1}) is the molecule location at the time $t=(i-1)\Delta t$, ($\Delta x_i, \Delta y_i, \Delta z_i$) is a random displacement over each spatial axis which follows the normal distribution $N(0,\sigma^2)$ with zero-mean and variance ($\sigma^2 = 2D_j\Delta t$) for $j=1, 2,\ldots,N$.

When a molecule, located in the j^{th} layer, moves across the interface to the adjacent layers, i.e., the $(j\pm1)^{th}$ layer, it will be influenced by the diffusion coefficient of the new $(j\pm1)^{th}$ layer and consequently, it will follow new mean-squared displacement. The molecule that reaches and enters the receiver volume will be counted without absorption, and then the receiver

counter increases by one at the end of the time step. Here, it is assumed that the receiver has counting capability of the received molecules during each time slot. The value of the receiver counter at each time step represents the total received molecules at that time, which acts as a received signal. Once the CIR is obtained from the simulation, the performance communication metrics are calculated following the procedure given in section 3.5. Assuming the receiver is sufficiently far from the transmitter, the concentration is uniform inside the receiver volume. Thus, the concentration can be evaluated by dividing the total number of the received molecules at each time step over the receiver volume.

3.7 Nanocarrier-based Targeted Drug Delivery System

In this section, we employ the proposed multilayer MCvD models for modelling intravascular release based targeted drug delivery system (TDDS) in tumor microenvironment (TME). We propose analytical and stochastic models for predicting the distribution and concentration of the anticancer drug in TME following intravascular release from drug-loaded nanocarriers (NCs).

In TDDSs, the therapeutic payloads will be specifically delivered to the target site to improve the therapeutic efficacy and to reduce the side effects on the other healthy parts in the body. However, a small amount of the injected NCs can accumulate in the target site even in tumors with high enhanced permeability and retention (EPR) effect due to multiple physiological barriers and high stochasticity of extravasation through the tumor vasculature [32, 131]. Also, actively targeted NCs need to extravasate across the endothelial barrier before reaching the tumor cells. The previous studies have shown that attaching targeting ligands on the surface of the NCs can facilitate their uptake by the target cells but do not significantly increase the tumor localization of the NCs [132]. The endothelial barrier is the main obstacle that prevents the majority of NCs from reaching the surrounding tumor tissue. Moreover, diffusion is the only transport mechanism for the NCs across the tumor microvessel wall due to absence of the pressure gradient in the interstitial space and consequently, absence of the convection [133]. However, diffusion of the NCs and macromolecules is very slow compared to other small free drug molecules.

3.7.1 Intravascular Drug Delivery Approach

Nanocarriers may releases their cargos intravascularly when they reach the tumor vasculature without needing to extravasate from the blood vasculature across the endothelial barrier, i.e., this approach is termed intravascular drug release approach [33, 85]. Then, the anticancer drug will diffuse across the tumor vasculature and achieve good spatial distribution inside the tumor. This approach can increase drug bioavailability in the tumor and provide high therapeutic efficacy [33]. To accomplish this goal, many tiny biocompatible drug-loaded nanocarriers can enter the body through intravenous injection and navigate autonomously in the body until reaching the tumor microvessels, as shown in Figure 3.4. Under normal conditions, the NCs do not release their cargos, see Figure 3.4 (A). Drug release from NCs can be induced by either binding of specific targeting ligands (attached to the surface of the NCs) with specific overexpressed receptors on the target cells, see Figure 3.4 (B), or by exposing the NCs to external stimuli, e.g., ultrasound, heat, or magnetic field, Figure 3.4 (C).

The tumor microenvironment is modeled as a multilayer MCvD medium which can be easily designed and used for drug delivery testing and other biomedical applications in vitro and in Lab-on-a-Chip devices. Moreover, the proposed multilayer model can provide analytical CIR expression to model the various drug delivery nanocarriers with different release patterns.

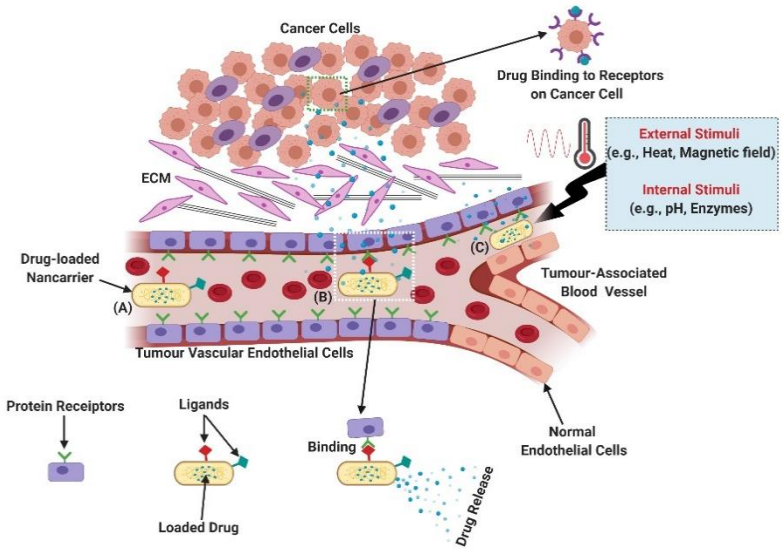

Figure 3.4: Schematic illustration of intravascular drug delivery using NCs in tumor microenvironment (TME). (This figure is created with BioRender)

3.7.2 Analytical and Stochastic Modelling

We utilize the multilayer MCvD models for modelling the release and transport of anticancer drug from drug-loaded NCs in the tumor microenvironment (TME). Impact of the blood-tumor barrier on the amount of anticancer drug that reaches the surrounding tumor tissue is modeled in terms of the permeability and diffusivity of the drug molecules across the tumor vasculature. The drug-loaded NCs are abstracted from the perspective of the MC paradigm as transmitters, which can enter the human body via intravenous injection. The NCs release their payloads, e.g., drug, intravascularly when exposed to internal or external stimuli. The releasing process can be abstracted as a transmission process in the MC paradigm. Here, the chemical properties of the drug molecules represent the information sent by the transmitters. The complex biological tissue in which the drug molecules transport act as a propagation channel that has specific characteristics and structures. The biological environment between the NCs and the target site is considered as a multilayer (multi-region) medium consists of the lumen, microvessel wall, and tumor tissue. Since the medium is Newtonian with constant viscosity, the diffusion coefficient of each layer is assumed to be constant. The mathematical and stochastic models can help in understanding the impact of the biological environment, including the physiological barriers, on the drug delivery process using the NCs to develop more sophisticated drug delivery strategies. As demonstrated in section 3.8, our proposed multilayer MCvD models show high capability in modelling the multilayer biological microenvironments, which can be useful for the design and operation of the NCs for targeted drug delivery applications.

In fact, the drug release process in this type of NCs can occur within a very short time. For example, Thermosensitive Liposomes (TSL) release doxorubicin (DOX) very rapidly within seconds (~2s) in a response to hyperthermia (HT), i.e., when they are heated to above 41ºC [134]. Therefore, the CIR due to impulsive release is suitable for modelling the rapid release process for such NCs. However, to make our model more flexible and suitable for other NCs with different release rate profiles, we include the release kinetics in our model as a decaying function of time [49]. Drug release from the NC can be considered as a diffusion process inside the NC, and it can be modelled using the following first-order equation assuming no drug is dissolved at the initial time [135-137]:

$$\frac{dC_t}{dt} = -k_r C_t \tag{3.75}$$

where C_t is the remaining drug concentration inside the NC at time t and k_r is the release rate constant.

Now, assuming that the encapsulated drug is homogeneously distributed over the entire volume of the NC, and thus the initial drug concentration inside the NC (C_0) is equal to the initial loaded drug mass (M_0) per the NC volume (V_{NC}). Thus, the solution of Eq. (3.75) can be expressed as

$$M_r = M_0 e^{-k_r t} \tag{3.76}$$

where M_r is the remaining mass (amount) of the drug inside the NC at time t.

The cumulative amount of released drug at time t can be expressed as a difference between the initial mass (M_0) and the remaining mass (M_r) of drug in the NC [137, 138].

$$M_t = M_0 M_\infty (1 - e^{-k_r t}) \tag{3.77}$$

where M_∞ is the fraction of total drug released at steady-state.

The fraction of cumulative drug released at time t can be expressed as

$$M = \frac{M_t}{M_0} = M_\infty (1 - e^{-k_r t}) \tag{3.78}$$

The release rate of drug from the NC at time t can be expressed as

$$F(t) = \frac{dM_t}{dt} = M_0 M_\infty k_r e^{-k_r t} \tag{3.79}$$

The Laplace transform of Eq. (3.79) can be expressed as

$$\tilde{F}(s) = M_0 M_\infty k_r \frac{1}{s + k_r} \tag{3.80}$$

It has been observed that the transport in the surrounding tissue is largely dominated by diffusion while the convection is neglected [6, 45]. Now, the drug concentration profile in the surrounding tissue due to drug release from the NCs inside the blood microvessel, can be

obtained via convolution between the CIR (a.k.a the unit impulse response) and the release rate function [139], as

$$P_{NC} = F(t) * P(t) \tag{3.81}$$

In the Laplace domain, the convolution will be converted to a multiplication of both the CIR (3.62) and the release rate expression (3.80) as

$$\tilde{P}_{NC} = M_0 M_\infty N_{NC} k_r \int_0^\infty \left[\delta_{i1} \frac{e^{-st_0}}{4\pi g_i D_i (s + k_r)} e^{-g_i |z - z_0|} + \frac{A_i e^{-g_i z} + B_i e^{g_i z}}{s + k_r} \right] J_0(\xi R) \xi d\xi \tag{3.82}$$

where N_{NC} is the total number of triggered NCs that release their cargos intravascularly.

Particularly, in the case of drug transport across the vascular wall, Eq. (3.82) can be reduced to a two-layer model with a semipermeable interface. After substituting the value of A_2 and B_2 from Eqs. (3.37) and (3.39) in (3.82), we get

$$\tilde{P}_{NC} = \frac{M_0 M_\infty N_{NC} k_r p_1}{2\pi (s + k_r)} \int_0^\infty \frac{exp(z g_2 - z_0 g_1)}{\left[k_1 p_1 D_1 g_1 + D_2 g_2 (p_1 + D_1 g_1) \right]} J_0(\xi R) \xi d\xi \tag{3.83}$$

The equation (3.83) is obtained using the following assumptions: the interface is located at z_1=0, the initial time is t_0=0, and $\delta_{i1} = 0$ for $i \neq 1$ because the virtual observer is located in the second layer. Here, two boundary conditions are used at the microvessel interface, i.e., Eqs. (3.13)-(3.14), where the diffusive flux into the tissue is determined by the permeability of the microvessel wall for the drug molecules p_1. The inverse Laplace transform of Eq. (3.83) can be obtained using Zakian's method for numerical inversion, which is presented in the subsection (3.3.2).

In the multilayer stochastic simulation model, we simulate the drug release process in the NC via uniform distribution of the drug molecules on the NC surface (virtual nanosphere) in each time step as shown in Figure 3.5. The location and number of the molecules on the NC surface is recorded using 3-D coordinate (x, y, z) according to the release kinetic model.

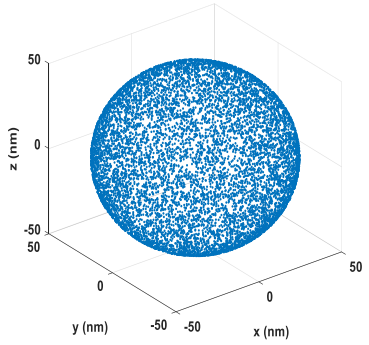

Figure 3.5: The uniformly distributed molecules on the nanocarrier surface captured from the stochastic particle-based simulator.

Assuming that the stimulus (trigger) is applied at time $t = 0$, the NC will release the molecules during each time-step, i.e., $[t, t+\Delta t]$, according to the following equation:

$$N(t, t+\Delta t) = Q\left[M(t+\Delta t) - M(t)\right] \tag{3.84}$$

where $N(t, t+\Delta t)$ is the number of released molecules at each time step and Q is the total number of released molecules from the NC.

After substituting (3.78) in (3.84), we get

$$N(t, t+\Delta t) = QM_{\infty}\left[e^{-k_r t} - e^{-k_r (t+\Delta t)}\right] \tag{3.85}$$

Then, we follow the stochastic simulation framework, given in section 3.6, for tracking the random diffusion of the molecules through the multilayer microenvironment. The microvessel wall is considered as a thin semipermeable layer with a specific thickness and effective diffusivity, which results in a specific effective permeability. A random number between zero and one is assigned for each molecule and the drug molecule can extravasate to the surrounding tissue if this value is larger than the following probability [61]:

$$P_t = \frac{k'_f}{(k'_f + k'_b)^2}\left[2(k'_f + k'_b) - \sqrt{\frac{\pi}{2}}\left(1 - e^{2(k'_f + k'_b)^2} erfc\left(\sqrt{2}(k'_f + k'_b)\right)\right)\right] \tag{3.86}$$

where,

$$k'_f = k_f\sqrt{\frac{\Delta t}{2D_1}} \tag{3.87}$$

$$k_b' = k_b \sqrt{\frac{\Delta t}{2D_2}} \tag{3.88}$$

where k_f' and k_b' are the dimensionless values of the permeability in both forward direction k_f and backward direction k_b, respectively.

We obtain the drug concentration profile at any location in the tissue by normalizing the CIR ($\bar{N}_t$) to the total number of the released molecules as

$$P_s = M_0 N_{NC} \frac{\bar{N}_t}{QV_{rx}} \tag{3.89}$$

In this model, the initial loaded drug inside the NC can be expressed in the terms of the initial concentration as

$$M_0 = V_{NC} C_0 \tag{3.90}$$

Furthermore, we can rewrite the initial amount of loaded drug in the unit of molecules as

$$N_0 = N_A \frac{M_0}{MW} \tag{3.91}$$

where N_0 is the initial number of loaded drug molecules in the nanocarrier, $N_A = 6.022 \times 10^{23}$ is Avogadro's number, and MW is the molecular weight of drug in (g/mole). The analytical and stochastic simulation results for this work are demonstrated in subsection 3.8.4.

3.8 Analytical and Simulation Results

In this section, the analytical and simulation results for diffusion-based molecular transport (or MCvD) in multilayer microenvironments are obtained using the derived expressions and stochastic particle-based simulator, which are presented in the previous sections. The analytical results are verified with the simulation results, which show a perfect match. All the simulation results are obtained by averaging over independent realizations from which the samples are selected for comparison with the analytical results. The system parameters used for simulation and analytical evaluations are listed in Table 3.2. In subsection 3.8.4, we present the results for nanocarrier-based TDDSs in TME as an application for the proposed multilayer channel model.

Table 3.2: The simulation and analytical system parameters (unless stated otherwise).

Parameter	Value	Unit	Description
Q	10^5	mol.	No. of released molecules by TN.
T_a	310	K	Absolute medium temperature.
η_{Water}	0.6913	g/m.s	Water viscosity [140].
η_{Blood}	2.46	g/m.s	Blood viscosity [141].
η_{Air}	0.01827	g/m.s	Air viscosity.
D_{water}	131.3	$\mu m^2/s$	Water diffusion coefficient calculated using (3.2).
D_{Blood}	36.9	$\mu m^2/s$	Blood diffusion coefficient calculated using (3.2).
D_{Air}	5000	$\mu m^2/s$	Air diffusion coefficient calculated using (3.2).
r_m	2.5	nm	Radius of insulin molecule [142].
R_{rx}	2	µm	Radius of RN.
(x_0, y_0, z_0)	(5, 5, 10)	µm	Coordinate of TN center.
$(x, y, z)_1$	(1, 1, 25)	µm	Coordinate of RN center in layer 1.
$(x, y, z)_2$	(1, 1, -5)	µm	Coordinate of RN center in layer 2.
d	5 – 30	µm	Distance between TN and RN.
(Z_{sep}, Z'_{sep})	1-10	µm	Separation from the interface to TN and RN along the z-axis, respectively.
Δt	0.1	ms	Simulation time step.
T_s	4	s	Total simulation time.
-	100	-	Number of the iterations.

The proposed models in this chapter can be applied for MCvD over both microscale and macroscale multilayer media. In this work, we focus on microscale MCvD to demonstrate the applicability and validity of the proposed models for multilayer biological microenvironments. In the literature, insulin is widely used as a messenger molecule in MCvD systems [55]. Hence, for the sake of calculations and comparison, the insulin molecule is chosen as an information molecule. The size of the natural biochemical molecules like hemoglobin, insulin, and albumin are 5-10 nm in diameter; therefore, the

radius of the insulin molecule is chosen to be 2.5 nm [142]. The whole blood is a natural mixture of blood plasma and blood cells. The diffusion coefficients for Insulin molecule in the whole blood, water, and air at human body temperature (310K) can be calculated using Eq. (3.2).

For the sake of analysis, the MC media is considered to have distinct layers of air, water, and blood. In this work, the transmitting nanomachine (TN) is always assumed to be in layer-1. The derived expressions of the CIR for multilayer MCvD media are compared with the averaging (steady-state) approach given in [51, 52]. The results indicate the inability of the averaging approach to accurately estimate the temporal channel characteristics. In this section, we use the notations, 'W', 'B', and 'A' to indicate water, blood, and air layers, respectively. As an example, the notation 'W-B' is used to indicate water in layer-1 and blood in layer-2, while the notation 'B-W' indicates the reverse order. Similar notation for a medium of three-layers is followed, e.g., denoting 'A-W-B' to indicate air, water, and blood forming the medium layers in that order, respectively.

We will also examine the effect of the interface locations with respect to the TN, i.e., Z_{sep}, and with respect to the RN, i.e., Z'_{sep}. Moreover, the effect of each layer thickness on the molecular concentration will be investigated. In this section, CIR_i refers to the CIR assuming that the RN is located in the i^{th} layer. In general, the CIR expressions of MCvD in multilayer media will be reduced to homogeneous single-layer media when the diffusion coefficients of all the layers are made equal. As an example, the CIR, the peak amplitude, and the peak time of two-layer medium can be reduced to that in a single-layer medium when the layers have the same diffusion coefficients. To verify this, a two-layer medium, i.e., N=2, is reduced to a single-layer medium by replacing the diffusion coefficients, D_1 and D_2, with single diffusion coefficient, $D=1\times10^{-9}$ m^2/s, in the analytical expressions of the molecular concentration.

These results match very well with the derived results as well as with the simulation results for a single-layer medium with $D=1\times10^{-9}$ m^2/s, as shown in Figure 3.6. In this figure, the separation distance between the TN and RN is chosen to be 3μm, the number of released molecules is equal to $Q=5\times10^5$, and the RN has a radius of 0.4 μm [130]. The simulation

results are compared for both a single realization and an average of 100 independent realizations.

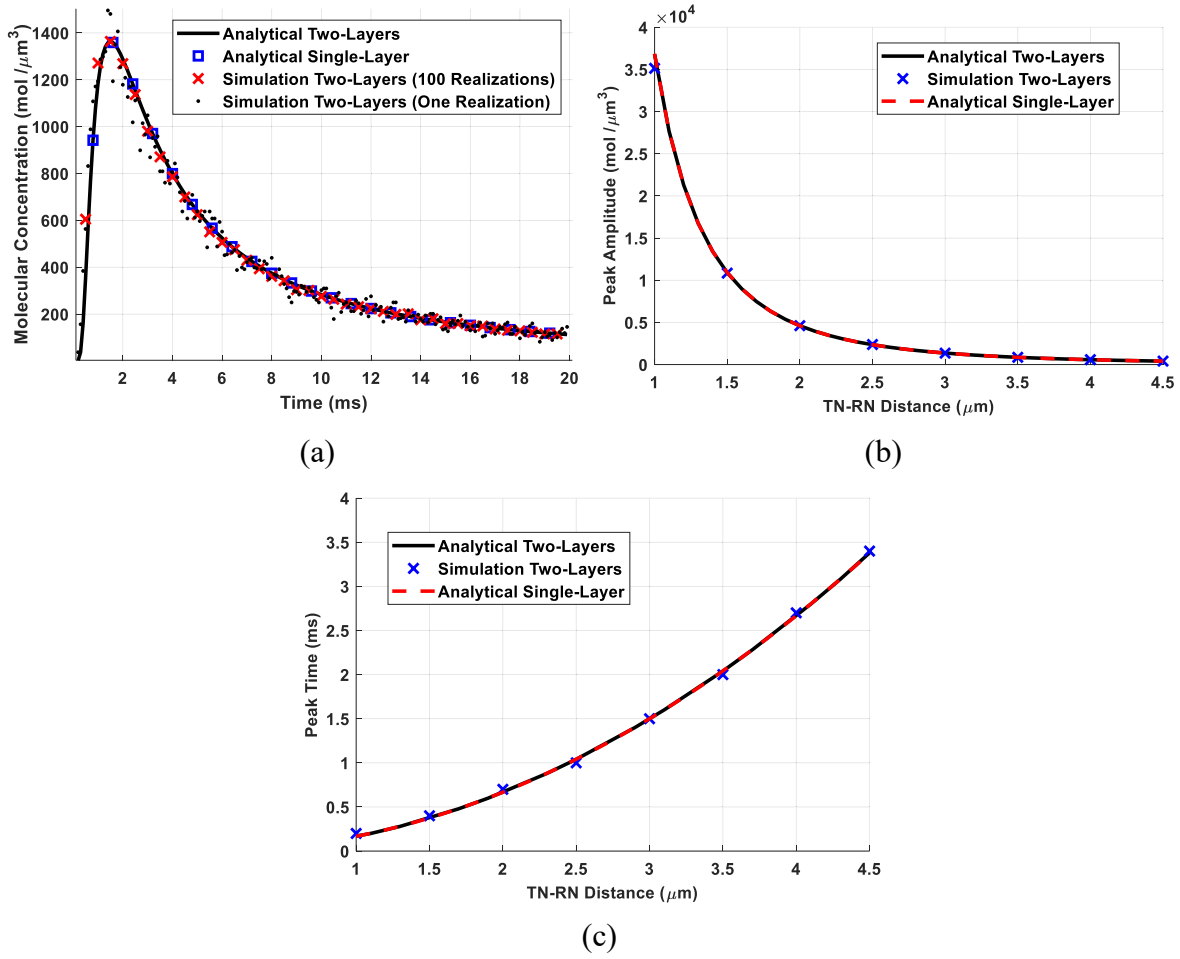

Figure 3.6: (a) Molecular concentration as a function of time, (b) peak amplitude and (c) peak time versus the separation distance between TN and RN for a single-layer and two-layer media with identical diffusion coefficients.

3.8.1 The CIR of Two-Layer Medium: TN and RN in Different Layers

The CIR in layer-2 (CIR_2) is calculated using Eqs. (3.30) and (3.60) when the RN is positioned in layer-2 for both 'W-B' and 'B-W' media for various interface separations, i.e., Z_{sep} and Z'_{sep}, as shown in Figure 3.7. Here, we assume the separation distance between the TN and the RN is fixed. In addition, the stochastic simulation results of the CIR are compared with the analytical results. The results show that the interface separations have a significant impact on the CIR in layer-2 (CIR_2). In the case of 'W-B' medium, with increasing Z_{sep}, the peak amplitude of the CIR_2 increases while both the signal peak time and width decrease.

However, the trend appears to be reversed with increasing of Z'_{sep}. This could be due to increased thickness of the water-region between the TN and the interface, that has higher diffusivity than blood. Hence, as Z_{sep} increases, the molecules will have a higher probability to diffuse faster from Water (layer-1) towards Blood (layer-2). Accordingly, a large number of the molecules can reach the receiver more quickly which leads to an increase in the peak amplitude with corresponding reduction in the signal peak time and width. As expected, if the order of the layers is reversed, i.e., for 'B-W' medium, the trend will be reversed since the thickness of the blood-filled region between the TN and the interface will increase.

In Figure 3.7, we can see how approximating the multilayer MCvD channel as a single-layer medium with averaged diffusion coefficient, i.e., the averaging approach as proposed in [51], leads to inaccurate prediction of the CIR. The results obtained using averaging method diverge significantly from our exact results for both 'W-B' and 'B-W' medium and for all interface separations, namely, Z_{sep} and Z'_{sep}. We find this holds true even for a multilayer channel (i.e., N>2) as will be discussed later. This confirms that the averaging approach cannot accurately model the MCvD in multilayer channels.

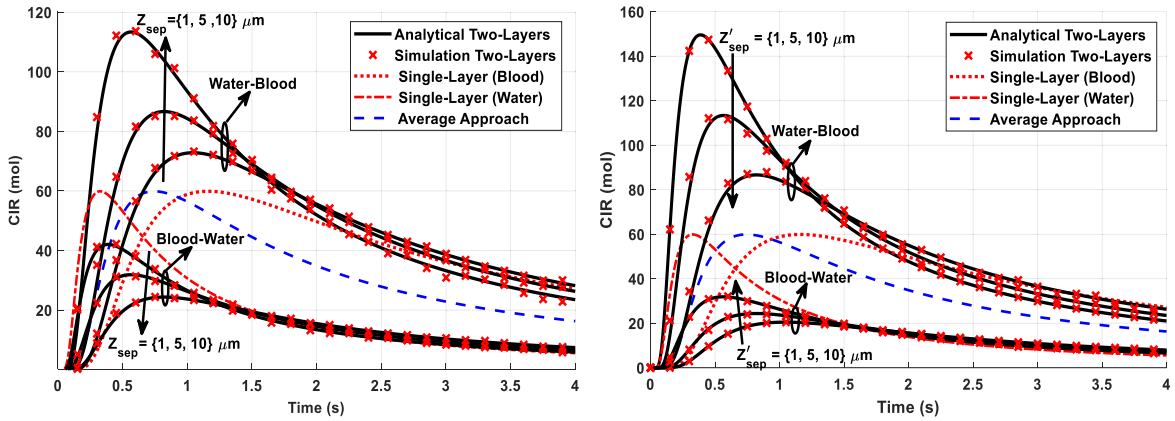

(a) (b)

Figure 3.7: The CIR in layer-2 (CIR_2) as a function of time in a two-layer medium for various separation distances between (a) the TN and the interface (Z_{sep}) (b) the RN and the interface (Z'_{sep}).

Also, the CIR of a single-layer medium using the diffusivity of layer-2 (D_2) is compared with the CIR of a two-layer medium, as indicated in Figure 3.7. The results show a larger mismatch between the two CIRs when the TN in layer-1 has moved far away from the

interface, e.g., Z_{sep}=10µm. However, this mismatch can be reduced if the TN moves closer to the interface, e.g., Z_{sep}=1µm. As the TN moves closer to the interface, most of the molecules move towards layer-2 where the RN is located. Therefore, the diffusivity of layer-2 (D_2) plays a dominant role as it contributes to reducing the mismatch between the two CIRs.

This mismatch seems to be smaller when the RN, located in layer-2, is moved far away from the interface, e.g., Z'_{sep}=10µm, and it increases as the RN gets closer to the interface. The reason is that as the RN moves closer to the interface, the molecules that contribute to the CIR_2 will mainly be affected by the diffusivity of layer-1 (D_1) most of the time because the thickness of the region between the RN and the interface decreases. Figure 3.7 also shows that the peak amplitude of the CIR for a single-layer medium, which is calculated using both our proposed expressions and the averaging approach given in [51], have identical values whatever the diffusivity value. This is because the peak amplitude of the CIR does not depend on the diffusion coefficient in a single-layer medium.

Influences of the diffusion coefficient of each layer on the temporal behaviour of the CIR_2 is examined and plotted in Figure 3.8. The diffusion coefficients are varied in integer multiples of water and blood diffusivities, viz., D_1= m×D_{Water} and D_2= m×D_{Blood}, where m=1, 2, 3. One can observe that, when the RN is positioned in layer-2, the diffusion coefficients influence the CIR_2, peak amplitude, peak time, and signal width significantly.

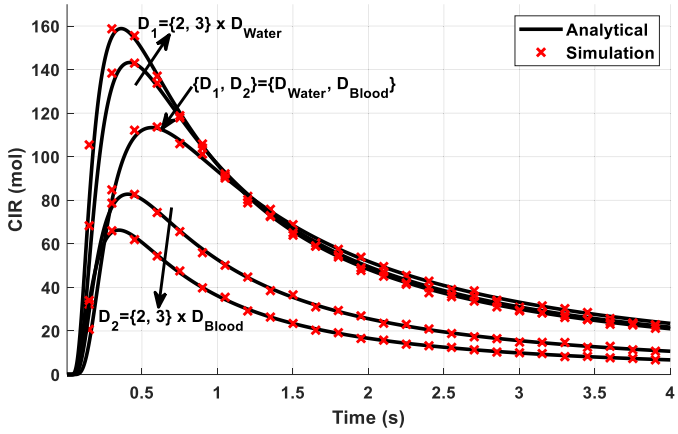

Figure 3.8: The CIR in layer-2 (CIR_2) as a function of time for diffusion coefficients (D_1, D_2) with values equal to integer multiples of D_{Water} and D_{Blood} when Z_{sep}=10µm.

The peak amplitude of the CIR in layer-2 (CIR_2) as a function of TN-RN separation is plotted

in Figure 3.9 for $D_1=m\times D_{Blood}$ and $D_2=m\times D_{Water}$, where m=1, 2 is an integer multiple. Here, we examine effect of the interface separation with respect to TN and RN locations assuming that the TN is located in layer-1 and the RN in layer-2. As the diffusivity D_1 increases, the molecules will diffuse faster across the interface from layer-1 into layer-2. Thus, the peak amplitude of the CIR at the RN in layer-2 will increase. However, the peak amplitude of CIR_2 decreases with increasing the diffusivity of layer-2 (D_2), because the molecules tend to return back from layer-2 to layer-1 with higher probability. Therefore, this could cause a significant reduction in the peak amplitude at the RN in layer-2. More importantly, these results show that in a two-layer MCvD medium, the peak amplitude is highly dependent on the diffusion coefficients, unlike in a single-layer medium where it is independent of the diffusivity [130].

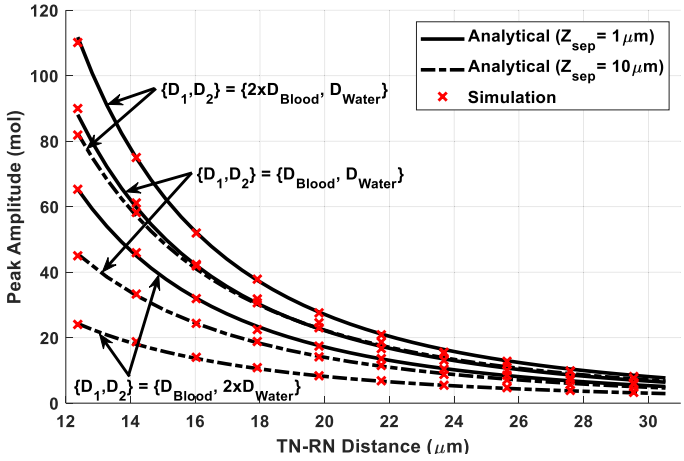

Figure 3.9: The peak amplitude of the CIR in layer-2 (CIR_2) versus TN-RN separation for different values of the diffusion coefficients.

Consider a specific example where the RN is located at a distance d=14μm from the TN that is placed near the interface with Z_{sep}=1μm. In this case, the peak amplitude shows an increase by a factor of 1.2 when $D_1=2\times D_{Blood}$ while it decreases by a factor of 0.7 when $D_2=2\times D_{Water}$. However, when the TN is located far away from the interface, i.e., Z_{sep}=10μm, the peak amplitude increases by a factor of 1.8 for $D_1=2\times D_{Blood}$, and it decreases by a factor of 0.4 for $D_2=2\times D_{Water}$. Also, we can see that the peak amplitude decreases as the separation distance between the TN and the RN increases since only a few molecules can reach the RN. For 'B-W' medium, when the TN is located near the interface (Z_{sep}=1μm), doubling the TN-RN separation distance reduces the peak amplitude by a factor of 1/8 approximately, i.e., $N_{peak} \propto 1/d^3$.

Figure 3.10 shows the peak time of the CIR in layer-2 (CIR_2) as a function of TN-RN separation distance for $D_1=m\times D_{Water}$ and $D_2=m\times D_{Blood}$, where m=1, 2 is an integer multiple. It can be observed that any increase in the diffusion coefficients, D_1 or D_2, leads to reducing of the peak time of CIR_2. We can see that the peak time is mainly influenced by the layer-2 diffusion coefficient (D_2). This is because the impact of the diffusion coefficient of layer-2 (D_2) on the peak time of CIR_2 is the dominant factor since the RN exists in layer-2. As D_2 increases, the peak time decreases sharply because the molecules in layer-2 will diffuse faster towards the RN, which consistent with the literature [130]. Results also indicate that there is a minor impact for D_1 on the peak time of CIR_2 when the TN is located closer to the interface, i.e., $Z_{sep}=1\mu m$. This could be due to the increased probability for the molecules to diffuse into layer-2 and consequently, they will be influenced by the diffusion coefficient of layer-2, most of the time. As an example, when the separation distance between the TN and the RN is equal to 28µm, and the TN is positioned closer to the interface, i.e., $Z_{sep}=1\mu m$, the peak time decreases by a factor of 0.97 for $D_1=2\times D_{Water}$ and by a factor of 0.5 for $D_2=2\times D_{Blood}$. On the other hand, when the TN is located far away from the interface, i.e., $Z_{sep}=10\mu m$, the peak time decreases by a factor of 0.9 for $D_1=2\times D_{Water}$ and by a factor of 0.6 for $D_2=2\times D_{Blood}$.

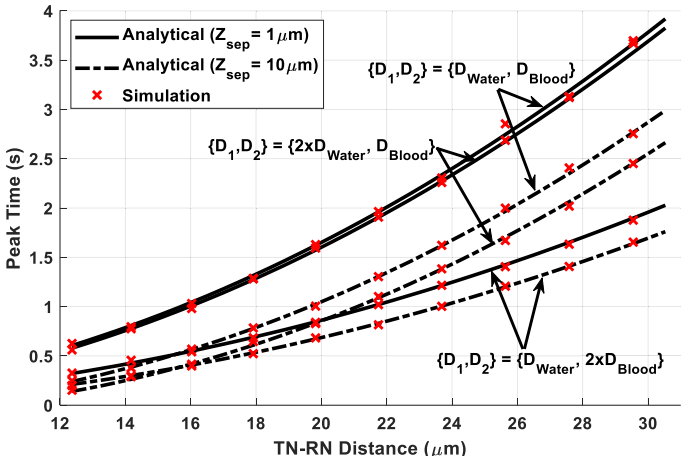

Figure 3.10: The peak time of the CIR in layer-2 (CIR_2) versus TN-RN separation for different values of the diffusion coefficients.

The peak time also increases as the separation distance between the TN and the RN increases since the molecules will take longer time to reach the RN. As an example, for 'W-B' medium and when the TN-RN separation distance is doubled, the peak time is four-times longer when

the TN is located near the interface, i.e., Z_{sep}=1μm, and six times longer when the TN is located far from the interface, i.e., Z_{sep}=10μm, as shown in Figure 3.10.

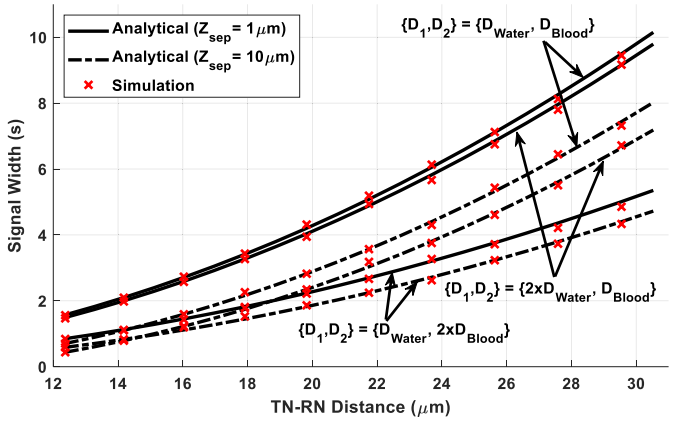

Figure 3.11: The width of the CIR in layer-2 (CIR_2) versus TN-RN separation for different values of the diffusion coefficients.

Figure 3.11 illustrates the width of the CIR in layer-2 versus the TN-RN separation distance when the diffusion coefficients, D_1 and D_2, have values equal to integer multiples of D_{Water} and D_{Blood}, respectively. As indicated in this figure, the signal width follows a similar trend as that of the peak time. As an example, doubling of the TN-RN separation distance results in four-times wider width in the CIR, as shown in Figure 3.11. Also, our results in a two-layer diffusive channel suggest that doubling the diffusion coefficient of layer-2 (D_2) will result in 50% reduction in the signal width.

3.8.2 The CIR of Two-Layer Medium: TN and RN in the Same Layer

The CIR in layer-1 (CIR_1) is calculated using Eqs. (3.30) and (3.57) when both the TN and the RN are located in layer-1 for both 'W-B' and 'B-W' media and for different interface separations, i.e., Z_{sep} and Z'_{sep}. The CIR in layer-1 (CIR_1) as a function of time is plotted in Figure 3.12 for both 'W-B' and 'B-W' media and various interface separation from the TN (Z_{sep}) and RN (Z'_{sep}). Since both the TN and the RN exist in the same layer (layer-1), their separations from the interface have the same effect on the CIR_1. We compare the CIR_1 for the two-layer medium with that obtained by approximating the channel as a single-layer medium, i.e., averaging approach [51], to further highlight the deficiency of the latter. As expected, for both 'W-B' and 'B-W' media, the averaging approach shows large mismatch

with our CIR_1 results for all interface separations. The peak amplitude of CIR_1 increases with an increase in either Z_{sep} or Z'_{sep} for 'W-B' medium, while the trend is reversed for 'B-W' medium. In case of 'W-B' medium, this may be due to the increased probability of the molecules that diffuse faster mainly under the diffusivity of layer-1 (water) while the reversing trend for 'B-W' medium, is because the blood has lower diffusivity than water.

One can see from Figure 3.12, as the TN gets closer to the interface, e.g., Z_{sep}=1μm, the mismatch increases while it decreases when the TN is located far away from the interface, e.g., Z_{sep}=10μm. This decreasing in the mismatch is due to increase the thickness of the region between the TN and the interface when Z_{sep} increases and thus helping the molecules to remain most of the time in layer-1. Consequently, the influence of layer-2 on the molecules can be neglected, which in order making the two-layer medium to behave as a homogeneous single-layer medium with the diffusion coefficient of layer-1 (D_1). However, if the TN becomes closer to the interface, this approximation cannot be used anymore to obtain the CIR_1 of a two-layer medium because most of the molecules will diffuse into layer-2 and they will mainly be influenced by diffusivity of layer-2.

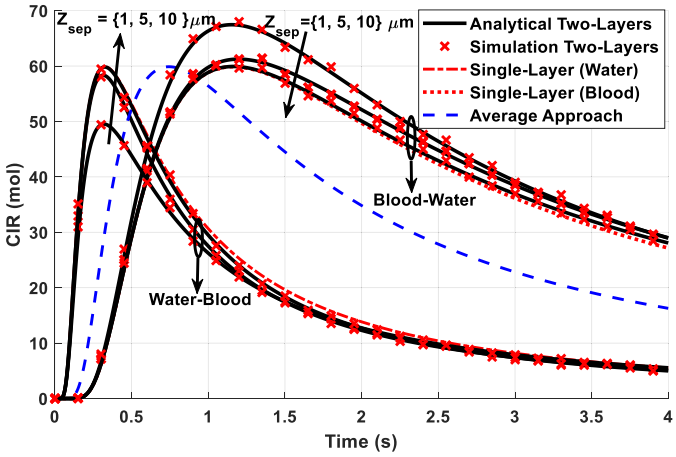

Figure 3.12: The CIR of layer-1 (CIR_1) as a function of time for varying separation distances between the TN and the interface (Z_{sep}).

Figure 3.13 shows the CIR of layer-1 (CIR_1) versus time when the diffusion coefficients of both the layers are increased in integer multiples of water and blood diffusivities, viz., $D_1=m\times D_{Blood}$, and $D_2=m\times D_{Water}$. We can see in this figure how varying the diffusion coefficients affects the characteristics of CIR_1 when the TN is located far away from the

interface, e.g., Z_{sep}=10μm. In this case, the diffusion coefficients, D_1 and D_2, have no influence on the peak amplitude of the CIR_1 since the medium effectively acts as a single-layer medium for which the peak amplitude is independent of the diffusivity. On the other hand, the results indicate that the diffusivities, D_1 and D_2, have a little impact on the peak amplitude only when the TN is located closer to the interface, e.g., Z_{sep}=1μm. One can observe that the peak time of the CIR_1 is mainly influenced by the diffusion coefficient of layer-1 (D_1) since the RN is positioned in layer-1. As the diffusivity (D_1) increases, the peak time decreases because the information molecules in layer-1 will diffuse faster to reach the RN, which exists in layer-1.

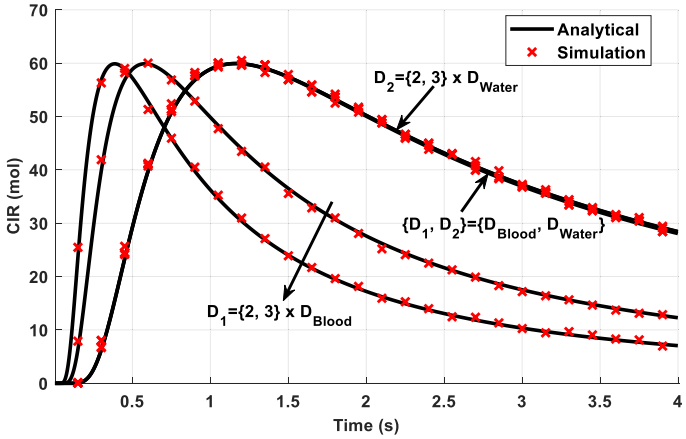

Figure 3.13: The CIR of layer-1 (CIR_1) as a function of time for varying diffusion coefficients (D_1, D_2).

In Figure 3.14, the performance metrics of the CIR in layer-1 (CIR_1) versus TN-RN separation is plotted for different values of the diffusion coefficients, i.e., for $D_1=m\times D_{Blood}$ and $D_2=m\times D_{Water}$, where m=1,2. Similar to the results in the previous subsection, the peak amplitude shows a decreasing trend over the separation distance between the TN and the RN while the peak time and signal width increase as the TN-RN separation distance increases. As an example, if the TN-RN distance is doubled, the peak amplitude will decrease by a factor of 1/8 while a four-fold increase in the peak time is observed. However, the impact of the diffusion coefficients on the peak amplitude is negligible when the separation distance between TN and RN is very large because the dominating factor on the peak amplitude is the distance rather than the diffusion coefficients. As previously mentioned, the signal width has a similar trend as the peak time.

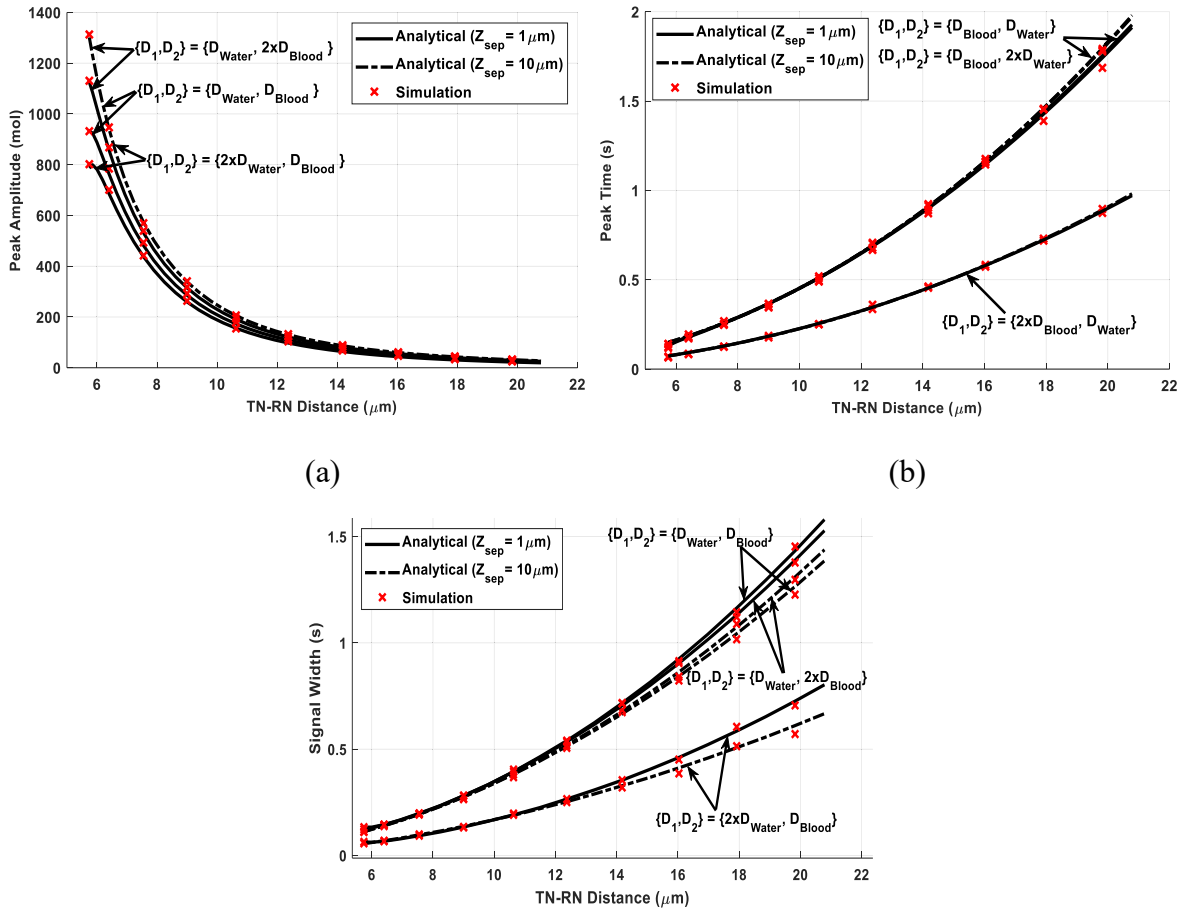

Figure 3.14: The communication metrics of the CIR in layer-1 (CIR_1) versus TN-RN separation for different values of the diffusion coefficients (a) the peak amplitude (b) the peak time (c) the signal width.

3.8.3 The CIR of Three- and Four-Layer Media: TN and RN in Different Layers

Now we show results for a three-layer medium (N=3) when the TN is located in layer-1 and the RN in layer-3 for 'A-W-B' and 'A-B-W' media. The CIR in layer-3 (CIR_3) as a function of time for a three-layer medium is plotted in Figure 3.15. The CIR_3 results are evaluated using Eqs. (3.30) and (3.67) for various values of the separation distance between the TN and the interface (Z_{sep}). The CIR_3 has higher peak amplitude and lower peak time for 'A-W-B' medium compared to the case when the second and third layers are swapped, i.e., for 'A-B-W' medium. This may be due to moving the molecules faster in the water layer, which has higher diffusivity than blood.

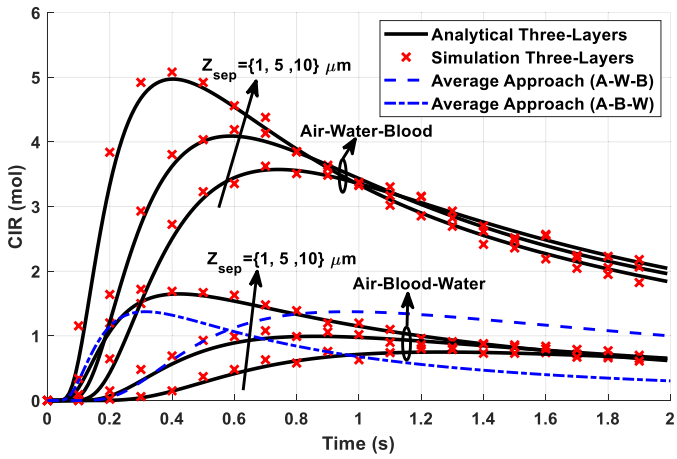

Figure 3.15: The CIR in layer-3 (CIR_3) as a function of time for three-layer medium with different interface separation from the TN (Z_{sep}).

As an example, when the medium is 'A-W-B', the molecules will move faster in layer-2 (water) and take a shorter time to enter the layer-3 (blood). Since most of the molecules enter layer-3 (blood) rapidly, the number of received molecules by the RN increases while the peak time decreases. As the separation distance from the TN to the interface between layer-1 and layer-2 (Z_{sep}) increases, the peak amplitude increases (but the peak time decreases) for both 'A-W-B' and 'A-B-W' media. Since the TN is located in the layer-1 (Air) which has higher diffusivity than both water and blood. Therefore, as the interface separation (Z_{sep}) increases, the thickness of the region, filled by air, increases which may make most of the molecules diffuse faster in layer-1 (air) before they reach layer-2. In order to confirm this result, we perform a stochastic simulation to monitor the number of molecules as a function of time in each layer, as shown in Figure 3.16. We find that the total number of the molecules in layer-2 (water) reaches its peak value in a short time, but it decreases rapidly compared to the case when the layer-2 is filled with blood. The reason for the high reduction in the molecules in layer-2 that is filled with water is due to the increased number of the molecules that move to layer-3, where the RN is located. However, only few molecules go back from layer-2 to layer-1. In case of 'A-W-B' medium, the molecules may stay shorter time in layer-2 (water) before they diffuse to layer-3, while for 'A-B-W' medium, most of the molecules spend a longer time in layer-2 (blood) before entering layer-3. This explains why the spatiotemporal channel characteristics change when the layers are swapped. As expected, the results that are

predicted by the averaging approach do not match with our exact CIR results for both ‘A-W-B’ and ‘A-B-W’ media, as shown in Figure 3.15.

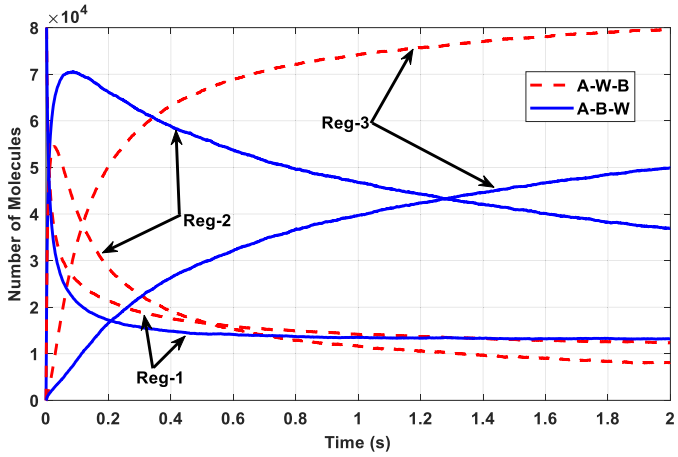

Figure 3.16: The total number of molecules in each layer as a function of time in ‘A-W-B’ and ‘A-B-W’ media.

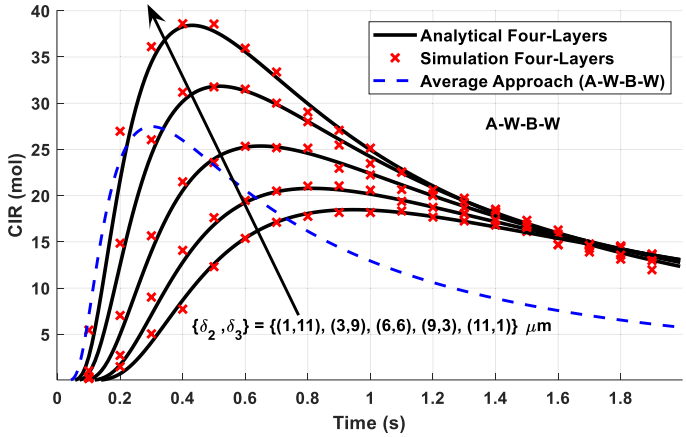

Figure 3.17: The CIR in layer-4 (CIR_4) as a function of time for a four-layer medium with different thicknesses of layer-2 and layer-3.

Now we consider a four-layer MCvD channel formed of ‘Air-Water-Blood-Water’ (A-W-B-W). The time dependency of the CIR in layer-4 (CIR_4) on the thicknesses of layer-2 and layer-3 is calculated using Eqs. (3.30) and (3.67) as shown in Figure 3.17. The results show that when the thickness of layer-2 (water) increases and the thickness of layer-3 (blood) decreases, we get higher amplitude and shorter peak time because the water has higher diffusivity than blood. Here, most of the molecules will diffuse most of the time in the water

layer rather than the blood layer. Hence, the number of molecules that diffuse into layer-4 increases, and particularly, they reach the RN in a shorter time as the thickness of the water layer gets wider. However, the averaging approach [51], clearly fails to give accurate predictions in a four-layer MCvD medium.

3.8.4 The Results for Intravascular Drug Delivery using Nanocarriers

In this model, we assume that the nanocarriers (NCs) are loaded with doxorubicin (DOX) anticancer drug and can release their payloads intravascularly in the tumor microenvironment (TME) as described in section 3.7. Whatever the type of the NCs and the triggering strategy of drug release, drug molecules need to get transported across the endothelial barrier to reach the tumor tissue, as shown in Figure 3.18. The therapeutic efficacy of the drug delivery system using NCs depends not only on the properties of the encapsulated drug but also on the drug biodistribution and drug release rates of the individual NC. In this model, the biological microenvironment consists of three regions (or layers), namely, lumen, endothelial barrier, and tumor tissue with thicknesses given in Table 3.3, [60, 143].

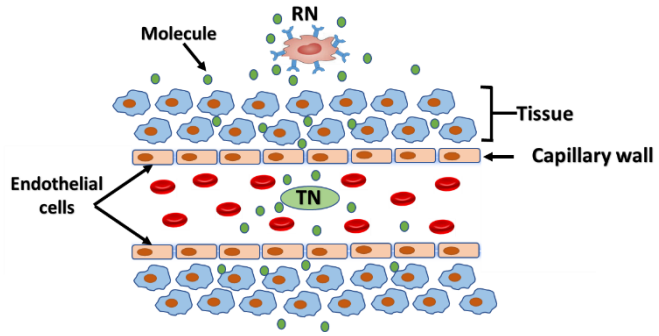

Figure 3.18: Transport of drug molecules across the endothelial barrier to the surrounding tissue following drug release from a nanocarrier.

Table 3.3: Thicknesses of the microenvironment layers.

Region	Thickness (µm)
Blood	15
Endothelial barrier	1
Tumor tissue	1000

The hydraulic radius of DOX molecule can be calculated as [144]:

$$r_m = \left[\frac{3(\mathrm{MW})}{4\pi N_A \rho}\right]^{1/3} \tag{3.92}$$

where MW is the molecular weight, ρ is the specific density, and N_A is Avogadro number. Then, the diffusivity of DOX in the lumen (blood) can be calculated using Eq. (3.2).

The model described in subsection 3.7 can be applied for different types of drug-loaded vesicles or nanocarriers. However, we have chosen DOX-loaded thermosensitive liposome (TSL) as a drug nanocarrier because it is highly suitable for intravascular release approach and there is a lot of experimental data available in the literature [85, 145]. Liposomes have been successfully developed and clinically approved as drug nanocarriers, e.g., Doxil®/Caelyx® [32]. Moreover, a new TSL version with ultrafast drug release patterns, lysolipid TSL (LTSL), is the most clinically successful TSL for triggered release of DOX (it is commercialized as ThermoDox®) [85, 145]. After injection of TSLs in the bloodstream and then reaching the tumor vasculature, localized intravascular drug release can be achieved by applying an external heat-trigger between 39°C and 42°C to the target area, i.e., hyperthermia (HT) [32]. Then, TSLs will release drug inside the tumor microvessels with high local concentration, which increases drug bioavailability in the tumor tissue.

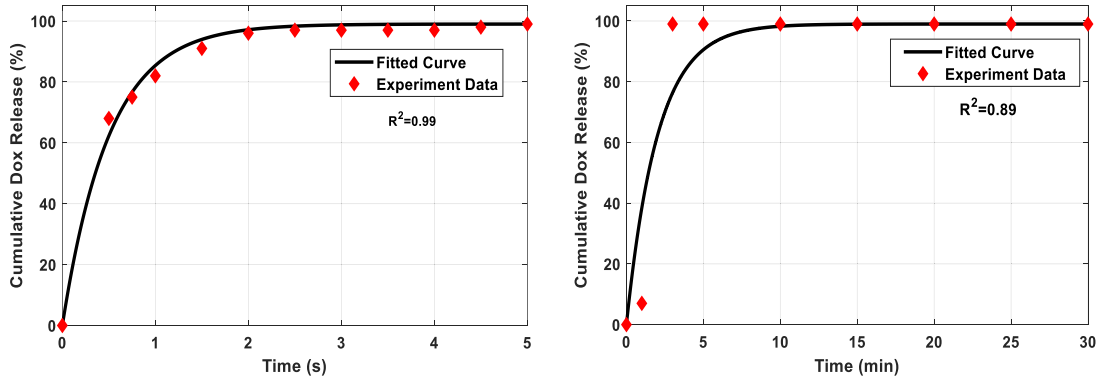

(a) (b)

Figure 3.19: Percentage cumulative release of doxorubicin from (a) NC1 and (b) NC3, fitted to the published experimental data in [49, 138].

We fit the expression of percentage cumulative drug release, Eq. (3.78), to the experimental release data of TSL nanocarriers in [49, 138]. Using nonlinear least-squares fitting method,

we obtain the release rate constants as listed in Table 3.4. As shown in Figure 3.19, the curve fitting shows high fitting accuracy with the experimental data.

In this section, we show the analytical and stochastic simulation results for DOX spatiotemporal distribution profile in tumor tissue after intravascular release of DOX drug from TSL nanocarrier. Here, we consider three nanocarriers, namely, NC1, NC2, and NC3, each has a different release rate constant as listed in Table 3.4. The system parameters, used in this model, are listed in Table 3.3, Table 3.4, and Table 3.5.

Table 3.4: Properties of the nanocarrier (TSL).

Parameter	Value	Unit	Description	References
C_0	2	mg/ml	Initial concentration of the loaded DOX.	[146]
k_{r_42C}	{2, 0.05, 0.008}	s^{-1}	Release rate constant at 42°C for NC1, NC2, and NC3, respectively.	[49, 138]
k_{r_37C}	0	s^{-1}	Release rate constant at 37°C.	[49, 138]
M_∞	99	%	Total percentage of cumulative release.	[49, 138]
r_{NC}	50	nm	Radius of the nanocarrier.	[49]

The simulation parameters, used in the stochastic simulation model, have the following values (unless stated otherwise): Q =10^5 molecules, Δt =0.1s, and the iterations number =100. These values are chosen based on conducting a trial and error run to get negligible change and variation in the simulation results. The drug nanocarrier is located in the center of the microvessel while the concentration is monitored using a virtual spherical observer located inside the tumor tissue at distance 250μm from the microvessel. Here, we assumed that HT is applied for a duration enough to release the total amount of loaded DOX from the nanocarrier. The DOX concentration is given in unit of (molecules/m^3) using Eq. (3.91). Impact of the blood flow inside the microvessels on the release and distribution processes of the drug will be left for future work.

Table 3.5: Properties of anticancer drug doxorubicin (DOX).

Parameter	Value	Unit	Description	References
P_{vt}	1	μm/s	Permeability of tumor vascular	[147, 148]
P_{vn}	0.333	μm/s	Permeability of normal vascular	[147]
MW	544	g/mol	Molecular weight	[147]
r_m	0.5126	nm	Hydraulic radius	Calculated using Eq. (3.92).
ρ	1.6	g/cm^3	Specific density	[149]
D_b	180	μm^2/s	Diffusivity in blood	Calculated using Eq. (3.2).
D_n	158	μm^2/s	Diffusivity in normal tissue	[49]
D_t	340	μm^2/s	Diffusivity in tumor tissue	[49]

The temporal drug concentration profiles in tumor tissue using NCs with different release rates, are shown in Figure 3.20. The DOX concentration in tumor tissue shows rapid rise in early time after the intravascular release of drug from the nanocarrier until reach the maximum value (C_{max}), then decreases slowly with the time. We can see that the release rate affects both time and amplitude characteristics of the drug concentration profile. The nanocarrier with higher release rate (NC1) leads to higher peak concentration (and lower peak time) compared to the nanocarrier with a slow-release rate (NC3). This trend coincides with the experimental results in the literature which indicated that the faster release TSLs lead to higher drug accumulation in the tumor tissue and provide better therapeutic efficiency compared to the slow release TSLs [1, 85, 150]. Therefore, it is important to characterize and optimize the release rate of the nanocarrier to get the desired concentration profile. We can observe that as the release rate becomes very rapid, the drug concentration profile becomes close to that due to impulse release which represents the basis for deriving the concentration profiles for other release patterns. Moreover, drug concentration profile in tumor tissue has different temporal characteristics for each nanocarrier. For example, the peak DOX concentration (C_{max}) is reached at 0.86 min and 2.86 min, using NC1 and NC3, respectively.

As shown in this figure, the nanocarrier with higher release rate (NC1) has an identical concentration profile to that obtained using the CIR alone. This indicates important of the

CIR which can be used for modelling the release and distribution of the drug in tissues either for nanocarriers with fast or slow release rates as demonstrated in subsection 3.7. The results show that any further increase in the release rate beyond a threshold value will not result in notable biodistribution changes compared to uncontrolled (impulse) drug release. Therefore, the drug release rate is an essential factor for the optimal formulation of the nanocarriers such as liposomes.

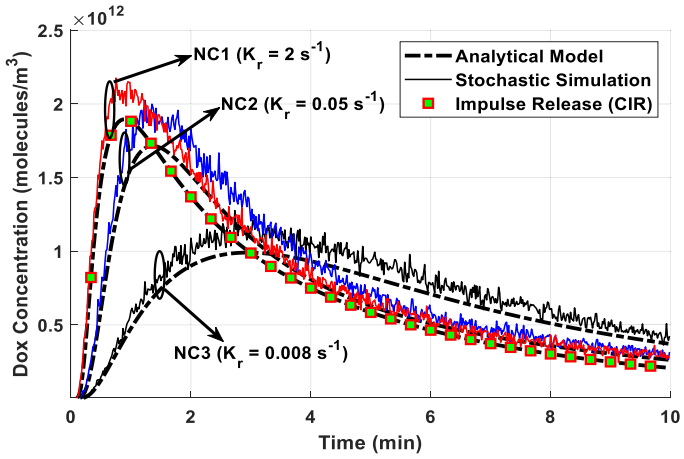

Figure 3.20: DOX drug concentration in tumor tissue for three nanocarriers with different release rate constants.

In Figure 3.21, the peak (maximum) DOX concentration and the corresponding peak time are plotted versus the distance from the microvessel for three nanocarriers (NC1, NC2, and NC3). As expected, the peak concentration decreases (and peak time increases) with the distance and thus the drug molecules can penetrate in the tumor tissue with limited depth. Also, the NC with faster releasing rate (e.g., NC1) results in higher peak concentration (and lower peak time) compared to other NCs which have slower release rates, e.g., NC3. This coincides with the experimental studies on heat triggered intravascular drug release from DOX-TSL. The experimental data show that the rapid release TSL resulted in a larger penetration depth compared to the low release liposomes such as Doxil™ [33, 151]. This indicates that the drug penetration depth in tumor tissue can be improved using NCs with rapid release patterns. Moreover, the experimental data show that the range of the penetration depth is in a micrometer scale. However, high drug concentration could lead to toxicity, and therefore, a trade-off between toxicity and therapeutic efficiency is necessary.

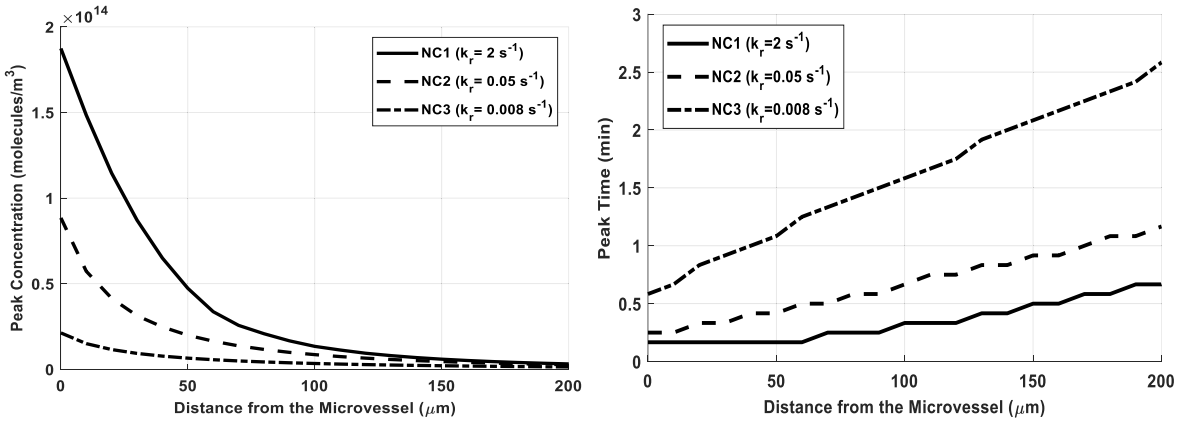

(a) (b)

Figure 3.21: (a) Peak concentration in tumor and (b) corresponding peak time versus the distance from the tumor microvessel for different nanocarriers.

Figure 3.22 shows the DOX concentration in tumor for three microvessels with different endothelial barrier permeabilities using NC1 and NC2. An increase in the vascular permeability will enhance the diffusion of drug molecules across the barrier into the surrounding tissue, which in order increases the drug accumulation in tumor tissue. The tumor vasculature has larger permeability compared to that in normal tissue due to the larger gaps between the endothelial cells that line the interior surface of the blood vessels, this is known as the enhanced permeability and retention (EPR) effect [152]. Therefore, higher amount of DOX drug accumulates in tumor compared to healthy tissue.

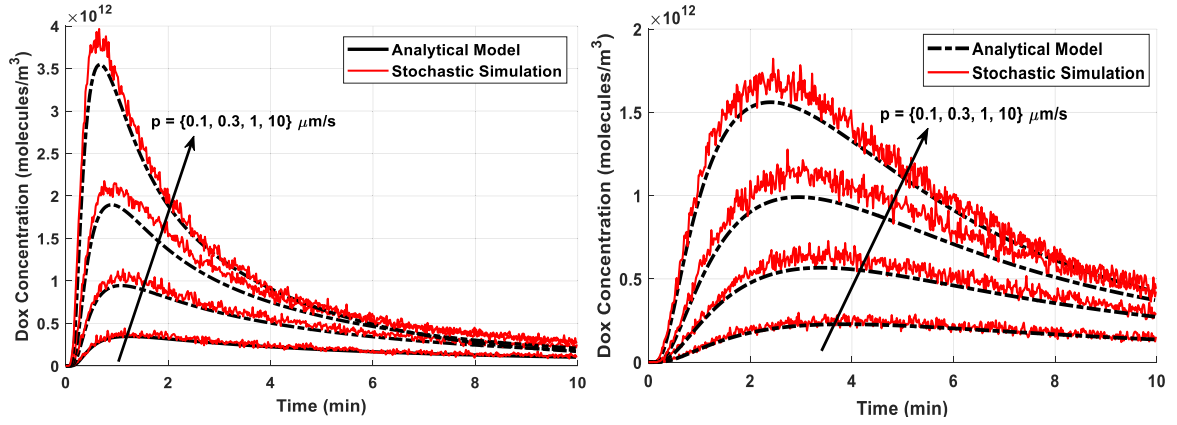

(a) (b)

Figure 3.22: Drug concentration profile in the tumor for different vascular permeabilities using (a) NC1 (b) NC3.

3.8.5 The Results for Biomarker Monitoring of Atherosclerosis in Artery Wall

Atherosclerosis is the most serious and common cardiovascular disease (CVD) and one of the leading causes of death in the world. Atherosclerosis blocks the artery and reduces the blood flow due to the accumulation of fatty deposits (plaque) in the arterial wall. The Pentraxin-3 (PTX3) is inflammatory biomarker, mainly produced by the various cells in atherosclerotic lesions. It can be used as an early indicator for detection of the vulnerable plaques to avoid the high-risk events such as heart attacks.

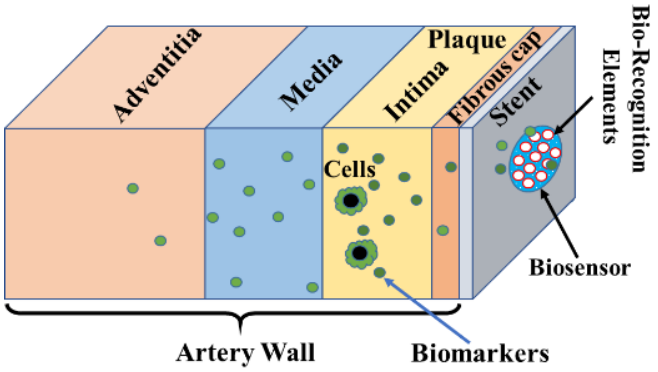

Figure 3.23: Transport of PTX3 biomarker from the molecular source to the biosensor through the atherosclerotic artery wall.

We have applied the mathematical and the stochastic simulation multilayer MCvD models for prediction of both the concentration of the PTX3 in the biosensor vicinity and the number of received PTX3 molecules by the biosensor. The molecular source is located in the first layer (i.e., intima) and the biosensor is attached to the stent in the last layer (i.e., at the interface between lumen and fibrous cap), as shown in Figure 3.23. The biological microenvironment between the molecular source (e.g., macrophage cells) and the biosensor is modelled as a multilayer medium.

In this section, we present analytical and simulation results for prediction number of the received PTX3 biomarker by the biosensor and the concentration in its vicinity. The simulation parameters, e.g., the time-step and the number of released molecules, are chosen by performing a trial and error run with different values to examine the variations in the output received signal. We found that a time-step with values less than 1s, will not lead to significant variation in the simulation results. The system parameters used in the computations are summarized in Table 3.6 and Table 3.7.

Table 3.6: System parameters of biomarker monitoring in atherosclerotic artery wall.

Parameter	Unit	Value
Simulation time	T	5 h
Time step	Δt	1 s
No. of released molecules	Q	1×10^5
Amount of released PTX3	M_0	1×10^{-4} ng/cell
Radius of Biosensor	r_b	0.5 mm
Thickness of Biosensor	L	10 µm
Molecular Weight of PTX3	MW_{PTX3}	45 kDa
Source Location	(x_0, y_0, z_0)	(0, 0, 25) µm
Number of iterations		100

Table 3.7: Parameters of the atherosclerotic intima.

Parameters	Plaque (Lipid Core)	Fibrous cap	
		Vulnerable	Stable
Thickness (µm)	650	(30, 65)	100
Diffusivity D_{PTX3} ($\mu m^2/s$)	0.043	1.72	1.72

The PTX3 concentration in the vicinity of the biosensor is plotted in Figure 3.24(a) for different thicknesses of the fibrous cap layer. The analytical concentration results show perfect match with the stochastic simulation results. The PTX3 concentration increases with the time to reach the peak value and then it begins to decrease to very low level. The PTX3 concentration in the biosensor vicinity has a higher value in the case of the vulnerable (unstable) plaque, i.e., with fibrous cap thickness (L = 30µm), compared to the stable plaque, i.e., L= 100µm. The results show that, as the fibrous cap thickness increases, the PTX3 concentration decreases while the peak time increases.

The accumulative number of received PTX3 molecules by the biosensor is obtained using the stochastic particle-based simulator for both vulnerable (L = 30µm) and stable plaques, as shown in Figure 3.24(b). As expected, the number of the received PTX3 molecules in the case of the vulnerable plaque is higher than that for stable plaque. This happens because the

concentration of PTX3 biomarker near the biosensor is higher in the case of the vulnerable plaque. The characteristics of the molecular received signal can provide critical information about the disease progression as well as the composition and thickness of the plaque and fibrous cap.

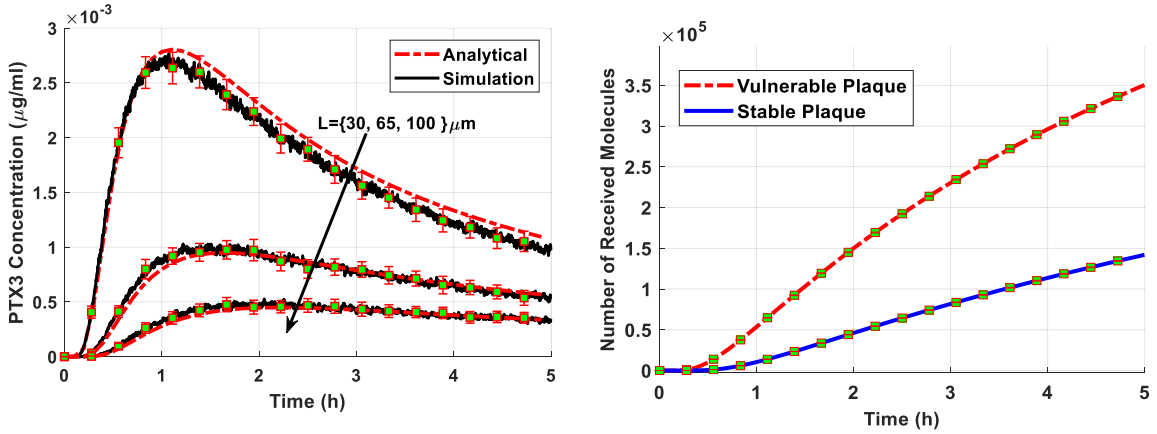

Figure 3.24: (a) The PTX3 concentration in the vicinity of the biosensor and (b) the cumulative number of received PTX3 molecules by the biosensor.

3.9 Summary

In this chapter, we present an original and rigorous mathematical and stochastic simulation models for molecular communication (transport) via diffusion in 3-D composite multilayer biological microenvironments. We derive closed-form analytical expression for the channel impulse response (CIR) of the molecular transport in multilayer media and the analytical results are validated with the stochastic simulation results. In addition, various performance metrics, namely, peak amplitude, peak time, and signal width, have been derived and evaluated for the proposed models. We examined the effects of the interface separation, the TN-RN separation, the diffusion coefficients, and the layer thickness on the CIR. We have demonstrated that the CIR for a multilayer medium reduces to that of a homogeneous single-layer medium when the diffusion coefficients of all the layers become equal. Also, when the RN is placed in multilayer media, the peak amplitude of the CIR depends on the diffusion coefficients, unlike that for the single-layer diffusive media. Our investigations have revealed that, when the TN and RN are positioned in different layers, the diffusivities, thickness of each layer, and the interface separations have a significant impact on the CIR. The work presented in this chapter can help in understanding the molecular transport in the multilayer

diffusive channels, which may provide a powerful tool to develop optimum transmitting and receiving nano-machines as well as detection techniques for MCvD systems in 3-D multilayer channels. However, the proposed models could be used for various applications that depend on the diffusion through multilayer environments.

Moreover, we exploit these models for modelling DOX drug transport across the endothelial barrier of the tumor vasculature into the surrounding tissue following intravascular drug release from the nanocarriers. We examine impact of the release rate and the endothelial barrier permeability on the drug concentration in tumor using TSL nanocarriers with different release rates. The drug concentration shows an increasing trend as the release rate or the vascular permeability increases. Moreover, we find that the drug release process by rapid release NCs can be modelled as an impulse release using the CIR alone. Furthermore, slow-release NCs still can be modelled via convolution between the CIR and the release profiles.

CHAPTER 4

Modelling of Ligand-Receptor Protein Interaction on Target Sites in Bounded Microenvironments

4.1 Introduction

Molecular communication (MC) is an emerging biologically inspired paradigm which is useful for understanding and modelling of the molecular transport and interaction between biological and/or synthetic nanomachines within aqueous biological microenvironments over nanometer to micrometer scales [7, 8]. In molecular communication via diffusion (MCvD), the information between the bio-nanomachines (e.g., living cells) is exchanged via free diffusion of chemical molecules that following random Brownian motion [8, 21]. In the previous chapter, we provide general multilayer MCvD models for predicting the molecular concentration in the vicinity of a receiver nanomachine (RN) (e.g., a target cell) after releasing of the molecules by a transmitter nanomachine (TN) (e.g., a nanocarrier) inside multilayer biological microenvironments. The interaction process between the extracellular molecules (ligands) and the surface protein receptors is highly influenced by the ligand's concentration in the vicinity of the target site (e.g., cell). The protein receptors on the cell surface act as sensors for sensing the extracellular molecular signals in both the cell-to-cell interactions and the interactions between the cell and other molecules in the environment [153]. This interaction represents the primary external stimuli for initiating the intracellular signaling pathways and the majority of current drugs depend on targeting specific receptors on the cells [154]. The biological cells may have many receptor proteins which can recognize different types of molecules. One of the examples is atherosclerosis in which the cytokine ligands (CD40L), released by platelets, bind with the CD40 receptors on the endothelial cells that cover the blood vessel wall [28, 29]. In addition, the cells can be synthesized to recognize

specific types of ligands via artificial cell surface receptors [155, 156]. However, the interactions between the ligands and the receptors may be difficult to quantify in in-vivo and in-vitro environments [153].

The MC paradigm is useful for abstraction and modelling of the drug delivery systems (DDSs). In MC paradigm, the drug source, e.g., nanocarrier, can be abstracted as a TN releasing the drug, that act as information molecules, to the target site (e.g., diseased cell) which act as a RN. The diffusive environment in which the drug molecules transport can be abstracted as a communication channel while drug degradation and elimination can be abstracted as the channel impairments. In this paradigm, the drug concentration in the vicinity of the target sites (cells) as well as the number of ligand-receptor complexes (bound protein receptors) at the target cells are abstracted as the molecular received signals. For modelling of the ligand-receptor interaction mechanism using MC paradigm, a realistic reversible reaction process between the molecules (ligands) and the receptors (proteins) should be employed at the RN (the target cell). In this process, the molecules may bind with the receptors on the receiver surface to create the ligand-receptor complexes. The ligand-receptor complexes may be dissociated, and then the molecules will be released into the environment [30, 64]. The binding and unbinding processes depend on the forward and backward reaction constants, respectively. Finally, when the number of activated receptors reach a specific threshold, a cascade of chemical reactions may be initiated inside the cell (i.e., intracellular signaling pathways) [28, 157].

In addition, for modelling of the reception mechanism at the RN, the optimum design of MC systems for various applications, e.g., drug delivery systems, requires accurate modelling of the biological environments (aka ‘propagation channels’) including the other reaction mechanisms such as metabolic reaction. The propagation channel model plays a significant role in predicting the molecular concentration profile accurately at the RN. The biological in-vivo and in-vitro environments are usually small bounded media which have a significant impact on transport and distribution of the diffusive molecules. Therefore, impact of the medium boundary needs to be considered in modelling of the drug transport and delivery in such environments. The biological environments inside the body are usually small and bounded by cell membranes usually covered by receptor proteins, e.g., stomach, alveoli,

blood vessels, etc. Even the cell itself is bounded by semipermeable plasma membrane surrounding the cytoplasm of the cell [158]. Thus, the molecules may react with the membrane and then absorbed and removed from the environment.

Moreover, in modelling of the drug delivery systems, the outer surfaces of the biological environments, e.g., spherical tumor models [48], are usually modelled using appropriate boundary conditions, e.g., [49, 115]. Also, on-chip MC systems is another example for MC in bounded (confined) channel, where the information is exchanged using chemical molecules on a chip device [159]. Furthermore, even for a medium with a large radius, when the bio-nanomachines (or drug nanocarriers) are located near to the medium boundary, a portion of the emitted molecules may react with the medium boundary as will be demonstrated later in this chapter. This reaction includes molecular transport into the surrounding media, e.g., via pores or receptors, and reflection of molecules at the boundary before reacting with the receptors located on the RN (the target cell). Thus, the medium boundary will highly affect the distribution of the molecules regardless of the medium dimensions. Therefore, if the effect of the medium boundary is ignored by assuming the medium to be unbounded, it can result in erroneous prediction of the molecular concentration around the RN.

Another important mechanism that should be considered is the molecular degradation in biological environments [9, 58]. The molecular deformation and cleavage occur due to enzymatic attacks or changes in pH level in the biological environment [50, 160]. Thus, the degraded molecules do not contribute to the received signal because they will not be recognized by the protein receptors on the target cells. As an example, the acetylcholine (Ach) molecules are degraded by ACh-hydrolyzing enzyme (AChE), which diffuse into the synaptic cleft between the axons and the dendrites of the brain neurons [50, 161].

In this chapter, we develop analytical and stochastic simulation MCvD models for predicting the ligand-receptor complexes on the target site (reversible spherical RN) in 3-D bounded biological microenvironments. We derive analytical expressions for both the Green's function as well as the expected number of ligand-receptor complexes on the receiver surface. The reception process at the receiver is modeled via a reversible reaction mechanism. In this

process, the ligands (molecules) react with the receptor proteins, which lying on the receiver surface, to form the ligand-receptor complexes. Here, the environment is approximated as a finite bounded spherical medium with a semipermeable (partially reflecting) boundary, which can be reduced to fully absorbing and fully reflecting boundaries. Degradation of the molecules due to enzymes and pH levels in the medium is included via first-order degradation reaction mechanism. Also, we develop a stochastic particle-based simulator for the proposed model that incorporates the various reaction processes, namely, reversible reaction between ligands and receptors at the receiver, molecule degradation in the medium, and reaction of molecules at the medium boundary. The simulation results are used to validate the results obtained from the analytical model. We also demonstrate, using analytical and stochastic evaluations, that our expressions for the expected received signal can be reduced to other special cases of an unbounded medium if the distance from the TN to the medium boundary is large enough. As an example, these models can be used for accurate prediction of the bound receptors at target cells assuming the biological environments are approximated by bounded spherical media such as a 3D spherical in-vitro tumor models [48]. Thus, this work can be useful for designing and modelling of drug delivery systems and In-body nanonetworks using bio-nanomachines.

The rest of this chapter is organized as follows. The structure and components of the proposed system are described in section 4.2. In section 4.3, we present the general mathematical formulation that governs the proposed model. A closed-form expression for Green's function, i.e., molecular distribution function, is derived in section 4.4 while an expression for expected number of bound receptors (received signal) is derived in section 4.5. In section 4.6, the stochastic particle-based simulator framework is presented. We discuss the analytical and simulation results in section 4.7. Finally, the summary is given in section 4.8.

4.2 System Topology using Molecular Communication Paradigm

In this model, molecular communication via diffusion (MCvD) system consists of a transmitting bio-nanomachine (TN), e.g., drug nanocarrier, which sends biochemical molecules, e.g., drug, to a reversible receiving bio-nanomachine (RN), e.g., diseased cell, in a 3-D spherically bounded biological microenvironment as shown in Figure 4.1 and Figure

4.2. Here, the diffusive environment has a finite radius r_s and a uniform diffusion coefficient D in all the directions, i.e., the diffusion is assumed to be isotropic. The TN is a point-like source, located at the point $\vec{r}_T = (x_T, y_T, z_T)$, and emits the molecules 'M' instantaneously into the environment at the time $t = t_0$. The molecules are biochemical compounds, e.g., anticancer drug, antibodies, proteins, etc., that diffuse randomly according to Brownian motion.

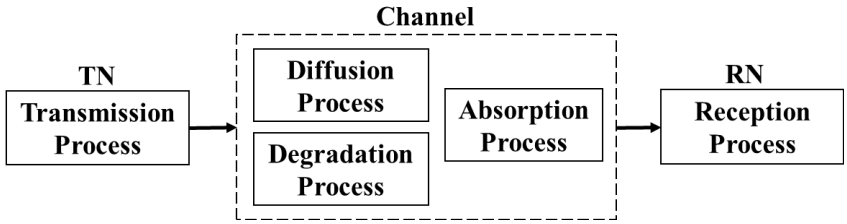

Figure 4.1: Block diagram of the end-to-end MCvD model using reversible RN including the various reaction processes in a bounded microenvironment.

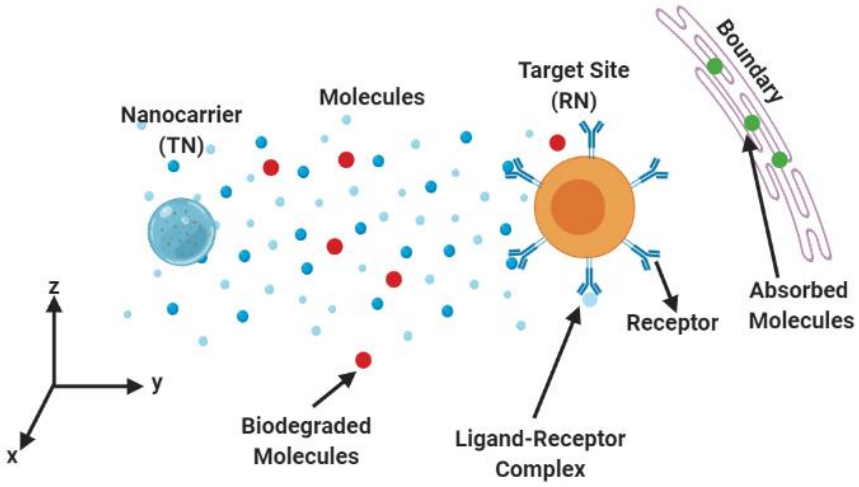

Figure 4.2: Graphical representation of MCvD using a reversible RN in a 3-D bounded microenvironment. (This figure is created with BioRender)

The molecules that reach the medium boundary may be absorbed and removed from the environment as follows

$$M \xrightarrow{k_r} \cancel{M} \tag{4.1}$$

where the parameter k_r is the absorption rate constant in (m/s).

The emitted molecule by the TN may be degraded and transformed into a new molecule, $\hat{\mathrm{M}}$, due to many factors such as enzymes, which cannot be recognized by the RN. A first-order degradation reaction mechanism can be described as

$$M \xrightarrow{k_d} \hat{M} \tag{4.2}$$

where, k_d is the degradation reaction constant in (s^{-1}).

The degraded molecules in the environment, as well as the absorbed molecules through the medium boundary, will be removed from the environment.

The RN is a spherical reactive receiver with a radius r_R , and it is located at the origin, as shown in Figure 4.2. The reaction between the molecules and the receptor proteins on the surface of the RN is characterized using a reversible reaction mechanism given by (4.3). The receiver surface is assumed to be fully covered by the receptor proteins and the number of receptors is much greater than the number of ligands [30]. This assumption is reasonable when the number of molecules which react with the RN is low or when the number of receptors is sufficiently large. The reaction of the ligands with the protein receptors is a stochastic process, which can lead to formation or dissociation of bound receptors. Finally, the ligand-receptor complexes 'MR' can be formed on the receiver surface depending on the forward-reaction rate constant k_f . Some of the ligand-receptor complexes may dissociate, and finally, the molecules return to the environment depending on the backward reaction constant k_d . The angle of incidence of the molecules on the receiver surface is neglected due to spherical symmetry. Furthermore, the ligand-receptor complexes 'MR' are assumed to be independently formed at any point on the RN surface with equal probability.

$$M + R \underset{k_b}{\overset{k_f}{\rightleftarrows}} MR \tag{4.3}$$

where k_f is the forward reaction constants in (m/s) and k_b is the backward reaction constants in (s^{-1}). It is worth mentioning that the forward reaction constant can be defined in different units, e.g., m^3/(mol.s), depending on the chosen adsorption model.

As a special case, when $k_b = 0$, the reversible receiver model reduces to an irreversible

receiver where the dissociation of ligand-receptor complexes cannot happen. Moreover, when k_f goes to infinity, the reversible receiver reduces to a fully absorbing receiver where each reaction between the ligand and the receptor becomes deterministic and may form the ligand-receptor complex. The receiver is assumed to have the capability of counting the total number of bound receptors after each reaction process. Here, the expected number of bound receptors, i.e., the number of 'MR' complexes, is interpreted as the received signal.

4.3 General Mathematical Formulation

In this section, we present a mathematical formulation for MCvD system in 3D spherical bounded microenvironment with a point like transmitter and a reversible spherical receiver. The concentration of the molecules in the vicinity of the receiver is highly affected by the molecular absorption and degradation in the environment as well as by the reaction with receptor proteins on the receiver surface.

The molecular diffusion with degradation reaction can be mathematically described by Fick's second law of diffusion with adding the degradation term, i.e., reaction-diffusion equation, given by [64] as

$$\frac{\partial P_M(\vec{r},t\,|\,\vec{r}_T,t_0)}{\partial t} = D\nabla^2 P_M(\vec{r},t\,|\,\vec{r}_T,t_0) - k_d P_M(\vec{r},t\,|\,\vec{r}_T,t_0) \tag{4.4}$$

where, $P_M(\vec{r},t\,|\,\vec{r}_T,t_0)$ is the molecular concentration at an arbitrary location $\vec{r}=(x,y,z)$ at time t with initial location $\vec{r}_T=(x_T,y_T,z_T)$ and initial time t_0. The operator ∇^2 is the Laplacian operator in a 3-D spherical coordinate system and D is the diffusion coefficient of the molecules in the propagation medium in (m^2/s).

The medium is assumed spherically symmetric; thus, the molecular distribution depends only on the radial distance and not on the azimuthal and polar angles. Therefore, we ignore the derivatives with respect to the azimuthal and polar angles. In this case, the reaction-diffusion equation (4.4) can be rewritten in spherical coordinates system as

$$\frac{\partial(rP_M(r,t\,|\,r_T,t_0))}{\partial t} = D\frac{\partial^2(rP_M(r,t\,|\,r_T,t_0))}{\partial r^2} - k_d rP_M(r,t\,|\,r_T,t_0) \tag{4.5}$$

The instantaneous release of the molecules by a point-like TN can be described using the

following initial condition,

$$P_M(r,t \to t_0 \mid r_T) = \frac{1}{4\pi r_T^2}\delta(r - r_T) \tag{4.6}$$

We assume that the molecules are released from point-like sources distributed on the surface of a spherical virtual shell having a radius r_T . Thus, the point TN is located at a distance r_T from the center of the receiver. Here, due to spherical symmetry, the angle at which the molecule hits the RN is ignored. Therefore, the RN can react with the released molecules from any point source located on this shell, with equal probability. Thus, the initial condition is normalized to the area of the spherical virtual shell, i.e., $4\pi r_T^2$, to take effect of a single-point source.

The Robin boundary condition is chosen to characterize the absorption and reflection of the molecules at the medium boundary, assuming that the absorbed molecules will be removed from the environment,

$$-D\frac{d}{dr}P_M(r,t \mid r_T,t_0)\Big|_{r\to r_s} = k_r\, P_M(r,t \mid r_T,t_0)\big|_{r\to r_s} \tag{4.7}$$

where, k_r is the absorption rate constant at the medium boundary in (m/s).

As a special case, for a medium with fully absorbing boundary $(k_r \to \infty)$, the Robin boundary condition reduces to

$$P_M(r \to r_s, t \mid r_T, t_0) = 0 \tag{4.8}$$

The reversible reaction mechanism, i.e., forward and backward reactions, of the molecules with the receiver receptors is characterized using Robin boundary condition given by [30, 61] as

$$D\frac{\partial P_M(r,t \mid r_T,t_0)}{\partial r}\Big|_{r=r_R} = k_f P_M(r_R,t \mid r_T,t_0) - k_b P_{MR}(t \mid r_T,t_0) \tag{4.9}$$

where, $P_M(r_R,t \mid r_T,t_0)$ is the molecular distribution in the receiver's vicinity at $r = r_R$, i.e., near the receiver's surface, and the distribution function, $P_{MR}(t \mid r_T,t_0)$, is the average surface

concentration of the ligand-receptor complexes on the receiver surface at time *t*. here, In this model, the effect of receptor occupancy is ignored and thus many molecules may react with the same receptor at the same time. Therefore, the number of unbound receptors can be approximated to be equal to the total number of receptors. This assumption is appropriate when the number of receptors is sufficiently large, or when the number of bound molecules is sufficiently small. Here, the total number of receptors on the receiver surface is combined into the forward reaction constant k_f .

The molecular distribution function, $P_M(r,t \mid r_T,t_0)$, can be obtained by solving Eq. (4.5) that satisfies the initial and boundary conditions given by Eqs. (4.6)-(4.9). This solution represents the Green's function which can be expressed as a superposition of two functions [30],

$$rP_M(r,t \mid r_T,t_0) = rC(r,t \mid r_T,t_0) + rV(r,t \mid r_T,t_0) \tag{4.10}$$

The first term on the r.h.s of Eq. (4.10), i.e., $rC(r,t \mid r_T,t_0)$, is the solution of the reaction-diffusion equation (4.11) with the initial condition (4.12) for unbounded medium with absence of the receiver, i.e., without applying the boundary condition (4.9).

$$\frac{\partial(rC(r,t \mid r_T,t_0))}{\partial t} = D\frac{\partial^2(rC(r,t \mid r_T,t_0))}{\partial r^2} - k_d rC(r,t \mid r_T,t_0) \tag{4.11}$$

$$rC(r,t \to t_0 \mid r_T) = \frac{1}{4\pi r_T}\delta(r - r_T) \tag{4.12}$$

In order to obtain an exact solution for Eq. (4.11), two boundary conditions are needed. Here, we assume the molecular distribution is finite at the medium center which vanishes at distance much higher than r_T . Thus, the boundary conditions can be expressed as,

$$\left|C(r \to 0,t \mid r_T,t_0)\right| < \infty, \quad t > t_0 \tag{4.13}$$

$$C(r \to \infty,t \mid r_T,t_0) = 0 \tag{4.14}$$

The second term on the r.h.s of Eq. (4.10), i.e., $rV(r,t \mid r_T,t_0)$, is the solution of the reaction-diffusion equation (4.15) that initially vanishes at the time $t = t_0$, i.e., satisfy the initial

condition given by Eq. (4.16) , and together with $C(r,t \mid r_T,t_0)$ satisfy the boundary conditions (4.8) and (4.9).

$$\frac{\partial(rV(r,t \mid r_T,t_0))}{\partial t} = D\frac{\partial^2(rV(r,t \mid r_T,t_0))}{\partial r^2} - k_d rV(r,t \mid r_T,t_0) \tag{4.15}$$

$$rV(r,t \to t_0 \mid r_T) = 0 \tag{4.16}$$

4.4 Molecular Concentration Distribution (Green's Function)

The molecular distribution due to release of the molecules instantaneously (i.e., via impulsive release) by a point source represents the Green's function (or the CIR). In general, Green's function is very important to obtain the system response (e.g., molecular distribution) due to any input (e.g., release pattern) by applying the convolution. In this section, we derive a closed-form expression of Green's function (or CIR) considering effects of the molecular degradation in the environment, the molecular absorption at the medium boundary, and the molecular reaction with receptor proteins on the receiver surface. A closed-form expression of Green's function can be obtained by solving the diffusion equations together with the initial and boundary conditions given in section 4.3. Now, the diffusion equation (4.11) will be solved in the Laplace domain after applying the initial condition (4.12) to obtain the following equation:

$$\frac{\partial^2 r\tilde{C}(r,s \mid r_T,t_0)}{\partial r^2} - \frac{(s+k_d)}{D} r\tilde{C}(r,s \mid r_T,t_0) = -\frac{1}{4D\pi r_T} e^{-st_0}\delta(r-r_T) \tag{4.17}$$

where, $\tilde{C}(r,s \mid r_T,t_0)$ is the Laplace transform of the concentration function $C(r,t \mid r_T,t_0)$.

The general solution of the second-order inhomogeneous differential equation (4.17) can be expressed as a superposition of the homogeneous (complementary) solution and the particular solution:

$$r\tilde{C}(r,s \mid r_T,t_0) = r\tilde{C}_h(r,s \mid r_T,t_0) + r\tilde{C}_p(r,s \mid r_T,t_0) \tag{4.18}$$

The homogeneous part of Eq. (4.17) has two distinct roots; therefore the homogeneous solution can be written as

$$r\tilde{C}_h(r,s \mid r_T,t_0) = c_1 e^{ru} + c_2 e^{-ru} \tag{4.19}$$

The particular solution of Eq. (4.17) can be obtained as

$$r\tilde{C}_p(r,s\,|\,r_T,t_0) = -\frac{e^{-st_0}}{8D\pi r_T u}\left(e^{(r-r_T)u} - e^{-(r-r_T)u}\right)H\left(r-r_T\right) \tag{4.20}$$

where the parameter u is given as

$$u = \sqrt{\left(s+k_d\right)/D} \tag{4.21}$$

The Heaviside function is given as

$$H\left(r-r_T\right) = \begin{cases} 1, & r \geq r_T \\ 0, & r < r_T \end{cases} \tag{4.22}$$

The general solution of Eq. (4.17) can be obtained by substituting (4.19) and (4.20) in (4.18) as

$$r\tilde{C}(r,s\,|\,r_T,t_0) = c_1 e^{ru} + c_2 e^{-ru} - \frac{e^{-st_0}}{8D\pi r_T u}\left(e^{(r-r_T)u} - e^{-(r-r_T)u}\right)H\left(r-r_T\right) \tag{4.23}$$

The parameters, c_1 and c_2, can be determined by applying the conditions (4.13) and (4.14) to (4.23). After applying the condition (4.13), we get

$$\tilde{C}(r\to 0,s\,|\,r_T,t_0) = \lim_{r\to 0}\left(\frac{c_1}{r}e^{ru} + \frac{c_2}{r}e^{-ru}\right) = \lim_{r\to 0}\frac{1}{r}\left(c_1+c_2\right) < \infty \tag{4.24}$$

The distribution $\tilde{C}(r,s\,|\,r_T,t_0)$ is finite at the center of the medium, and the factor $(1/r)$ goes to infinity as r goes to zero, therefore (c_1+c_2) should have a zero value and thus we get the following result:

$$c_1 = -c_2 \tag{4.25}$$

Now, after applying the condition (4.14) to Eq. (4.23), we get

$$\lim_{r\to\infty}\frac{e^{ru}}{r}\left(c_1 - \frac{e^{-st_0}}{8D\pi r_T u}e^{-r_T u}\right) = 0 \tag{4.26}$$

The limit in (4.26) cannot be obtained directly, therefore we use L'Hospital's rule as

$$\lim_{r\to\infty} ue^{ru}\left(c_1 - \frac{e^{-st_0}}{8D\pi r_T u}e^{-r_T u}\right) = 0 \tag{4.27}$$

As the radial distance r goes to infinity in Eq. (4.27), the factor e^{ru} goes to infinity, therefore we conclude the following

$$c_1 = \frac{e^{-st_0}}{8D\pi r_T u}e^{-r_T u} \tag{4.28}$$

Substituting the values of c_1 and c_2 from Eqs. (4.25) and (4.28) in (4.23), and with some algebraic manipulations, we get the general solution of Eq. (4.17) as

$$r\tilde{C}(r,s\,|\,r_T,t_0) = \frac{e^{-st_0}}{8\pi D r_T u}\times\begin{cases} e^{-(r-r_T)u} - e^{-(r+r_T)u}, & r \geq r_T \\ e^{(r-r_T)u} - e^{-(r+r_T)u}, & r < r_T \end{cases} \tag{4.29}$$

The equation (4.29) can be expressed in terms of the hyperbolic sine function as

$$r\tilde{C}(r,s\,|\,r_T,t_0) = \frac{e^{-st_0}}{4\pi D r_T u}\times\begin{cases} e^{-ru}\sinh(r_T u), & r \geq r_T \\ e^{-r_T u}\sinh(ru), & r < r_T \end{cases} \tag{4.30}$$

where $\sinh(\cdot)$ is the hyperbolic sine function.

Now, the solution of Eq. (4.15) in the Laplace domain, i.e., $r\tilde{V}(r,s\,|\,r_T,t_0)$, can be obtained by applying the Laplace transform and then substituting the initial condition (4.16) to get

$$\frac{\partial^2\left(r\tilde{V}\left(r,s\,|\,r_T,t_0\right)\right)}{\partial r^2} - \frac{s+k_d}{D}r\tilde{V}\left(r,s\,|\,r_T,t_0\right) = 0 \tag{4.31}$$

The equation (4.31) is a homogeneous second-order differential equation with two distinct roots, and thus its solution can be expressed in terms of the hyperbolic sine and cosine functions as

$$r\tilde{V}(r,s\,|\,r_T,t_0) = A\sinh(ru) + B\cosh(ru) \tag{4.32}$$

where A and B are functions of (s,r_R,r_s,r_T).

Now, taking the Laplace transform of Eq. (4.10), the total solution can be expressed as a

superposition of Eqs. (4.30) and (4.32).

$$r\tilde{P}(r,s\,|\,r_T,t_0) = r\tilde{C}(r,s\,|\,r_T,t_0) + A\sinh(ru) + B\cosh(ru) \tag{4.33}$$

where the term $r\tilde{C}(r,s\,|\,r_T,t_0)$ can be chosen from Eq. (4.30) depending on the radial distance at which the molecular distribution need to be evaluated.

Here, we will apply a fully absorbing boundary condition at the medium boundary to make the derivations tractable while a partially absorbing boundary is simulated using our stochastic particle-based simulator which shows a high degree of accuracy as will be discussed later. In order to obtain the functions A and B, we will convert the boundary conditions (4.8) and (4.9) to the Laplace domain as

$$\tilde{P}_M(r \to r_s, s\,|\,r_T,t_0) = 0 \tag{4.34}$$

$$D\frac{\partial \tilde{P}_M(r,s\,|\,r_T,t_0)}{\partial r}\bigg|_{r=r_R} = k_f\tilde{P}_M(r_R,s\,|\,r_T,t_0) - k_b\tilde{P}_{MR}(s\,|\,r_T,t_0) \tag{4.35}$$

The temporal distribution of the ligand-receptor complexes ‘MR’ on the receiver surface, is equal to the flux of molecules in the receiver vicinity towards its surface. It is given by the following conservation identity [30, Eq. (6)],

$$\frac{\partial P_{MR}(t\,|\,r_T,t_0)}{\partial t} = D\frac{\partial P_M(r,t\,|\,r_T,t_0)}{\partial r}\bigg|_{r=r_R} \tag{4.36}$$

Now, taking the Laplace transform of Eq. (4.36) and considering the fact that the distribution of the ligand-receptor complexes ‘MR’ on the receiver surface is equal to zero at the initial time instant $t = t_0$, we get

$$\tilde{P}_{MR}(s\,|\,r_T,t_0) = \frac{D}{s}\frac{\partial \tilde{P}_M(r,s\,|\,r_T,t_0)}{\partial r}\bigg|_{r=r_R} \tag{4.37}$$

Substituting (4.37) in (4.35), we get

$$\frac{\partial \tilde{P}_M(r,s\,|\,r_T,t_0)}{\partial r}\bigg|_{r=r_R} = \frac{sk_f}{D(s+k_b)}\tilde{P}_M(r_R,s\,|\,r_T,t_0) \tag{4.38}$$

Using the product rule of derivatives, the derivative of $r\tilde{P}_M(r,s\,|\,r_T,t_0)$ with respect to r at

$r = r_R$ can be expressed as

$$\left.\frac{\partial(r\tilde{P}_M(r,s\mid r_T,t_0))}{\partial r}\right|_{r=r_R} = r_R \left.\frac{\partial\tilde{P}_M(r,s\mid r_T,t_0)}{\partial r}\right|_{r=r_R} + \tilde{P}_M(r_R,s\mid r_T,t_0) \tag{4.39}$$

Now, substituting (4.38) in (4.39), we get

$$\left.\frac{\partial(r\tilde{P}_M(r,s\mid r_T,t_0))}{\partial r}\right|_{r=r_R} = r_R\tilde{P}_M(r_R,s\mid r_T,t_0)\frac{\omega_1}{\omega_2} \tag{4.40}$$

where,

$$\omega_1 = s(r_R k_f + D) + Dk_b \tag{4.41}$$

$$\omega_2 = r_R D(s + k_b) \tag{4.42}$$

After applying the boundary conditions (4.34) and (4.40) to Eq. (4.33), respectively, we get the following:

$$B = -\frac{e^{-st_0}}{4\pi Drr_T u}\frac{e^{-r_s u}\sinh(r_T u)}{\cosh(r_s u)} - A\frac{\sinh(r_s u)}{\cosh(r_s u)} \tag{4.43}$$

$$A = -\frac{e^{-st_0}e^{-r_T u}}{4\pi Drr_T u} + B\frac{u\omega_2\sinh(r_R u) - \omega_1\cosh(r_R u)}{\omega_1\sinh(r_R u) - u\omega_2\cosh(r_R u)} \tag{4.44}$$

The functions A and B can be obtained by solving (4.43) and (4.44) as

$$A = \frac{e^{-st_0}}{4\pi Drr_T u}\left[\frac{e^{-r_T u}\cosh(r_s u)\left(u\omega_2\cosh(r_R u) - \omega_1\sinh(r_R u)\right)}{\omega_1\sinh\left((r_R - r_s)u\right) - u\omega_2\cosh\left((r_R - r_s)u\right)}\right.$$

$$\left. - \frac{e^{-r_s u}\sinh(r_T u)\left(u\omega_2\sinh(r_R u) - \omega_1\cosh(r_R u)\right)}{\omega_1\sinh\left((r_R - r_s)u\right) - u\omega_2\cosh\left((r_R - r_s)u\right)}\right] \tag{4.45}$$

$$B = -\frac{e^{-st_0}}{4\pi Drr_T u}\left[\frac{e^{-r_s u}\sinh(r_T u)}{\cosh(r_s u)} + \frac{e^{-r_T u}\sinh(r_s u)\cosh(r_s u)\left(u\omega_2\cosh(r_R u) - \omega_1\sinh(r_R u)\right)}{\left(\omega_1\sinh\left((r_R - r_s)u\right) - u\omega_2\cosh\left((r_R - r_s)u\right)\right)\cosh(r_s u)}\right.$$

$$\left. - \frac{e^{-r_s u}\sinh(r_T u)\sinh(r_s u)\left(u\omega_2\sinh(r_R u) - \omega_1\cosh(r_R u)\right)}{\left(\omega_1\sinh\left((r_R - r_s)u\right) - u\omega_2\cosh\left((r_R - r_s)u\right)\right)\cosh(r_s u)}\right] \tag{4.46}$$

The functions A and B can be rewritten as,

$$A = \frac{e^{-st_0}}{4\pi D r_T u}\left[\frac{e^{-r_s u}\sinh\left(r_T u\right) f_2(u) - e^{-r_T u}\cosh\left(r_s u\right) f_1(u)}{f_3(u)}\right] \tag{4.47}$$

$$B = -\frac{e^{-st_0}}{4\pi D r_T u}\frac{1}{f_3(u)\cosh\left(r_s u\right)}\Big[e^{-r_s u} f_3(u)\sinh\left(r_T u\right) + e^{-r_T u}\sinh\left(r_s u\right)\cosh\left(r_s u\right) f_1(u)$$

$$-e^{-r_s u}\sinh\left(r_T u\right)\sinh\left(r_s u\right) f_2(u)\Big] \tag{4.48}$$

where,

$$f_1(u) = u\omega_2\cosh\left(r_R u\right) - \omega_1\sinh\left(r_R u\right) \tag{4.49}$$

$$f_2(u) = u\omega_2\sinh\left(r_R u\right) - \omega_1\cosh\left(r_R u\right) \tag{4.50}$$

$$f_3(u) = \omega_1\sinh\left(\left(r_s - r_R\right)u\right) + u\omega_2\cosh\left(\left(r_s - r_R\right)u\right) \tag{4.51}$$

The number of ligand-receptor complexes on the receiver surface can be obtained by substituting Eqs. (4.30) and (4.47)-(4.48) in (4.33) for $r < r_T$, where the RN is located.

$$\tilde{P}_M(r,u \mid r_T,t_0) = \frac{e^{-st_0}}{4\pi D r r_T u}\Bigg[e^{-r_T u}\sinh\left(ru\right) - \frac{e^{-r_s u}\cosh\left(ru\right)\sinh\left(r_T u\right)}{\cosh\left(r_s u\right)}$$

$$+\frac{\sinh\left(\left(r_s - r\right)u\right)\left(e^{-r_T u} f_1(u)\cosh\left(r_s u\right) - e^{-r_s u} f_2(u)\sinh\left(r_T u\right)\right)}{f_3(u)\cosh\left(r_s u\right)}\Bigg] \tag{4.52}$$

Now, replacing the exponential factors in (4.52) by their equivalent hyperbolic functions and using some algebraic manipulations, we get

$$\tilde{P}_M(r,u \mid r_T,t_0) = \frac{e^{-st_0}}{4\pi D r r_T}\frac{1}{u f_3(u)}\Big[\sinh\left((r - r_T)u\right) f_3(u) + \sinh\left(\left(r_s - r\right)u\right)$$

$$\times\left(\omega_1\sinh\left(\left(r_T - r_R\right)u\right) + u\omega_2\cosh\left(\left(r_T - r_R\right)u\right)\right)\Big] \tag{4.53}$$

The inverse Laplace transform of Eq. (4.53) can be evaluated using the residue theorem [162] as

$$P_M(r,t\,|\,r_T,t_0)=\sum_{\substack{Poles\ of\\ \tilde{P}_M(r,s|r_T,t_0)}}\mathrm{Res}\left(\tilde{P}_M(r,s\,|\,r_T,t_0)e^{st}\right) \tag{4.54}$$

where, $\mathrm{Res}(F(s))$ is the residue of $F(s)$.

Despite the function (4.53) includes a square root, i.e., $u=\sqrt{(s+k_d)/D}$, it is a meromorphic function, even function in u, and it does not have a branch point at $u=0$, i.e., $s=-k_d$. Therefore, we can directly use the residue theorem. To prove that, we rewrite (4.53) using Taylor series expansions of the hyperbolic functions as

$$\tilde{P}_M(r,u\,|\,r_T,t_0)=\frac{e^{-st_0}}{4\pi Drr_T}\left[H_1+\frac{H_2H_3}{H_4}\right] \tag{4.55}$$

where,

$$H_1=\frac{\sinh\left((r-r_T)u\right)}{u}=\frac{(r-r_T)u+\dfrac{(r-r_T)^3u^3}{3!}+\ldots}{u}=(r-r_T)+\frac{(r-r_T)^3u^2}{3!}+\ldots \tag{4.56}$$

$$H_2=\frac{\sinh\left((r_s-r)u\right)}{u}=\frac{(r_s-r)u+\dfrac{(r_s-r)^3u^3}{3!}+\ldots}{u}=(r_s-r)+\frac{(r_s-r)^3u^2}{3!}+\ldots \tag{4.57}$$

$$H_3=\frac{\omega_1\sinh\left((r_T-r_R)u\right)+u\omega_2\cosh\left((r_T-r_R)u\right)}{u}$$

$$=\omega_1\left((r_T-r_R)+\frac{(r_T-r_R)^3u^2}{3!}+\ldots\right)+\omega_2\left(1+\frac{(r_T-r_R)^2u^2}{2!}+\ldots\right) \tag{4.58}$$

$$H_4=\frac{\omega_1\sinh\left((r_s-r_R)u\right)+u\omega_2\cosh\left((r_s-r_R)u\right)}{u}$$

$$=\omega_1\left((r_T-r_R)+\frac{(r_s-r_R)^3u^2}{3!}+\ldots\right)+\omega_2\left(1+\frac{(r_s-r_R)^2u^2}{2!}+\ldots\right)u \tag{4.59}$$

Thus, we can see from Eqs. (4.56)-(4.59) that the function (4.53) is a meromorphic and even function of u and therefore there is no branch point at $u = 0$.

The expression (4.53) has a simple pole at $u = 0$ and an infinite number of simple poles at the roots of $f_3(u)$ in Eq. (4.51). The residue at the simple pole $u = 0$, i.e., $s = -k_d$, can be evaluated as

$$\text{Res}_{s=-k_d} = \frac{1}{4\pi r r_T} \lim_{s \to -k_d} e^{s(t-t_0)} \frac{u \sinh\left((r_s - r)u\right)\left(\omega_1 \sinh\left((r_T - r_R)u\right) + u\omega_2 \cosh\left((r_T - r_R)u\right)\right)}{f_3(u)} \tag{4.60}$$

After evaluating the limit in Eq. (4.60) using L'Hospital's rule, we get zero residue.

The residues at the other simple poles, i.e., the roots of $f_3(u)$, can be obtained by substituting the value of ω_1 and ω_2 from Eqs. (4.41)-(4.42) in (4.51), then we get

$$f_3(u) = (s(r_R k_f + D) + Dk_b)\sinh((r_s - r_R)u) + ur_R D(s + k_b)\cosh((r_s - r_R)u) \tag{4.61}$$

Now, replacing the parameter 's' in Eq. (4.61) by its equivalent, i.e., $s = u^2 D - k_d$, and then by setting $f_3(u) = 0$ at the poles of Eq. (4.53), we get

$$\tanh((r_s - r_R)u) = -\frac{ur_R D(u^2 D - k_d + k_b)}{(u^2 D - k_d)(r_R k_f + D) + Dk_b} \tag{4.62}$$

After converting the hyperbolic tangent function in Eq. (4.62) to its equivalent trigonometric tangent function and making the parameter $\kappa_n = iu$, we obtain the following

$$\tan\left(\left(r_s - r_R\right)\kappa_n\right) = -\frac{\kappa_n r_R D(\kappa_n^2 D + k_d - k_b)}{(\kappa_n^2 D + k_d)(r_R k_f + D) - Dk_b} \tag{4.63}$$

Then, Eq. (4.63) can be rewritten as

$$\tan\left(\left(r_s - r_R\right)\kappa_n\right) = -\frac{\lambda_n \alpha_n}{\beta_n} \tag{4.64}$$

where, the parameters α_n, β_n, and λ_n for $n = 1, ..., \infty$ are defined as follows

$$\alpha_n = D\kappa_n^2 + k_d - k_b \tag{4.65}$$

$$\beta_n = \alpha_n(r_R k_f + D) + r_R k_f k_b \tag{4.66}$$

$$\lambda_n = Dr_R \kappa_n \tag{4.67}$$

The residue at the n[th] simple pole, κ_n, can be derived as

$$\mathrm{Res}_{s=-\left(\kappa_n^2 D+k_d\right)}=\frac{1}{4\pi Drr_T}\lim_{s\to-\left(\kappa_n^2 D+k_d\right)}\frac{e^{s(t-t_0)}}{u}\left[\frac{df_3(u)}{ds}\right]^{-1}\Big[\sinh\left((r-r_T)u\right)f_3(u)$$

$$+\sinh\left((r_s-r)u\right)\left(\omega_1\sinh\left((r_T-r_R)u\right)+u\omega_2\cosh\left((r_T-r_R)u\right)\right)\Big] \tag{4.68}$$

Then, after evaluating the derivative in (4.68), we get

$$\mathrm{Res}_{s=-(\kappa_n^2 D+k_d)}=\frac{1}{2\pi rr_T}\lim_{s\to-(\kappa_n^2 D+k_d)}e^{s(t-t_0)}\sinh\left((r_s-r)u\right)$$

$$\times\left(\omega_1\sinh\left((r_T-r_R)u\right)+u\omega_2\cosh\left((r_T-r_R)u\right)\right)\Bigg[\sinh\left((r_s-r_R)u\right)\left(2Du\frac{d\omega_1}{ds}+(r_s-r_R)u\omega_2\right)$$

$$+\cosh\left((r_s-r_R)u\right)\left((r_s-r_R)\omega_1+\left(\omega_2+2Du^2\frac{d\omega_2}{ds}\right)\right)\Bigg]^{-1} \tag{4.69}$$

We use the fact that $f_3(u)=0$ at the poles of Eq. (4.53), to get the following identity

$$\cos\left((r_s-r_R)\kappa_n\right)=-(\beta_n/(\lambda_n\alpha_n))\sin\left((r_s-r_R)\kappa_n\right) \tag{4.70}$$

By substituting the value of ω_1 and ω_2 from (4.41)-(4.42) and their derivatives w.r.t 's' in Eq. (4.69), then converting the hyperbolic functions to their equivalent trigonometric functions and with the help of (4.70), we get

$$\mathrm{Res}_{s=-\left(\kappa_n^2 D+k_d\right)}=\frac{1}{2\pi rr_T}e^{-(\alpha_n+k_b)(t-t_0)}\frac{\sin\left((r_s-r)\kappa_n\right)}{\sin\left((r_s-r_R)\kappa_n\right)}$$

$$\times\frac{\alpha_n\beta_n\lambda_n\sin\left((r_T-r_R)\kappa_n\right)+\alpha_n^2\lambda_n^2\cos\left((r_T-r_R)\kappa_n\right)}{(r_s-r_R)\left(\lambda_n^2\alpha_n^2+\beta_n^2\right)+\alpha_n\beta_n Dr_R+2\lambda_n^2k_fk_b} \tag{4.71}$$

Since the residue at the simple pole $s=-k_d$ is equal to zero, then the inverse Laplace transform of (4.53) can be expressed as a summation of the residues at the other simple poles κ_n for $n=1,...,\infty$.

Thus, we get the following spatiotemporal distribution:

$$P_M(r,t \mid r_T,t_0) = \frac{1}{2\pi r r_T}\sum_{n=1}^{\infty} e^{-(\alpha_n+k_b)(t-t_0)}\,\frac{\sin\left(\left(r_s-r\right)\kappa_n\right)}{\sin\left(\left(r_s-r_R\right)\kappa_n\right)}$$

$$\times\frac{\alpha_n\beta_n\lambda_n\sin\left(\left(r_T-r_R\right)\kappa_n\right)+\alpha_n^2\lambda_n^2\cos\left(\left(r_T-r_R\right)\kappa_n\right)}{\left(r_s-r_R\right)\left(\lambda_n^2\alpha_n^2+\beta_n^2\right)+\alpha_n\beta_n Dr_R+2\lambda_n^2 k_f k_b} \qquad (4.72)$$

where, κ_n is the n^{th} positive root of the identity (4.64) and the parameters α_n, β_n, and λ_n for $n=1,...,\infty$ are defined in Eqs. (4.65)-(4.67).

Now, we will show that the roots of Eq. (4.64) are always positive and they consist of an infinite number of simple roots along the positive real axis and possibly another simple imagery root on the positive imaginary axis depending on the system parameters.

Firstly, we will show that the roots of Eq. (4.64) are always positive. In the case that $s > -k_d$, the parameter u is positive real and thus $\kappa_n = -iu$ is always negative imaginary. Therefore, the term on the l.h.s of (4.64) is continuous and strictly monotonically increasing function everywhere on the negative imaginary axis, i.e., it increases from -1 to 0, and the term on the r.h.s of (4.64) is continuous and strictly monotonically decreasing function everywhere on the imaginary axis, i.e., it decreases from ∞ to 0. Therefore, the two terms in this interval have one intersection point at zero. On the other hand, if $s < -k_d$, then u is positive imaginary and thus $\kappa_n = -iu$ is always positive real. Therefore, the term on the l.h.s of (4.64) is continuous and strictly monotonically increasing function in each interval along the positive real axis, i.e., $I_n = [-\pi p/2 \quad \pi p/2] + n\pi p$, where p is a scale factor equal to $(r_s - r_R)^{-1}$ and the term on the r.h.s of (4.64) is continuous and strictly decreasing function everywhere along the positive real axis. Since the l.h.s and the r.h.s terms of Eq. (4.64) have opposite monotonic behaviors in each interval I_n and the l.h.s has value from $-\infty$ to ∞, then each interval I_n has exactly one intersection point (i.e., one root) and thus an infinite number of intersection points along the positive real axis. Therefore, the roots of (4.64) are positive real.

However, it is possible to have another simple imaginary root on the positive imaginary axis depending on the values of the system parameters, i.e., the discriminant of the quadratic function β_n. In order to determine this root, we firstly should find the discriminant of β_n and

if it is positive, i.e., $\left(k_b - k_d\right) > (r_R k_f k_d / D)$, then the root is real and located around the positive zero of β_n and if the discriminant is negative, then the root is imaginary and located around the negative zero of β_n. This additional imaginary root can have a significant effect on the behavior of the model, especially on the reversible reaction process at the RN. Hence, it is important to determine this imaginary root by precisely scanning the region around the positive zeros of β_n in (4.66). For this, we develop an algorithm in MATLAB to find the first N roots, which provide very accurate results while ensuring that the remaining roots will have a negligible effect on the final expression (4.72).

4.5 Received Signal: Expected Number of Ligand-Receptor Complexes

The coupling reaction rate between the molecules and the receptor proteins on the receiver surface in (mol./s) is given as

$$R(t \mid r_T, t_0) = A_{RN} D \left. \frac{\partial P_M(r, t \mid r_T, t_0)}{\partial r} \right|_{r=r_R} \tag{4.73}$$

where, $A_{RN} = 4\pi r_R^2$ is the surface area of the RN.

The cumulative expected number of the bound receptors, i.e., the ligand-receptor complexes, on the surface of the RN can be expressed as

$$N\left(t\right) = N_m \int_{t_0}^{t} R(\tau \mid r_T, t_0) d\tau \tag{4.74}$$

where N_m is the total number of released molecules by the TN.

Substituting (4.73) in (4.74), we get

$$N\left(t\right) = N_m A_{RN} D \int_{t_0}^{t} \left. \frac{\partial P_M(r, \tau \mid r_T, t_0)}{\partial r} \right|_{r=r_R} d\tau \tag{4.75}$$

Now, taking the derivative of Eq. (4.72) with respect to r and then evaluating the integral in (4.75) with respect to τ, we get

$$N(t)=\frac{2DN_m}{r_T}\sum_{n=1}^{\infty}\left[\kappa_n r_R\cot\left(\left(r_s-r_R\right)\kappa_n\right)+1\right]\left[e^{-(\alpha_n+k_b)(t-t_0)}-1\right]$$

$$\times\left[\frac{\alpha_n\beta_n\lambda_n\sin\left(\left(r_T-r_R\right)\kappa_n\right)+\alpha_n^2\lambda_n^2\cos\left(\left(r_T-r_R\right)\kappa_n\right)}{\left(\alpha_n+k_b\right)\left(\left(r_s-r_R\right)\left(\beta_n^2+\alpha_n^2\lambda_n^2\right)+r_R D\alpha_n\beta_n+2\lambda_n^2k_fk_b\right)}\right] \quad (4.76)$$

where, cot(·) is the cotangent function.

We use the identity (4.64) to rewrite the cotangent function in Eq. (4.76) as

$$N(t)=\frac{2N_mk_fr_R}{r_T}\sum_{n=1}^{\infty}\left[1-e^{-(\alpha_n+k_b)(t-t_0)}\right]\frac{\beta_n\lambda_n\sin\left(\left(r_T-r_R\right)\kappa_n\right)+\alpha_n\lambda_n^2\cos\left(\left(r_T-r_R\right)\kappa_n\right)}{\left(r_s-r_R\right)\left(\beta_n^2+\alpha_n^2\lambda_n^2\right)+r_RD\alpha_n\beta_n+2\lambda^2k_fk_b} \quad (4.77)$$

The cumulative number of ligand-receptor complexes given by (4.77) is a general expression for the received signal by a reversible RN located in bounded diffusive microenvironment which can be reduced to the following special cases:

(i) *Irreversible fully absorbing receiver* $(k_f\to\infty,\ k_b=0)$:

Multiplying both the numerator and the denominator of (4.77) by the factor $(1/k_f^2)$ and then taking the limit as $k_f\to\infty$, we get the expected received signal for a fully-absorbing RN with molecular degradation in the environment:

$$N_{FD}(t)=\frac{2DN_mr_R}{\left(r_s-r_R\right)r_T}\sum_{n=1}^{\infty}\frac{\kappa_n\sin\left(\left(r_T-r_R\right)\kappa_n\right)}{\kappa_n^2D+k_d}\left(1-e^{-\left(\kappa_n^2D+k_d\right)(t-t_0)}\right) \quad (4.78)$$

where κ_n is the n$^{\text{th}}$ positive root of Eq. (4.64) when the forward reaction rate constant goes to infinity, i.e., $k_f\to\infty$, and is given by

$$\kappa_n=\frac{n\pi}{r_s-r_R} \quad (4.79)$$

The expected received signal without molecular degradation in the environment can be obtained by substituting $k_d=0$ in (4.78) as

$$N_{FA}(t)=\frac{2N_mr_R}{r_T\left(r_s-r_R\right)}\sum_{n=1}^{\infty}\frac{\sin\left(\left(r_T-r_R\right)\kappa_n\right)}{\kappa_n}\left(1-e^{-\kappa_n^2D(t-t_0)}\right) \quad (4.80)$$

(ii) *Irreversible partially absorbing receiver* $(k_b = 0)$:

The expected received signal for a partially absorbing receiver with molecular degradation in the medium can be obtained by substituting $k_b = 0$ in the general expression (4.77).

$$N_{PD}(t) = \frac{2N_m k_f r_R}{r_T} \sum_{n=1}^{\infty} \left(1 - e^{-\left(\kappa_n^2 D + k_d\right)(t-t_0)}\right) \frac{\lambda_n q \sin\left(\left(r_T - r_R\right)\kappa_n\right) + \lambda_n^2 \cos\left(\left(r_T - r_R\right)\kappa_n\right)}{\left(\kappa_n^2 D + k_d\right)\left(\left(r_s - r_R\right)\left(q^2 + \lambda_n^2\right) + D r_R q\right)} \quad (4.81)$$

where,

$$q = D + r_R k_f \quad (4.82)$$

If we substitute $k_b = 0$ in (4.64), κ_n becomes the n^{th} positive root of the following equation,

$$\tan\left(\left(r_s - r_R\right)\kappa_n\right) = -\frac{\lambda_n}{q} \quad (4.83)$$

The expected received signal for a partially absorbing receiver without degradation can be derived by substituting $k_d = 0$ in (4.81) as

$$N_{PA}(t) = \frac{2N_m k_f r_R^2}{r_T} \sum_{n=1}^{\infty} \left(1 - e^{-\kappa_n^2 D(t-t_0)}\right) \frac{q \sin\left(\left(r_T - r_R\right)\kappa_n\right) + \lambda_n \cos\left(\left(r_T - r_R\right)\kappa_n\right)}{\kappa_n \left(\left(r_s - r_R\right)\left(q^2 + \lambda_n^2\right) + D r_R q\right)} \quad (4.84)$$

The expected received signal by an irreversible receiver, i.e., fully or partially absorber, does not depend on the backward reaction constant, i.e., $k_b = 0$. This is due to the fact that the ligand-receptor complex cannot be dissociated because of the forward reaction constant, k_f, goes to infinity and any unbound molecule released from the receiver surface will be absorbed immediately by the receiver.

(iii) *Steady-state case* $(t \to \infty)$:

The expected received signal by the RN at the equilibrium, i.e., steady-state, can be obtained by evaluating the limit of (4.77) as the time approaches infinity to get,

$$N(t \to \infty) = \frac{2N_m k_f r_R}{r_T} \sum_{n=1}^{\infty} \frac{\beta_n \lambda_n \sin\left(\left(r_T - r_R\right)\kappa_n\right) + \alpha_n \lambda_n^2 \cos\left(\left(r_T - r_R\right)\kappa_n\right)}{\left(r_s - r_R\right)\left(\beta_n^2 + \alpha_n^2 \lambda_n^2\right) + D r_R \alpha_n \beta_n - 2\lambda_n^2 k_f k_b} \quad (4.85)$$

The asymptotic steady-state expressions for other special cases of an irreversible receiver can

also be derived using a similar procedure.

(iv) *Unbounded medium* $(r_s \to \infty)$:

The expected received signal for an unbounded medium can be analytically obtained by choosing a very large value for the medium radius r_s in Eq. (4.77). A comparison of results for this case will be discussed later. The expressions derived in this section for a bounded environment can reduce to the expressions of an unbounded medium when the separation distance between the TN and the RN is quite small compared to the medium radius assuming they are located far enough from the medium boundary.

4.6 Proposed Stochastic Simulator

In this section, we will introduce the 3-D stochastic particle-based simulator that has been developed to verify the accuracy of the proposed analytical expressions derived in section 4.5. This simulator can also be used as an alternative approach for modelling the complex ligand-receptor protein interaction inside biological bounded media. In this simulation framework, the total simulation time T is divided into N small time steps of width Δt. The number of remaining molecules and their precise locations are tracked and recorded at each time step during the simulation. The simulation procedure can be described throughout the following processes:

(i) *Molecular signal transmission*: the emitted impulsive signal represents the molecules 'M' that are instantaneously released by a point source, i.e., TN, at the time t_0 at the location (x_T, y_T, z_T) in a 3-D spherical bounded environment.

(ii) *Molecular diffusion*: the transmitted molecules move randomly and independently of each other according to Brownian motion in all direction in 3-D bounded environment, and the precise position of each molecule in the simulation environment is tracked and updated at each time step as follow:

$$\left(x_i, y_i, z_i\right) = \left(x_{i-1}, y_{i-1}, z_{i-1}\right) + \left(\Delta x_i, \Delta y_i, \Delta z_i\right), \quad i = 1, ..., N \tag{4.86}$$

where, N is the total number of time steps, (x_i, y_i, z_i) is the new location of each molecule at the i^{th} time step, $(x_{i-1}, y_{i-1}, z_{i-1})$ is the previous location of each molecule at the $(i\text{-}1)^{th}$ time step, and $(\Delta x_i, \Delta y_i, \Delta z_i)$ is the random displacements over each spatial

axis at the i^{th} time step which follows the normal distribution $N(0,\sigma^2)$ with zero-mean and variance $\sigma^2 = 2D\Delta t$.

(iii) *Molecular degradation*: biodegradation of the molecules during diffusion in the environment is modelled by a first-order degradation reaction mechanism. At each time step, a uniformly distributed random number a_d with a value between zero and one is assigned for each molecule. If the degradation probability, evaluated using (4.87) [64], is greater than a_d , then the molecule will be removed from the simulation environment.

$$P_d = 1 - e^{-k_d \Delta t} \tag{4.87}$$

(iv) *Molecular reaction/absorption at the medium boundary*: the position of each molecule is checked at the end of each time step, and then if the molecule reaches the medium boundary it will be either removed from the environment or reflected into the environment depending on the absorption rate constant of the medium boundary k_r .

(v) *Forward reaction of the molecules with the receptors (binding)*: the reaction of the molecules with the receptors on the RN surface is modelled via a reversible reaction mechanism. If the molecule hit the receiver, it can either bind to the receptor on the receiver surface or reflect into the environment depending on the forward reaction probability P_f , which is given in (4.88), [30].

$$P_f = k_f \sqrt{\frac{\pi \Delta t}{D}} \tag{4.88}$$

However, if the molecules fall inside the receiver volume during each simulation time step, i.e., not exactly on the receiver surface, then the molecules should be relocated to their correct locations on the receiver surface. Thus, the exact binding location (site) in the current time-step [$t_{j\text{-}1}$ t_j] is the intersection point between the receiver surface and the line passing throughout the molecule location at the beginning of the current simulation time-step, $(x_{j-1}, y_{j-1}, z_{j-1})$, and the final location of the molecule at the end of the current simulation time-step (x_j, y_j, z_j). Mathematically, this point can be determined by finding the intersection point of the sphere and line equations as

$$(x, y, z) = (x_{j-1}, y_{j-1}, z_{j-1}) + (\Delta x, \Delta y, \Delta z)h \tag{4.89}$$

where,

$$\Delta m = (m_j - m_{j-1}), \quad m \in \{x, y, z\} \tag{4.90}$$

$$h = \frac{-b - \sqrt{b^2 - 4ac}}{2a} \tag{4.91}$$

$$a = (x_j - x_{j-1})^2 + (y_j - y_{j-1})^2 + (z_j - z_{j-1})^2 \tag{4.92}$$

$$b = 2\left[(x_j - x_{j-1})(x_{j-1} - x_R) + (y_j - y_{j-1})(y_{j-1} - y_R) + (z_j - x_{j-1})(z_{j-1} - z_R)\right] \tag{4.93}$$

$$c = (x_{j-1} - x_R)^2 + (y_{j-1} - y_R)^2 + (z_{j-1} - z_R)^2 - r_R^2 \tag{4.94}$$

where, (x_R, y_R, z_R) is the coordinates of the RN center.

(vi) *Backward reaction of the molecules with the receptors*: each ligand-receptor complex, 'MR', on the RN has a dissociation (unbound) probability where the information molecule 'M' could be rereleased to the environment depending on the backward reaction probability given by [30] as

$$P_b = 1 - e^{-k_b \Delta t} \tag{4.95}$$

At each time step, a uniformly distributed random number a_b with a value between zero and one is assigned for each ligand-receptor complex 'MR'. If the backward reaction probability P_b is less than a_b, then the ligand remains bound to the receptor on the receiver surface. On the other hand, if the backward reaction probability is higher than a_b, then the ligand-receptor complex will dissociate, and the ligand will return to the environment to an approximate location given by [30] as

$$(x, y, z) = (x_{j-1}, y_{j-1}, z_{j-1}) + (\Delta x_R, \Delta y_R, \Delta z_R) \tag{4.96}$$

where,

$$\Delta m_R = \text{sgn}(m_{j-1} - m_R)\, p(a_m), \quad m \in \{x, y, z\} \tag{4.97}$$

$$p(a_m) = \frac{\sqrt{2D\Delta t}\left(0.571825\ a_m - 0.552246\ a_m^2\right)}{1 - 1.53908\ a_m\ +\ 0.546424\ a_m^2} \tag{4.98}$$

The random numbers a_m for $m \in \{x, y, z\}$ are uniformly distributed between zero and one and $\text{sgn}(\cdot)$ is the signum function.

(vii) *Molecular signal reception*: when a molecule binds to a receptor on the RN, it will be removed from the environment, and the RN counter will be increased by one. At the end of each time step, the total change in the number of the ligand-receptor complexes 'MR' on the receiver surface represents the expected received signal.

Compared to the simulation of MCvD in an unbounded medium and/or using a passive receiver, the absorption and degradation of the molecules in our model reduce the number of the remaining free molecules in the simulation environment. Thus, the total computation and simulation time will be reduced.

4.7 Analytical and Simulation Results

In this section, the analytical and simulation results of the expected number of ligand-receptor complexes (received signal) on a reversible RN (a target site) in a 3-D bounded biological microenvironment, are plotted and compared. We can observe that the analytical and simulation results have a perfect matching. Furthermore, the results show that the received signal can reduce to that of an unbounded medium when the medium radius becomes very large. All the simulation results are averaged over 100 independent realizations. The common system parameters are listed in Table 4.1 while other specific parameters are indicated separately for each case.

Table 4.1: The System Parameters (unless stated otherwise).

Parameters	Value	Unit	Description
N_m	10^5	Molecule	No. of the released molecules.
D	1×10^{-9}	m^2/s	Diffusion coefficient.
r_R	5	μm	The radius of the RN.
r_T	7	μm	The radial distance of the TN.
r_s	10	μm	The radius of the medium.
Δt	10^{-6}	s	Simulation time step.
T_s	0.2	s	Total Simulation Time.
# of realizations	100	-	-

In Figure 4.3, we plot the analytical and simulation results of the molecular received signal as a function of time in a bounded spherical medium with different radii and with fully-

absorbing boundary. This figure clearly shows that an increase in the medium radius leads to a corresponding increase in the amplitude and peak time of the received signal. This happens because as the medium radius becomes smaller, a portion of the emitted molecules will hit the medium boundary within a short time. Thus, the probability that the molecules be absorbed by the fully absorbing boundary is quite high. As a result, the absorbed molecules by the medium boundary, will be removed from the environment and will not contribute to the received signal. Therefore, one can see a reduction in the expected received signal. However, as the medium radius increases, the molecules have higher chances to react with the receptors on the receiver surface before being absorbed by the medium boundary. Then, the reaction between the molecules and the receptors may lead to forming ligand-receptor complexes on the receiver surface. The peak time increases with increasing the medium radius because the molecules that travel far away from the receiver will take a longer time to reach the receiver and to contribute to the received signal. It is worth repeating here that for relatively large radius of the bounded medium, our expressions can be reduced for unbounded medium which will be used for comparison with the published results in the literature, e.g., [30, 64, 163].

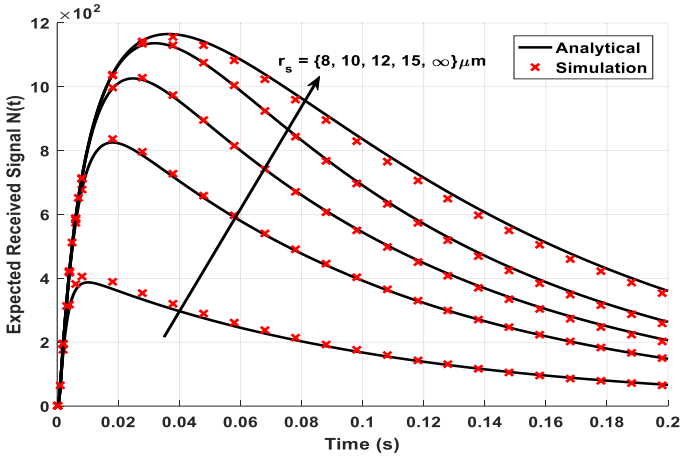

Figure 4.3: The expected received signal as a function of time for various medium radii using the following reaction parameters: $k_f = 50$ µm/s, $k_b = 5$ s^{-1}, and $k_d = 200$ s^{-1}.

As seen in Figure 4.3 and also in other figures in this section, the increasing trend of the expected received signal with time could be due to the forward reaction process which leads to an increase in the total bound receptors, i.e., ligand-receptor complexes, on the RN surface.

However, the decreasing trend at a later time may be due to the backward reaction process, which tends to reduce the total number of bound receptors on the receiver surface via dissociation of the ligand-receptor complexes into 'M' molecules. Both the forward and backward reaction processes are modelled via a reversible reaction process. As shown in Figure 4.3, after a lapse of long time interval, i.e., at steady-state, the expected received signal becomes very small due to the backward reaction process that leads to dissociation of the ligand-receptor complexes.

The influence of the forward reaction constant k_f on the expected received signal is shown in Figure 4.4. We can observe in this figure; that the total number of ligand-receptor complexes on the receiver surface have a higher amplitude when the forward reaction constant is increased. On the other hand, if the forward-reaction constant is reduced, the molecules that hit the receptors will have a lower probability to bind with the receptors, and they have higher probability to reflect into the environment. These molecules may diffuse far away and do not react again with the receiver receptors. Therefore, there is a corresponding decrease in the received signal.

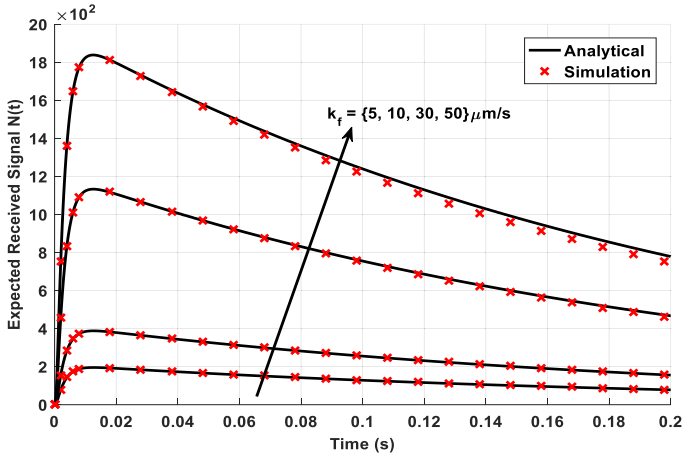

Figure 4.4: The expected received signal as a function of time for various values of the forward reaction constant using the following parameters: $k_b = 5$ s^{-1}, $k_d = 200$ s^{-1}, and $r_s = 10$ μm.

In Figure 4.5, the impact of the backward reaction constant on the expected received signal is plotted. In this figure, we can observe that the expected received signal decreases with increasing the backward reaction constant. This happens due to an increase in the dissociation

probability of the ligand-receptor complexes 'MR' on the receiver surface. As a result, the dissociated receptors will release the molecules (ligands) again to the medium. The newly dissociated molecules will diffuse in the environment with other molecules, which may either react again with the receiver receptors or move away without visiting the receiver again. Furthermore, the results in Figure 4.5 show a faster decreasing trend (higher decreasing slope) with time for the expected received signal as the backward reaction constant increases. This could be attributed to the faster dissociation process, and as a result, the ligand-receptor complexes get dissociated quickly as soon as they are formed. However, the increasing and decreasing trends of the expected received signal with time are mainly due to the forward and backward reaction processes, respectively, as discussed earlier.

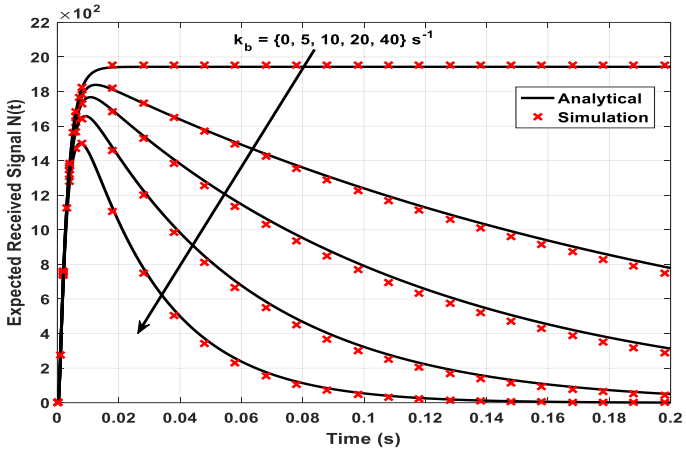

Figure 4.5: The expected received signal for various values of the backward reaction constant using the following parameters: k_f= 50 µm/s, k_d = 200 s^{-1}, and r_s = 10 µm.

The effect of degradation reaction in the environment is shown in Figure 4.6. The molecular degradation inside the medium is modeled via a first-order reaction process. As expected, the molecular received signal decreases with increasing value of the degradation reaction constant due to the increasing number of the degraded molecules in the environment. The degraded molecules will not be recognized by the RN thereafter and thus cannot bind to the receptors on the receiver surface. Thus, the amplitude of the received signal will decrease.

Now, we will demonstrate as to how the derived expressions published in the literature [64, 163] for the received signal in unbounded media are special cases of our model. The simulation and analytical results of the received signal in unbounded medium are calculated

by substituting a very large radius for the medium (e.g., infinity) in our expressions. As shown in Figure 4.7, the analytical and simulation results of the special cases agree well with the results in the published literature [64, 163]. Moreover, the results show that the amplitude of the received signal in a medium with molecular degradation is lower than the amplitude with the absence of the molecular degradation. However, to compare our model with the results in [64], we should multiply the forward reaction constant k_f by the receiver surface area, i.e., $4\pi r_R^2$, and then calculate the dimensionless parameters using [64, Eq. (11)]. This conversion is required because the boundary condition used in [64, Eq. (9)] differs from the boundary condition (4.9) used in this chapter by a factor equal to the receiver surface area.

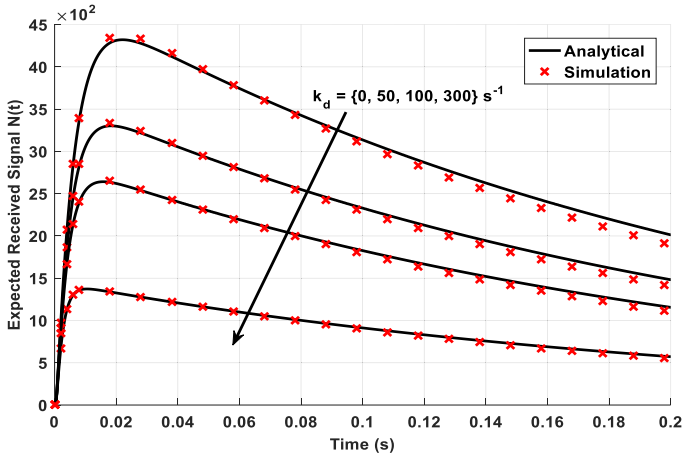

Figure 4.6: The expected received signal for various values of the degradation constant when other parameters have the following values: k_f = 50 µm/s, k_b = 5 s^{-1}, and r_s = 10 µm.

The results obtained using our models for the expected received signal of fully absorbing receiver with degradation (FD) and without degradation (FA) in the medium agree well with the available results in the literature for unbounded medium, [163, Eq. (116)], [64, Eq. (31)]. The fully absorbing receiver without degradation (FA) has the largest expected received signal compared to other receiver types. This is because the forward reaction constant is very large (infinity) while both backward reaction and degradation reaction are equal to zero. As a result, each reaction between a ligand (molecule) and a receptor on the receiver surface will lead to the formation of ligand-receptor complex without any possibility for the dissociation at a later time. The expected received signal for partially absorbing receiver obtained using

our model either with degradation (PD) or without degradation (PA) is always less than the received signal for both fully absorbing receivers, namely, FA and FD receivers. In addition, these results agree well with the results available in the literature for unbounded medium, [163, Eq. (114)], [64, Eq. (30)]. This may be due to the finite forward reaction for a partially absorbing receiver and consequently not all the reactions, between the ligands and the receptors, would lead to formation of the ligand-receptor complexes on the receiver surface.

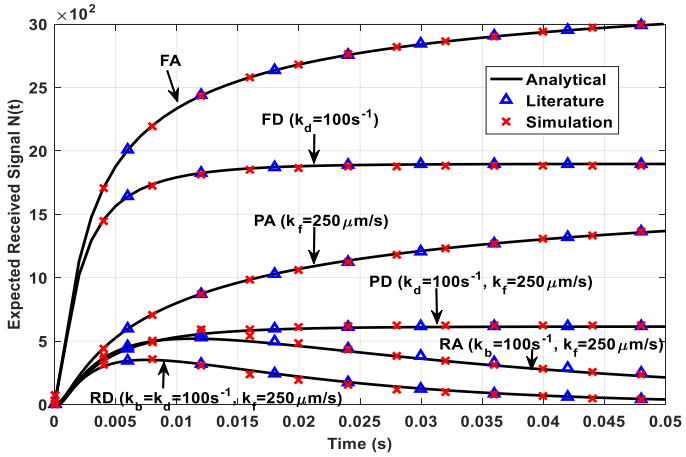

Figure 4.7: The expected received signal as a function of time in an unbounded environment for N_A=5000 molecules.

Furthermore, in Figure 4.7, the results obtained using Eq. (4.77) for a generalized case of the reversible receiver with/without degradation (RD, RA) in unbounded medium are plotted. We can observe that these results reduce to the special cases of unbounded medium which match well with the corresponding previous published works. The received signal has increasing amplitude with time for irreversible receiver, and after specific time it reaches a fixed value. This means that no further molecules will react with the receptors on the receiver surface. However, in case of the reversible receiver, the received signal amplitude starts to decrease after reaching the peak value. This may be because of the reverse reaction where some of the ligand-receptor complexes on the receiver surface get dissociated and then the molecules released back to the environment.

In Figure 4.8, the number of the ligand-receptor complexes (molecular received signal) is plotted using the stochastic particle-based simulator for various reaction rates at the medium boundary. As shown in this figure, a medium with fully reflecting boundary (k_r = 0 µm/s) has

the highest received signal compared to other cases while a medium with fully-absorbing boundary ($k_r \rightarrow \infty$) gives the lowest amplitude. Moreover, in the case of a partially absorbing boundary, an increase in the absorption (reaction) rate leads to further reduction in the expected received signal. This happens because probability of removing the molecules from the environment increases as the boundary reaction rate increases. Thus, fewer number of free molecules will be available in the environment to react with the receptors, and as a result the amplitude of the received signal will be reduced.

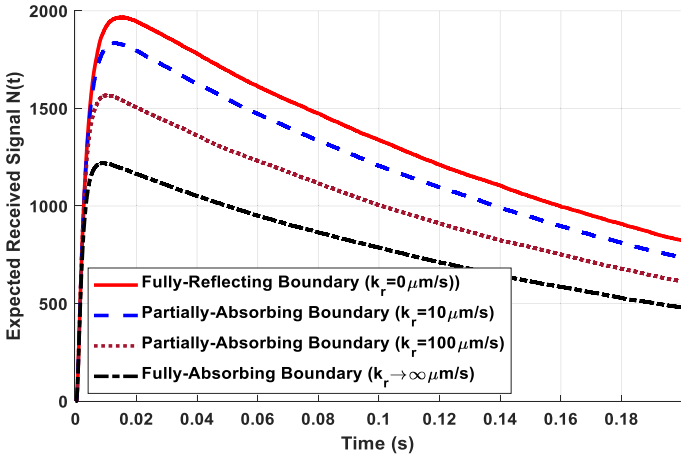

Figure 4.8: The expected received signal for different reaction rates at the medium boundary when the other parameters have the following values: k_f = 50 µm/s, k_b = 5 s^{-1}, and r_s = 8 µm.

4.8 Summary

In this chapter, we propose novel and accurate models for prediction of the ligand-receptor protein interaction on the surface of the target site (e.g., cell), which acts as a receiving nanomachine (RN), in 3-D bounded biological microenvironments using both analytical and stochastic simulation approaches based on molecular communication (MC) paradigm. We derived closed-form analytical expressions for the number of ligand-receptor complexes on the surface of the target site and the molecular concentration in its vicinity, including impact of the medium boundary. A reversible reaction mechanism is used to model the reception process on the receiver surface where the molecules reversibly react with the receptors to form the ligand-receptor complexes. Moreover, degradation of the molecules to other unrecognized molecules in the environment is modelled via a first-order reaction mechanism. Furthermore, we develop a stochastic particle-based simulator for the proposed model

including the reversible reaction at the receiver together with the molecular degradation and the reaction at the medium boundary. The perfect match between the simulations and analytical results indicates validity of the derived model.

In addition, we show that the derived expressions for the expected received signal in a bounded medium can be reduced to other special cases published in the literature for unbounded environments. The results indicate that the medium boundary affects the number of molecules that visit the receiver which in turn affects the amplitude and the time characteristics of the received signal. The impacts of other reaction rate parameters, namely, forward reaction, backward reaction, and degradation reaction, on the expected received signal are examined.

Noise affects the dynamics of cellular processes in the biological systems. Noise sources include intrinsic noise due to the stochastic nature of biochemical reactions in the cell and extrinsic noise due to variations in the microenvironmental conditions (temperature, pH, etc.). Extrinsic noise can lead to fluctuations in the molecular signals and thus affects the intercellular communication. Also, intrinsic noise due the stochastic nature of the biochemical reaction of the ligands with the cell's receptors, will cause fluctuation in number of the occupied receptors, i.e., counting/reception noise. As a result, this may affect the signaling pathways and cellular function inside the cells. Moreover, non-specific binding of the drug molecules to other unintended sites such as cell membrane and unintended protein receptors, may cause toxic side effects and may affect the therapeutic effect. Therefore, the noise sources and the non-specific binding events may affect the number of the activated receptors which in order will affect the intracellular signalling pathways. In future work, we will consider modelling of the various noise sources and their impacts on the number of activated receptors and on the drug delivery efficiency.

The proposed models can be used in the medical applications for example, for predicting the spatiotemporal drug concentration profile and the molecular reaction at the target cells, e.g., cancer cells. Also, these models can help in design and understand the reception and sensing mechanisms for detecting the molecular triggers and signaling molecules by the bio-nanomachines, bio-nanorobots, or synthetic cells.

CHAPTER 5

Influence of Anisotropy and Reactive Obstacles on Extracellular Molecular Communication via Diffusion

5.1 Introduction

Molecular communication (MC) enables the communication between the natural biological cells or the synthetic bio-nanomachines inside the body using chemical molecules such as ions and proteins [8, 9]. Therefore, it is suitable for many biomedical applications such as targeted drug delivery, disease diagnosis, and in-body area nanonetworks [17]. In this chapter, we will examine influence of the anisotropy and reactive biological obstacles (e.g., cells), on the molecular communication via diffusion (MCvD) between a transmitting nanomachine (TN) and a receiving nanomachine (RN) in the extracellular space (ECS). The TN could be a drug nanocarrier (or a sending cell) which releases drug molecules (or signaling molecules) through the ECS to finally reach the RN which may act as a diseased cell (or a receiving cell) [164]. The ECS may contain various obstacles which may hinder the diffusion of molecules via collision and interaction before reaching the destination [165, 166]. Moreover, some biological tissues in the body show anisotropic diffusion which affects the extracellular molecular transport [76, 167].

This chapter is organized as follows. Firstly, the impact of the reactive obstacles on the molecular received signal by bio-nanomachines in a diffusive environment is examined and presented in section 5.2. In section 5.3, we propose stochastic particle-based simulation model to examine the influence of anisotropy on molecular communication between bio-nanomachines which is verified by the analytical expressions. Finally, the summary is presented in section 5.4.

5.2 Influence of Reactive Obstacles on Molecular Communication via Diffusion

The reaction between the emitted biochemical molecules and the existing reactive obstacles, e.g., cells and other larger molecules, in the diffusive channel is very important to predict the molecular received signal at the destination (e.g., the RN or the target cell). The interaction with the various elements and obstacles in the ECS affects the molecular signal movement, i.e., alter and hinder diffusion of the molecules [164]. In the literature, only a few works investigated the impact of the reactive objects on the molecular concentration in the vicinity of the target cell or the RN in the extracellular microenvironments. In [74, 75], the effect of interfering fully absorptive receiver on another in MCvD channel has been addressed from the perspective of the communication theory. However, the interfering receiver was modelled as a perfect fully absorbing node, which represents an idealization or special case of an irreversible receiver (partially absorber/reflector). The reactive elements usually have limited reaction (binding/absorption) rate where some of the molecules will reflect on the obstacle surface and then will not be absorbed. In this section, we study impact of a partially absorptive obstacle, e.g., a biological cell, located in the diffusion path between the TN and RN, on the molecular received signal by the RN. Modelling the obstacle as a partially absorptive node can characterize different obstacle types which may found in the channel, e.g., inactive (fully reflecting) obstacle and reactive (partially or fully absorbing) obstacle.

We assume there is a reactive obstacle placed between a TN (e.g., a nanocarrier or a sending cell) and a RN (e.g., a target cell or a receiving cell) in molecular diffusive microenvironment which hinders the movement of the molecules as illustrated in Figure 5.1. The TN is assumed to be a point-like source emitting the molecules instantaneously into the environment. The size of the TN is assumed to be negligible when compared with the relative distance between the TN and RN. Moreover, the diffusion coefficient is assumed to be constant and uniform in all the directions, i.e., isotropic diffusion. Here, our focus will be on estimating the impact of the obstacles on the molecular received signal.

Once released, the molecules diffuse randomly in all directions in the environment according to Brownian motion. We assume that the collisions of the molecules with the boundary are

elastic, i.e., unbounded environment, and we are mainly focused on the impact of the size and the reaction characteristics of the obstacle. The molecules will collide and react with a partially absorptive obstacle located between the TN and the RN. This obstacle will absorb some of the molecules, and some of them will be reflected before they reach the RN depending on the reaction probability of the obstacle. The molecules will travel a more indirect path around the cellular obstacle before arriving at their destination, as compared to their path in the obstacle-free medium. At the target site, the molecules which succeed in reaching the RN will be either counted without absorbing for the passive virtual RN or they will be absorbed and removed from the propagation environment for the fully absorptive RN. The number of the received molecules over the time at the RN represents the molecular received signal.

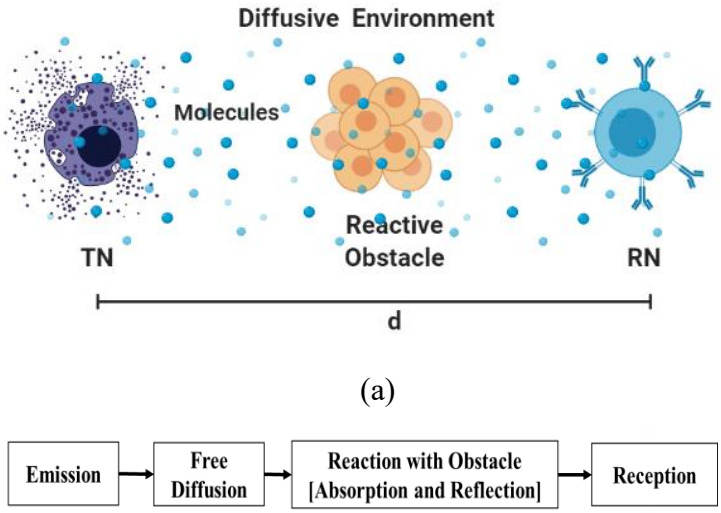

Figure 5.1: Molecular communication in a diffusive environment with a reactive obstacle. (a) Graphical representation (b) Block diagram representation for the processes. (This figure is created with BioRender)

5.2.1 Analytical Model

The existence of a passive RN in the microenvironment will not affect the diffusion of the released molecules; because it is just a virtual volume and the molecules will cross the receiver boundary without any physical or chemical reactions. Thus, the spatiotemporal distribution of the molecules at any arbitrary location (x, y, z) at the time t due to release the molecules

instantaneously from a TN located at the coordinate (x_0, y_0, z_0) and at the time $t = 0$, i.e., the channel impulse response (CIR), can be written as [130],

$$C(x,y,z,t) = \frac{1}{(4\pi Dt)^{3/2}} \exp\left(-\frac{d^2}{4Dt}\right), \quad t \geq 0 \tag{5.1}$$

where D is the diffusion coefficient of the molecules in the environment in (m^2/s) and d is the distance between the TN and the RN, given as $d = ((x-x_0)^2+(y-y_0)^2+(y-y_0)^2)^{1/2}$.

In general, the total number of the received molecules by a passive RN can be calculated by integrating the CIR over the RN volume then multiplying the result by the initial strength of the source (i.e., the total released molecules at time $t = 0$). Under the assumption that the distance between the TN and the RN is large compared to the RN size, then the concentration inside the receiver volume can be considered uniformly distributed. Thus, the number of received molecules by a passive RN can be expressed as

$$N_P = Q\ V_{rx}\ C(x,y,z,t) \tag{5.2}$$

where Q is the total number of released molecules at the time $t = 0$ and V_{rx} is the volume of the spherical RN.

The signal peak time is the time at which the signal achieves the maximum amplitude. The expressions for the peak time and peak amplitude of the molecular received signal for a passive RN, are given by [130], as

$$t_{\max} = \frac{d^2}{6D} \tag{5.3}$$

$$N_{\max} = \frac{Q}{d^3}\left(\frac{3}{2\pi e}\right)^{3/2} \tag{5.4}$$

The molecules react with the protein receptors on the surface of the RN once they hit its boundary, and thus, they may be absorbed or reflected by the RN. This means that the molecules contribute to the signal once in a short duration. Therefore, existence of an absorptive RN will affect the CIR. For a fully-absorbing RN located in an unbounded environment, the accumulative number of received molecules until the time t is given by [55] as

$$N_A = Q\frac{R_{rx}}{d}\,erfc\left(\frac{d - r_{rx}}{\sqrt{4Dt}}\right) \tag{5.5}$$

where r_{rx} is the RN radius and $erfc(\cdot)$ is the complementary error function.

5.2.2 Stochastic Particle-based Simulation for MCvD with Reactive Obstacles

Here, we develop a stochastic particle-based simulator to examine influence of the reactive obstacle on the molecular received signal in the diffusive microenvironment. In this simulator, the total simulation time T is divided into N time steps of width Δt. The molecules are released by a point-like TN at the time $t = 0$ and at the location (x_0, y_0, z_0). Then, the molecules move randomly and independently of each other according to Brownian motion in all direction in the microenvironment. The precise position of each molecule in the environment is tracked and updated at each time step following the procedure described in the previous chapters. Each molecule that hits the obstacle will be assigned with a uniformly distributed random number between zero and one. Then, if the assigned number is smaller than the reaction (absorption) probability given by Eq. (5.6) [30], the molecule will be absorbed by the obstacle which will then be removed from the simulation environment. Otherwise, the molecule will reflect-back into the environment.

$$P = k_a\sqrt{\frac{\pi\Delta t}{D}} \tag{5.6}$$

where, k_a is the association (absorption) rate constant.

Finally, the remaining molecules which reach the RN will be counted. For the fully absorptive RN, the molecules will be absorbed and removed from the environment following the same procedure which is performed for the reactive obstacle.

5.2.3 Analytical and Simulation Results

We examine impact of a reactive obstacle, located between the TN and the RN, on the molecular received signal for both passive and absorptive RN using stochastic reaction-diffusion based simulation. The radius and reaction probability of the obstacle are varied to examine their impact on the number of the received molecules by the RN. Then, these results are compared with the analytical results in the case of obstacle-free medium (i.e., absence of

the obstacle). The simulation parameters are listed in Table 5.1 (unless stated otherwise).

Table 5.1: System parameters for MCvD with existence of a reactive obstacle.

Parameter	Unit	Value	Description
T	s	1-5	Simulation time
Δt	ms	1	Time step
Q	molecules	10,000	No. of emitted molecules
D	$\mu m^2/s$	100	Diffusion coefficient
r_{rx}	µm	2	RN radius
r_{obs}	µm	2	Obstacle radius
d	µm	10	Distance between TN and RN
k_a	µm/s	0, 90 ,180	Obstacle reaction rate constant
P	-	0, 0.5, 1	Obstacle reaction probability
Iterations No.	-	200	-

Figure 5.2, shows the number of received molecules as a function of time for a passive RN with and without existing of the obstacle between the TN and the RN for different reaction probability at the obstacle. When the obstacle is absent (with an obstacle-free medium), the molecular received signal is higher than when it is present. Moreover, as the reaction probability of the obstacle increases, the amplitude of the received signal decreases. This is because some of the molecules will be absorbed by the obstacle and will not reach the receiver to contribute to the received signal. The chance for the molecules to be absorbed by the obstacle increases as the reaction probability increases and thus the number of the received molecule at the RN will be reduced. Here, the inactive obstacle has a fully reflective boundary which reflects any molecule hits the obstacle surface. It can be used to characterize an obstacle in the channel that may hinder diffusion of the molecules but without causing any binding reaction. Moreover, the peak time will increase with existence of the obstacle because the molecules will travel along circuitous path around the cellular obstacle before reaching their destination, as compared to their path in obstacle-free medium [165].

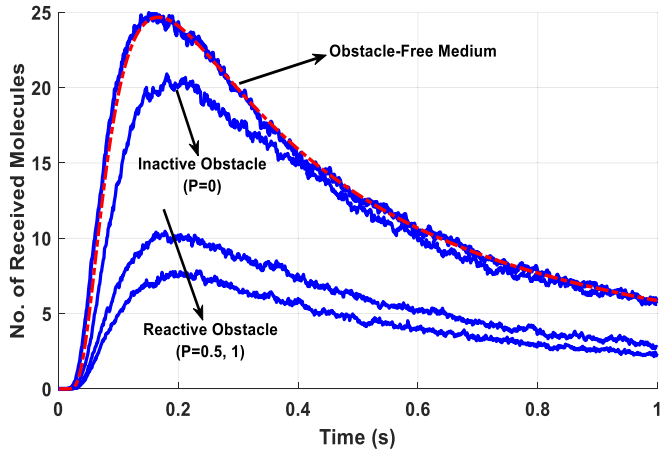

Figure 5.2: The number of received molecules by a passive RN for obstacle-free medium, inactive obstacle, and reactive obstacle with different reaction rates.

The peak amplitude of the received signal as a function of the obstacle's radius for a passive RN is shown in Figure 5.3 for different reaction probabilities on the obstacle. As shown in this figure, the peak amplitude of the received signal decreases as the obstacle's size increases. As the radius of the obstacle increases, the chances for the molecules to get absorbed by the obstacle increases, and thus fewer molecules can make it to the receiver. However, when the obstacle is absent, the peak amplitude is higher than when it is present for all the values of the reaction probability.

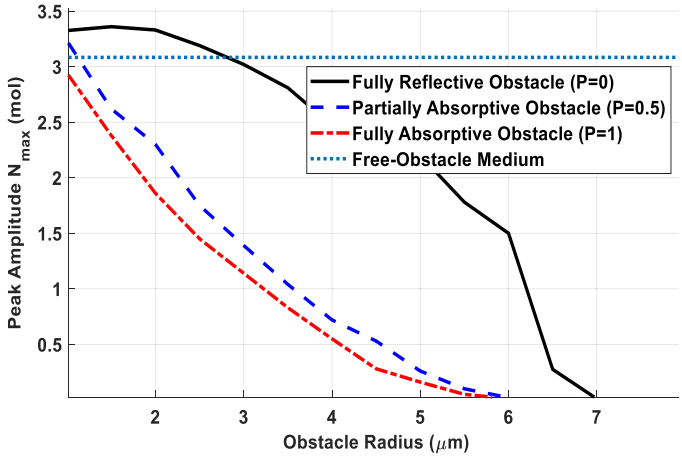

Figure 5.3: The peak amplitude of the received signal by a passive receiver versus the obstacle radius for different reaction probability on the obstacle. The distance between the TN and the RN is 20 μm.

Figure 5.4 shows the cumulative number of the received molecules by a fully absorptive RN with/without the existence of the obstacle and for different reaction probabilities. As expected, even using an active RN, absence of the obstacle (free-obstacle medium) leads to higher amplitude compared to existence of the obstacle between the TN and the RN. Furthermore, an obstacle with higher reaction probability (e.g., fully absorptive obstacle) leads to lower amplitude. At a very large time, the received signal reaches the steady-state and becomes fixed with time.

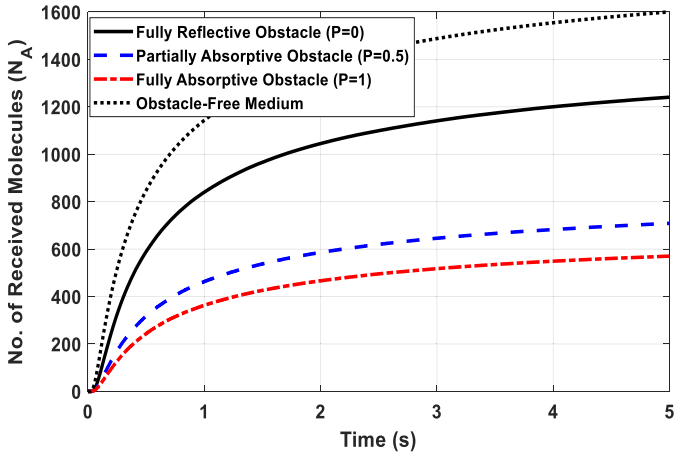

Figure 5.4: The expected number of received molecules for a fully absorptive receiver as a function of time with an obstacle for different reaction probabilities.

5.3 Effect of Anisotropic Microenvironments on the Molecular Received Signal

Diffusion plays a crucial role in the body as a transport mechanism to exchange the signaling molecules between the cells as well as to deliver other molecules (e.g., glucose, oxygen, and drugs) to the cells. Isotropic diffusion is suitable to characterize the movement of molecules in the biological environments which have identical structure and diffusion properties in all the directions. However, some biological tissues inside the body are highly anisotropic where the diffusion coefficients vary with the spatial dimension, e.g., the brain white matter [76, 167]. The mathematical and simulation models can provide a practical alternative method to estimate the molecular distribution and interaction in the various anisotropic tissues within the body by incorporating the experimentally determined parameters. However, it is important to include the anisotropy in modelling of the MCvD in the biological

microenvironments for accurate prediction of the spatiotemporal distribution of the molecules in the vicinity of the RN or the target site at various locations. Moreover, modelling of the diffusive environment using the CIR through convolution approach may help in modelling more complex systems using drug sources with different release profiles. This assumes greater significance as the development of drug-loaded bio-nanocarriers and bio-nanorobots have become a reality [34]. In this section, we propose a stochastic simulation model for MCvD where a point-like TN communicates (or emits molecules) to a passive RN placed inside a three-dimensional (3D) anisotropic microenvironment, see Figure 5.5. The RN is placed at different locations but with equal distance from the TN to examine impact of the anisotropy on the location of the RN. The stochastic particle-based simulation model is then validated using analytical CIR. In this model, the TN may act as a drug-loaded nanocarrier (or a sending cell) while the RN could be a target site (or a receiving cell). Here, the transmitted molecules may act as either signaling or drug molecules.

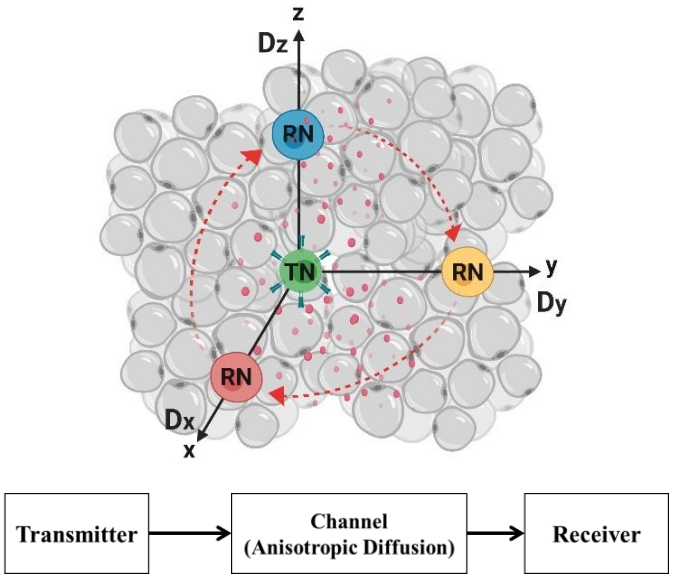

Figure 5.5: Molecular communication via diffusion in anisotropic microenvironment with different RN locations. (This figure is created with BioRender)

5.3.1 Analytical Model

Anisotropic diffusion is mathematically described by Fick's second law of diffusion [22],

$$\frac{\partial C(x,y,z,t)}{\partial t} = \nabla\left(\mathbf{D}\nabla C(x,y,z,t)\right) \tag{5.7}$$

where $C(x, y, z, t)$ is the molecular concentration at the location (x, y, z) at the time t, ∇ is the vector differential operator, and **D** is the diffusion tensor.

In 3-D anisotropic diffusive media, the diffusion is described by [3×3] diffusion tensor (**D**). The diagonal elements of the diffusion tensor represent the diffusion coefficients along each coordinate axis. The off-diagonal elements represent the correlation between the random motions in each pair of directions. The effective diffusion tensor incorporates crucial information which can be represented by an effective diffusion ellipsoid. In this work, the off-diagonal elements in the diffusion tensor are equal to zero as given in Eq. (5.8). This means that the structure and characteristic of the media in the direction of x, y, and z-axes are non-identical.

$$\mathbf{D} = \begin{bmatrix} D_{xx} & 0 & 0 \\ 0 & D_{yy} & 0 \\ 0 & 0 & D_{zz} \end{bmatrix} \tag{5.8}$$

where D_{xx}, D_{yy}, and D_{zz} are the diffusion coefficients along x, y, and z directions, respectively.

The solution for Eq. (5.7), assuming an instantaneous release of a single molecule by the TN at the position (x_0, y_0, z_0) at the initial time $t = 0$ in an unbounded medium, represents the displacement probability function. This function has been widely used for estimation of the diffusion tensor and the other transport properties in anisotropic media using different measuring techniques such as diffusion tensor imaging (DTI) [76, 77, 167]. A mathematical expression for the displacement probability function due to a 3-D anisotropic diffusion is given as [167],

$$C_A(x, y, z, t) = \frac{1}{\sqrt{D_{xx} D_{yy} D_{zz}}\,(4\pi t)^{3/2}} \exp\left(-\frac{\lambda}{4t}\right) \tag{5.9}$$

where,

$$\lambda = \frac{(x - x_0)^2}{D_{xx}} + \frac{(y - y_0)^2}{D_{yy}} + \frac{(z - z_0)^2}{D_{zz}} \tag{5.10}$$

In the case of an isotropic medium, i.e., all the tensor elements are equal to a single scalar value D, Eq. (5.9) reduces to (5.1).

The peak (maximum) time is the time instant at which the displacement probability function has the maximum amplitude. After making the time-derivative of (5.9) equal to zero, the peak time is obtained as

$$t_{\max} = \frac{\lambda}{6} \tag{5.11}$$

Now, by substituting (5.11) in (5.9), we get the peak amplitude expression as

$$C_{\max} = \frac{3^{3/2}}{\sqrt{D_{xx}D_{yy}D_{zz}}\left(2\lambda\pi e\right)^{3/2}} \tag{5.12}$$

Here, we assume that the RN is a virtual spherical observer (i.e., passive receiver). The molecular concentration inside the passive receiver volume is expected to be uniformly distributed when the distance between the TN and RN is large compared to the RN size. Thus, the expected number of received molecules by the RN, i.e., the channel impulse response (CIR), can be expressed as

$$N_P = Q\ V_{rx}\ C_A(x,y,z,t)\,. \tag{5.13}$$

where Q is the total number of released molecules at a time $t = 0$ and V_{rx} is the volume of the spherical RN.

5.3.2 Stochastic Particle-based Simulation for Anisotropic Microenvironments

Here, we present a stochastic particle-based simulator for MCvD between a point-like TN and a spherical passive RN inside a 3-D anisotropic microenvironment that has different diffusion properties along each axis. The simulation is developed using MATLAB software package. In this stochastic simulation model, the simulation time T is divided into N small time steps Δt. The molecules are instantaneously emitted from a point TN that is located at the position (x_0, y_0, z_0). Then, they are made to move randomly following Brownian motion in all the directions. The accurate number and locations of the molecules are tracked and recorded at the end of each time step. Since the simulation environment is anisotropic, the randomly propagating molecules experience different diffusivities in each direction and consequently result in different mean-square displacements (MSD) in the direction of each axis. The precise location of each molecule is updated at each time step similar to that in the

stochastic simulator, described in the previous chapters, but with random displacements follow a normal distribution $N(0,\sigma_u^2)$ with different variances as

$$\sigma_u^2 = 2D_u\Delta t, \quad u \in \{xx, yy, zz\} \tag{5.14}$$

Finally, at the end of each time step, the total number of molecules that reach the RN is recorded which is denoted as the received signal (or the CIR). Here, the RN is located at different positions to investigate how the location of the RN with respect to the TN location will affect the distribution of the molecules near the RN even when the TN-RN distance is made equal.

5.3.3 Analytical and Stochastic Simulation Results

The analytical and simulation results of the CIR and its peak amplitude and peak time are plotted for different diffusion tensors as well as for different locations and distances between the nanomachines. The simulation results are compared with the analytical results for validation. For the sake of analysis, we use the following simulation parameters: Q =10^5, Δt = 0.1ms, r_{rx} = 2μm, $(x_0, y_0, z_0) = (0,0,0)\mu m$, and the iterations number = 100. Here, the simulation environment has the following dimensions: 60×60×60 μm.

For the sake of analysis, the diffusion tensor for anisotropic media, given in [77], is chosen to obtain the CIR as shown in Figure 5.6. This tensor represents the effective diffusion coefficients, which include effect of the various properties such as the volume fraction and the tortuosity. Since the simulated time needed for the molecules to diffuse between the source and destination is very short, we assume that the cells to be stationary (immobile) and will not grow or divide in the ECS during the simulation time similar to that used in [168]. To get a fair comparison, the RN is moved between various locations but with keeping the same distance from the TN (the origin point), i.e., d = 10 μm. As shown in Figure 5.6, the CIR shows the highest amplitude (and the lowest peak time) when the RN is located at the position (10, 0, 0) μm on the x-axis but as the RN moves away from the x-axis, e.g., when the RN is located at (5.7, 5.7, 5.7) μm, the amplitude decreases with corresponding increase in the peak time. The worst case of the lowest amplitude and longest peak time happens when the RN is located on y- or z- axes. This may be due to fact that the diffusion tensor exhibits

diffusion preference towards x-axis direction rather than y- and z- axes. Thus, if the RN is located near the x-axis, it will fall within the diffusion ellipsoid of the molecule distribution, and thus enabling a greater number of molecules to reach the RN within a shorter time.

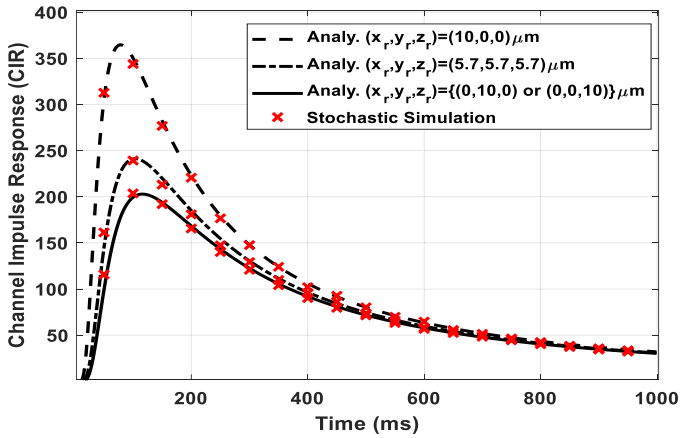

Figure 5.6: The CIR for various RN locations in 3D anisotropic environment for D = $(2.1,1.4,1.4)\times10^{-10}$ m^2/s.

The anisotropic diffusion tensor can be viewed using the diffusion ellipsoid whose main axis is parallel to the principal diffusion direction whereas for isotropic diffusion, the ellipsoid reduces to a sphere [167]. The visualization of diffusion ellipsoid for the diffusive molecules in a 3D anisotropic environment with different diffusion tensors is obtained from our particle-based simulator as shown in Figure 5.7. The molecular distributions (diffusion ellipsoids) are captured from the simulator at a time instant equal to the peak time of the CIR when the RN is located at the point (10, 0, 0) μm. The darker regions represent higher molecule density, and the larger spread area represents the longer diffusion time. As shown in Figure 5.7a, the diffusion is reduced to the case of an isotropic environment when $D=(5,5,5)\times10^{-9}$ m^2/s, and the diffusion ellipsoid becomes a sphere. Thus, for an isotropic case, whatever be the RN location (as long as it is equidistant from TN), the CIR will have identical characteristics. However, as shown in Figure 5.7b, for an anisotropic environment with $D=(5,1,1)\times10^{-9}$ m^2/s, the diffusion ellipsoid shows preference in the direction of x-axis (major axis) while the diffusion is restricted but identical in other directions (minor axes). One can observe circular diffusion spread in y-z plane because the diffusion coefficient components are equal in that plane. Therefore, the highest amplitude and the lowest peak time can be achieved

when the RN is positioned on x-axis, i.e., the major axis of the diffusion ellipsoid.

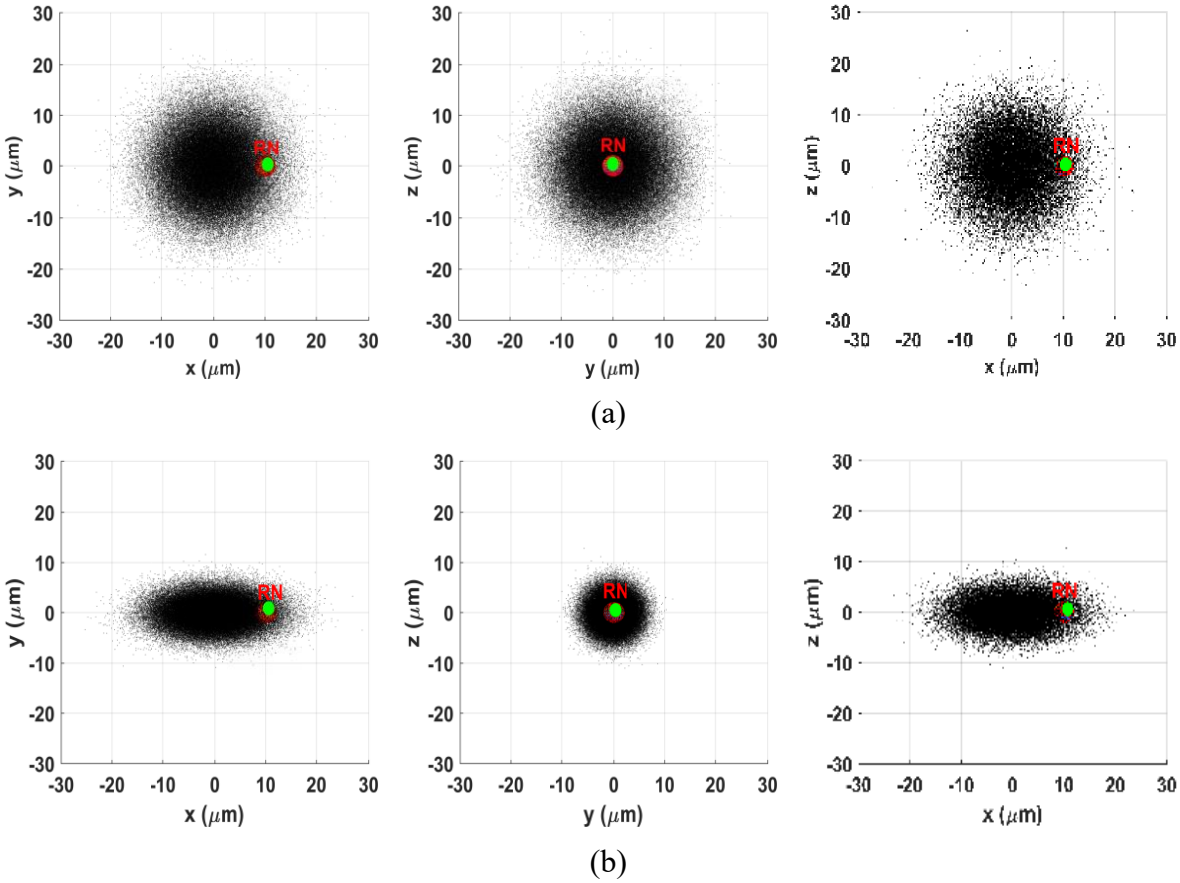

Figure 5.7: Visualization of the diffusion ellipsoid in 3-D anisotropic environment for (*a*) $D = (5,5,5)\times10^{-9}$ m^2/s and (b) $D= (5,1,1)\times10^{-9}$ m^2/s.

The peak amplitude and peak time of the CIR as a function of the separation distance between the TN and RN are plotted in Figure 5.8, for various diffusion tensors. As expected, the peak amplitude shows a decreasing trend while the peak time shows increasing trend as the TN-RN separation distance increases. As the separation distance increases lesser number of molecules may succeed in reaching the RN, and thus only few numbers of molecules will be detected by the RN. Moreover, the molecules will take longer time to reach the RN as the separation distance increases.

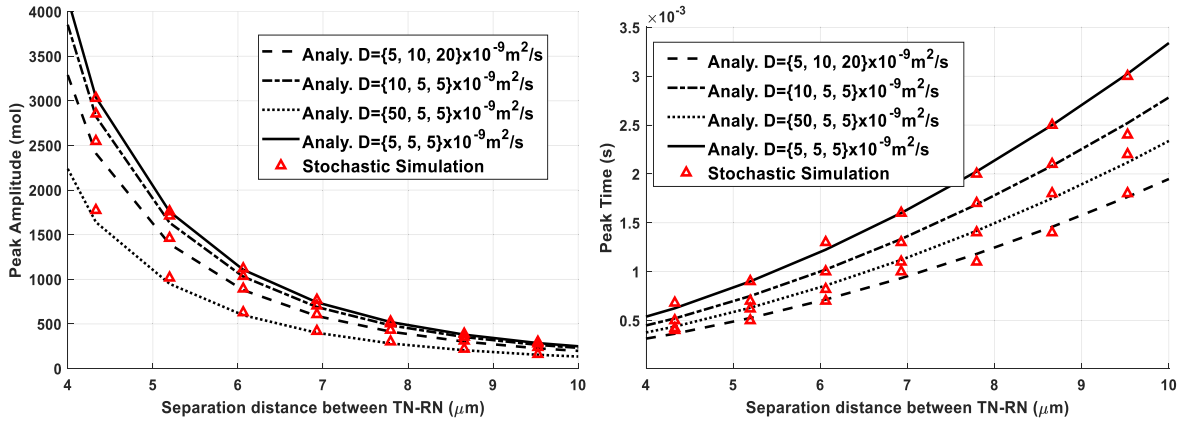

(a) (b)

Figure 5.8: (a) Peak amplitude and (b) peak time as a function of TN-RN separation distance for various diffusion tensors.

5.4 Summary

In this chapter, firstly, we examine impact of the reactive obstacle, located between the TN and the RN, on the molecular received signal. We develop stochastic particle-based simulator to predict the number of received molecules at both the passive and absorptive RNs. The influence of the radius and the reaction probability of the obstacle on the received signal are examined. The results show that the obstacle has a significant impact on the molecular received signal. The amplitude of the received signal decreases when an obstacle is present irrespective of whether the RN is passive or absorptive receiver. This reduction increases as the reaction probability and size of the obstacle increases. Therefore, it is essential to consider impact of the reactive obstacles in the propgation medium (channel) to accurately predict the molecular received signal at the RN (e.g., the target or receiving cell).

Secondly, the impact of anisotropy on MCvD is examined by comparing the stochastic simulation and analytical results of the CIR in an anisotropic diffusive microenvironment. We present an improved stochastic molecular communication framework to model the interaction between bio-nanomachines in 3D anisotropic microenvironment. The results obtained using the stochastic particle-based simulation are validated with the analytical expressions. We also derive expressions for the peak amplitude and peak time of the received molecular signal. The results demonstrate that the CIR in the anisotropic biological media

depends significantly on the diffusion tensor as well as on the locations of the nanomachines (not only on the TN-RN distance). The peak amplitude of the CIR for an anisotropic environment highly depends on the diffusion tensor, unlike an isotropic case where the peak amplitude is independent of the diffusivity. The amplitude and time characteristics of the CIR not only depend on the distance between the nanomachines as in the case of isotropic diffusion, but they also show high dependency on the locations of the nanomachines inside the environments. Thus, this work could help in design the drug delivery and diagnostic systems over micrometer scale as well as for In-Body nanonetworks and bionanomachine applications inside the biological microenvironments.

CHAPTER 6

Modelling of Implantable Drug Delivery System in Tumor using Molecular Communication Paradigm

6.1 Introduction

Cancer is a group of diseases characterized by uncontrolled growth and spread of abnormal cells [169]. Cancer can be treated using many treatment techniques, e.g., surgery, chemotherapy, etc. However, these types of conventional treatment techniques may have unwanted side effects and even could be quite expensive. Although systemic drug delivery is widely used as a preferred technique for administration of anticancer drugs, the main drawbacks for this technique are the poor drug bioavailability (due to high elimination, enzymatic degradation, and barriers) and the toxic side-effects (due to accumulation in other healthy parts of the body) [2, 3]. Therefore, a new alternative technique of drug delivery for cancer treatment is preferable. Drug delivery from a miniaturized implant offers an efficient alternative or adjunctive therapy to other treatment techniques, e.g., intratumoral injection, thermal ablation, and systemic delivery, particularly when the conventional therapies fail or cannot be applied [15]. The implantable drug delivery systems (IDDSs) are attractive strategies that provide lower toxicity and higher drug bioavailability compared to systemic chemotherapy [170]. In this approach, anticancer drug will be delivered locally inside the tumor over a prolonged period of time ranging from days to years without having to pass through the physiological barriers, i.e., the endothelial barrier of tumor vasculature. Thus, a very low dose of anticancer drug may result in better therapeutic outcomes compared to systemic delivery. In addition, a combination of different drugs could be released from the same implant. Recently, continuous intratumoral chemotherapy has been used for treatment of the tumor using cisplatin-loaded and methotrexate-loaded poly(lactic-co-glycolic acid)

(PLGA) implants [37, 171]. In [39], the authors investigated the efficiency of doxorubicin (DOX)-loaded, in situ-forming PLGA implant as an adjunct treatment after thermal ablation to destroy the residual tumors and to prevent tumor recurrence. The results show efficiency of using DOX-loaded PLGA implant after thermal ablation which leads to significant tumor shrinkage. Doxorubicin is one of the most efficient and widely used chemotherapeutic agents for the treatment of a wide range of malignancies [172]. In addition, a number of experimental studies are available in the literature on the use of DOX in tumor and other tissues due to its intrinsic fluorescence characteristics compared to other drug molecules [12].

The death of cancer cells depends on the anticancer drug concentration in their vicinity where a minimum drug concentration level (threshold) is required to kill the cells. Therefore, a minimum effective concentration (MEC) of the anticancer drug is required in each part of the tumor to provide an effective treatment [173]. Knowing the drug concentration profile, we can obtain the other useful pharmacokinetic (PK) parameters such as drug maximum (peak) concentration, peak time, and area under the curve (AUC). In addition, the drug concentration profile as a function of distance from the implant and the drug penetration depth, i.e., the distance from the implant at which the minimum concentration is achieved, are very useful and critical issues in design of the implants. Thus, spatiotemporal drug concentration profile in the tumor is essential for design the IDDSs which will help in choosing the appropriate insertion locations and the optimum releasing rates. Drug concentration in the tumor depends on various biochemical and biophysical processes, i.e., drug release, diffusion, and elimination [45]. Direct measuring of drug concentration and drug elimination in human tissues is quite complicated and cannot be readily obtained [12, 103]. Therefore, analytical and stochastic modelling can offer complementary ways to understand the drug distribution and elimination mechanisms in tumors and normal tissues.

Mathematical and stochastic models can help us to understand and predict the spatiotemporal distribution and pharmacokinetic behaviour of drugs following insertion of the drug implants in tumors. These models allow researchers to extrapolate in-vivo results from animal models to humans by linking the laboratory experiments with clinical applications [12, 45]. Also, mathematical modelling provides important insight for examining the various biophysical and biochemical features of drug and tumor tissue which contribute significantly in poor drug

uptake and limited drug penetration [12, 45]. These models can be applied to both preclinical and clinical trials to improve drug delivery and development processes. Therefore, they would be of great help in design and optimize various drug delivery systems (DDSs) including the IDDSs. This will save cost and time as well as reduce the number of animals used in the biomedical experiments.

Although, many experimental studies are available on measuring of the local biodistribution of the anticancer drug in the tumors, following insertion of the implants, e.g., [90, 144, 174-176], only few simplified models have been reported in the literature, e.g., [86, 101, 115, 177]. These models either assume constant drug release pattern at the implant/tissue interface or/and were solved for steady-state and in one-dimensional space. However, these assumptions are not reasonable for realistic implants where the drug release rate decreases with time. Moreover, these models are restricted for specified conditions and assumptions mainly due to limitations in the employed analytical techniques or limitations of the numerical computation software packages. These models do not provide mathematical expressions for the drug distribution profiles and do not offer impulse response. A more flexible and accurate mathematical and stochastic models with higher spatial and temporal resolution are needed for obtaining the drug concentration profile in tumors and other tissues. Also, providing a general model which can be applied to a wide range of implants with different release characteristics and therapeutic drugs will be a great benefit. Moreover, the release pattern should be characterized in an optimum way by fitting the release rate function to the experimental release data of the implants.

In contrast to other modelling approaches, linear systems analysis approach using convolution with time-varying impulse response provides generalized modelling with flexible and faster evaluation of the kinetics using fewer assumptions which are simple to verify experimentally [11, 12]. In addition, using this approach, we can obtain the input release function via deconvolution by knowing the output function, i.e., the drug concentration profile [178, 179]. Thus, we can link in-vitro and in-vivo experiments to predict drug concentration and to adjust the design and formulation parameters in the IDDSs.

In this chapter, we propose new mathematical and stochastic models to characterize and

predict the release and distribution of anticancer drug following implantation of a dual-release implant in tumor microenvironment (TME). The proposed mathematical model is derived by applying the system analysis approach using the impulse response convolution based on abstraction of the molecular communication (MC) paradigm. This approach is a more general and flexible approach than other modeling methods [103]. This model can be used for obtaining the spatiotemporal drug concentration profile in different tissues using a wide range of implants with different release rates and sizes as well as various therapeutic drugs. We can model both dual-release and sustained release implants by adjusting the release parameters. As an example, in-situ forming implants (ISFI) release drug over burst and sustained phases [39]. Also, we develop a novel accurate stochastic molecular-based simulation framework for the proposed IDDS model to validate the derived analytical model by individual tracking of each molecule in the environment. Stochastic particle-based simulation provides powerful alternative approach to mathematical and computational modelling, and it can be used as a benchmark tool for examining accuracy of the analytical models. Moreover, we compare our model with the available published experimental data in the literature to verify accuracy and validity of the proposed models.

The remainder of this chapter is organized as follows. In Section 6.2, we present the modelling approach based on the CIR and the MC abstraction. The mathematical derivation of the CIR is presented in section 6.3. The CIR is evaluated based on many roots obtained using the roots-finding algorithm, which is described in section 6.4. In section 6.5, we derive the drug release kinetic model which is fitted to published experimental release data. An expression for the spatiotemporal drug concentration profile in the tumor is obtained in section 6.6. In section 6.7, we develop a stochastic particle-based simulator for prediction the drug distribution in the vicinity of the implant through the tumor tissue. The results are discussed in section 6.8. Finally, the chapter summary is given in section 6.9.

6.2 Abstraction of the Implantable DDS in Tumor using MC Paradigm

Molecular communication (MC) paradigm can be used for modelling and abstraction of the DDSs by dividing the system into many processes in a systematic way. The MC paradigm provides accurate models with less complication and high spatiotemporal resolution for

prediction of the drug distribution and the PK parameters in the body. For example, in [26, 180], targeted drug delivery system (TDDS) is analytically modelled using MC abstraction, and drug biodistribution is predicted using communication metrics, such as channel delay and path loss.

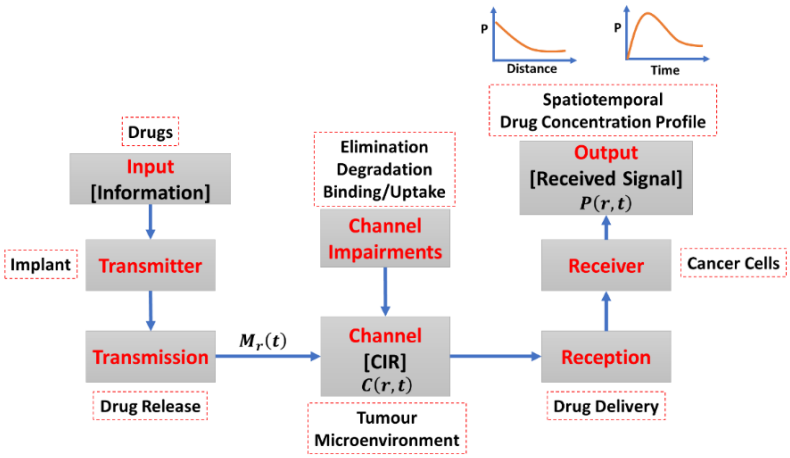

Figure 6.1: Abstraction of the implantable drug delivery system using MC paradigm.

Since we use system analysis approach for modelling of the IDDSs, which depends on the convolution with the CIR, we can use MC abstraction to simplify and understand the model structure and the various processes as shown in Figure 6.1. In MC paradigm, the implant acts as a transmitter while the target site, i.e., malignant cells, act as a receiver. From the perspective of MC paradigm, the anticancer therapeutic agent, i.e., doxorubicin, represents the input for the transmitter (information molecules). Process of drug release from the implant (release function) is abstracted as a transmission mechanism, and the drug delivery process at the target cells is abstracted as a reception mechanism. Here, the tumor environment represents the channel between the transmitter and the receiver which can be model using the CIR. The various PK processes that affect distribution of the drug in tumor (e.g., elimination and degradation) represent the impairments in the communication channel. Finally, the spatiotemporal drug concentration profile at the target cells acts as the receiver output (the received signal). The spatiotemporal drug concentration profile can be used as an input for evaluating the response and impact of drug on the cells using pharmacodynamic (PD) models as will be discussed in the next chapter.

Linear systems analysis is a generalized modelling approach that applies general linear

principles and mechanisms such as convolution and deconvolution to predict drug distribution and other PK characteristics in tumor and normal tissues [181]. We model the dynamics of drug release from the implant as well as distribution and elimination of drug molecules within the tumor tissue. In this work, the release pattern of the implant consists of both burst and sustained release phases. The release rate is obtained by fitting the implant release rate function to published experimental data of a dual-release implant [39]. Then, we derive a channel impulse response (CIR) which characterizes the whole system components. Finally, we derive closed-form analytical expression for anticancer drug concentration profile in the tumor by applying the convolution between the channel input (the release rate function) and the CIR.

6.3 Mathematical Formulation of Channel Impulse Response

In this work, drug source is assumed to be a miniaturized implant located inside a spherically shaped isolated tumor, as shown in Figure 6.2. The implant is surrounded by biological tumor tissue, composed of cells and an extracellular space (ECS) filled with extracellular fluid. The implant is loaded with anticancer drug doxorubicin that is immediately released into the vicinity of the implant after implantation. The released drug will transport through the ECS in the surrounding tissue via diffusion and convection. However, transport of small drug molecules in the tissue is dominated by diffusion rather than convection as in the case of the macromolecules [133, 144]. Previous studies showed that the interstitial convection in tumor has negligible impact on the distribution and elimination of small size drug molecules [101, 144]. Moreover, we found that the convection may have small influence on distribution of drug molecules only near the tumor boundary as will be discussed in the next chapter. In this chapter, the convection is assumed to be negligible throughout most parts of the tumor tissues [133]. Some drug molecules may uptake and bind to fixed elements, e.g., cells, in the surrounding tissue through passive, active, or facilitated transport paths. Moreover, drugs could be eliminated into the systemic circulation via diffusion across the semipermeable membranes of the capillaries. Other drug molecules may convert into other compounds due to various factors such as enzymes. The chemical alteration or degradation of drug molecules due to metabolism, such as enzymatic reaction, may convert drug molecules to other inactive substances. All the processes mentioned above affect the efficiency of drug therapy.

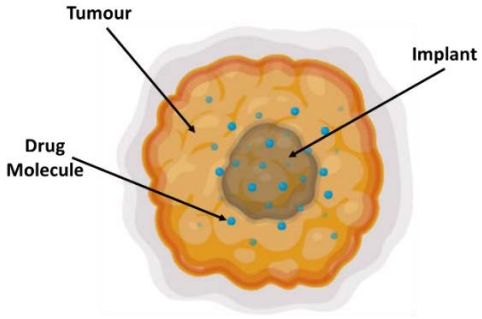

Figure 6.2: Graphical illustration of the implantable drug delivery system in a tumor microenvironment. (This figure is created with BioRender)

Tumor tissues can be considered as porous media because the length scale of the intercapillary distances (i.e., the average distances between the capillaries) is much smaller than the length scale of tumor radius [182]. Moreover, the tumor is assumed to be isolated from the surrounding normal tissues, i.e., an isolated tumor [182]. Therefore, drug transport in the tissue surrounding the implant is mathematically governed by the following diffusion equation:

$$\frac{\partial C}{\partial t} = D\nabla^2 C - \gamma C \tag{6.1}$$

where, ∇^2 is the Laplacian operator, C is the spatiotemporal distribution of drug molecules in the tumor, D is the effective (apparent) diffusion coefficient of drug in tumor tissue in (m^2/s), γ is the apparent lumped first-order elimination rate constant due to (degradation, permeation/clearance through blood capillaries, and binding or uptake into the cells), and t is the time after implantation.

When the binding and uptake process is very fast compared to the diffusion process, the local equilibrium between the free and bound molecules will be attained [183]. Therefore, the apparent diffusion coefficient (ADC) and the apparent first-order elimination rate constant can be expressed as follows, respectively, [95, 115]:

$$D = \frac{D_w}{k_{bind} + 1} \tag{6.2}$$

$$\gamma = \frac{\gamma_w}{k_{bind} + 1} \tag{6.3}$$

where, D_w and γ_w are the drug diffusivity and the lumped first-order loss rate constant without including the binding or uptake effect. The parameter k_{bind} is the binding constant of the drug molecules with other elements in the environment, e.g., cells, proteins, etc.

In the implantable drug delivery systems (IDDSs), the rapid elimination (perfusion) of drug molecules through the capillaries is the most significant factor that affects drug distribution. Assuming that the concentration of drug in the blood is small compared to that in the tissue and drug in the tissue is low enough that any enzymatic reactions, thus the elimination and degradation kinetics can be approximated to first-order processes [95, 99]. The lumped elimination rate constant in the tumor microenvironment (TME) can be defined as

$$\gamma_w = \gamma_v + \gamma_e + \gamma_o \tag{6.4}$$

where γ_v is the loss rate constant due to permeation/clearance through blood capillaries, γ_e is the degradation rate constant due to enzymatic reaction, and γ_o is the degradation rate constant due other factors. In this work, we assume the drug elimination rate due to lymphatic drainage is equal to zero, due to lack of lymphatic system inside the tumors [49, 144]. The chemical alteration (or degradation) of drug molecules due to metabolism, such as enzymatic reaction, may convert drug molecules into other inactive substances.

Assuming a spherical shape tumor, Eq. (6.1) can be expressed in the spherical symmetric coordinate systems, as

$$\frac{\partial\left(rC\left(r,t;r_0,t_0\right)\right)}{\partial t} = D\frac{\partial^2\left(rC\left(r,t;r_0,t_0\right)\right)}{\partial r^2} - \gamma rC\left(r,t;r_0,t_0\right) \tag{6.5}$$

where $C(r,t;r_0,t_0)$ is the drug molecules distribution at the time t and at the radial distance r due to release the drug molecules at the time t_0 and at the radial distance r_0.

In order to obtain the channel impulse response (CIR), i.e., the Green's function, we assume that the drug is instantaneously released at the time $t = t_0$ (i.e., the time of implantation) at the radial position $r = r_0$ from the implant. Thus, the following initial condition is applied.

$$C\left(r,t \to t_0\right) = \delta\left(r - r_0\right)\delta\left(t - t_0\right) \tag{6.6}$$

where r_0 is the implant radius and $\delta(\cdot)$ is Dirac Delta function. This initial condition represents

the instantaneous release of the drug molecules by point-like sources uniformly distributed on the surface of a spherical implant with radius r_0.

In this model, two boundary conditions must be defined, namely, the inner boundary at the center of the implant and the outer boundary at the tumor surface. The drug concentration is assumed to be finite at the center of the implant (i.e., $r \to 0$). Thus, the following additional boundary condition can be applied.

$$C\left(r,t;r_0,t_0\right) \text{is finite at } r \to 0 \tag{6.7}$$

To keep the generality of the model, Robin boundary condition [61, 184], is chosen as a general flux boundary condition at the outer surface of the tumor.

$$-D\nabla C\left(r,t;r_0,t_0\right)\Big|_{r=r_t} = \omega C\left(r,t;r_0,t_0\right)\Big|_{r=r_t} \tag{6.8}$$

where, ω is reaction rate (or loss rate) at the tumor boundary in the unit of (m/s) and r_t is the tumor radius. As a special case, the Robin boundary condition can be reduced to fully permeable (perfect-sink) and impermeable (no-flux) conditions by adjusting the loss rate ω. This condition can be used to reflect the effect of drug elimination into the neighboring tissues or the drug leakage through the exchange blood, and lymphatic vessels at the outer boundary of the tumor where many exchange vessels exist which may act as a sink for drug molecules [116, 182].

The distribution function $C(r,t;r_0,t_0)$ represents the final CIR which needs to be derived. Now, the drug distribution at the location r at the time t due to an instantaneous release of drug from a point-like source at the position $r = r_0$ at the time $t = t_0$ inside an unbounded medium is given by [130]. This distribution function can be rewritten by adding the general initial release time and the elimination rate term, as

$$C_u = \frac{1}{(4\pi D(t-t_0))^{3/2}} \exp\left(-\frac{\|r-r_0\|^2}{4D(t-t_0)} - \gamma(t-t_0) \right) \tag{6.9}$$

where, $\|r-r_0\|$ is the separation distance between the drug point-like source and the observation point (i.e., the virtual receiver).

The final CIR can be obtained by integrating the CIR due to a point-like source, i.e., Eq. (6.9) , over the implant surface area (A) by transforming the parameters to the spherical coordinate system, as follows

$$C_s = \frac{1}{A} r_0^2 \int_0^{2\pi} \int_0^{\pi} C_u\left(r, \phi, \theta, t\right) \sin\left(\phi_0\right) d\phi_0 d\theta_0 \tag{6.10}$$

where $(0 \le \theta < 2\pi)$ is the azimuth angle and $(0 \le \phi \le \pi)$ is the polar angle.

By transforming the CIR (6.9) to spherical coordinate system depending on the fact that the medium is spherically symmetric (i.e., $\phi = \theta = 0$) and the point-like source is located at the position (r_0, ϕ_0, θ_0) , we get

$$C_u = \frac{1}{(4\pi D_t (t - t_0))^{3/2}} \exp\left(-\frac{r_0^2 + r^2 - 2 r r_0 \cos(\phi_0)}{4D(t - t_0)} - \gamma(t - t_0) \right) \tag{6.11}$$

By substituting (6.11) in (6.10), we get

$$C_s = \frac{1}{2(4\pi D(t - t_0))^{3/2}} \exp\left(-\frac{r_0^2 + r^2}{4D(t - t_0)} - \gamma(t - t_0) \right) \int_0^{\pi} \exp\left(\frac{r r_0 \cos(\phi_0)}{2D(t - t_0)} \right) \sin(\phi_0) d\phi_0 \tag{6.12}$$

Now, after evaluating the integral in (6.12) using [128, Eq. (3.915.1)], C_s can be written as

$$C_s = \frac{1}{4\pi r_0 r (4\pi D(t - t_0))^{1/2}} \left[\exp\left(-\frac{(r - r_0)^2}{4D(t - t_0)} - \gamma(t - t_0) \right) - \exp\left(-\frac{(r + r_0)^2}{4D(t - t_0)} - \gamma(t - t_0) \right) \right] \tag{6.13}$$

The Laplace transform of Eq. (6.13) can be evaluated with the help of [125, Eq. (29.3.84)] as follows

$$\tilde{C}_s = \frac{e^{\gamma t_0} e^{-s t_0}}{4\pi r_0 r D \zeta} \times \begin{cases} e^{-r_0 \zeta} \sinh\left(r\zeta\right), & r < r_0 \\ e^{-r\zeta} \sinh\left(r_0 \zeta\right), & r > r_0 \end{cases} \tag{6.14}$$

where $\tilde{C}_s$ is the Laplace transform of C_s and

$$\zeta = \sqrt{(s + \gamma)/D} \tag{6.15}$$

The CIR due to an instantaneous drug release from the implant can be expressed as a superposition of two functions using a mathematical technique similar to that used in [30, 163],

$$C = C_s + C_b \tag{6.16}$$

Here, the parameters $(r, t; r_0, t_0)$ are omitted to simplify the mathematical notation. The total solution (6.16) can be written in the Laplace domain as

$$r\tilde{C} = r\tilde{C}_s + r\tilde{C}_b \tag{6.17}$$

where $\tilde{C}$ is the Laplace transform of C and the multiplication factor r is used to simplify the mathematical derivation.

The term C_b is the solution of the following diffusion equation which vanishes at $t = t_0$ and when it is added to C_s satisfies the boundary conditions (6.7)-(6.8).

$$\frac{\partial\left(rC_b\right)}{\partial t} = D\frac{\partial^2\left(rC_b\right)}{\partial r^2} - \gamma r C_b \tag{6.18}$$

Now, Eq. (6.18) can be converted into an ordinary differential equation (ODE) using the Laplace transform as

$$\frac{\partial^2\left(r\tilde{C}_b\right)}{\partial r^2} - \zeta^2 r\tilde{C}_b = 0 \tag{6.19}$$

The diffusion equation (6.19) is a second-order ODE which has two roots, i.e., $\pm\zeta$. Thus, the solution of Eq. (6.19) can be expressed as

$$r\tilde{C}_b = A\sinh(r\zeta) + B\cosh(r\zeta) \tag{6.20}$$

After substituting Eqs. (6.14) and (6.20) in (6.17) for the case of $r > r_0$, we get

$$r\tilde{C} = \frac{e^{\gamma t_0}e^{-st_0}\sinh\left(r_0\zeta\right)e^{-r\zeta}}{4\pi r_0 D\zeta}H\left(r - r_0\right) + A\sinh(r\zeta) + B\cosh(r\zeta) \tag{6.21}$$

The boundary conditions (6.7)-(6.8) can be converted to the Laplace domain as

$$\tilde{C}\Big|_{r=0} \text{ is finite} \tag{6.22}$$

$$-D\frac{\partial\tilde{C}}{\partial r}\bigg|_{r=r_t} = \omega\tilde{C}\Big|_{r=r_t} \tag{6.23}$$

We will rewrite the boundary condition (6.23) in an appropriate form to make the derivation mathematically tractable. Thus, using the product rule of differentiation, we get

$$\left.\frac{\partial\left(r\tilde{C}\right)}{\partial r}\right|_{r=r_t} = \left.\tilde{C}\right|_{r=r_t} + r_t \left.\frac{\partial\tilde{C}}{\partial r}\right|_{r=r_t} \tag{6.24}$$

By combining Eqs. (6.23) and (6.24), we get

$$\left.\frac{\partial\left(r\tilde{C}\right)}{\partial r}\right|_{r=r_t} = r_t\lambda\left.\tilde{C}\right|_{r=r_t} \tag{6.25}$$

where,

$$\lambda = \frac{D-\omega r_t}{Dr_t} \tag{6.26}$$

After applying the boundary conditions (6.22) and (6.25) to Eq. (6.21), we can obtain the values of A and B as

$$A = -\frac{e^{-st_0}}{4\pi r_0 D\zeta}\frac{e^{-r_t\zeta}\sinh\left(r_0\zeta\right)\left(\zeta+\lambda\right)}{\left(\lambda\sinh\left(r_t\zeta\right)-\zeta\cosh\left(r_t\zeta\right)\right)} \tag{6.27}$$

$$B = 0 \tag{6.28}$$

The total solution (i.e., the CIR) is obtained by substituting Eqs. (6.27)-(6.28) in (6.21) as follows

$$\tilde{C} = \frac{e^{-st_0}}{4\pi r_0 rD}\sinh\left(r_0\zeta\right)\left(\frac{e^{-r\zeta}\left(\lambda\sinh\left(r_t\zeta\right)-\zeta\cosh\left(r_t\zeta\right)\right)-e^{-r_t\zeta}\sinh\left(r\zeta\right)\left(\zeta+\lambda\right)}{\zeta\left(\lambda\sinh\left(r_t\zeta\right)-\zeta\cosh\left(r_t\zeta\right)\right)}\right) \tag{6.29}$$

The inverse Laplace transform of Eq. (6.29) can be obtained using Cauchy's residue theorem [185],

$$C = \sum_{poles\ of\ \tilde{C}} \mathrm{Res}\left(\tilde{C}e^{st}\right) \tag{6.30}$$

where, $\mathrm{Res}(\tilde{C})$ is the residue of $\tilde{C}$.

The expression (6.29) has a simple pole at $s=-\gamma$ with zero residue and an infinite number of simple poles at $s=-\left(D\kappa_n^2/r_t^2+\gamma\right)$ for n=1, 2,…, ∞. The parameter κ_n is the real positive roots

of the following equation:

$$\varphi(\kappa_n) = \lambda r_t \tan(\kappa_n) - \kappa_n \tag{6.31}$$

Thus, the inverse Laplace transform of (6.29) can be written as

$$C = \frac{1}{2\pi r_0 r_t r} \sum_{n=1}^{\infty} e^{-\left(D\kappa_n^2/r_t^2+\gamma\right)(t-t_0)} e^{-i\kappa_n} \frac{\sin\left(r_0\kappa_n/r_t\right)\sin\left(r\kappa_n/r_t\right)\left(i\kappa_n + r_t\lambda\right)}{\left(\cos\left(\kappa_n\right)\left(\lambda r_t - 1\right) + \kappa_n \sin\left(\kappa_n\right)\right)} \tag{6.32}$$

At the roots of Eq. (6.31), we get the following identity

$$\sin\left(\kappa_n\right) = \frac{\kappa_n}{\lambda r_t \cos\left(\kappa_n\right)} \tag{6.33}$$

After applying Euler's formula on the exponential ($e^{-i\kappa_n}$) and then substituting Eq. (6.33) in (6.32), we get

$$C = \frac{1}{2\pi r_0 r_t r} \sum_{n=1}^{\infty} \frac{\sin\left(\kappa_n r_0/r_t\right)\sin\left(\kappa_n r/r_t\right)}{\kappa_n^2 + \lambda r_t\left(\lambda r_t - 1\right)} \left(\kappa_n^2 + \lambda^2 r_t^2\right) e^{-\left(D\kappa_n^2/r_t^2+\gamma\right)(t-t_0)} \tag{6.34}$$

Equation (6.34) represents the CIR expression due to drug release instantaneously from a spherical drug implant inserted inside an isolated tumor. As a special case, the outer boundary of the tumor can be chosen as either an impermeable (zero-flux) or fully permeable (perfect-sink); thus, the CIR can be reduced as follows:

(i) Fully permeable boundary $(\omega \to \infty)$:

$$C_{FP} = \frac{1}{2\pi r_0 r_t r} \sum_{n=1}^{\infty} \sin\left(\frac{\kappa_n r_0}{r_t}\right) \sin\left(\frac{\kappa_n r}{r_t}\right) e^{-\left(D\kappa_n^2/r_t^2+\gamma\right)(t-t_0)} \tag{6.35}$$

where, κ_n are the positive roots of (6.31) when $(\omega \to \infty)$, i.e., $\kappa_n = n\pi$. Thus, Eq. (6.35) can be written as

$$C_{FP} = \frac{1}{2\pi r_0 r_t r} \sum_{n=1}^{\infty} \sin\left(\frac{n\pi r_0}{r_t}\right) \sin\left(\frac{n\pi r}{r_t}\right) e^{-\left(Dn^2\pi^2/r_t^2+\gamma\right)(t-t_0)} \tag{6.36}$$

(ii) Impermeable boundary $(\omega = 0)$:

$$C_{IP} = \frac{1}{2\pi r_0 r_t r} \sum_{n=1}^{\infty} \frac{\kappa_n^2 + 1}{\kappa_n^2} \sin\left(\frac{\kappa_n r_0}{r_t}\right) \sin\left(\frac{\kappa_n r}{r_t}\right) e^{-\left(D\kappa_n^2/r_t^2+\gamma\right)(t-t_0)} \tag{6.37}$$

where, κ_n are the positive roots of (6.31) when $(\omega = 0)$, i.e., $\tan\left(\kappa_n\right) = \kappa_n$.

6.4 Root Finding Algorithm

Although the expression (6.34) is an infinite series and has infinite roots, it converges for a finite number of roots while the remaining roots have negligible contribution which can be ignored. To obtain highly accurate results, we implement a rigorous algorithm in MATLAB to find the roots of $\varphi(\kappa_n)$ which have a significant impact on evaluation of the expression (6.34), which is given below in Algorithm 6.1. However, other roots that have a negligible effect on the final result are removed.

Algorithm 6.1: Finding Roots of $\varphi(\kappa_n)$

Initialize the parameters $\{F, \alpha, \varepsilon$, RMSE, n, m, N$\}$
While (RMSE $> \varepsilon$) do
  $m \leftarrow m+1$
  For all the integers $i \in [0\ F]$ do
    Find a zero κ_i for $\varphi(\kappa_i)$ in the interval $(m-1)+[(i-1)/F \quad i/F]$
    If $|\varphi(\kappa_i)| < \alpha$ then
      Update the nth root: $\kappa_n \leftarrow \kappa_i$
      $n \leftarrow n+1$
      Exit from 'for loop'
    End if
  End for
  If n is a multiple of N then
    Evaluate C using all the roots from κ_1 to κ_n
    Calculate RMSE between C and h for all time steps
    Update $h \leftarrow C$
  End if
End while
Roots $\leftarrow [\kappa_1, ..., \kappa_n]$

The roots of $\varphi(\kappa_n)$ can be obtained after setting this term equal to zero, i.e.,

$\tan(\kappa_n) = \kappa_n / \lambda r_t$. Therefore, the term on the l.h.s $\tan(\kappa_n)$ is continuous and strictly monotonically increasing function everywhere on the imaginary axis, i.e., it increases from -1 to 1, and the term on the r.h.s ($\kappa_n / \lambda r_t$) is continuous and strictly monotonically decreasing function everywhere on the imaginary axis, i.e., it decreases from ∞ to $-\infty$. Therefore, the two terms have one intersection point at zero (i.e., single root at zero). On the other hand, the term $\tan(\kappa_n)$ is continuous and strictly monotonically increasing function in each interval along the positive real axis, i.e., $I_n = [-\pi/2 \quad \pi/2] + n\pi$ and the term ($\kappa_n / \lambda r_t$) is continuous and strictly decreasing function everywhere along the positive real axis. Since the l.h.s and the r.h.s terms have opposite monotonic behaviors in each interval I_n and the l.h.s has value from $-\infty$ to ∞, then each interval I_n has exactly one intersection point (i.e., one root) and thus an infinite number of intersection points along the positive real axis.

Firstly, the parameters are initialized in Algorithm 6.1. Then, the positive real axis is divided into many small intervals. The search accuracy depends on the parameter (F), where a higher value of F result in finer search outcomes. Each interval is scanned to find the root (κ_i) that makes Eq. (6.31) has a value less than the accuracy-threshold value (α) and then if this root is found, the n^{th} root value will be updated by the value of κ_i. Then, the algorithm will search the next interval for any possible root. Here, we do not need to search the remaining part of the interval because there is only one root in each interval. This because the spacing between the roots is larger than one. Therefore, this task will reduce the total processing time required to find the whole roots. Each time we obtain a number of roots (N), the concentration expression (C), given by (6.34), will be evaluated using all the previous obtained roots, i.e., $\kappa_1, .., \kappa_n$. Then, the root-mean square error (RMSE) will be evaluated between the current evaluated expression C and previous evaluated expression h. The value of h will be updated by the current evaluation of C to be used in the next evaluation of the RMSE. Now, the RMSE value, which is evaluated in the previous iteration, will be compared with the precision-threshold (ε). If the RMSE value becomes smaller than ε, then we will get all the desired roots and the search process will be finished. The precision-threshold (ε) can be chosen depending on the required degree of accuracy for the expression (6.34). A higher degree of

accuracy can be achieved by choosing a smaller value of ε and thus a larger number of roots will be used in evaluation of (6.34). However, if the parameter F increases or the parameters (ε, α) decrease, the algorithm will require longer time for searching more precise roots.

6.5 Drug Release Kinetics

The use of drug implants with a desirable release rate and over a long period is a promising approach in modern medicine. The primary design parameter in the implants is the release rate across the implant surface. The release rate depends on the implant formation and the physicochemical properties of the loaded drug, which can be adjusted during the design phase by selecting appropriate materials, e.g., polymer and drugs [186]. Moreover, the external tissue surrounding the implant may affect the drug release due to the interactions with the tissue and the tissue mechanical properties which may explain the differences between in-vivo and in-vitro drug release [187]. In general, the release profiles from the implants can be measured by monitoring the local drug concentrations in the vicinity of the implant over time [188]. Then, the drug release rate parameters can be obtained by fitting the experimental data to a relevant mathematical kinetic model, e.g., zero-order, first-order, Weibull, Higuchi, etc [189].

In this work, to provide our model with the capability for modelling different types of implants, we assume that the implant releases drug over two phases, namely, burst and sustained releases. Thus, we can model both dual-release and sustained release implants by adjusting the release parameters. For example, in-situ forming implants (ISFI) release drug over burst and sustained phases [39]. During the burst release phase, drug will be released with a fast release rate over short time followed by slow release over an extended period of time during the sustained release phase. In addition, burst and sustained releases can be achieved by design a double-layer implant by varying the layer compositions [106]. Thus, the cumulative amount of released drug at time t can be mathematically modelled using a first-order bi-exponential kinetic model as given by Eq. (6.38). This model shows high fitting agreement with the experimental release data as will be demonstrated in section 6.8.

$$W(t) = W_{\infty}\left(1 - f_1 \cdot e^{-k_f t} - f_2 \cdot e^{-k_s t}\right) \tag{6.38}$$

where $W(t)$ is the percentage of cumulative drug released at time t and W_∞ is the total percentage of drug released at a steady state. The parameters f_1 and f_2 are the drug fractions released during burst and sustained phases, respectively. The constants k_f and k_s are the release rate constants of burst and sustained release process, respectively. We still have flexibility to model the sustained release implant by removing the burst release phase, i.e., f_1=0. The cumulative amount of the released drug at time t can be expressed as

$$M(t) = M_0 W(t) \tag{6.39}$$

where M_0 is the total amount of loaded drug in the implant in (mg).

Drug is assumed to be uniformly distributed in the implant, which leads to spatially uniform release profile from the implant surface [90]. Thus, the drug release rate from the implant at time t can be expressed as

$$M_r(t) = \frac{dM}{dt} = M_0 W_\infty \left(k_f f_1 e^{-k_f t} + k_s f_2 e^{-k_s t} \right) \tag{6.40}$$

The drug release rate can be approximated as [98],

$$M_r(t) \approx \frac{M(t, t+\Delta t)}{\Delta t} = \frac{M(t+\Delta t) - M(t)}{\Delta t} \tag{6.41}$$

It is reasonable to assume that the size of the implant remains constant over the release duration since the implant releases drug prior to any significant degradation [105]. Thus, in this model, the size variation of the implant due to biodegradation is assumed to be negligible during the observation time [39, 105].

6.6 Spatiotemporal Drug Concentration Profile

Using linear system analysis technique [103], drug concentration profile at any location inside the tumor can be obtained by applying the convolution between the channel impulse response (6.34) and the release rate expression (6.40).

$$P(r,t) = C(r,t) * M_r(t) = \int_0^t C(r, t-\tau) * M_r(\tau)\, d\tau \tag{6.42}$$

Knowledge of two functions allows the other unknown function to be determined by performing either convolution or deconvolution. Although we derived the drug concentration

profile based on a first-order bi-exponential kinetic model, we still can model other implants with different drug release patterns in similar way using the derived CIR. These advantages are due to using a flexible system analysis approach based on the derived impulse response function.

After substituting Eqs. (6.34) and (6.40) in (6.42), we get the drug concentration profile as a function of time and radial distance for $t>t_0$.

$$P(r,t)=\frac{M_0W_\infty}{2\pi r_0r_tr}\sum_{n=1}^{\infty}\frac{\sin(\kappa_n r_0/r_t)\sin(\kappa_n r/r_t)}{\kappa_n^2+\lambda r_t(\lambda r_t-1)}(\kappa_n^2+\lambda^2r_t^2)$$
$$\times\int_{-\infty}^{\infty}e^{-(D\kappa_n^2/r_t^2+\gamma)(\tau-t_0)}H(\tau-t_0)\left(k_ff_1e^{-k_f(t-\tau)}+k_sf_2e^{-k_s(t-\tau)}\right)H(t-\tau-t_0)\,d\tau \qquad (6.43)$$

where $H(t)$ is the unit (or Heaviside) step function.

Using the definition of Heaviside step function, Eq. (6.43) can be written as

$$P(r,t)=\frac{M_0W_\infty}{2\pi r_0r_tr}\sum_{n=1}^{\infty}\frac{\sin(\kappa_n r_0/r_t)\sin(\kappa_n r/r_t)}{\kappa_n^2+\lambda r_t(\lambda r_t-1)}(\kappa_n^2+\lambda^2r_t^2)e^{(D\kappa_n^2/r_t^2+\gamma)t_0}$$
$$\times\left[k_ff_1e^{-k_ft}\int_{t_0}^{t-t_0}e^{(k_f-D\kappa_n^2/r_t^2-\gamma)\tau}d\tau+k_sf_2e^{-k_st}\int_{t_0}^{t-t_0}e^{(k_s-D\kappa_n^2/r_t^2-\gamma)\tau}d\tau\right] \qquad (6.44)$$

Solving the integrals in (6.44), we get

$$P(r,t)=\frac{M_0W_\infty}{2\pi r_0r_tr}\sum_{n=1}^{\infty}\frac{\sin(\kappa_n r_0/r_t)\sin(\kappa_n r/r_t)}{\kappa_n^2+\lambda r_t(\lambda r_t-1)}(\kappa_n^2+\lambda^2r_t^2)e^{(D\kappa_n^2/r_t^2+\gamma)t_0}$$
$$\times\left[k_ff_1e^{-k_ft}\frac{e^{(k_f-D\kappa_n^2/r_t^2-\gamma)\tau}}{k_f-D\kappa_n^2/r_t^2-\gamma}\Bigg|_{t_0}^{t-t_0}+k_sf_2e^{-k_st}\frac{e^{(k_s-D\kappa_n^2/r_t^2-\gamma)\tau}}{k_s-D\kappa_n^2/r_t^2-\gamma}\Bigg|_{t_0}^{t-t_0}\right] \qquad (6.45)$$

Now, assuming that the initial release time is $t_0=0$, Eq. (6.45) can be expressed as

$$P(r,t)=\frac{M_0W_\infty}{2\pi r_0r_tr}\sum_{n=1}^{\infty}\frac{\alpha_n\sin(\kappa_n r_0/r_t)\sin(\kappa_n r/r_t)}{\alpha_n-\lambda r_t}\left(E_{fn}e^{-k_ft}+E_{sn}e^{-k_st}\right) \qquad (6.46)$$

where,

$$E_{fn} = \frac{k_f f_1}{\beta_{fn}}\left(e^{\beta_{fn} t} - 1\right) \tag{6.47}$$

$$E_{sn} = \frac{k_s f_2}{\beta_{sn}}\left(e^{\beta_{sn} t} - 1\right) \tag{6.48}$$

$$\alpha_n = \kappa_n^2 + \left(\lambda r_t\right)^2 \tag{6.49}$$

$$\beta_{fn} = k_f - D\kappa_n^2 / r_t^2 - \gamma \tag{6.50}$$

$$\beta_{sn} = k_s - D\kappa_n^2 / r_t^2 - \gamma \tag{6.51}$$

6.7 Stochastic Particle-based Simulation for the implantable DDS in Tumor Microenvironment

Stochastic simulations play an important role in understanding and modelling of drug transport and interaction mechanisms. We implement a stochastic particle-based simulator in MATLAB for simulation of drug release from polymer implant and drug transport through the surrounding tissue in a 3-D bounded spherical tumor microenvironment. The total simulation time is divided into small time steps and each time step has duration Δt.

The release process following insertion of the implant inside the tumor is performed according to experimentally fitted bi-exponential model. Amount of the released drug during each time-step, i.e., $[t, t+\Delta t]$, can be expressed as

$$M\left(t, t+\Delta t\right) = M\left(t+\Delta t\right) - M\left(t\right) \tag{6.52}$$

The drug molecules are uniformly distributed and released on the implant surface in each time step, as shown in Figure 6.3.

Substituting Eqs. (6.38) and (6.39) in (6.52), we get

$$M\left(t, t+\Delta t\right) = M_0 W_\infty \left(1 - f_1 e^{-k_f\left(t+\Delta t\right)} - f_2 e^{-k_s\left(t+\Delta t\right)}\right) - M_0 W_\infty \left(1 - f_1 e^{-k_f t} - f_2 e^{-k_s t}\right)$$

$$= M_0 W_\infty \left[f_1 \left(e^{-k_f t} - e^{-k_f\left(t+\Delta t\right)}\right) + f_2 \left(e^{-k_s t} - e^{-k_s\left(t+\Delta t\right)}\right)\right] \tag{6.53}$$

However, to obtain the CIR using stochastic simulation, the total molecules should be released at the first-time step, i.e., instantaneously.

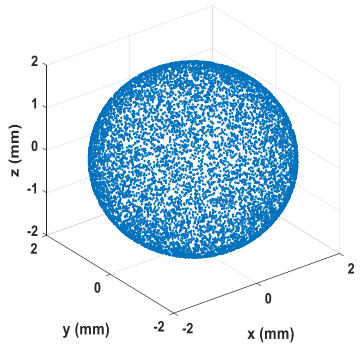

Figure 6.3: Uniformly distributed molecules on the implant surface captured from the stochastic particle-based simulator.

Molecules diffuse into the surrounding tumor tissue according to Brownian motion which can be characterized using the apparent (or effective) diffusivity. The apparent diffusion coefficient (ADC) depends on the physiochemical properties of both the molecules and the ECS, including effect of the binding and uptake by the ECS components [165]. This allows us to use the ADC together with time-step to calculate the spatial displacements of molecules that follow random Brownian motion. The new position of each molecule is tracked and stored using the following equation [74]:

$$(x_i, y_i, z_i) = (x_{i-1}, y_{i-1}, z_{i-1}) + (\Delta x_i, \Delta y_i, \Delta z_i) \tag{6.54}$$

where, the index i refers to the current time-step, (x_i, y_i, z_i) is coordinates of the current location of drug molecules at i^{th} time-step, $(x_{i-1}, y_{i-1}, z_{i-1})$ is coordinates of the previous location of drug molecules at $(i\text{-}1)^{\text{th}}$ time-step, and $(\Delta x_i, \Delta y_i, \Delta z_i)$ is the random displacements which follow the normal distribution $N(0, \sigma^2)$ with zero mean and variance equal to $\sigma^2 = 2D\Delta t$.

Drug elimination in the simulation environment due to the various processes, namely, clearance through the capillaries, degradation, and cellular uptake/binding are modelled using a first-order degradation reaction mechanism. At each time step, a uniformly distributed random number (R_1) between zero and one is generated for each molecule. Then, the generated random numbers are compared with the elimination probability in Eq. (6.55) [64]. If the elimination probability is larger than the random number (R_1), the molecule will be removed from the simulation environment.

$$P_{\gamma} = 1 - \exp(-\gamma \Delta t) \tag{6.55}$$

where γ is the apparent lumped first-order elimination rate constant.

The outer surface of the simulation environment is modelled as a general partially reflecting boundary, which is equivalent to Robin boundary condition used in the analytical model given in section 6.3. Some of the molecules will be reflected back when they reach the boundary and others will be removed from the environment. A random number (R_2), uniformly distributed between zero and one, is assigned to each molecule that hits the medium boundary. Then, if the probability, given by (6.56) [30], is larger than the random number (R_2), the drug molecule will be removed from the simulation environment. Otherwise, the drug molecule will reflect back to the previous location inside the environment.

$$P_{\omega} = \omega \sqrt{\frac{\pi \Delta t}{D}} \tag{6.56}$$

The impermeable (no-flux) boundary condition can be used when no loss or absorption of molecules takes place at the boundary, i.e., $\omega = 0$. On the other hand, when each collision between the molecule and the boundary leads to absorption or transmission, a fully permeable boundary condition can be applied, i.e., $\omega = \infty$. The drug concentration profile at any location inside the simulation environment can be estimated using a virtual spherical observer that does not hinder movements of the molecules. At each time step, the drug molecules that enter the observer volume will contribute to the total received molecules. Then, the drug concentration profile can be obtained as follows

$$P_{sim}(r,t) = \frac{N}{N_0 V_{rx}} \tag{6.57}$$

where N is the number of received molecules, N_0 is the total number of released molecules from the source (the implant), and V_{rx} is the receiver volume.

6.8 Analytical and Stochastics Simulation Results

In this section, we compare and verify the accuracy of the CIR and the spatiotemporal drug concentration profile, derived analytically in the previous sections, with the results obtained from stochastic simulation results. We examine effect of the various system parameters on

transport of anticancer drug DOX in terms of the drug concentration profile and the maximum concentration after implantation of a dual-release implant in the tumor. To verify accuracy and validity of our models, the concentration profile as a function of distance from the implant is compared with the published experimental data on DOX biodistribution in tumor in [117]. The system and environment parameters are listed in Table 6.1. The DOX diffusivity in tumor is chosen within the range of the experimentally measured data [116, 190]. We conduct a trial and error run with different values of the simulation parameters (i.e., time-step, number of transmitted molecules, and number of iterations) to examine the concentration profile variations. For example, we find that a time-step with value less than 0.1h does not show significant change and variation in the simulation results. Moreover, the tumors may have different sizes, e.g., the tumor diameter in rat and rabbit ranges from 0.5-2 cm [116]; therefore the tumor radius in this work is chosen to be 1 cm. The radius of the virtual observer (r_{rx}) is chosen to be 0.5 mm so that enough molecules can contribute to estimate the concentration within the receiver volume. The elimination rate constant may have a range of values, and thus different values are chosen to examine its effect on the drug distribution profile.

Table 6.1: System and environment parameters (unless stated otherwise).

Parameter	**Unit**	**Value**
T	h	150
Δt	h	0.1
N_0	molecule	10^5
D	m^2/s	4×10^{-11}
ω	μm/s	10
γ	s^{-1}	5×10^{-6}
r_t	mm	10
r_{rx}	mm	0.1
$(x, y, z)_{rx}$	mm	(0, 0, 5)
Iterations	-	100

A group of researchers measured the DOX concentration with the distance from polymer implant (millirod) placed in a liver tumor in [117, 175, 177]. To verify the accuracy and validity of our proposed models, we compare the results predicted by both of our proposed models with the published experimental data extracted from [117]. The system parameters that are extracted from the experimental data in the literature [117, 175, 177], are used to

compute our results. Drug transport from this implant to surrounding tissue is symmetric around the implant axis due to the geometry of the implant. The diameter of the implant and tumor are equal to 1.6 mm and 1.1 cm, respectively. We estimate the implant release rate constant (0.5341 day^{-1}) by curve fitting the experimental release data. The amount of loaded DOX in the implant is 2.99 mg, and 93.7% of the loaded drug is released on the fourth day, i.e., 2.8 mg. The apparent diffusivity and apparent elimination rate constant of DOX in liver tumor tissue are given as $D = 50\ \mu m^2/s$ and $\gamma = 0.58\times10^{-4}\ s^{-1}$, respectively [116].

Figure 6.4 shows a comparison of DOX concentration obtained using our proposed models with the published experimental data as a function of the radial distance from the implant surface on the fourth day after implantation in the tumor. The density of tumor and liver tissues is equal to ~1.04 g/cm^3; therefore volume can be replaced with mass for obtaining the concentration in unit of (µg/g) [191]. It can be seen that the results obtained using our analytical and stochastic models agree well with the results extracted from the published experimental data in [117]. As expected, the measured concentration shows a decreasing trend with the radial distance from the implant. In general, our proposed models can predict the DOX concentration in the tumor at different radial distances from the implant accurately. Moreover, the experimental data extracted from the literature and plotted in this figure represent the mean values, and the predicted results by our models fall within the standard deviation of the mean.

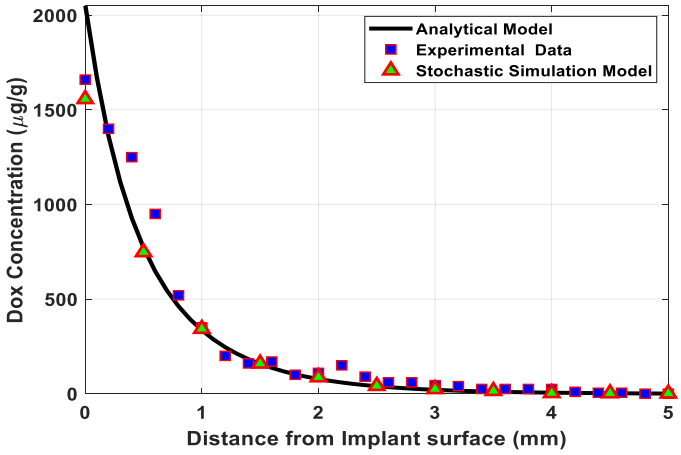

Figure 6.4: Drug concentration on the fourth day versus the distance from the implant/tissue boundary compared to the mean value of the published experimental data in [117].

We use the bi-exponential kinetic model, given by Eq. (6.38), to fit the experimental release data of PLGA implant given in [39]. Using nonlinear least-squares fitting method, we obtain the release rate constants as listed in Table 6.2. As shown in Figure 6.5, the fitted curve indicates high agreement with the experimental data.

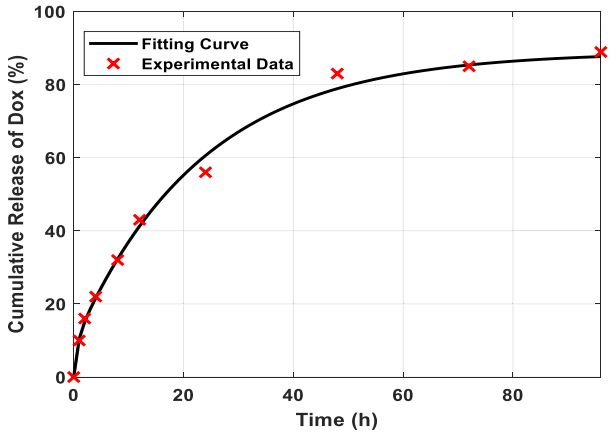

Figure 6.5: Percentage cumulative release of DOX from the implant, fitted to the experimental data in [39], $R^2 = 0.9956$.

Table 6.2: Drug implant parameters.

Parameter	Value	Unit	Description
M_0	5	mg	Total loaded DOX in the implant. The implant can also be loaded with different amount of drug.
f_1	0.1	-	DOX fraction released during the burst phase [39].
f_2	0.9	-	DOX fraction released during the sustained phase where f_2=1-f_1 [39].
r_0	1	mm	The implant radius. The implant can have different radii.
W_∞	88.9	%	Total percentage of DOX released at steady state [39].
k_f	4.3×10^{-4}	s^{-1}	Burst release rate constant. It is obtained by fitting Eq. (6.38) to the experimental data in [39].
k_s	1.2×10^{-5}	s^{-1}	The sustained-release rate constant. It is obtained by fitting Eq. (6.38) to the experimental data in [39].

In Figure 6.6, we plot the CIR and the drug concentration profile for different values of the apparent elimination (loss) rate constant. This figure shows a similar trend with time for both the CIR and the drug concentration profile. The analytical results obtained using the expressions (6.34) and (6.46), match well with the stochastic particle-based simulation results. Thus, the derived CIR is an accurate impulse response function for obtaining the drug concentration profile in tumor via convolution with the release expression of the implant. Drug concentration increases with time to reach the peak value and then it decreases gradually until reaching a very small value, i.e., zero. As expected, an increase in the drug elimination rate due to different factors, e.g., clearance through the capillaries, binding and cellular uptake, enzymatic and non-enzymatic reaction, etc., will result in a decrease in the drug concentration in the tumor. Thus, the drug metabolisms and drug clearance through the capillaries reduce the amount of the drug in the tissue.

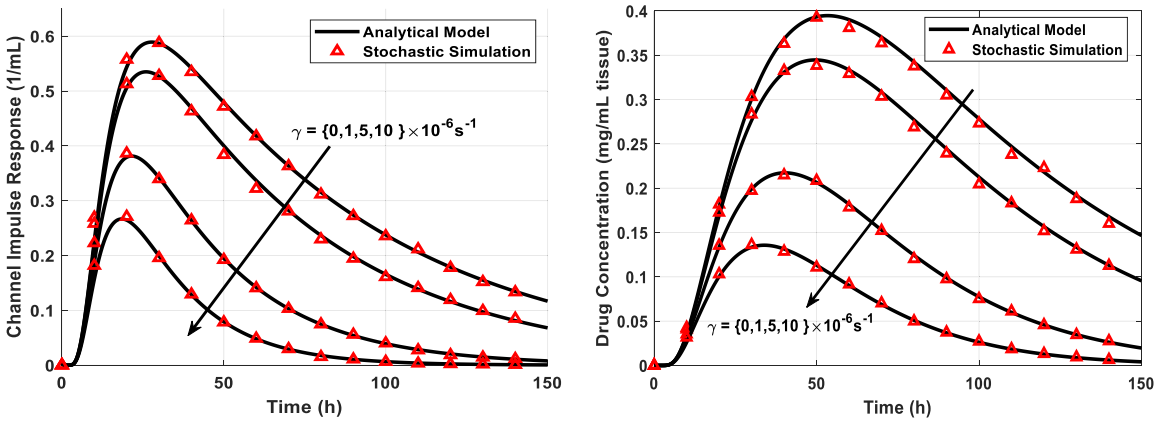

(a) (b)

Figure 6.6: (a) The channel impulse response and (b) drug concentration profile for various values of the drug elimination rate constant in the tumor microenvironment.

The maximum (or peak) drug concentration and the corresponding peak time at a specified location in the tissue, e.g., at the target site, represent important pharmacokinetic metrics. In this section, these metrics are obtained from the drug concentration profile using analytical and simulation models. Figure 6.7 shows the maximum drug concentration as a function of the separation distance from the implant/tissue interface. The results in this figure are obtained using analytical and stochastic simulation models for various drug elimination rates as shown in Figure 6.7 (a) and for different diffusion coefficients as shown in Figure 6.7 (b).

This figure gives important indication about the drug penetration depth inside the tumor tissue. Drug concentration decreases as the distance from the implant increases and finally reaches zero value at the tumor boundary. Moreover, the higher elimination rate results in lower maximum drug concentration as shown in Figure 6.7 (a). Also, the effective drug diffusivity has impact on transport and distribution of drug in tumor as shown in Figure 6.7 (b) where the higher diffusivity leads to lower peak concentration. However, the maximum concentration converges as the distance increases whatever the value of drug elimination rate constant and drug diffusivity.

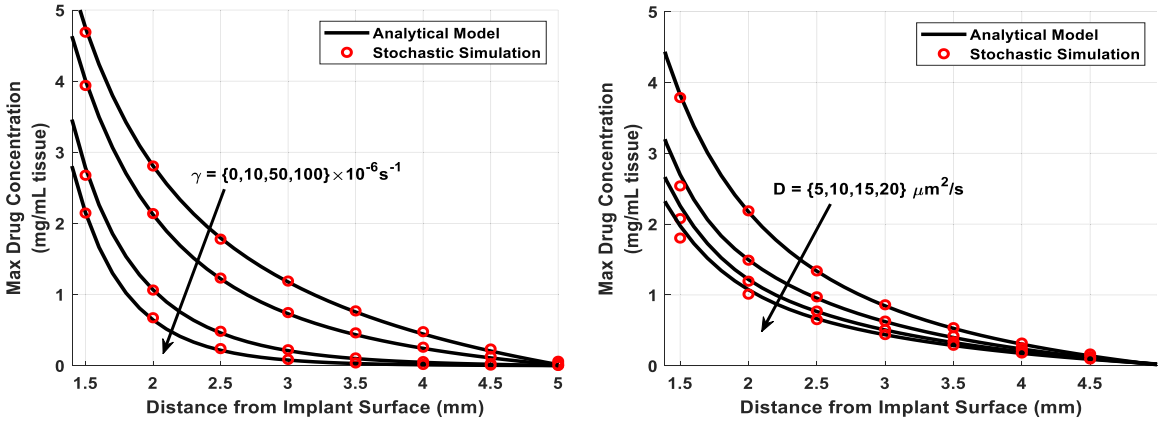

(a) (b)

Figure 6.7: Maximum drug concentration versus distance from the implant/tissue interface when ω = 1μm/s and r_t = 5mm for (a) the various elimination rate constants and (b) the different diffusion coefficients.

Impacts of the sustained release rate on both the maximum drug concentration and the corresponding peak time instant are plotted in Figure 6.8 versus the separation distance from the implant/tissue interface. As shown in Figure 6.8 (a), the maximum drug concertation increases as the sustained release rate constant increases because more drug will be released from the implant in a shorter time period. Impact of the sustained release rate on the maximum drug concentration will decrease as the distance from the implant increases, and finally the maximum concentration converges for all the release rates where the distance becomes the main dominant factor. On the other hand, the peak time at which the concentration has the maximum value becomes shorter as the sustained release rate increases because higher amount of drug will be released within shorter time.

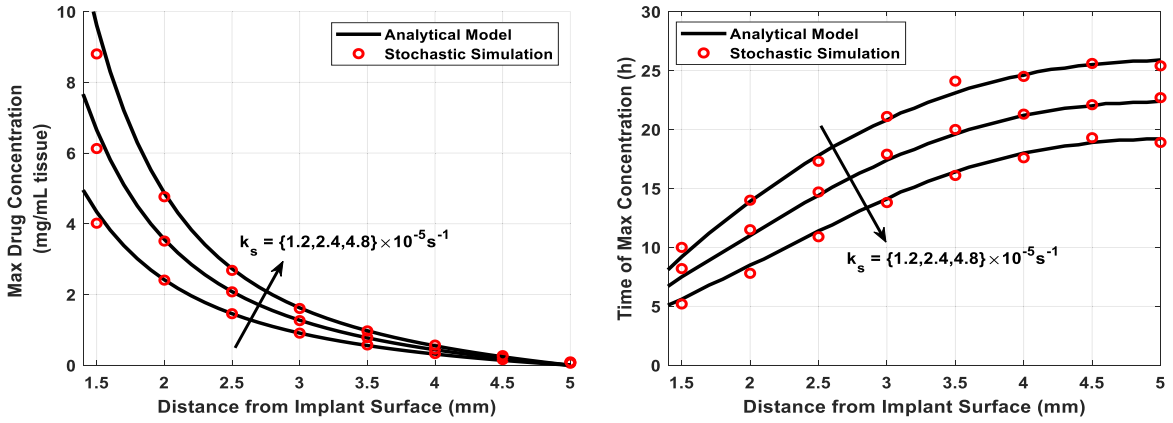

(a) (b)

Figure 6.8: (a) Maximum drug concentration and (b) peak time of maximum drug concentration versus the distance from the implant/tissue interface for various sustained release rate constants.

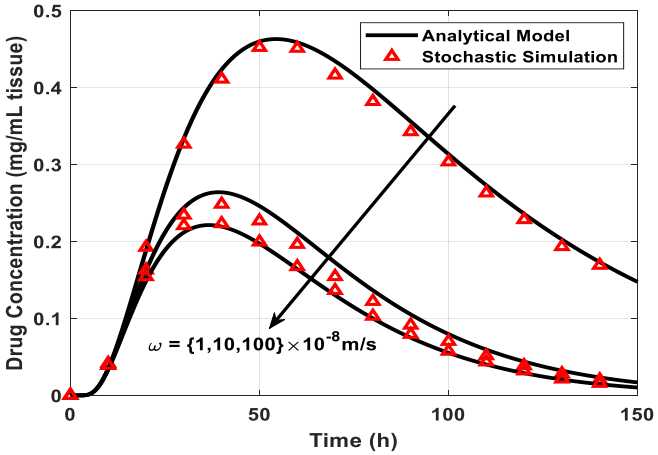

Figure 6.9: Drug concentration profile as a function of time for different loss rate constants at the tumor boundary.

Figure 6.9 shows the impact of the reaction (loss) rate at the tumor boundary on the drug concentration profile inside the tumor. This loss could be due drug elimination into the surrounding normal tissue including the exchange blood and lymphatic vessels at the outer boundary of the tumor. Drug concentration decreases as the loss rate constant increases. This happens because the probability of drug elimination through the boundary will increase as the loss rate increases. Adding the loss rate ω to our models via Robin boundary condition (or the partially reflecting boundary in the stochastic simulator) will enable us to select appropriate boundary condition at the tumor boundary by adjusting the value of ω, e.g., no-flux (ω=0).

6.9 Summary

In this chapter, we propose analytical and stochastic simulation models to predict the spatiotemporal distribution of the anticancer drug in tumor following insertion of a dual-release implant. A closed-form analytical expression for the drug concentration profile in tumor is derived using system analysis approach via convolution with the derived CIR. We examine the proposed models in tumor tissues using a dual-release implant loaded with anticancer drug doxorubicin (DOX). Moreover, the model is compared with the published experimental data for DOX distribution in tumors using sustained-release polymer implant. Accuracy and validity of the proposed models can be seen from the perfect match between analytical and stochastic simulation results as well as with the published experimental data. We study impact of the various parameters, i.e., the elimination rate, the diffusivity, the loss rate at the tumor boundary, and the implant release rate, on the spatiotemporal drug concentration profile. In addition, peak drug concentration and peak time are obtained with respect to the radial distance from the implant/tissue interface.

The proposed models can help in design the implantable drug delivery systems (IDDSs) for tumor treatment using different drugs and release patterns. Moreover, these models can help us to understand the distribution and elimination of drug in tumor tissue and other tissues in flexible way by adjusting the system parameters. Using these models, we can choose the optimum design parameters for the implants such as the release rate and size as well as the optimum insertion location in tumor to improve therapeutic efficacy. Furthermore, the proposed models can be used to obtain the release profile via deconvolution by knowing the drug concentration profile. Therefore, number of the experimental trials can be reduced, and as a result this will save time and reduce cost. The derived CIR can also be applied in the same way to analyze and predict the drug concentration in the tissues using other local administration forms such as intratumoral bolus or infusion injection, which can serve as an aid to design optimal dosing protocols.

CHAPTER 7

Modelling of Combination Therapy: Implantable Anticancer Drug Delivery with Thermal Ablation in Solid Tumors

7.1 Introduction and Motivation

Cancer is one of the most dangerous and deadliest diseases that cause deaths of millions of people around the world each year. More than 85% of human cancers appear as solid tumors [144]. Delivery of anticancer drugs to tumor via systemic administration (through bloodstream) suffers from high drug elimination and enzymatic degradation. Majority of anticancer drugs will accumulate in other parts of the body, e.g., liver, lung, kidneys, and spleen [3]. Thus, systemic drug delivery results in high toxicity and many side effects. A small amount of administrated drug will reach the site of action (tumor) by enhanced permeability and retention (EPR) effect. However, some tumors have low EPR, practically for drug nanocarriers or macromolecules such as liposomes, and adjunct strategies are needed to increase the enhanced permeability and retention (EPR) effect. As an example, ultrasound is used for reducing tumor pressure and increasing vascular permeability to increase accumulation of liposomes in tumors [192].

Furthermore, the drug fraction that succeeds in reaching the tumor after passing the endothelium barrier will also encounter many challenges due to various physiological conditions inside the tumor microenvironments. The core of solid tumor shows an absence of vasculatures because the solid stress caused by fast proliferating of tumor cells will compress the lymphatic and blood vessels [144]. Therefore, solid tumors have higher interstitial fluid pressure (IFP) than healthy tissues due to lack of lymphatic vessels. The

values of IFP vary depending on many factors such as tumor size, shape, and type. The IFP will reduce inward convective transport from the tumor periphery toward the inner core, which may add another challenge for using systemic drug delivery in solid tumors [193].

Minimally invasive thermal ablation techniques using radio frequency (RF), ultrasound, microwave, laser, etc., have been used for the treatment of tumors [109, 111]. In particular, they are used as an alternative for systemic administration and surgical interventions for unresectable tumors or when other therapies have high-level risks [110]. Thermal ablation has many advantages over the surgical resection such as less invasive, less risk and damage to surrounding healthy tissue, reduced morbidity, shorter stay in the hospital without the need for general anaesthetic, cost-effective, and repeatability [41]. Radiofrequency ablation (RFA) is one of the most powerful ablation techniques for the treatment of small solid tumors (< 3cm) due to its simplicity, high response rates, and relatively low side effects [110]. It can be applied for tumors in many locations inside the body including liver, lung, breasts, bones, and kidneys [40, 110]. The RFA is minimally invasive, image-guided, thermal ablation technique for local treatment of malignant solid tumors. In this technique, a current-carrying needle electrode will be inserted inside the tumor under image guidance techniques, as shown in Figure 7.1.

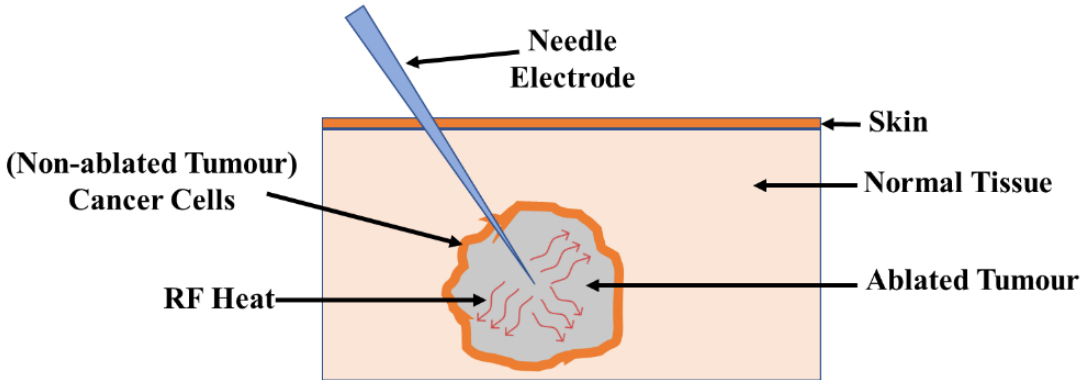

Figure 7.1: Schematic illustration of the radiofrequency ablation (RFA) for tumor treatment.

Image guidance techniques such as magnetic resonance imaging (MRI), computed tomography (CT), or ultrasound imaging, can be used to achieve accurate placement of the electrode needle inside the tumor [176]. Once inserted, the tumor tissue will be locally heated using a high frequency alternating electric current, which will be supplied by an external

power generator with frequency and power equal to ~500 kHz and ~50 watts, respectively. Thus, the temperature in the tumor tissue will rise above 50ºC (e.g., 60ºC to 100ºC) which is enough to destroy the tissues by inducing coagulation necrosis [110]. However, the main limitation and challenge of thermal ablation is the risk of local recurrence and residual tumor after the ablation, particularly, at the tumor periphery due to incomplete destruction of the tumor [194-196]. A recurrence rate of 49% to 74% was found following the treatment using RFA [112]. Furthermore, it had been shown that the recurrent tumor after RFA has more growth rate and vascular invasion than the tumor without RFA [113].

Anticancer drug delivery from miniaturized implants offers an efficient alternative approach to both intratumoral injection and systemic delivery [15]. Local implantable drug delivery systems (IDDSs) are attractive strategies that provide lower toxicity and higher drug bioavailability compared to systemic chemotherapy which may result in better therapeutic efficiency [2]. In this approach, the drug does not need to bypass the physiological barriers which it encounters using systemic administration, particularly, the endothelial barrier. The efficiency and release profiles of the implants depends on the amount and type of the loaded drug, the implant size, and the materials as well as on the surrounding environment. Many IDDSs are clinically approved for local delivery of chemotherapy such as Gliadel® polymer implants for the treatment of malignant gliomas [88]. The IDDSs provide efficient and powerful treatment technique to kill the residual tumor cells after thermal ablation. Many experimental studies showed high therapeutic efficiency of the combination therapy using local IDDSs to kill residual cancer cells and prevent tumor recurrence at the periphery of thermally ablated tumors [39, 42, 175]. Recently, doxorubicin-loaded PLGA polymer implant is used to destroy the residual tumor after applying thermal ablation that caused significant tumor volume shrinkage [39]. In [175], polymer implant is designed to deliver doxorubicin (DOX) anticancer drug to residual cancer cells at the boundary of solid tumor after RFA. In [42], local delivery of 5-fluorouracil (5-FU) from polymer implants were used as an adjunct to RFA to control growth of tumor in rabbits which provided a significant reduction in tumor size compared with RFA alone. In addition, clinical success of local intratumoral IDDSs for treatment of the solid tumors, requires more improvements in addressing the physiological barriers. Thus, thermally ablated tumor can enhance efficiency

of the IDDSs by increasing the penetration of anticancer drug in the interstitial space of solid tumor and reducing the drug elimination via tumor vasculatures [114, 176]. Therefore, using anticancer drug loaded implants following thermal ablation for treatment of the solid tumors is significantly more effective than using single therapy alone, i.e., thermal ablation alone or implant alone.

Anticancer drug distribution and fluid flow within solid tumors are essential factors that affect the clinical efficiency of anticancer drug therapies. In addition to that, pharmacokinetic processes, including, drug efflux/influx into cells, drug binding/unbinding with interstitial proteins, perfusion into blood capillaries, and degradation, have a significant impact on the therapeutic outcomes. Moreover, one of the most important challenges in the development of new DDS is ensuring that the optimal amount of drug is achieved in tumor versus normal tissues to avoid toxicity in the healthy tissues. For example, dual-release implants such as in-situ forming implants (ISFIs), lead to a large undesirable burst release which may cause major toxicity problems and consume the loaded drug in the implants rapidly [107]. Designing this type of the implants with minimum initial burst release become an attractive challenge and one of the key issues in the design of ISFIs and many studies tried to solve this issue, e.g., [108]. Therefore, providing mathematical models to examine and analysis impact of the anticancer drug on the surrounding tissue of the implants, i.e., pharmacodynamic model, is necessary for design the IDDSs. Mathematical pharmacokinetic and pharmacodynamic (PK/PD) models have played a vital role in the advancement of drug delivery systems. Mathematical models provide a powerful tool for understanding both drug transport and other complex pharmacokinetic processes and their impact on the tumor cells and the surrounding tissues (pharmacodynamics). As a result, they can help in optimize and design of the drug delivery systems. These models allow researchers to extrapolate in-vivo results from animal models to humans by linking the laboratory experiments with clinical applications [12, 45]. Therefore, they reduce the number of animals and experimental trails in the laboratory which save cost and time. Most of the mathematical works on anticancer drug transport and PK/PD modelling are limited to systemic drug delivery while few simplified models on the IDDSs are reported [106, 116, 117].

In this chapter, we develop comprehensive mathematical PK/PD models for combination therapy using local IDDS inside the solid tumor with/without thermal RFA with the help of molecular communication abstraction. In this model, millimeter-scale dual-release implant, loaded with anticancer DOX drug, is assumed to be inserted inside a solid tumor to release DOX anticancer agents. Here, we consider two solid tumor models, namely, thermally ablated and non-ablated tumors, that are surrounded by normal tissues. Here, we do not model the thermal ablation mechanism, but we assumed that the drug implant is placed inside thermally ablated tumor. The interstitial fluid pressure (IFP) and interstitial velocity field (IVF) in the solid tumor and normal tissue are obtained using Darcy's law. The binding and unbinding processes of DOX with albumin-proteins in the interstitial extracellular space are modelled via a separate diffusion-convection-reaction equation. Moreover, cellular influx (uptake) and efflux of DOX molecules across the cellular membranes are characterized using a specified model. Also, we model elimination of DOX into the blood and lymphatic vessels depending on the vascular characteristics and the IFP. Impacts of all the above-mentioned pharmacokinetic processes are included in the drug transport model for predicting the extracellular and intracellular concentrations of both free and bound DOX.

Furthermore, this model enables estimation of the anticancer drug toxicity on tumor cells and surrounding healthy tissue. Impact of DOX on the cancer cells is evaluated using a pharmacodynamic model that depends on the spatiotemporal intracellular concentration of DOX as well as on the characteristics of both the DOX and tumor cells. Moreover, concentration of DOX in normal tissue is evaluated, which can be used for toxicity assessment. Accuracy and validity of our proposed model are verified and compared with the published experimental data in [117] as well as with the analytical and stochastic simulation models assuming impact of the various pharmacokinetic parameters are combined in the apparent diffusivity and apparent elimination constant. To the best of our knowledge, there is no work available in the literature that provides a comprehensive PK/PD model that simultaneously captures and addresses the anticancer drug transport, pharmacokinetics, and pharmacodynamics using intratumoral dual-release drug implants in malignant solid tumors with or without RFA. Thus, the work reported in this chapter aims to fill the gap of knowledge.

This chapter is organized as follow. Section 7.2 presents the molecular communication paradigm for modelling and abstraction of the IDDS inside the solid tumor with/without RFA. Mathematical formulations of the fluid flow and drug transport including various pharmacokinetic processes in tumor are given in section 7.3. In section 7.4, we present a pharmacodynamic model for impact of the anticancer drug on the tumor cell density. The drug release kinetics of the dual-release implant is proposed in section 7.5. The model parameters, geometry, and boundary conditions are discussed in detail in sections 7.6, 7.7, and 7.8, respectively. In section 7.9, we demonstrate the computational numerical method used for solving the mathematical model. The results are discussed in section 7.10. Finally, the chapter summary is given in section 7.11.

7.2 Model Abstraction using Molecular Communication Paradigm

One of the most important applications of molecular communication (MC) paradigm is modelling and abstraction of the drug delivery systems, particularly, for providing the drug at the site of action and minimizing the drug in the healthy tissues [5, 14]. In this work, we use MC paradigm for modelling a miniaturized IDDS placed inside a cancerous solid tumor following thermal ablation. It is important to make clear that we do not model the thermal ablation here. We assumed that the implant is inserted inside thermally ablated tumor by incorporating the characteristics of the ablated tumor tissue in our model.

In this paradigm, the implantable drug delivery device (implant) acts as a transmitter while the target site, i.e., malignant cell, act as a receiver. From the perspective of MC, the anticancer therapeutic agent, i.e., DOX, can be abstracted as information molecules. At the target sites, the intracellular concentration of DOX should reach a minimum threshold to kill the cancer cells. In MC paradigm, this can be considered as a reception mechanism where the intracellular concentration is the received signal while the death of cancer cells is the output response. The tumor microenvironment is a 3-D medium that consists of tumor surrounded by normal tissue, as shown in Figure 7.2. Here, this environment represents the molecular communication channel. However, the MC channel can be modified via thermal ablation which leads to changes in its structure and characteristics. Thus, thermal ablation will destroy the cellular and vasculature structures which results in a new ablated tissue with

different characteristics compared to the original tissue. However, residual cancer cells may remain after thermal ablation along the outer tumor rim which represents the risk region (or the non-ablated region) in this work. Therefore, from MC perspective, the thermally ablated tumor can be considered as a new modified MC channel. In this case, the tumor microenvironment forms three regions, namely, ablated tumor, non-ablated tumor, and normal region.

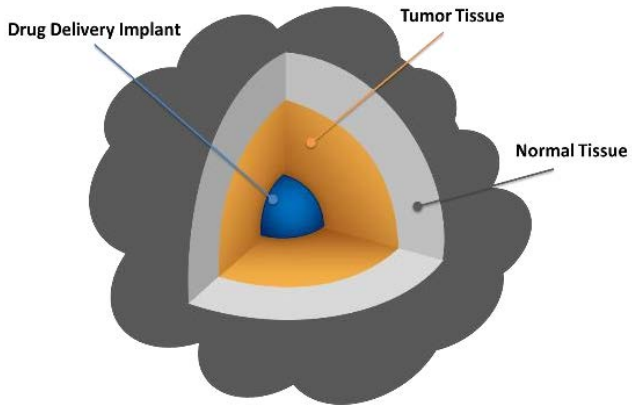

Figure 7.2: Graphical illustration of drug implant inserted in 3-D solid tumor.

7.3 Channel Modelling: Drug Transport and Fluid Flow in Tumor

Solid tumors are heterogeneous media due to spatial heterogeneity of the tumor vasculature (blood and lymphatic vessels) and the cells. However, due to lack of the experimental heterogeneity data of solid tumors and to simplify the analysis, we will consider solid tumors as spatially homogeneous media following the trends in the literature [49, 182, 197-199]. Thus, we do not discriminate between the necrotic and viable tumor regions. Moreover, we assume that the growth timescale of the tumor and normal tissues is much longer than the timescale of the transport phenomena and the observation time window. Thus, it would be reasonable to assume that the system physiological parameters to be time-independent [49]. Incomplete or insufficient RFA will result in an ablated zone, with no viable cancer cells, surrounded by a tumor rim (risk region) that shows a high density of the viable malignant cells, as shown in Figure 7.3.

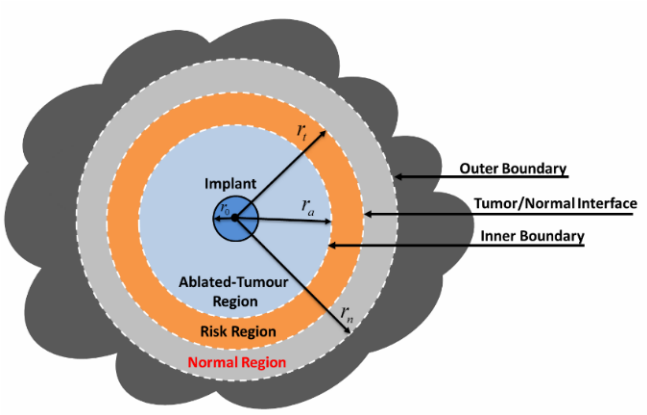

Figure 7.3: Schematic illustration of a cross-section view of a 3-D solid tumor, including the drug implant after RFA.

7.3.1 Interstitial Fluid Flow

As previously mentioned, the tumor and surrounding tissue can be treated as porous media because the length scale of the intercapillary distances (the average distances between the capillaries) is much smaller than the length scale of the tumor radius [49, 182, 200, 201]. Thus, the variations over the microscopic length scales can be averaged out, and the interstitial fluid flow (IFF) is defined by coupling the mass and momentum conservation equations.

Conservation of momentum (momentum balance equation):

In general, the mass flow in a compressible Newtonian fluid is governed by the Navier-Stokes equation [49, 200].

$$\underbrace{\rho_i\left(\frac{\partial \vec{v}_i}{\partial t}+\left(\vec{v}_i\cdot\nabla\right)\vec{v}_i\right)}_{1}=\underbrace{-\nabla P_i}_{2}+\underbrace{\nabla\cdot\left[\mu_i\left(\nabla\vec{v}_i+\left(\nabla\vec{v}_i\right)^T\right)-\frac{2}{3}\mu_i\left(\nabla\cdot\vec{v}_i\right)\mathrm{I}\right]}_{3}+\underbrace{F_{ex}}_{4}+\underbrace{F_{D_i}}_{5} \tag{7.1}$$

where, $\vec{v}_i$ is the interstitial velocity field (IVF) in (m/s), P_i is the interstitial fluid pressure (IFP) in (Pa) or (mmHg), ρ_i is the interstitial fluid density in (kg/m^3), μ_i is the interstitial fluid dynamic viscosity in $(\mathrm{Pa}\cdot\mathrm{s})$, and I is the unit tensor.

The index (i) refers to the interstitial space in ablated-tumor tissue 'a', non-ablated tumor tissue 't', and normal tissue 'n', i.e., $i\in\{\mathrm{a},\mathrm{t},\mathrm{n}\}$. The terms in Eq. (7.1) are defined as follow: the first term is the inertial forces, the second term is the pressure forces, the third term is the

viscous forces (stress tensor), the fourth term is the external forces applied to the fluid (e.g., gravity), and the last term is Darcian resistance to fluid flow. Here, the effect of the external forces is neglected.

The Darcian resistance to fluid flow in porous media is given as

$$F_{Di} = W_i \mu_i \vec{v}_i + \frac{1}{2}\mathbf{C}\rho_i |\vec{v}_i| \vec{v}_i \tag{7.2}$$

where **C** is a matrix of the inertial loss term, W_i is a diagonal matrix with the elements $W_i = 1/\eta_i$, and η_i is the permeability of the interstitial porous medium.

The interstitial fluid is Newtonian with low velocity in the tissues, i.e., $|\vec{v}_i| << 1$ m/s, therefore the inertial loss term can be neglected when compared to the first term on RHS of Eq. (7.2). Thus, the Darcian resistance to fluid flow in Eq. (7.2) is reduced to

$$F_{Di} = W_i \mu_i \vec{v}_i \tag{7.3}$$

The interstitial fluid in tumor and normal tissues is considered incompressible with constant fluid density. Thus, the continuity equation reduces to $\nabla \cdot \vec{v}_i = 0$, i.e., the divergence of the velocity is equal to zero. Therefore, the term $2/3\,\mu_i (\nabla \cdot \vec{v}_i)\mathrm{I}$ in Eq. (7.1) is equal to zero. Since the velocity is very small, the inertial force (the first term in Eq. (7.1)) is very small and it can be neglected at a steady state (i.e., $\partial \vec{v}_i / \partial t = 0$). By neglecting the friction within the fluid and between the fluid and solid phases, i.e., $\nabla \vec{v}_i + (\nabla \vec{v}_i)^T = 0$, the Navier-Stokes equation is simplified to Darcy's law [200].

$$\nabla P_i = -\frac{\mu_i}{\eta_i}\vec{v}_i \tag{7.4}$$

$$\vec{v}_i = -k_i \nabla P_i \tag{7.5}$$

where, $k_i = \eta_i / \mu_i$ is the hydraulic conductivity of the interstitial fluid in $(\mathrm{m}^2/(\mathrm{Pa}\cdot\mathrm{s}))$ which depends on the physiological conditions such as the concentration of collagen and hyaluronan. Generally, the hydraulic conductivity in the anisotropic heterogeneous porous media is a tensor that varies with the location in the interstitial space. The convection velocity depends on the hydraulic conductivity, pressure gradient, and any external body movements

that cause mixing or stirring.

Conservation of mass (mass balance equation):

The mass continuity (balance) equation for a fluid in the porous media with source and sink of mass is given as [49]

$$\frac{\partial \rho_i}{\partial t} + \nabla \cdot \left(\rho_i \vec{v}_i \right) = \left(\phi_{vi} - \phi_{li} \right) \rho_i \tag{7.6}$$

where, ϕ_{vi} is the mass fluid source term which represents the fluid flow rate per unit volume of tissue from the blood vessels into the interstitial space in (1/s) and ϕ_{li} is the lymphatic drainage (sink) term that represents the fluid flow rate per unit volume of tissue from the interstitial space into the lymph vessels in (1/s). The equation (7.6) is applicable to both normal and cancerous biological tissues.

The mass fluid source term ϕ_{vi} is governed by Starling's law [49, 182] as

$$\phi_{vi} = \frac{L_{vi} S_{vi}}{V_i} \left(P_{vi} - P_i - \sigma_i \left(\pi_{vi} - \pi_i \right) \right) \tag{7.7}$$

where, P_{vi} is the intervascular blood pressure (IBP) in (Pa), π_{vi} is the osmotic pressure of the plasma in (Pa), π_i is the osmotic pressure of the interstitial fluid in (Pa), L_{vi} is the hydraulic conductivity of the blood vessel walls in (m/Pa.s), σ_i is the average osmotic reflection coefficient for plasma proteins, and S_{vi}/V_i is the surface area of the blood vessels per unit volume of tissue in (1/m).

The lymphatic drainage term ϕ_{li} is given as [49, 182],

$$\phi_{li} = \frac{L_{li} S_{li}}{V_i} \left(P_i - P_{li} \right) \tag{7.8}$$

where, P_{li} is the hydrostatic pressure of intra-lymphatic in (Pa), L_l is the hydraulic conductivity of the lymphatic wall in (m/(Pa.s)), S_{li}/V_i is the surface area of the lymphatic vessels per unit volume of tissue in (1/m), and $L_l S_l / V$ is the lymphatic filtration coefficient in (1/(Pa.s)).

The interstitial pressure, which yields zero net volume flux out of the vasculature, is called the effective pressure, and it can be evaluated by making Eq. (7.7) equal to zero as follows

[182, 198]:

$$\phi_{vi} = \frac{L_{vi} S_i}{V_i}\left(P_{vi} - P_{efi} - \sigma_i\left(\pi_{vi} - \pi_i\right)\right) = 0 \tag{7.9}$$

Then, the effective pressure is given as

$$P_{efi} = P_{vi} - \sigma_i\left(\pi_{vi} - \pi_i\right) \tag{7.10}$$

The interstitial pressure at which the influx into lymphatics equal to the efflux out from vasculature is called the steady-state pressure, and it can be obtained by making Eqs. (7.7) and (7.8) equal to each other [182, 198].

$$\frac{L_{vi} S_i}{V_i}\left(P_{vi} - P_{ssi} - \sigma_i\left(\pi_{vi} - \pi_i\right)\right) = \frac{L_{li} S_{li}}{V_i}\left(P_{ssi} - P_{li}\right) \tag{7.11}$$

After solving Eq. (7.11), the steady-state pressure is given as

$$P_{ssi} = \frac{P_{li}\ L_{li} S_{li}/V_i + P_{efi}\ L_{vi} S_i/V_i}{L_{li} S_{li}/V_i + L_{vi} S_i/V_i} \tag{7.12}$$

$$P_{ssi} = \frac{L_{li} S_{li} P_{li} + L_{vi} S_i P_{efi}}{L_{li} S_{li} + L_{vi} S_i} \tag{7.13}$$

The mass continuity equation for incompressible flow in porous media reduces to

$$\nabla \cdot \vec{v}_i = \phi_{vi} - \phi_{li} \tag{7.14}$$

Now, by combining Darcy's law (7.5) and the mass continuity equation (7.14), we get

$$-k_i \nabla^2 P_i = \phi_{vi} - \phi_{li} \tag{7.15}$$

where ∇^2 is the Laplacian operator.

The lymphatic drainage term is equal to zero in the tumor region due to the lack of lymphatic systems in the tumor. Moreover, the mass fluid source term is equal to zero in the ablated-tumor region because the RFA destroys the vascular network. Thus, Eq. (7.15) can be rewritten as

$$-k_i \nabla^2 P_i = \begin{cases} 0 & \text{, Ablated Tumour} \\ \phi_{vi} & \text{, Non-Ablated Tumour} \\ \phi_{vi} - \phi_{li} & \text{, Normal Tissue} \end{cases} \tag{7.16}$$

Equation (7.16), together with the boundary conditions given in section 7.8, can be solved analytically or numerically. However, the analytical solution can be quite complex for a

three-region problem. Thus, we will use COMSOL Multiphysics® software package to obtain the solution numerically. The obtained IVF and IFP will be used in the drug transport model in the next subsection.

7.3.2 Drug Transport Model

In this model, the drug source (acts as a transmitter) is a miniaturized implant loaded with DOX anticancer drug and inserted inside a solid tumor. The implant will release the anticancer drug which diffuses through the surrounding tissue and will be influenced by the various pharmacokinetic processes including, drug efflux/influx into cells, drug binding/unbinding with interstitial proteins, elimination into blood capillaries, and degradation. These factors have a significant impact on the therapeutic efficacy.

(i) *Extracellular free-doxorubicin concentration*:

Transport of free-DOX in the interstitial space can be mathematically modelled using the following diffusion-convection-reaction equation:

$$\frac{\partial C_{exi}}{\partial t} + \nabla \cdot \left(r_F v_i C_{exi} \right) = \nabla \cdot \left(D_{Fi} \nabla C_{exi} \right) + F_{Bi} + F_{Ci} - \gamma_i C_{exi} \tag{7.17}$$

where ∇ is the Del gradient operator and the index $i \in \{a, t, n\}$ refers to the ablated tumor, the non-ablated tumor, and the normal tissues. The function C_{exi} is the spatiotemporal extracellular concentration of free-DOX in the interstitial space in the unit of grams per interstitial volume (g/m^3) and D_{Fi} is the diffusion coefficient of free-DOX molecules in the interstitial space, which has different value in each region. The retardation factor r_F is the ratio of the solute velocity to the fluid velocity which is equal to one for tumor microenvironment [198]. We assume that the DOX transport does not affect density and flow of the interstitial fluid. Thus, the interstitial velocity field, v_i, is obtained in the previous section independently of the DOX transport model.

The free DOX loss rate γ_i is due to drug drainage in the lymphatic vessels and elimination by the blood vessels.

$$\gamma_i = \begin{cases} 0 & \text{, Ablated Tumor} \\ \gamma_{vi} & \text{, Non-ablated Tumor} \\ \gamma_{vi} + \phi_{li} & \text{, Normal Tissue} \end{cases} \tag{7.18}$$

Free DOX loss rate due to lymphatic drainage (ϕ_{li}) is given by (7.8). Since lack of lymphatic system in the tumor region [144, 182, 198], we set the DOX loss rate due to lymphatic drainage equal to zero in both the ablated and non-ablated tumor regions. Moreover, the experimental studies showed that thermal ablation, e.g., RFA and HIFU, destroy the vascular structure inside the ablated tumor zone and therefore the DOX loss into the blood in this region is neglected, see section 7.6. However, several blood vessels may appear in the peripheral region of the ablation zone [202]. Moreover, the initial DOX concentration in the plasma is assumed to be zero where the implant is the only drug source [105].

The loss rate of free-DOX due to elimination by the blood vessels (γ_{vi}) can be expressed [105, 136] as

$$\gamma_{vi} = \frac{P_{Fi} S_{vi}}{V_i} \tag{7.19}$$

where P_{Fi} is the permeability coefficient of the blood vessel wall to free-DOX in (m/s).

The term F_B accounts for binding and unbinding of DOX with proteins such as Albumin in the interstitial space.

$$F_{Bi} = k_d C_{bi} - k_a C_{exi} \tag{7.20}$$

where k_a and k_d are the DOX-protein association and dissociation reaction rates, respectively, and C_{bi} is the spatiotemporal bound-DOX concertation in the tissues.

The doxorubicin molecules can transport to/from the interior of the cell across the cell membrane. Thus, the effect of cellular uptake (influx) and efflux is modelled using the following cellular influx/efflux rate:

$$F_{Ci} = D_c \left(\zeta_{eff} - \zeta_{\inf} \right) \tag{7.21}$$

where D_c is the cancer cells density in (10^5 cells/m^3). The cellular influx and efflux functions, $\zeta_{\inf}$ and ζ_{eff}, are given in Eqs. (7.23) and (7.24), respectively.

(ii) *Intracellular doxorubicin concentration*:

The drug doxorubicin can be transported across the cell membrane via passive diffusion and carrier-mediated transport [203]. Here, we assume that only the free-DOX can uptake by the

cells, and therefore the intracellular concentration is a function of the extracellular free-DOX concentration. Some DOX molecules may not get out from the cells due to binding with the intracellular sites or storing inside the cell. The intracellular DOX concentration C_c is expressed in the unit of $(\mathrm{ng}/10^5\mathrm{cells})$ and it changes with the time according to the following ordinary differential equation [147, 204].

$$\frac{dC_c}{dt} = \zeta_{\mathrm{inf}} - \zeta_{eff} \tag{7.22}$$

$$\zeta_{\mathrm{inf}} = V_{\max} \frac{C_{exi}}{C_{exi} + k_e \phi_e} \tag{7.23}$$

$$\zeta_{\mathrm{eff}} = V_{\max} \frac{C_c}{C_c + k_c} \tag{7.24}$$

where ζ_{inf} and ζ_{eff} are the cellular influx and efflux functions, $V_{\max}$ is the maximum rate of transmembrane transport, and ϕ_e is the extracellular volume fraction. The parameters $V_{\max}$, k_e, and k_c are experimentally fitted parameters given in [147]. The parameters mentioned above are listed in Table 7.1.

Table 7.1: Pharmacodynamic and intracellular model parameters.

Parameter	Unit	Value	References
$V_{\max}$	ng/(s.10^5 cells)	4.67×10^{-3}	[49, 147, 204-207]
k_e	kg/m^3	2.19×10^{-4}	[49, 147, 204-207]
k_c	ng/10^5 cells	1.37	[49, 147, 204-207]
ϕ_e	-	0.4	[49, 147, 205, 206]
D_{c0}	10^5 cells/m^3	1×10^{10}	[49, 204-207]
k_{gr}	s^{-1}	5.78×10^{-6}	[204, 207]
k_{dr}	s^{-1}	2.78×10^{-6}	[204, 207]
k_m	m^3/(s.10^5 cells)	3×10^{-16}	[49, 204, 207]
$k_{\max}$	s^{-1}	1.67×10^{-5}	[49, 208]
EC_{50}	ng/10^5 cells	0.5	[49, 208]

(iii) *Extracellular Bound-doxorubicin concentration*:

Some of free-DOX molecules may bind to proteins, such as Albumin, in the interstitial space. The bound-DOX may unbind from the DOX-protein complexes and then becomes free. The spatiotemporal transport of bound-DOX in the extracellular space can be modelled using the following diffusion-convection-reaction equation:

$$\frac{\partial C_{bi}}{\partial t} + \nabla \cdot \left(r_F v_i C_{bi} \right) = \nabla \cdot \left(D_{Bi} \nabla C_{bi} \right) - F_{Bi} - \gamma_i C_{exi} \tag{7.25}$$

where D_{Bi} is the diffusion coefficient of bound-DOX in the interstitial space, which has a different value in each region. Here, the spatiotemporal extracellular concentration of bound-DOX (C_{exi}) in the interstitial space in (kg/m^3).

The bound-DOX loss rate γ_i is due to drug drainage in the lymphatic vessels and elimination by the blood vessels. It is given by Eq. (7.19) but with replacing the drug loss rate due to elimination to the following rate:

$$\gamma_{vi} = \frac{P_{Bi} S_{vi}}{V_i} \tag{7.26}$$

where P_{Bi} is the permeability coefficient of the blood vessel wall to bound-DOX.

7.4 Pharmacodynamic Model: Impact of Anticancer Drug on Tumor Cell Density

The cancer cell density can be described using an ordinary differential equation that describes the natural growth and death of cells which leads to a steady-state balance [204]. Moreover, the death of cancer cells due to effect of DOX intracellular concentration can be included in this equation [208, 209]. The tumor cell density D_c in the unit (10^5cells/m^3) can be described using the following equation [49, 204].

$$\frac{dD_c}{dt} = \left(k_{gr} - k_{dr} \right) D_c - K D_c - k_m D_c^2 \tag{7.27}$$

$$K = \frac{k_{\max} C_c}{C_c + EC_{50}} \tag{7.28}$$

where k_{gr} and k_{dr} are the natural growth and decay rate constants of the tumor cells, respectively, and k_m is the saturation constant. The nonlinear function *K* reflects the effect of the anticancer drug which depends on the following: the intracellular concentration of free-DOX, the maximal DOX cell killing rate ($k_{\max}$), and drug concentration that produces 50% of $k_{\max}$ (EC_{50}), which has the unit of the intracellular DOX concentration. The initial tumor cell density is used as an initial condition for solving Eq. (7.27). The parameters mentioned above are listed in Table 7.1.

7.5 Release Kinetics Model of Dual-Release Implant

In this model, the drug implant (acts as a MC transmitter) is loaded with anticancer drug DOX. The main design parameters in the implant are the release rate, the implant size, and the amount of loaded drug. The release rate depends on the implant formation and the physicochemical properties of the loaded drug, which can be adjusted during the design phase by selecting appropriate materials, e.g., polymer and drugs [186]. The optimal release rate can help in improving the therapeutic outcomes with reducing the side effects, which in order save time and cost. The amount of the released drug can be experimentally monitored over the time to obtain the release profiles. Relevant mathematical models for the release kinetic can be fitted to the experimentally measured release curves to predict the release rate constants [210].

Similar to the implant release model used in the previous chapter, here the implant has dual-release pattern, i.e., it releases DOX over two phases: fast burst release over short time duration followed by slow sustained release over extended period of time. Thus, we can model both dual-release and sustained release implants by adjusting the release parameters. For example, in-situ forming implants (ISFIs) have dual-release pattern [39] and also dual-release pattern can be achieved by designing a double-layer implant [106]. However, the burst release in ISFIs represents the main drawback that may cause toxicity to healthy cells and consume the loaded drug; thus, it should be minimized.

The cumulative amount of the released DOX at the time *t* can be mathematically modelled using the bi-exponential first-order kinetic model as

$$M(t) = M_0 W_\infty \left(1 - f \cdot e^{-k_f t} - (1-f) \cdot e^{-k_s t}\right) \tag{7.29}$$

where M_0 is the total amount of loaded-drug in the implant in (mg), W_∞ is the total fraction of drug released at steady state, f is a fraction of drug released during the burst phase, and k_f and k_s are the release rate constants for burst and sustained release phases in (s^{-1}), respectively.

Now, the rate of drug release across the spherical implant surface at time t per unit area of the implant surface in $g/(s \cdot m^2)$, i.e., the flux, can be expressed as

$$F_{rs}(t) = \frac{1}{A}\frac{dM}{dt} = \frac{M_0 W_\infty}{A}\left(f \cdot k_f e^{-k_f t} + (1-f) \cdot k_s e^{-k_s t}\right) \tag{7.30}$$

where $A = 4\pi r_0^2$ is the surface area of the implant and r_0 is the implant radius.

The characteristic parameters of the dual-release implant are listed in Table 7.2. Similar to the experimental release data in [39], we chose 10% of the loaded drug to be released within the first hour while different values of the sustained-release rate constant are examined.

Table 7.2: The dual-release implant parameters.

Parameter	Value	Unit
M_0	5	mg
k_f	5×10^{-4}	s^{-1}
k_s	$1\text{-}25\times10^{-6}$	s^{-1}
f	0.1	-
W_∞	1	-
r_0	1.5	mm

The experimental studies in the literature showed insignificant variation in the size of the implant during the release duration since the implant releases drug prior to any significant degradation [105]. Thus, it is reasonable to assume that the size variation due to biodegradation is negligible during the observation time [39, 105].

7.6 Tumor Microenvironment Parameters

In this work, the values of the model parameters are obtained from the published experimental data and other studies in the literature assuming that the growth of the tissues is negligible during the observation timeframe. The parameters are defined through this chapter and summarized in Table 7.1 to Table 7.4.

(i) *Microvasculature Density* (*S/V*):

The microvasculature density is the ratio of vascular surface area per unit volume of tissue. The microvasculature density of capillaries highly varies among tumor types and within the same type of tumor [201]. Different studies show that the larger tumors have smaller microvasculature densities. For a tumor with 2 cm diameter (i.e., volume = 4188 mm^3), the surface area of the blood vessels per unit volume of tumor tissue is approximately equal to 10^4 1/m [201]. However, the experimental data show a leak of lymph vessels in the tumor tissues. In normal tissues, the surface area of the blood vessels per unit volume of tissue is measured as 7×10^3 1/m [49, 211]. As mentioned before, the histological analysis confirms that the thermal ablation destroys the vascular network and tumor cells in ablated tumor tissue [176, 195]. Thus, the effect of microvasculature density and consequently, drug loss through the blood microvessels in the ablated tumor tissue are neglected. As observed in [116, 118], several days after RFA, new blood vessels may be developed in the ablated region, and thus drug elimination through the blood will start to increase linearly with the time. However, in this study, the simulation timeframe is four days, and therefore our assumption is reasonable to ignore the drug elimination by the blood microvessels.

(ii) *Extracellular space fraction* (ϕ_e) :

The volume fraction of extracellular space in the tumor is much larger than that in the normal tissue, and it ranges from 0.2 to 0.6 with tumor cell density ranges from 0.955-15.3 10^5cells/mm^3 [205]. In this study, the volume fraction of extracellular space ϕ_e and the initial cell density D_{c0} are chosen equal to 0.4 and 10 10^5cells/mm^3, respectively.

(iii) *Microvasculature permeability* (P_F, P_B):

The vasculature permeability measures the capability of the capillary or lymph vessel wall to exchange various substances in and out of the vasculature. The vasculature permeability of

Albumin bound-DOX and free-DOX is approximately three-fold higher in tumor than normal tissues [205].

Table 7.3: Fluid transport parameters.

Parameter	Unit	Tumor Tissue	Normal Tissue	References
π_i	Pa	2000	1333	[49, 182, 198, 199, 211-213]
π_{vi}	Pa	2666	2666	[49, 182, 198, 199, 211-213]
ρ_i	kg/m^3	1000	1000	[49, 199]
μ_i	Pa.s	7.8×10^{-4}	7.8×10^{-4}	[49, 199]
k_i	m^2/(Pa.s)	3.10×10^{-14}	6.40×10^{-15}	[49, 182, 198, 199, 211-213]
S_{vi}/V_i	m^{-1}	10000	7000	[49, 182, 198, 199, 201, 211-215]
L_{vi}	m/(Pa.s)	2.10×10^{-11}	2.70×10^{-12}	[49, 182, 198, 199, 211-213]
L_lS_l/V	1/(Pa.s)	0	4.17×10^{-7}	[49, 182]
P_{li}	Pa	0	0	[49, 182]
P_{vi}	Pa	2080	2080	[49, 182, 198, 199, 211-213]
σ_i	-	0.82	0.91	[49, 182, 198, 199, 211-213]

(iv) *Diffusion coefficients* (D_F, D_B):

The diffusivity of free-DOX is higher than Albumin-bound DOX as the molecular weight (MW) of free-DOX is 544 Da while Albumin-bound DOX has MW of 69 kDa. Moreover, the diffusivity of free and bound DOX in tumor is larger than that in normal tissues as listed in Table 7.4. However, the experimental studies found that the diffusivity of DOX near the center of the ablated tumor after RFA, D_{ac}, is 75% higher than that in non-ablated tumor [116, 118]. Based on the histological findings in ablated tumor tissues, the diffusivity shows dependency on the radial distance with higher value at the center of ablated tumor (near the ablation probe where the temperature is higher), than the outer periphery region. The diffusion coefficient in the outer region of the ablated tumor ($r_c \le r \le r_a$) is characterized in [116, 118] as

$$D_a = D_{ac} - \frac{r - r_c}{r_a - r_c}\left(D_{ac} - D_t\right) \tag{7.31}$$

where r_a is the ablation zone radius, $r_c = \alpha r_a$ is the radius of the central tumor region, and $\alpha = 0.47$.

The diffusivity D_{ac} of the tumor center decreases linearly with the radial distance to finally reach the diffusivity of the non-ablated (risk) tumor, i.e., D_t. In this model, we use an average diffusion coefficient within the ablated tumor tissue. The mean diffusivity of outer ablated region is calculated using scale relationship of DOX diffusivity in ablated and non-ablated tissues, then by taking average of the diffusivity given by equation (7.31).

Table 7.4: Free and bound doxorubicin parameters.

Parameter	Unit	Free DOX	Bound DOX	References
D_a	m^2/s	5.34×10^{-10}	13.95×10^{-12}	Calculated in section 7.6 according to the experimental data [116, 118].
D_t	m^2/s	3.40×10^{-10}	8.89×10^{-12}	[49, 147, 199, 204-207, 216-218]
D_n	m^2/s	1.58×10^{-10}	4.17×10^{-12}	[49, 147, 199, 204-207, 216-218]
k_a	s^{-1}	0.833	-	[49, 204-207]
k_d	s^{-1}	-	0.278	[49, 204-207]
P_t	m/s	1×10^{-6}	7.8×10^{-9}	[49, 147, 205, 219]
P_n	m/s	3.33×10^{-7}	2.6×10^{-9}	[49, 147, 205, 219]
MW	kg/mol	0.544	69	[49, 147, 199, 206]

7.7 Model Geometry

In this work, a 3-D spherical solid tumor is used with a diameter of 2 cm, as shown in Figure 7.2 and Figure 7.3. We consider three cases for the tumor microenvironment, namely, non-ablated tumor, 80% ablated tumor, and 90% ablated tumor. For example, the 80% ablated tumor means that a region with radius ($0.8\times r_t$) is ablated inside the tumor. In case of the ablated tumor, a thin rim of viable cancer cells (risk region) will remain at the tumor periphery. The thickness of the risk regions with 80% and 90% ablation zones are chosen

equal to 2 mm and 1 mm, respectively. Here, thickness of the normal region is chosen to be 5mm. The implant has radius of 1.5 mm, and it is located at the tumor center. The model geometry and mesh are created using built-in CAD kernel in COMSOL Multiphysics® package. The mesh size is chosen as "Finer" based on a convergence mesh independence test which shows that 5-times decrease in the mesh element size will provide a negligible enhancement, i.e., < 5%, in DOX concentration profiles. Moreover, we refine the mesh using "Boundary Layer Setting" at the implant/tissue boundary and other interface boundaries between the various regions, to handle the rapid change for drug concentration, velocity, and pressure at these interface layers.

7.8 Boundary Conditions

Due to spherical symmetry, the pressure at the tumor center is characterized using no-flux boundary condition as

$$\nabla P_i\big|_{r=0} = 0 \tag{7.32}$$

In this work, the observation time scale in the numerical analysis is assumed to be much shorter than the time scale for growth of the tumor and normal tissues [49]. Therefore, the interface boundary between the ablated tumor and the non-ablated (risk) region as well as the boundary between the risk region and the normal tissue are assumed to be fixed as shown in Figure 7.3. The continuity boundary conditions of the interstitial pressure and fluid flux are imposed at these interface boundaries as

$$P_i\big|_{r=r_a^-} = P_i\big|_{r=r_a^+} \tag{7.33}$$

$$P_i\big|_{r=r_t^-} = P_i\big|_{r=r_t^+} \tag{7.34}$$

$$-k_a \nabla P_i\big|_{r=r_a^-} = -k_t \nabla P_i\big|_{r=r_a^+} \tag{7.35}$$

$$-k_t \nabla P_i\big|_{r=r_t^-} = -k_n \nabla P_i\big|_{r=r_t^+} \tag{7.36}$$

In addition, the outer boundary of the normal region is assumed to be fixed. The interstitial fluid pressure at this boundary has a minimal constant value. Thus, Dirichlet boundary condition can be applied at the outer boundary as

$$P_i\big|_{r=r_n} = P_\infty \tag{7.37}$$

The total interstitial drug flux is a combination of diffusion and convection fluxes. In this model, the interstitial velocity field mainly appears at the interface boundary between the tumor and the normal tissues due to the large pressure difference at that layer. The continuity boundary conditions of drug flux and concentration are applied at the interface boundaries between the ablated tumor and the risk region as well as between the risk and normal regions. The continuity boundary conditions are applied for both free and bound DOX as

$$\left(-D_{aj}\nabla C_j + v_i C_j\right)\Big|_{r=r_a^-} = \left(-D_{tj}\nabla C_j + v_i C_j\right)\Big|_{r=r_a^+} \tag{7.38}$$

$$\left(-D_{tj}\nabla C_j + v_i C_j\right)\Big|_{r=r_t^-} = \left(-D_{nj}\nabla C_j + v_i C_j\right)\Big|_{r=r_t^+} \tag{7.39}$$

$$C_j\big|_{r=r_a^-} = C_j\big|_{r=r_a^+} \tag{7.40}$$

$$C_j\big|_{r=r_t^-} = C_j\big|_{r=r_t^+} \tag{7.41}$$

where $\nabla = \partial/\partial r$ is the gradient operator in the spherical coordinate system and the index j is used to indicate either the free or bound DOX.

No flux (Neumann) boundary condition is applied at the outer boundary of the normal region as

$$\left(-D_{nj}\nabla C_j + v_i C_j\right)\Big|_{r=r_n} = 0 \tag{7.42}$$

The release process of DOX drug from the implant is modelled using the following flux boundary condition:

$$-D_{doxi}\nabla C_{exi}\big|_{r=r_0} = F_{rs}(t) \tag{7.43}$$

where $F_{rs}(t)$ is given by Eq. (7.30).

7.9 Numerical Solution using COMSOL

The system of mathematical equations that describe the proposed model cannot be solved analytically. Therefore, we use COMSOL Multiphysics® package to numerically solve the proposed mathematical models. In COMSOL Multiphysics®, we solve the interstitial fluid flow and drug transport models together with the pharmacodynamic model. Firstly, the interstitial fluid flow model is implemented using 'Darcy's Law Physics' and it is solved

using the stationary fully coupled direct linear solver 'NUMPS'. Secondly, 'Transport of Diluted Species Physics' is used to implement the interstitial drug transport model. Then, it is solved using the time-dependent fully coupled direct linear solver 'NUMPS'. The pharmacodynamic model of the tumor cell density and the intracellular DOX concentration model are solved simultaneously with the other models using 'Global Ordinary Differential Equation Physics' (ODEs). Both the fluid flow and the drug transport models are solved under relative tolerance of 10^{-6} and absolute tolerance 10^{-7}. The time stepping method 'BDF' is chosen with an intermediate time step and a maximum time step of 6 min based on a time-step sensitivity test. The steady-state solutions of the interstitial velocity and pressure fields are applied to the drug transport model. The numerical simulation was allowed to run over a timeframe of 4 days (96 hours) assuming the initial time is the time of insertion of the implant in the tumor.

7.10 Numerical Results

The proposed model predicts the spatiotemporal concentration of both free-DOX and bound-DOX inside the ablated and non-ablated tumors under different processes including diffusion, convection, binding/unbinding to albumin proteins, clearance by blood and lymphatic vessels, and influx/efflux by tumor cells. Moreover, we obtain the intracellular DOX concentration, which used for predicting the density and killing rate of the cancer cells in the risk region. In this model, the tumor characteristics as well as the drug parameters, are taken from the published experimental works and other studies in the literature. In this study, we assume that the implant is inserted inside thermally ablated solid tumors with 80% and 90% ablation regions (i.e., the ablation zone radius is 80% and 90% of the tumor radius). The diffusion and elimination properties of DOX in the thermally ablated tumor is obtained based on the published experimental studies in the literature. Moreover, we examine the results without applying RFA to the solid tumor. The parameters used in this study are given in Table 7.1 to Table 7.4.

As shown in Figure 7.4 and Figure 7.5, the average IFP in the solid tumor is equal to 1466 Pa (the maximum value is 1533 Pa or 11.5 mmHg). However, the average pressure in the normal tissue is equal to 50 Pa which is significantly lower than the pressure in tumor tissue.

Furthermore, there is a sharp pressure gradient (and consequently high-velocity field) at the interface boundary between the tumor and normal tissues, as shown in Figure 7.4 and Figure 7.5. However, the velocity field can be considered negligible except at the boundary between the tumor and normal tissues. This result is not surprising due to the lack of the lymph vasculature in the tumor compared to the normal tissue. These results and trends agree well with the previous studies in the literature [49, 144, 198].

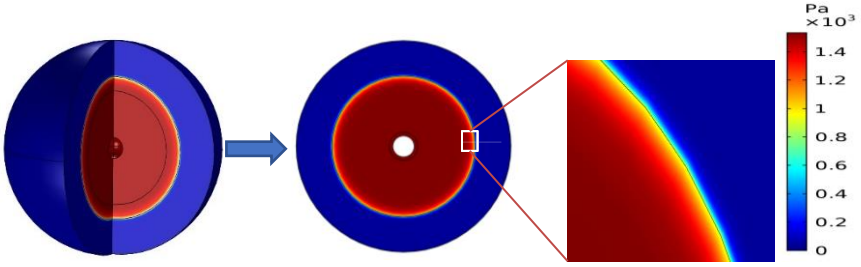

Figure 7.4: The spatial distribution of interstitial fluid pressure in tumor and normal tissues.

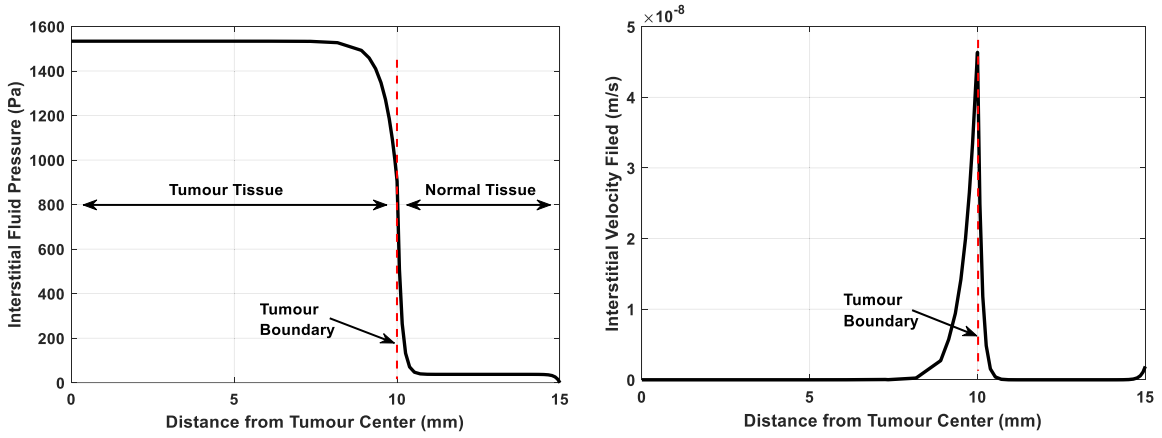

(a) (b)

Figure 7.5: (a) Interstitial fluid pressure and (b) velocity field in the tumor and normal tissues with the radial distance from the tumor center.

A group of researchers conducted experiments for measuring the DOX concentration with the distance from a polymer implant placed inside thermally ablated liver tumor in [116, 117, 175, 177]. In Figure 7.6, we verify the accuracy and validity of our drug transport model by comparing the results with the published experimental data in [117]. The experimental data provides the mean value of DOX concentration with the distance from a polymer implant on the fourth day following the implantation in thermally ablated liver tumor. The impact of the

various processes in tumor including the binding effect are given in terms of the apparent elimination rate constant and apparent diffusivity [116]. In order to perform the comparison, we need to reduce our model by removing the terms that account for DOX-proteins binding and cellular influx/efflux in Eq. (7.17) assuming negligible fluid flow. Also, the normal tissue is ignored from the model because the experimental data is given only in the tumor tissue. The parameters used in this comparison are same as that used in [117]. Drug transport from the implant to the surrounding tissue is symmetric around the implant axis. The implant diameter is 1.6 mm while the tumor diameter is 1.1 cm with 4 mm ablation radius. We estimate the implant release rate constant (0.5341 day^{-1}) by fitting the drug release model to the experimental release data given in [177]. The amount of loaded DOX in the implant is 2.99 mg, and 93.7% of the loaded drug is released on the fourth day, i.e., 2.8 mg [117, 175]. The apparent diffusivity of DOX in liver tumor is given as D = 50 $\mu m^2/s$ while it varies within the thermally ablated tumor; thus we use an average value of 78.2 $\mu m^2/s$ [116]. The apparent elimination rate constant of DOX in liver tumor is $\gamma = 0.58\times10^{-4}$ s^{-1} and it is negligible in the ablated tumor within the first four days, i.e., $\gamma = 0$ s^{-1} [116].

As expected, the measured concentration shows a decreasing trend with respect to the radial distance from the implant. It can be seen that the results obtained using our numerical COMSOL model agree well with the results extracted from the published experimental data in [117]. Moreover, we obtain the results using our analytical and stochastic simulation model described in the previous chapter in sections (6.6) and (6.7) under the following assumption and approximation: the tumor region is totally ablated (i.e., with single diffusion coefficient is equal to $D = 78.2$ $\mu m^2/s$), the fluid flow is negligible, the various processes, e.g., DOX-proteins binding and cellular influx/efflux, are modelled using the apparent elimination rate and apparent diffusivity. As described in the previous chapter, since the radius of the virtual observer, used in stochastic simulation, is equal to 0.5 mm, we start recording the concentration at a distance 0.5 mm from the implant surface to avoid the intersection between the virtual receiver and the implant. As shown in Figure 7.6, the analytical and stochastic results match well with the numerical COMSOL model. Moreover, the experimental data extracted from the literature and plotted in this figure represent the mean values, and the predicted results by our models fall within the standard deviation of the mean. This indicate accuracy and validity of

the proposed drug release and transport model which forms the main part of this chapter.

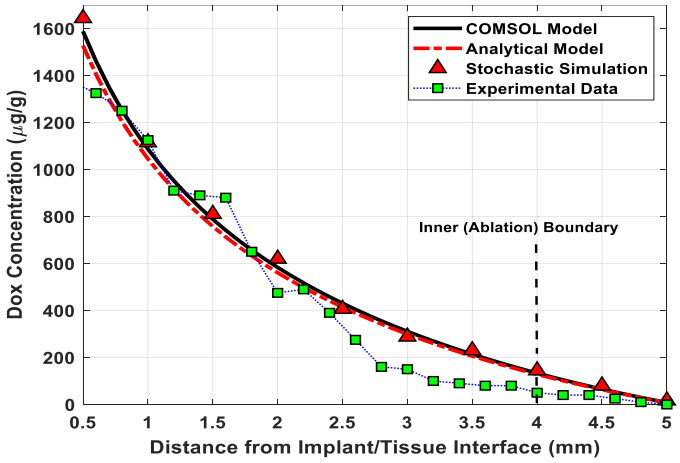

Figure 7.6: Comparison of DOX concentration obtained from the experimental data given by [117] with our models using apparent diffusivity and apparent elimination rate.

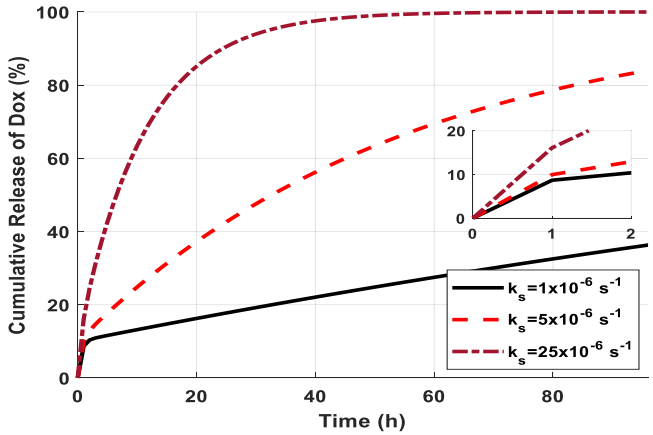

Figure 7.7: The cumulative release profile of DOX from the dual-release implant for various sustained release rate constants.

The cumulative release profile of DOX from a dual-release implant for various release rate constants is shown in Figure 7.7. In the burst release phase, 10-15 % of the loaded DOX (i.e., 0.5-0.75 mg) is rapidly released within the first hour after implantation for k_f=5×10^{-4} s^{-1}. In the next phase, i.e., the sustained release, the implant will release the remaining amount of DOX over different extended time durations based on the chosen sustained release rate constants as shown in Figure 7.7. During the release process, the remaining amount of drug inside the implant will decrease, and consequently the drug release rate also will decrease.

In this study, the concentration distribution profiles in both 80% and 90% ablated tumors have similar trend with the time and distance but with slightly different amplitudes. Therefore, we do not show all the results in this chapter to eliminate redundancy. Figure 7.8 shows the spatial-mean extracellular concentration profiles of free-DOX as a function of time in the ablated and risk regions of 90% ablated tumor. The extracellular DOX concentration in the ablated region increases rapidly and immediately after insertion of the implant. The implant with a higher release rate leads to a larger peak concentration and lower peak time in both the ablated and risk regions, as shown in Figure 7.8a and Figure 7.8b.

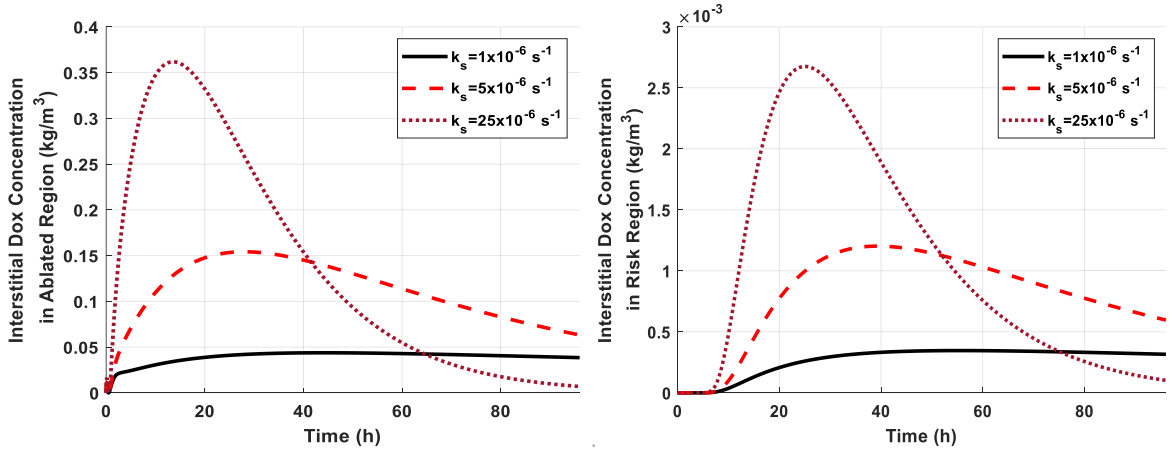

(a) (b)

Figure 7.8: Spatial-mean temporal profile of free-DOX extracellular concentration in (a) the ablated region and (b) the risk region, with 90% ablated tumor for various sustained release rate constants.

The extracellular DOX concentration in the ablated and risk regions reaches the peak value at the times {50, 28, 14}h and {57, 40, 25}h, respectively, for the following sustained release rate constants, $k_s = \{1, 5, 25\}\times10^{-6}$ s^{-1}, respectively. As the release rate increases, amount of the released DOX will increase rapidly, and thus the peak concentration will reach a higher value within a shorter time. After insertion the implant, the drug needs time, i.e., ~7h, to reach the risk region, which is located at the outer rim of the ablated region, as shown in Figure 7.8b. The decay in DOX concentration after it reaches the peak value is due to reduction in the released drug from the implant and because drug will transport from the ablated region to the risk region and normal tissue which have high drug elimination through the blood vessels and cellular uptake.

The spatial-mean temporal profile of extracellular bound-DOX concentration in the risk region of 90% ablated tumor is shown in Figure 7.9. We found that the bound-DOX concentration has a similar trend as the free-DOX concentration for various sustained release rate constants but with approximately three-fold higher amplitude. Therefore, we show few samples in this chapter for bound-DOX concentration profiles. The increasing and decreasing rates of the extracellular concentration for both free and bound-DOX become sharper as the release rate constant increases.

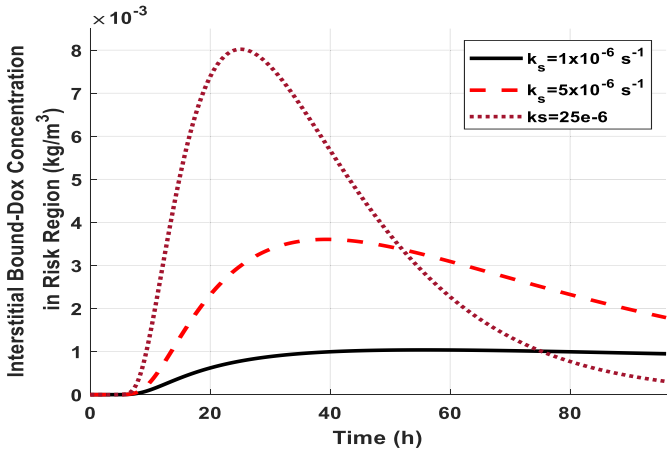

Figure 7.9: Spatial-mean temporal profile of extracellular bound-DOX concentration in the risk region of 90% ablated tumor.

On the other hand, the extracellular free and bound-DOX concentrations in the non-ablated solid tumor, i.e., without applying RFA, will immediately and sharply decrease following insertion of the implant, as shown in Figure 7.10. However, in thermally ablated solid tumor, we observe that the concentration of free and bound-DOX decreases after 14h and 25h in the ablated and risk regions, respectively, as shown in Figure 7.8 and Figure 7.9. This happens because in the non-ablated tumor, the cells and blood vasculature structures, which cover a large volume of the solid tumor, have high impact on elimination of the DOX via cellular uptake and perfusion into the blood vessels. However, due to lack of vascular clearance and cellular uptake in the ablated tumor, the ablated region will act as a large drug reservoir which supplies DOX to the risk region after the implant release rate decreases. It seems that the impact of the ablated region as a reservoir is similar to effect of the necrosis on drug transport in solid tumor which was observed in the literature but for other purposes [198, 211]. This is

reasonable because the ablated region has a similar structure as the necrotic with absence of the vasculature and the viable cells. Also, the concentration of bound-DOX is roughly three-fold higher than free-DOX.

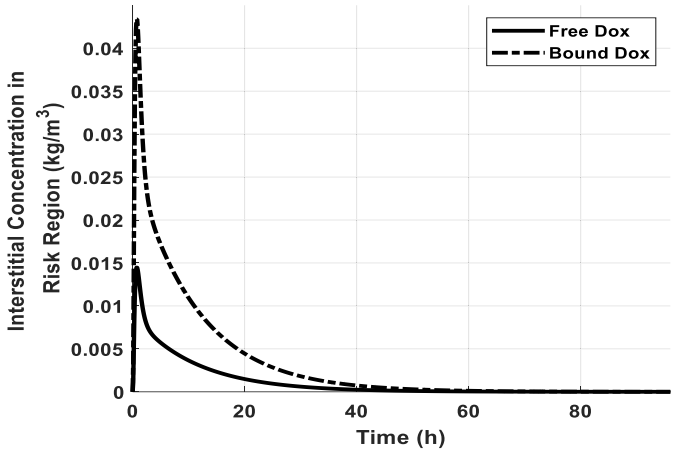

Figure 7.10: Spatial-mean temporal profile of extracellular concentration of free and bound-DOX in the non-ablated tumor (without RFA) when k_s=25×10^{-6} s^{-1}.

Figure 7.11 shows the extracellular DOX concentration versus the distance from the implant/tissue interface in ablated and non-ablated solid tumors. The extracellular DOX concentration in a solid tumor without applying RFA has a smaller amplitude than the concentration in ablated tumor. Furthermore, drug can penetrate a larger distance and cover a larger volume in the ablated tumor compared to the non-ablated tumor. Also, tumor with larger ablation radius (e.g., 90%) shows higher DOX concentration and larger penetration compared to smaller ablation radius (e.g., 80%) on the fourth day as shown in Figure 7.11b. The observed impact of the thermal ablation on the drug distribution in tumors agrees with the experimental data in the literature [39, 117, 175].

The intracellular concentrations of free-DOX in the risk region of 90% ablated tumor as well as in a solid tumor without RFA are shown in Figure 7.12. The DOX intracellular concentration follows a similar trend as the extracellular concentration because it highly depends on the extracellular DOX levels. The higher peak amplitude of the intracellular concentration can be achieved using faster release implant.

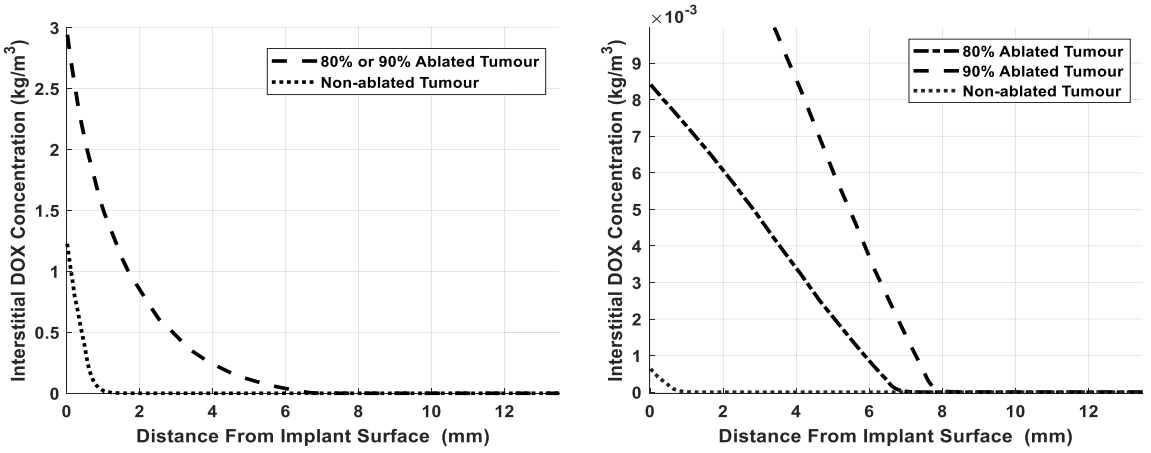

(a) (b)

Figure 7.11: Spatial extracellular concentration of free-DOX at the time (a) t = 12h and (b) t = 96h, after insertion the implant in a solid tumor with/without RFA.

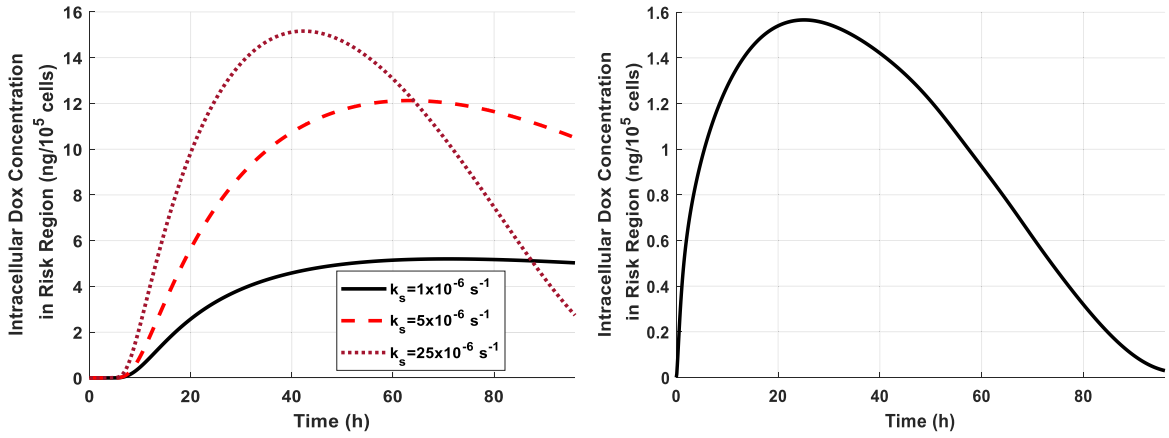

(a) (b)

Figure 7.12: Spatial-mean temporal profile of free-DOX intracellular concentration in (a) risk region of 90% ablated tumor and (b) tumor without RFA when k_s=25×10^{-6} s^{-1}.

The spatial distributions of intracellular DOX in the risk region of 90% and 80% ablated tumors for various release rate constants are shown in Figure 7.13 and Figure 7.14, respectively. This figure shows decreasing behaviour for the intracellular concentration as the distance increases from the inner boundary of the risk region. This happens because the extracellular DOX concentration decreases with the distance from the inner boundary of the risk region, and it has direct influence on the intracellular uptake and consequently on the intracellular DOX concentration.

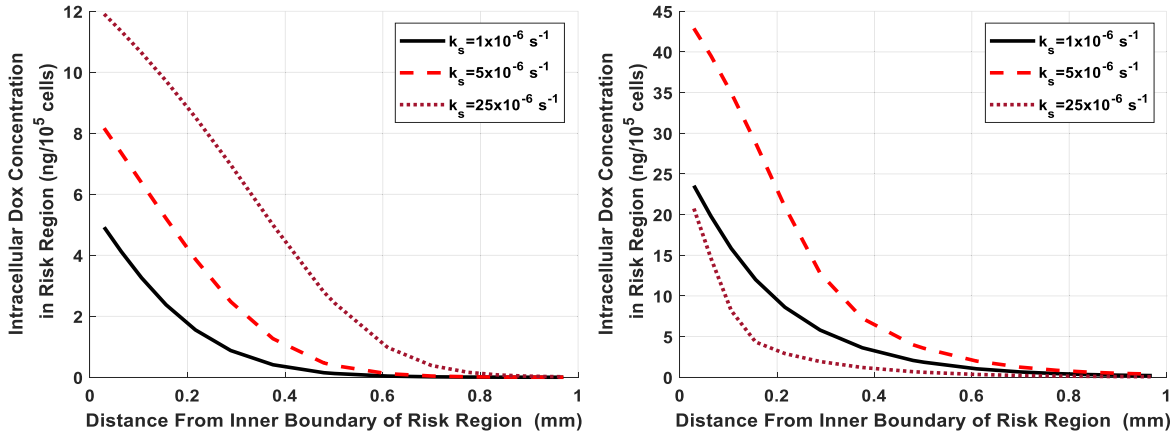

(a) (b)

Figure 7.13: Spatial intracellular concentration of free-DOX in the risk region of 90% ablated tumor for various sustained release rate constants at the time (a) t=12h and (b) t=96h.

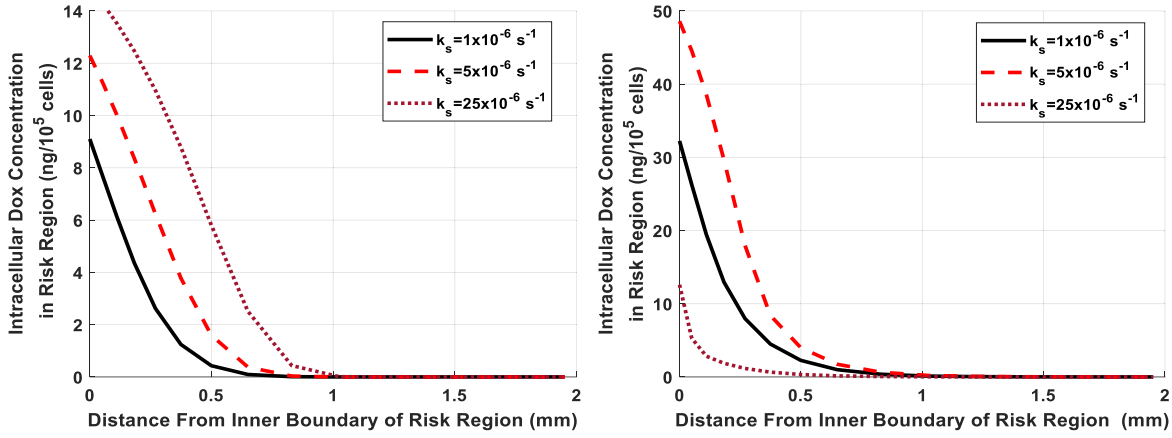

(a) (b)

Figure 7.14: Spatial intracellular concentration of free-DOX in the risk region of 80% ablated tumor for various sustained release rate constants at the time (a) t=12h and (b) t=96h.

Figure 7.15 shows the tumor cell density in the risk region with the radial distance from the inner boundary of the risk region of 80% and 90% ablated tumors at various times following insertion of the implant. Tumor cell density shows heterogeneous distribution along the radial direction where it increases with the distance with minimum density appears near the inner boundary of the risk region. This can also be seen in the color map of the spatial distribution of tumor cell density in Figure 7.17. Moreover, there is a significant reduction in the tumor

cell density over the time following insertion of the implant. In the case of 80% ablated tumor, the risk region will have higher density of the tumor cells compared with 90% ablated tumor on the fourth day (at t=96h), particularly, at the periphery of the risk region as shown in Figure 7.15. In 90% ablated tumor, DOX will kill most of the tumor cells in the risk region on the last day (t=96h). Furthermore, we found that the implant with the release rate constants k_s={5, 25}×10^{-6} s^{-1} will almost have the same therapeutic effect on the last day of treatment. However, using a smaller release rate will consume less amount of the drug with minimum toxicity on the normal tissue. Therefore, design the implant with optimal release rate is very important to get a high therapeutic efficacy.

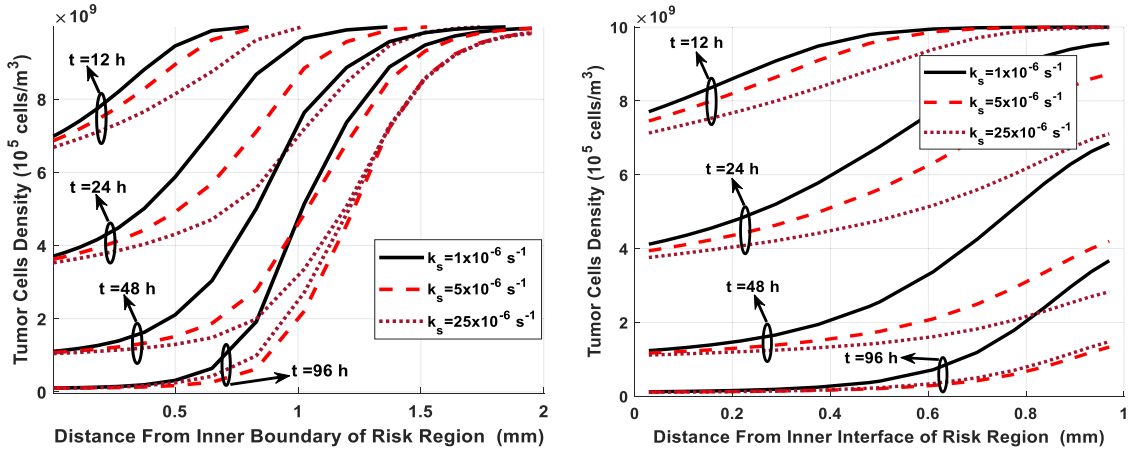

(a) (b)

Figure 7.15: Spatial distribution of tumor cell density in the risk region of (a) 80% ablated tumor and (b) 90% ablated tumor for various sustained release rate constants.

The final therapeutic outcomes of the combination therapy using DOX-loaded implant and RFA can be obtained from the tumor survival curves as shown in Figure 7.16. We can see that using the implant alone for tumor treatment without RFA leads to negligible impact on the tumor cell density, even with a high release rate, i.e., 90% of the tumor cells survive at the end of the treatment (at t = 96h). In the case of 80% ablated tumor, there is about 40% cancer cells survive on the last day of the treatment. However, for 90% ablated tumor, most of the tumor cells are killed on the last day, i.e., only 4% survival cells. This can also be confirmed in the color map of tumor cell distribution as shown in Figure 7.17. Thus, the combination treatment using the implant following RFA will result in high therapeutic

efficacy in destroying the residual tumor cells compared to single therapy approach. Moreover, the release rate constants, k_s={5, 25}×10^{-6} s^{-1}, show similar therapeutic effect on the last day (at t = 96h) with lower tumor survival compared to k_s=1×10^{-6} s^{-1}. Therefore, it is important to optimize the release rate to get high therapeutic effect with less drug and less toxicity on the surrounding healthy tissue.

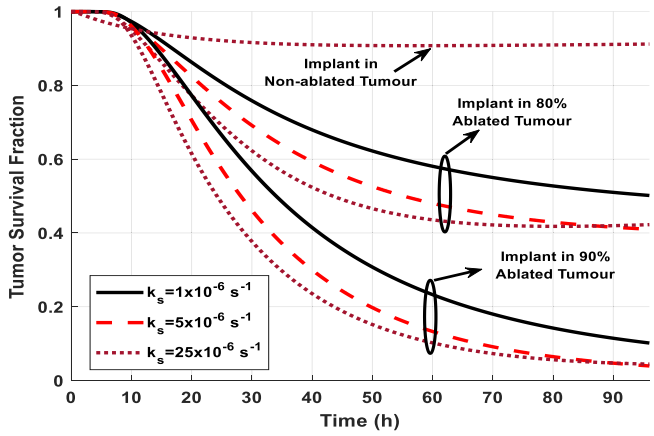

Figure 7.16: The survival fraction of tumor cells in non-ablated and ablated tumors for various sustained release rate constants.

In general, the IDDSs have negligible toxicity on the surrounding healthy tissue and do not cause systemic toxicity. However, for some IDDSs such as in-situ forming implants (ISFIs) there are some key issues that remain to be solved such as the undesirable high initial burst release which may consume the loaded drug and other toxicity issues [107, 108, 220]. Amount of DOX which may reach to the normal tissue should be minimized to reduce the toxicity risks. The DOX level in the normal tissue can be used as a metric to predict the toxicity. Figure 7.18a shows the spatial-mean extracellular concentration of free-DOX in the normal tissue for the case of 90% ablated tumor. As the release rate increases, free-DOX (and consequently bound-DOX) levels will increase in the normal tissue. In this study, the peak DOX concentration in normal tissue under all the examined release rates as listed in Table 7.5, is found to be lower than the half-maximal inhibitory concentration (IC_{50} = 4.13×10^{-5} kg/m^3) [49]. The peak extracellular concentration of free and bound-DOX in solid tumor without RFA has very small and negligible values as shown in Figure 7.18b. In non-ablated solid tumor, the released DOX from the implant will be affected by the cellular uptake and

the elimination through the blood vessels before reaching the normal tissue. This explains why the amount of DOX that appears in the normal tissue is very small in the case of non-ablated tumor compared to ablated tumor where the vascular and cellular structures are destroyed.

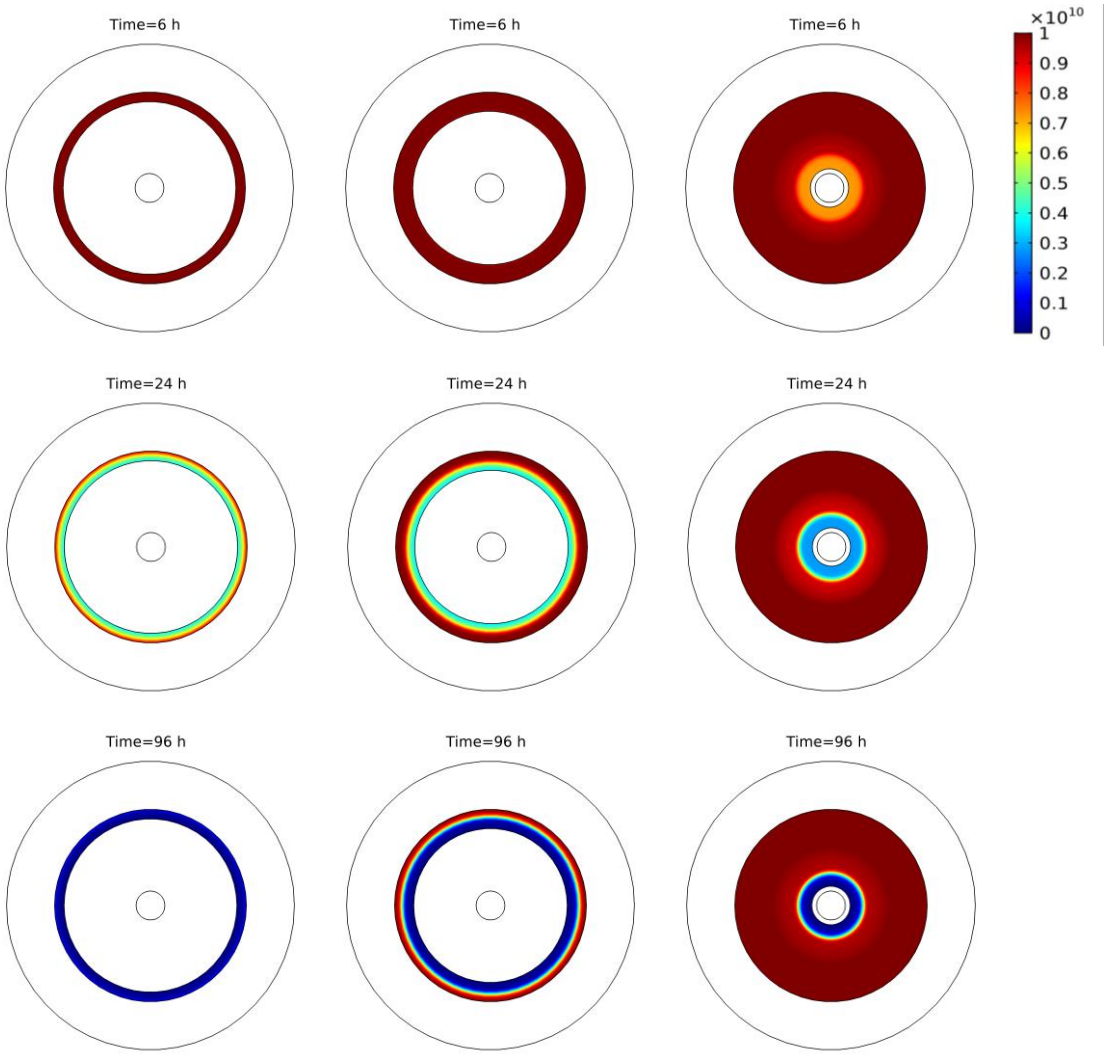

(a) (b) (c)

Figure 7.17: Cross-sectional view of the spatial distribution of tumor cell density in the risk region at different times for (a) 90% ablated tumor, (b) 80% ablated tumor, and (c) tumor without RFA when $k_s=5\times10^{-6}\ s^{-1}$.

Table 7.5: The maximum DOX concentration in normal tissue for various release rate constants in ablated and non-ablated tumors.

Thermal Ablation	C_{max} (kg/m^3)	k_s=1×10^{-6} s^{-1}	k_s=5×10^{-6} s^{-1}	k_s=25×10^{-6} s^{-1}
90% Ablated Tumor	Free DOX	58.9×10^{-8}	202×10^{-8}	430×10^{-8}
	Bound DOX	176×10^{-8}	608×10^{-8}	1280×10^{-8}
80% Ablated Tumor	Free DOX	0.28×10^{-8}	0.99×10^{-8}	2.04×10^{-8}
	Bound DOX	0.85×10^{-8}	2.98×10^{-8}	6.13×10^{-8}
Without RFA	Free DOX	0.72×10^{-12}	0.74×10^{-12}	1.10×10^{-12}
	Bound DOX	2.16×10^{-12}	2.21×10^{-12}	3.32×10^{-12}

However, the cell killing rate is found to be related to the area under the curve (AUC) of the extracellular concentration [221, 222]. The AUC of free and bound-DOX concentration in the normal tissue is summarized in Table 7.6. Similar to the scale relationship between concentration of free and bound-DOX, the AUC of bound-DOX is three-fold higher than the AUC of free-DOX. The results show that five-fold increase in the release rate (k_s=5×10^{-6} s^{-1}) will result in three-fold rise in AUC and 3.5-fold increase of the peak concentration for both free and bound-DOX. However, further increase in the release rate constant (k_s=25×10^{-6} s^{-1}) will lead to about 1.3-fold increase of the AUC and two-fold increase of the peak concentration compared to that with the release rate k_s=5×10^{-6} s^{-1}.

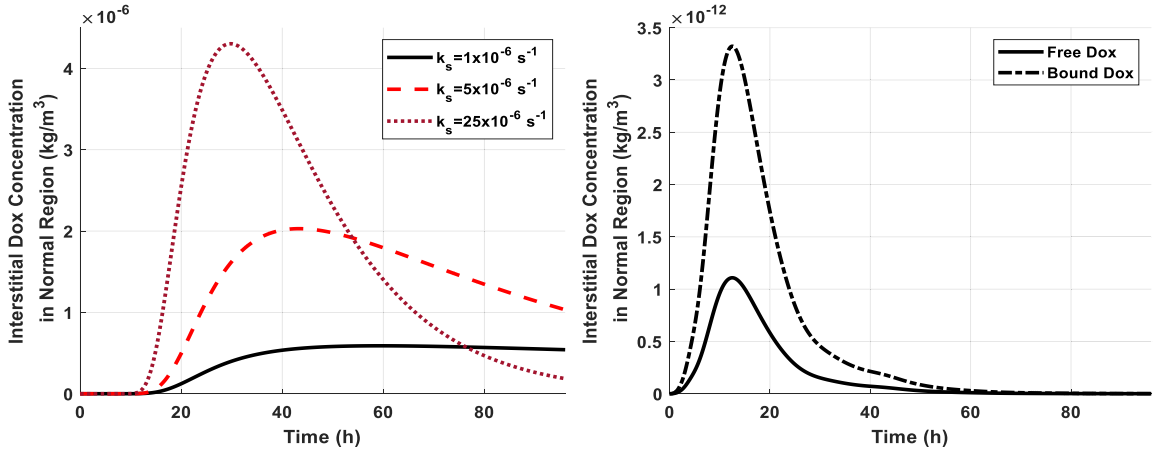

(a) (b)

Figure 7.18: Spatial-mean temporal profile of extracellular concentration in the normal tissue for (a) free-DOX with 90% ablated tumor for various sustained release rate constants and (b) free and bound-DOX without RFA when k_s=25×10^{-6} s^{-1}.

Table 7.6: The area under the curve (AUC) of DOX concentration in the normal tissue for various release rates in ablated and non-ablated tumors.

Thermal Ablation	**AUC (kg.h/m^3)**	**k_s=1×10^{-6} s^{-1}**	**k_s=5×10^{-6} s^{-1}**	**k_s=25×10^{-6} s^{-1}**
90% Ablated Tumor	Free DOX	39.8×10^{-6}	120×10^{-6}	154×10^{-6}
	Bound DOX	119×10^{-6}	361×10^{-6}	464×10^{-6}
80% Ablated Tumor	Free DOX	0.16×10^{-6}	0.52×10^{-6}	0.66×10^{-6}
	Bound DOX	0.50×10^{-6}	1.56×10^{-6}	2.00×10^{-6}
Without RFA	Free DOX	1.24×10^{-11}	1.43×10^{-11}	1.73×10^{-11}
	Bound DOX	3.73×10^{-11}	4.29×10^{-11}	5.20×10^{-11}

7.11 Summary

In this chapter, we propose novel mathematical models based on molecular communication paradigm for combination therapy using local implantable drug delivery system (IDDS) in solid tumors following thermal radiofrequency ablation (RFA). We develop drug transport model for anticancer doxorubicin (DOX), released from dual-release implant, in thermally ablated and non-ablated solid tumors for predicting the extracellular and intracellular concentrations of both free and bound-DOX. This model includes impact of the various pharmacokinetic processes such as binding/unbinding of DOX to proteins in the interstitial space, cellular influx and efflux of DOX, and elimination of DOX into the blood and lymphatic vessels. Also, we investigate impact of the interstitial fluid pressure (IFP) and interstitial velocity field (IVF) on DOX distribution in tumor and surrounding healthy tissue. The results show that the IVF is negligible except at the interface boundary between the tumor and normal regions. Accuracy and validity of the proposed transport model are verified with the published experimental data. This is done assuming that the impact of the various pharmacokinetic parameters is combined in the apparent diffusivity and apparent elimination constant.

Moreover, impact of the anticancer DOX on the tumor cell density is examined using a pharmacodynamic model. There is a significant reduction in the tumor cell density over time

after insertion of the implant. Therefore, the combination therapy using the IDDSs following thermal ablation will result in high therapeutic efficacy. Moreover, we evaluate the toxicity of DOX on the surrounding normal tissue in terms of the peak concentration and the area under the curve (AUC) of the interstitial free and bound DOX. The proposed model can help in optimize and design of the IDDSs for treatment of the solid tumors following thermal ablation. Thus, it can help to reduce the clinical trials and the number of animals used in biomedical research to save cost and time.

CHAPTER 8

Conclusions and Scope for Future Work

8.1 Introduction

Molecular communication (MC) is an umbrella term for any communication system that is inspired by the intracellular and intercellular communication in the living organisms. Molecular communication via diffusion (MCvD) is an emerging nanoscale communication mechanism that provides communication and coordinated actions between cells or synthetic nanodevices (e.g., nanomachines and nanorobots) in the body using diffusion of chemical molecules. The increasing popularity of MC for medical applications, particularly for drug delivery systems (DDSs), has been supported by the rapid developments in bio-nanotechnology through fabrication nanoscale synthetic entities. The MC paradigm is highly appropriate for modelling and abstraction of the DDSs to simplify the underlying complex processes that govern the release, transport, and reaction of the drug over a wide range of spatiotemporal scales. The synthetic nanocarriers (NCs) and the miniaturized implants can be used as means of implementing the targeted DDSs (TDDSs) and the implantable DDSs (IDDSs) for tumor treatment which provide lower toxicity and higher drug bioavailability compared to conventional chemotherapy.

In this chapter, we present concluding remarks and a summary of the research contributions made in this thesis. Moreover, we outline the scope for future research.

8.2 Contributions and Conclusions

The aim of this research is to develop diffusion-based MC models in various complex biological microenvironments for applications of the targeted and implantable DDSs. We have developed mathematical and stochastic simulation models for diffusion-based MC in complex biological environments over microscopic scale, including multilayer media,

bounded media, and extracellular environments with anisotropic diffusion and reactive obstacles. These models are useful for modelling and design of the TDDSs and MC between nanomachines or cells using biochemical molecules in such complex environments with high spatial resolution over microscopic scale. Also, we have utilized the proposed multilayer MCvD models for modelling the intravascular anticancer drug release from drug-loaded NCs and drug transport across the endothelial barrier of tumor vasculature into the surrounding tissue in tumor microenvironment (TME). We have also developed novel mathematical and stochastic models for the IDDSs to characterize and predict the release and distribution of anticancer drugs following insertion of a miniaturized implant in TME based on the MC abstraction and the convolution approach. In addition, we provide mathematical pharmacokinetic and pharmacodynamic models for combination therapy using local IDDS in solid tumors following thermal ablation based on the MC abstraction. In this thesis, the targeted and implantable DDSs are modelled through MC paradigm by abstracting the drug source (e.g., the NC and implant) as a transmitter, the biological environment (e.g., tumor) as a communication channel, and the target site (e.g., cancer cell) as a receiver.

Moreover, we have exploited the channel impulse response (CIR) characteristic for modelling the DDSs using linear system analysis approach via convolution which offer more general and flexible modelling compared to other modelling approaches such as classical compartment models. Fick's laws of diffusion and Einstein equations for Brownian motion represent the basis for the mathematical and stochastic modelling approaches proposed in this thesis. The main contributions included in each chapter of this thesis are summarized below.

8.2.1 Contributions and Conclusions of Chapter 3

The contributions in Chapter 3 are focused on modelling the molecular transport via diffusion in multilayer (multi-region) biological microenvironments using MC paradigm via mathematical and stochastic simulation approaches. In the literature, the multilayer MCvD microenvironments were simplified as an equivalent homogeneous region with an average diffusion coefficient under the conditions of steady-state and one-dimensional diffusion [51, 52]. However, the results show that this averaging model can lead to inaccurate prediction in the molecular received signal inside the multilayer biological microenvironments. Compared

to the previous averaging models, we proposed more realistic models by considering the temporal variation of the channel impulse response (or the molecular concentration) by taking effects of the different diffusivities, layer thicknesses, and the interface boundary conditions, simultaneously. To the best of our knowledge, this is the first time such a closed-form exact analytical model or stochastic particle-based simulator for MCvD in 3-D diffusive medium with multiple layers (regions) is presented. Also, the proposed multilayer channel models are utilized to model the intravascular nanocarrier-based TDDS in TME based on a general system approach over high spatiotemporal resolutions. The contributions in Chapter 3 are summarized as follows:

- A generalized closed-form CIR expression for MCvD in multilayer biological microenvironments is derived with arbitrary placement of the transmitting nanomachine (TN) and the receiving nanomachine (RN). In this model, we include the simultaneous impacts of the boundary interfaces and the various diffusion characteristics of the layers which have not been considered in the previous averaging models in the literature.
- A stochastic simulation framework for MCvD in multilayer biological microenvironments is developed by tracking and recording the random Brownian motion of each molecule individually within the simulation environment. This stochastic simulation model is the first model which simulates the actual random motion of molecules through the multilayer MCvD microenvironments. It includes the simultaneous impacts of the diffusion properties of each layer separately and impact of the boundary interfaces between the layers.
- Various metrics of the CIR for multilayer microenvironments, i.e., peak amplitude, peak time, and signal width, have been obtained using analytical and stochastic simulation models. Also, the impact of the following factors on the CIR have been examined: the interface separation between the layers, the distance between the TN and RN, the diffusion coefficients, and thicknesses of the layers.
- The derived multilayer CIR has been extended using system approach via mathematical convolution for predicting the drug concentration in the surrounding tissue (e.g., tumor) after intravascular drug release from the NCs inside the blood microvessel. We examine impact of the release rate and the permeability of microvessel barrier on the drug

concentration in the surrounding tumor tissue using thermosensitive liposome (TSL) nanocarriers. The previous works mainly focused on modelling of the TDDS using extravascular drug release from the NCs, e.g., [5, 6], while other models were developed for intravascular drug release based on compartmental approach assuming homogeneous characteristics and identical drug distribution in the tissue, e.g., [1]. However, our model is derived based on a general and flexible system analysis approach via convolution which provides more precise model over high spatiotemporal resolutions.

- A release kinetics model has been developed for the NCs. Further, by fitting this model to published experimental release data of DOX-loaded TSL, the release rate parameters have been obtained.
- The proposed multilayer stochastic simulator is expanded to characterize the release process from the NCs and to control drug extravasation to the surrounding tissue depending on the microvessel permeability.
- The validity and accuracy of the proposed analytical models have been verified with the stochastic simulation results.
- We applied the proposed multilayer molecular communication models for monitoring the plaque vulnerability in atherosclerotic arterial wall via detection and prediction of the inflammatory biomarker Pentraxin-3 (PTX3) using biosensor attached to a vascular stent inside the artery. The proposed platform and models can help in the localized sensing of the atherosclerotic biomarkers for monitoring of the plaque progression and for early warning of certain disorders such as heart attack.

The proposed multilayer MCvD models can be applied to a wide range of applications in multilayer biological media for both microscopic and macroscopic scales. The results show that the peak amplitude of the CIR for the multilayer media depends on the diffusivity, unlike that for the single-layer diffusive media. We have verified that the CIR for multilayer medium can be reduced to that of a single-layer medium when all diffusivities are made equal with fully permeable interfaces. We observed that the characteristics of the multilayer media have a significant impact on the CIR when both the TN and RN are in different layers with negligible impact when they located in the same layer. Through the results of the intravascular NC-based targeted drug delivery model, we observe that the higher release rate

or higher vascular permeability leads to larger drug concentration and larger penetration depth in the surrounding tumor tissue. The trends here coincide with the experiments in the literature on heat triggered drug release from DOX-TSLs [1, 33, 85, 150, 151]. Also, we observe that the drug concentration due to rapid release NCs can be approximated using the CIR, while slow-release NCs can be characterized by incorporating the appropriate release rate parameters.

8.2.2 Contributions and Conclusions of Chapter 4

The main contributions in Chapter 4 are focused on the modelling of the ligand-receptor protein interaction on the target site (acts as a RN) after releasing the molecules (ligands) from a point source (acts as a TN) in 3-D bounded MCvD microenvironments. The previous MCvD models in the literature, assumed simplified unbounded media to simplify the mathematical derivations, e.g., [30, 64]. The work presented in this chapter is the first published work on deriving closed-form analytical expressions for both the Green's function (or CIR) and the number of ligand-receptor complexes for the reversible interaction between ligands and protein receptors on the receiver surface (the target site) inside bounded MCvD microenvironment. Later, some MCvD models have been published in the literature with bounded media but using either passive or fully absorbing receiver without modelling the reversible interaction mechanism [67-72]. The previous works did not examine the simultaneous influence of both the interaction process at the target site together with the reaction/elimination at the medium boundary. The contributions in this chapter are summarized as follows:

- We developed analytical and stochastic simulation MCvD models involving point TN and reversible RN in 3-D spherical bounded microenvironments.
- The reception mechanism at the RN, which involves ligand interaction with the protein receptors on the receiver surface, is modelled using a reversible reaction. Also, we include the impact of the degradation due to enzymatic reaction and other factors in the environment via first-order degradation reaction.
- We derived closed-form analytical expressions for both the Green's function (or CIR) and the expected number of ligand-receptor complexes (bound receptors) on the receiver

surface in a 3-D bounded spherical environment. The impact of the semipermeable medium boundary on the diffusive molecules is included in the proposed model.

- We developed a rigorous algorithm to find the required roots for evaluating the analytical expressions, which provide very accurate results with removing the remaining roots that have a negligible effect.
- We built a precise stochastic simulator that incorporates the various reaction processes by tracking the locations of molecules in the environment and the exact binding and reflecting sites on the receiver surface and the medium boundary in each time step.
- The simulation results are used to validate and compare the results obtained from the analytical model.

Through the comparison of the analytical and simulation results, we have observed the validity of the derived model. The results indicate that the medium radius affects the CIR and the expected number of bound receptors. Therefore, unbounded medium assumption could result in inaccurate predictions compared to the realistic small bounded environments or when the TN is located near the medium boundary. The influences of the reaction rates, i.e., forward, backward, and degradation reaction, on the expected received signal are examined. Also, the results show generality of our models, which can be reduced to other special cases for obtaining the received signal using different receivers in unbounded media. This work can be useful for designing and modelling of the TDDSs using NCs by predicting the drug concentration and the bound receptors at the target site. Also, it can help us understand and model the sensing mechanisms in the synthetic nanomachines and cells for detecting the molecular signals.

8.2.3 Contributions and Conclusions of Chapter 5

The main contributions in Chapter 5 focus on studying the influence of the anisotropy and the reactive obstacles in the diffusive extracellular microenvironments on the molecular transport between a sending cell or NC (i.e., acts as a TN) and a receiving cell or target cell (i.e., acts as a RN). In the literature, few works investigated impact of the reactive object (or an interfering MC receiver) on the molecular concentration in the vicinity of a target cell (or an intended MC receiver), e.g., [74, 75]. These models assumed that the interfering receiver

is a fully absorbing node. However, the reactive elements usually have limited reaction rate which can characterize different obstacle types. Moreover, the impulse response function (or the displacement probability function) for anisotropic media has been widely studied in the literature for prediction of the diffusion tensor and other transport properties [76, 77, 167]. However, it is important to study and analyze the media anisotropy from the prospective of the MC for accurate prediction of the molecular concentration in the vicinity of the target site (or the RN). In this chapter, we developed particle-based stochastic simulators for prediction of the molecular received signal at the RN considering impact of the reactive obstacle and the anisotropy in 3-D microenvironments over microscopic scale.

The simulation results are validated with simplified analytical expressions from the literature. The results show that the obstacle leads to a significant reduction in the received signal (the CIR), particularly as the reaction probability and the size of the obstacle increase. Thus, it may affect the communication capability between the nanomachines or cells or the drug delivery to target site. Also, the results reveal that the peak amplitude of the CIR for an anisotropic environment highly depends on the diffusion tensor, unlike that for isotropic media where the peak amplitude is independent of the diffusivity. The CIR not only depends on the distance between the nanomachines as in the case of the isotropic diffusion but also depends on the locations of the nanomachines inside the environments. This work could help in design the drug delivery and diagnosis systems inside the extracellular biological environments over microscopic scale.

8.2.4 Contributions and Conclusions of Chapter 6

The main contributions in Chapter 6 are devoted to developing novel mathematical and stochastic simulation models for IDDS in TME using system analysis approach through abstraction of MC paradigm, and the contributions are summarized as follows:

- Novel mathematical and stochastic simulation models have been proposed to characterize and predict the release and distribution of anticancer drugs following insertion of a dual-release implant in TME.
- The reported implantable drug delivery models in the literature either have been solved for steady state and/or the release function assumed to be constant or simple decaying

function e.g., [95-100]. However, in our model, the release process in the implant has been charctrized by fitting the published experimental release data of DOX-loaded dual-release implant with the bi-exponatial release function. Thus we can obtain more realistic release rate constants and patterns to be used in our implantable drug delivery model.

- We derived closed-form expressions for the CIR and the spatiotemporal concentration of anticancer drugs in TME using the convolution approach coupled with MC paradigm. This system analysis approach with the CIR offers a powerful and general models for drug transport and pharmacokinetics using different release patterns compared to the prevuous works in the litriture.
- The outer tumor boundary is defined using Robin boundary condition, which may reflect drug loss effect into the neighbouring tissues or through the blood and lymphatic microvessels, which may act as a sink for the drug. This condition can be reduced to fully permeable (perfect-sink) and impermeable (no-flux) conditions.
- A novel stochastic simulation framework has been developed for the proposed IDDS in TME, which can be used as an alternative to the analytical model or for validation purposes. Using this simulator, the drug release from the implant and drug transport via diffusion (Brownian motion) through the surrounding TME tissue, can be simulated accurately. To the best of our knowledge, no stochastic particle-based simulation model was proposed in the literature for the release and distribution of anticancer drug in tumors using the IDDS.
- We obtained the peak concentration and peak time metrics from the spatiotemporal drug concentration profile using analytical and simulation models.
- The impact of the various characteristics of both the TME and the implant on DOX transport have been studied in terms of the spatiotemporal drug concentration profile as well as the peak concentration and peak time with the distance from the implant.
- Accuracy and validity of the proposed models have been verified by comparing the published experimental data on DOX distribution in liver tumor after released from implant [117].

The proposed models can be used for modelling the IDDSs for different drugs and tissues by incorporating their characteristic parameters. Also, the derived CIR can be utilized for

modelling a wide range of implants with different characteristics. Impacts of the drug degradation in the tissue and drug clearance through the blood capillaries are combined in the lumped elimination rate constant while effects of drug binding/uptake into the cells are included in the apparent diffusivity and apparent elimination rate constant. Through the results, we observe that the drug metabolisms and elimination due to various factors reduce the amount of the drug in the tumor tissue. The peak concentration in tumor increases as the release rate from the implant increases while the peak time becomes shorter. Drug concentration decreases as the distance from the implant increases and finally reaches negligible value at the tumor boundary. Also, our models agree well with the results extracted from the published experimental data in the literature [117]. The proposed models can help in design the IDDSs by choosing the optimum design parameters of the implants to improve the therapeutic efficacy. Therefore, this can reduce the number of animal experiments, and as a result, save time and reduce cost.

8.2.5 Contributions and Conclusions of Chapter 7

The main contributions in Chapter 7 are focused on mathematical pharmacokinetic and pharmacodynamic (PK/PD) modelling of combination therapy using IDDS to destroy the residual tumor cells after thermal ablation in solid tumors with the help of MC abstraction. The previous works in the literature, e.g., [106, 115-118], were derived based on many simplified assumptions including average equilibrium parameters for the drug pharmacokinetics without modeling the various processes such as elimination, cellular uptake/efflux, and binding. Moreover, these models did not characterize and predict the dynamic intracellular concentration of anticancer drug and binding of anticancer drug with proteins in the tissue. Also, they did not provide any pharmacodynamic model for evaluating the anticancer drug toxicity on tumor and healthy tissues. Compared to the previous works in the literature, our contributions in this chapter can be summarized as follows:

- We developed a comprehensive mathematical and computational model for anticancer DOX transport in thermally ablated and non-ablated solid tumors, after released from a dual-release implant, for predicting the extracellular and intracellular concentrations of both free and bound doxorubicin. To the best of our knowledge, this work is the first comprehensive mathematical PK/PD model that addresses the combination therapy

using intratumorally IDDS inside malignant solid tumors with/without thermal ablation under various physicochemical processes simultaneously.

- In this work, the tumor tissue is assumed to be first treated using radiofrequency ablation (RFA), which destroys the cellular and vasculature structure inside the ablation zone. This ablated tumor zone is modelled as a modified MC channel with different diffusion and elimination characteristics compared to the original non-ablated tumor tissue.
- The impacts of the various PK processes are included by specifying a detailed model for each process, namely, DOX distribution, binding/unbinding to albumin proteins, cellular influx/efflux, degradation, and elimination through the blood/lymphatic microvessels.
- The influence of the interstitial fluid velocity and pressure on drug transport is included by modelling the interstitial fluid transport in tumor and healthy tissues.
- We proposed a spatiotemporal PD model to examine the impact of DOX on death of the cancer cells in the tumor. Also, the toxicity of DOX on the healthy tissue is evaluated in terms of the peak concentration and the area under curve (AUC).
- This model can capture and characterize the various processes of drug transport, pharmacokinetics, and pharmacodynamics simultaneously.
- Assuming impact of the various PK processes are combined in the apparent diffusivity and apparent elimination rate, then the accuracy and validity of the proposed model are verified with the published experimental data on DOX-loaded implant in thermally ablated liver tumor as well as with the analytical and stochastic simulation models given in Chapter 6.

The system of mathematical equations that describe the proposed model is numerically solved using COMSOL Multiphysics® package. Through the results, we have observed that the interstitial velocity field (IVF) is negligible except at tumor periphery due to the large pressure gradient. The results show that the peak concentration increases (and peak time decreases) as the implant release rate increases in both the ablated and risk (non-ablated) regions. The concentration of bound-DOX shows similar trend with three-fold higher amplitude compared to free-DOX. Also, anticancer drugs can penetrate a larger distance with higher levels in the tumor after thermal ablation. The tumor cells in the risk region have minimum density at the inner boundary with increasing density as the radial distance from

the implant increases. There is a significant reduction in the tumor cell density over time after insertion of the implant following thermal ablation. The results show that the combination therapy using the IDDS following thermal ablation will result in high therapeutic efficacy. The results obtained based on the implant characteristics in this study show that the peak DOX concentration in the healthy tissue is under the toxicity level. Also, the AUC in the healthy tissue shows negligible values in the non-ablated tumor compared to that in the ablated tumor. The proposed model can help in optimize and design of the IDDSs for treatment of solid tumors following thermal ablation to improve the therapeutic efficiency and to save time and reduce cost.

8.3 Scope for Future Work

Here, we will propose some directions as to how the work presented in this thesis can be extended in future:

1. The multilayer diffusive model can be extended by including the impact of the fluid flow, which could be useful for characterizing the blood flow or the interstitial fluid flow. This will allow to study the impact of the blood flow on the intravascular nanocarrier-based TDDS in TME.
2. An open research issue in MC is the design of an interface system between the biological entities inside the body and the external world. Our models can help to develop new interface model using nanomachines and biosensors for disease detection applications.
3. The target site is assumed to be equipped with an unlimited number of protein receptors. However, one can extend our model to include the target site for the case of high ligand concentration or limited number of receptors, which affect the ligand-receptor reaction process.
4. Improve the IDDS by modelling the impact of the implant biodegradation and drug interactions with the tissue surrounding the implant on the drug release process. Also, the proposed IDDSs can be extended for modelling other implants for different diseases. Moreover, the derived CIR can be utilized for modelling local bolus or infusion injection in the tumor to design optimal dosing protocols.

Appendix A: Derivations for Chapter 3

A. 1 Derivation of Equations (3.38)-(3.39)

Applying the boundary conditions (3.15)-(3.16) for Eqs. (3.35)-(3.36), we get

$$\lim_{z\to\infty}\int_0^\infty\left[\frac{e^{-st_0}e^{-g_1|z-z_0|}}{4\pi D_1 g_1}+A_1e^{-g_1z}+B_1e^{g_1z}\right]J_0\left(\xi\mathrm{R}\right)\xi d\xi=0 \tag{A.1}$$

$$\lim_{z\to-\infty}\int_0^\infty\left[A_2e^{-g_2z}+B_2e^{g_2z}\right]J_0\left(\xi\mathrm{R}\right)\xi d\xi=0 \tag{A.2}$$

Then, the limits in Eqs. (A.1)-(A.2) can be evaluated as follows

$$\frac{e^{-st_0}}{4\pi D_1}\frac{1}{g_1}e^{-\infty}+A_1e^{-\infty}+B_1e^{\infty}=0 \tag{A.3}$$

$$A_2e^{\infty}+B_2e^{-\infty}=0 \tag{A.4}$$

By solving Eqs. (A.3)-(A.4), we get values of A_2 and B_1.

$$A_2=B_1=0 \tag{A.5}$$

Now, we will find the unknown functions, A_1 and B_2. Substituting (A.5) in Eqs. (3.35)-(3.36) and then applying the boundary conditions (3.13)-(3.14), we get

$$\frac{e^{-st_0}}{4\pi}e^{g_1(z_1-z_0)}-A_1D_1\,g_1\,e^{-g_1z_1}=D_2B_2\,g_2\,e^{g_2z_1} \tag{A.6}$$

$$\frac{e^{-st_0}}{4\pi D_1g_1}e^{g_1(z_1-z_0)}\left(D_1g_1-p_1\right)-D_1A_1g_1\,e^{-g_1z_1}=p_1\left(A_1\,e^{-g_1z_1}-k_1B_2\,e^{g_2z_1}\right) \tag{A.7}$$

The TN is located in the first layer, i.e., $z_1<z_0$, thus the absolute value function in Eq. (3.35) is given by $|z_1\text{-}z_0| = -(z_1\text{-}z_0)$, where z_1 is the interface location along the z-axis. Then, Eqs. (A.6) and (A.7) can be rearranged as follows

$$A_1=\frac{1}{p_1+D_1}\left[\frac{1}{4\pi}\left(1-\frac{p_1}{D_1g_1}\right)e^{-st_0}e^{g_1(2x_1-x_0)}+p_1k_1B_2\,e^{x_1(g_1+g_2)}\right] \tag{A.8}$$

$$B_2 = D_1\left[\frac{e^{-st_0}}{4\pi D_1 D_2 g_2} e^{g_1(z_1-z_0)-g_2 z_1} - A_1 \frac{g_1}{D_2 g_2} e^{-z_1(g_1+g_2)}\right] \tag{A.9}$$

After solving Eqs. (A.8)-(A.9), we get the functions A_1 and B_2 as given in Eqs. (3.38)-(3.39)

.

A. 2 Derivation of Equations (3.53)-(3.54)

The inverse Laplace transform of Eq. (3.52) can be expressed as

$$f_3 = \frac{k_1}{2\pi}\int_0^\infty\int_0^\infty \mathcal{L}^{-1}\left[e^{-\sqrt{D_2\xi^2+s}\frac{mD_2}{\sqrt{D_2}}} e^{-\sqrt{D_1\xi^2+s}\frac{\left(mk_1 D_1+(z_0+z-2z_1)\right)}{\sqrt{D_1}}} e^{-st_0}\right] J_0\left(\xi R\right) dm\, d\xi \tag{A.10}$$

Applying the identity [125, Eq. (29.3.82)] and the convolution theorem, [223, Eq. (1.25)], with the help of the time and complex shifting properties of the Laplace transform, Eq. (A.10) can be evaluated as follows

$$f_3 = \frac{k_1}{2\pi}\int_0^\infty\int_0^\infty\int_0^t \frac{mD_2}{2\sqrt{\pi D_2\left(t'-\tau-t_0\right)^3}} exp\left(-\frac{\left(mD_2\right)^2}{4D_2\left(t'-\tau-t_0\right)}\right) exp\left(-D_2\xi^2\left(t'-\tau-t_0\right)\right)$$

$$\times\frac{\left(mk_1 D_1+\left(z_0+z-2z_1\right)\right)}{2\sqrt{\pi D_1\left(\tau-t_0\right)^3}} exp\left(-\frac{\left(mk_1 D_1+\left(z_0+z-2z_1\right)\right)^2}{4D_1\left(\tau-t_0\right)}\right)$$

$$\times\exp\left(-D_1\xi^2\left(\tau-t_0\right)\right) J_0\left(\xi R\right) d\tau\, dm\, d\xi \tag{A.11}$$

Finally, Eq. (A.11) can be rearranged as

$$f_3 = \frac{k_1}{2\pi}\int_0^\infty\int_0^t\int_0^\infty exp\left(-\xi^2\left(D_1\left(\tau-t_0\right)+D_2\left(t-\tau-t_0\right)\right)\right) J_0\left(\xi R\right)\xi d\xi \frac{\left(mk_1 D_1+\left(z_0+z-2z_1\right)\right)}{2\sqrt{\pi D_1\left(\tau-t_0\right)^3}}$$

$$\times\frac{mD_2}{2\sqrt{\pi D_2\left(t-\tau-t_0\right)^3}}\exp\left(-\frac{\left(mk_1 D_1+\left(z_0+z-2z_1\right)\right)^2}{4D_1\left(\tau-t_0\right)}-\frac{\left(mD_2\right)^2}{4D_2\left(t-\tau-t_0\right)}\right) d\tau\, dm \tag{A.12}$$

Now, using [125, Eq. (11.4.29)], Eq. (A.12) can be written as follows

$$f_3 = \frac{k_1}{16\pi^2\sqrt{D_1 D_2}} \int_0^t \frac{1}{(\tau - t_0)^{\frac{3}{2}} (t - \tau - t_0)^{\frac{3}{2}} \left(D_1(\tau - t_0) + D_2(t - \tau - t_0)\right)}$$

$$\times exp\left(-\frac{R^2}{4\left(D_1(\tau - t_0) + D_2(t - \tau - t_0)\right)} \right) \int_0^\infty \left(m^2 D_1 D_2 k_1 - m D_2 (2z_1 - z_0 - z) \right)$$

$$\times exp\left(-m^2 \frac{\left(k_1^2 D_1(t - \tau - t_0) + D_2(\tau - t_0)\right)}{4(t - \tau - t_0)(\tau - t_0)} - 2m \frac{-k_1(2z_1 - z_0 - z)}{4(\tau - t_0)} - \frac{(2z_1 - z_0 - z)^2}{4D_1(\tau - t_0)} \right) dm d\tau \tag{A.13}$$

The integral with respect to the variable m in (A.13) can be written as follows

$$\int_0^\infty \left(b_1 m^2 - b_2 m \right) \exp\left(-c_1 m^2 - 2mc_2 - c_3 \right) dm \tag{A.14}$$

where,

$$c_1 = \frac{\left(k_1^2 D_1(t - \tau - t_0) + D_2(\tau - t_0)\right)}{4(t - \tau - t_0)(\tau - t_0)} \tag{A.15}$$

$$c_2 = -\frac{k_1(2z_1 - z_0 - z)}{4(\tau - t_0)} \tag{A.16}$$

$$c_3 = \frac{(2z_1 - z_0 - z)^2}{4D_1(\tau - t_0)} \tag{A.17}$$

$$b_1 = D_1 D_2 k_1 \tag{A.18}$$

$$b_2 = D_2(2z_1 - z_0 - z) \tag{A.19}$$

The integral (A.14) can be evaluated using identities [128, Eqs. (3.462.5) and (3.462.7)] or directly using numerical computing software such as Mathematica.

$$\int_0^{\infty}\left(b_1 m^2 - b_2 \mathrm{m}\right) e^{-c_1 m^2 - 2mc_2 - c_3}\ \ dm = -\frac{c_2 b_1 + c_1 b_2}{2c_1^2} e^{-c_3} + \frac{\sqrt{\pi} e^{\frac{c_2^2}{c_1} - c_3}}{4c_1^{\frac{3}{2}}}\left(\frac{2c_2^2 b_1}{c_1} + b_1 + 2c_2 b_2\right) erfc\left(\frac{c_2}{\sqrt{c_1}}\right)$$

(A.20)

In order to find the final form of the integral (A.20), we evaluate the following terms individually using Eqs. (A.15)-(A.19) and using variable interchange $\tau = vt$:

$$\frac{c_2 b_1 + c_1 b_2}{2c_1^2} e^{-c_3} = \frac{2t^{3/2}\sqrt{D_1}\left(1 - v - t_0'\right)\left(v - t_0'\right)\left(z_0' + z'\right)\left(v - t_0'\right)}{\left(k_1^2\alpha^2\left(1 - v - t_0'\right) + \left(v - t_0'\right)\right)^2} e^{-\frac{\left(z_0' + z'\right)^2}{4\left(v - t_0'\right)}} \tag{A.21}$$

$$e^{\frac{c_2^2}{c_1} - c_3} = \exp\left(\frac{-\left(z_0' + z'\right)^2}{4\left(k_1^2\alpha^2\left(1 - v - t_0'\right) + \left(v - t_0'\right)\right)}\right) \tag{A.22}$$

$$\frac{1}{c_1^{3/2}} = \frac{\left(4t\left(1 - v - t_0'\right)\left(v - t_0'\right)\right)^{3/2}}{D_2^{3/2}\left(k_1^2\alpha^2\left(1 - v - t_0'\right) + \left(v - t_0'\right)\right)^{3/2}} \tag{A.23}$$

$$\frac{2c_2^2 b_1}{c_1} + \left(b_1 + 2c_2 b_2\right) = D_1 D_2 k_1\left[1 - \frac{\left(z_0' + z'\right)^2}{2\left(k_1^2\alpha^2\left(1 - v - t_0'\right) + \left(v - t_0'\right)\right)}\right] \tag{A.24}$$

$$erfc\left(\frac{c_2}{\sqrt{c_1}}\right) = erfc\left(\frac{-k_1\left(z_0' + z'\right)\left(1 - v - t_0'\right)^{1/2}}{2\left(v - t_0'\right)^{1/2}\left(k_1^2\left(1 - v - t_0'\right) + \beta^2\left(v - t_0'\right)\right)^{1/2}}\right) \tag{A.25}$$

where, the dimensionless parameters are defined below:

$$t_0' = \frac{t_0}{t}, \quad R' = \frac{R}{\sqrt{D_1 t}}, \quad \alpha = \sqrt{\frac{D_1}{D_2}}, \quad z_0' = \frac{z_1 - z_0}{\sqrt{D_1 t}}, \quad z' = \frac{z_1 - z}{\sqrt{D_1 t}} \tag{A.26}$$

After substituting Eqs. (A.21)-(A.25) in (A.20) and then substituting Eq. (A.20) in (A.13) with interchange the variable of integration to $v = \tau/t$, we get Eqs. (3.53)-(3.54).

Bibliography

[1] A. Gasselhuber, M. R. Dreher, F. Rattay, B. J. Wood, and D. Haemmerich, "Comparison of conventional chemotherapy, stealth liposomes and temperature-sensitive liposomes in a mathematical model," *PloS one,* vol. 7, no. 10, p. e47453, 2012.

[2] D. Rosenblum, N. Joshi, W. Tao, J. M. Karp, and D. Peer, "Progress and challenges towards targeted delivery of cancer therapeutics," *Nat Commun,* vol. 9, no. 1, p. 1410, 2018.

[3] Y. H. Bae and K. Park, "Targeted drug delivery to tumors: myths, reality and possibility," *J Control Release,* vol. 153, no. 3, pp. 198-205, 2011.

[4] T. Székely Jr and K. Burrage, "Stochastic simulation in systems biology," *Computational and Structural Biotechnology Journal,* vol. 12, no. 20-21, pp. 14-25, 2014.

[5] Y. Chahibi, M. Pierobon, S. O. Song, and I. F. Akyildiz, "A Molecular Communication System Model for Particulate Drug Delivery Systems," *IEEE Trans Biomed Eng,* vol. 60, no. 12, pp. 3468-3483, 2013.

[6] Y. Chahibi, I. F. Akyildiz, S. Balasubramaniam, and Y. Koucheryavy, "Molecular Communication Modeling of Antibody-Mediated Drug Delivery Systems," *IEEE Trans Biomed Eng,* vol. 62, no. 7, pp. 1683-1695, 2015.

[7] I. F. Akyildiz, J. M. Jornet, and M. Pierobon, "Nanonetworks: A new frontier in communications," *Communications of the ACM,* vol. 54, no. 11, pp. 84-89, 2011.

[8] T. Nakano, A. W. Eckford, and T. Haraguchi, *Molecular communication*. Cambridge, U.K: Cambridge University Press, 2013.

[9] N. Farsad, H. B. Yilmaz, A. Eckford, C.-B. Chae, and W. Guo, "A comprehensive survey of recent advancements in molecular communication," *IEEE Communications Surveys & Tutorials,* vol. 18, no. 3, pp. 1887-1919, 2016.

[10] S. Willmann *et al.*, "Development of a physiology-based whole-body population model for assessing the influence of individual variability on the pharmacokinetics of drugs," *Journal of pharmacokinetics and pharmacodynamics,* vol. 34, no. 3, pp. 401-431, 2007.

[11] P. Veng-Pedersen, "Linear and nonlinear system approaches in pharmacokinetics: how much do they have to offer? I. General considerations," *Journal of pharmacokinetics and biopharmaceutics,* vol. 16, no. 4, pp. 413-472, 1988.

[12] G. M. Thurber and R. Weissleder, "A systems approach for tumor pharmacokinetics," *PLoS One,* vol. 6, no. 9, p. e24696, 2011.

[13] G. V. da Silva Luz *et al.*, "Nanorobotics in drug delivery systems for treatment of cancer: a review," *Journal of Materials Science Engineering A,* vol. 6, no. 5-6, pp. 167-180, 2016.

[14] L. Felicetti, M. Femminella, G. Reali, and P. Liò, "Applications of molecular communications to medicine: A survey," *Nano Communication Networks,* vol. 7, pp. 27-45, 2016.
[15] J. B. Wolinsky, Y. L. Colson, and M. W. Grinstaff, "Local drug delivery strategies for cancer treatment: gels, nanoparticles, polymeric films, rods, and wafers," *J Control Release,* vol. 159, no. 1, pp. 14-26, 2012.
[16] J. L. Terrell *et al.*, "Nano-guided cell networks as conveyors of molecular communication," *Nature communications,* vol. 6, p. 8500, 2015.
[17] T. Nakano, M. J. Moore, F. Wei, A. V. Vasilakos, and J. Shuai, "Molecular communication and networking: opportunities and challenges," *IEEE Trans Nanobioscience,* vol. 11, no. 2, pp. 135-148, 2012.
[18] I. F. Akyildiz, F. Brunetti, and C. Blázquez, "Nanonetworks: A new communication paradigm," *Computer Networks,* vol. 52, no. 12, pp. 2260-2279, 2008.
[19] A. Holm and E. Vikström, "Quorum sensing communication between bacteria and human cells: signals, targets, and functions," *Frontiers in plant science,* vol. 5, p. 309, 2014.
[20] H. C. Berg, *Random walks in biology*. Princeton, NJ: Princeton University Press, 1993.
[21] P.-C. Yeh *et al.*, "A new frontier of wireless communication theory: diffusion-based molecular communications," *IEEE Wireless Communications,* vol. 19, no. 5, pp. 28-35, 2012.
[22] J. Crank, *The mathematics of diffusion*. Oxford, UK: Oxford University Press, 1979.
[23] A. Einstein, "On the motion of small particles suspended in liquids at rest required by the molecular-kinetic theory of heat," *Annalen der physik,* vol. 17, pp. 549-560, 1905.
[24] A. Einstein, "Investigations on the Theory of the Brownian Movement," *Ann. D. Phys.,* vol. 17, p. 549, 1905.
[25] M. Pierobon and I. F. Akyildiz, "A physical end-to-end model for molecular communication in nanonetworks," *IEEE Journal on Selected Areas in Communications,* vol. 28, no. 4, pp. 602-611, 2010.
[26] Y. Chahibi, M. Pierobon, and I. F. Akyildiz, "Pharmacokinetic modeling and biodistribution estimation through the molecular communication paradigm," *IEEE Transactions on Biomedical Engineering,* vol. 62, no. 10, pp. 2410-2420, 2015.
[27] R. Edmondson, J. J. Broglie, A. F. Adcock, and L. Yang, "Three-dimensional cell culture systems and their applications in drug discovery and cell-based biosensors," *Assay drug development technologies,* vol. 12, no. 4, pp. 207-218, 2014.
[28] L. Felicetti, M. Femminella, G. Reali, P. Gresele, M. Malvestiti, and J. N. Daigle, "Modeling CD40-based molecular communications in blood vessels," *IEEE Trans Nanobioscience,* vol. 13, no. 3, pp. 230-243, 2014.
[29] V. Henn *et al.*, "CD40 ligand on activated platelets triggers an inflammatory reaction of endothelial cells," *Nature,* vol. 391, no. 6667, pp. 591-594, 1998.
[30] Y. Deng, A. Noel, M. Elkashlan, A. Nallanathan, and K. C. Cheung, "Modeling and simulation of molecular communication systems with a reversible adsorption receiver," *IEEE Transactions on Molecular, Biological and Multi-Scale Communications,* vol. 1, no. 4, pp. 347-362, 2015.

[31] J. K. Patra *et al.*, "Nano based drug delivery systems: recent developments and future prospects," *J Nanobiotechnology,* vol. 16, no. 1, p. 71, 2018.
[32] B. Kneidl, M. Peller, G. Winter, L. H. Lindner, and M. Hossann, "Thermosensitive liposomal drug delivery systems: state of the art review," *International journal of nanomedicine,* vol. 9, p. 4387, 2014.
[33] A. A. Manzoor *et al.*, "Overcoming limitations in nanoparticle drug delivery: triggered, intravascular release to improve drug penetration into tumors," *Cancer research,* vol. 72, no. 21, pp. 5566-5575, 2012.
[34] S. Li *et al.*, "A DNA nanorobot functions as a cancer therapeutic in response to a molecular trigger in vivo," *Nature biotechnology,* vol. 36, no. 3, p. 258, 2018.
[35] L. W. Kleiner, J. C. Wright, and Y. Wang, "Evolution of implantable and insertable drug delivery systems," *J Control Release,* vol. 181, pp. 1-10, 2014.
[36] S. A. Stewart, J. Dominguez-Robles, R. F. Donnelly, and E. Larraneta, "Implantable Polymeric Drug Delivery Devices: Classification, Manufacture, Materials, and Clinical Applications," *Polymers (Basel),* vol. 10, no. 12, p. 1379, 2018.
[37] L. Gao *et al.*, "The improved antitumor efficacy of continuous intratumoral chemotherapy with cisplatin-loaded implants for the treatment of sarcoma 180 tumor-bearing mice," *Drug Deliv,* vol. 26, no. 1, pp. 208-215, 2019.
[38] Y. Sun, H. Jensen, N. J. Petersen, S. W. Larsen, and J. Østergaard, "Concomitant monitoring of implant formation and drug release of in situ forming poly (lactide-co-glycolide acid) implants in a hydrogel matrix mimicking the subcutis using UV–vis imaging," *Journal of pharmaceutical and biomedical analysis,* vol. 150, pp. 95-106, 2018.
[39] J. Li *et al.*, "Liquid-solid phase-inversion PLGA implant for the treatment of residual tumor tissue after HIFU ablation," *PLoS One,* vol. 10, no. 2, p. e0117358, 2015.
[40] H. Rhim *et al.*, "Essential techniques for successful radio-frequency thermal ablation of malignant hepatic tumors," *Radiographics,* vol. 21, pp. S17-S35, 2001.
[41] T. W. Kang, H. K. Lim, and D. I. Cha, "Aggressive tumor recurrence after radiofrequency ablation for hepatocellular carcinoma," *Clin Mol Hepatol,* vol. 23, no. 1, pp. 95-101, 2017.
[42] J. R. Haaga, A. A. Exner, Y. Wang, N. T. Stowe, and P. J. Tarcha, "Combined tumor therapy by using radiofrequency ablation and 5-FU–laden polymer implants: evaluation in rats and rabbits," *Radiology,* vol. 237, no. 3, pp. 911-918, 2005.
[43] O. Reynaud, "Time-dependent diffusion MRI in cancer: tissue modeling and applications," *Frontiers in Physics,* vol. 5, p. 58, 2017.
[44] Food.Drug.Administration(FDA), "Extended Release Oral Dosage Forms: development, evaluation and application of in vitro-in vivo correlations," *Center for Drug Evaluation and Research, Maryland,* pp. 1-24, 1997.
[45] M. Kim, R. J. Gillies, and K. A. Rejniak, "Current advances in mathematical modeling of anti-cancer drug penetration into tumor tissues," *J Frontiers in oncology,* vol. 3, p. 278, 2013.
[46] S. McGinty, "A decade of modelling drug release from arterial stents," *Math Biosci,* vol. 257, pp. 80-90, 2014.
[47] B. K. Lawther, S. Kumar, and H. Krovvidi, "Blood–brain barrier," *Continuing Education in Anaesthesia, Critical Care & Pain,* vol. 11, no. 4, pp. 128-132, 2011.

[48] L. B. Weiswald, D. Bellet, and V. Dangles-Marie, "Spherical cancer models in tumor biology," *Neoplasia,* vol. 17, no. 1, pp. 1-15, 2015.
[49] W. Zhan and X. Y. Xu, "A mathematical model for thermosensitive liposomal delivery of Doxorubicin to solid tumour," *J Drug Deliv,* vol. 2013, p. 172529, 2013.
[50] L. S. Goodman, *Goodman and Gilman's the pharmacological basis of therapeutics*. New York: McGraw-Hill, 1996.
[51] S. M. Mustam, S. K. Syed Yusof, and S. Nejatian, "Multilayer diffusion-based molecular communication," *Transactions on Emerging Telecommunications Technologies,* vol. 28, no. 1, p. e2935, 2017.
[52] S. M. Mustam, S. K. Syed-Yusof, and S. Zubair, "Capacity and Delay Spread in Multilayer Diffusion-Based Molecular Communication (DBMC) Channel," *IEEE Transactions on Nanobioscience,* vol. 15, no. 7, pp. 599-612, 2016.
[53] A. Noel, K. C. Cheung, and R. Schober, "Optimal receiver design for diffusive molecular communication with flow and additive noise," *IEEE Trans Nanobioscience,* vol. 13, no. 3, pp. 350-362, 2014.
[54] D. Kilinc and O. B. Akan, "Receiver design for molecular communication," *IEEE Journal on Selected Areas in Communications,* vol. 31, no. 12, pp. 705-714, 2013.
[55] H. B. Yilmaz, A. C. Heren, T. Tugcu, and C.-B. Chae, "Three-Dimensional Channel Characteristics for Molecular Communications With an Absorbing Receiver," *IEEE Communications Letters,* vol. 6, no. 18, pp. 929-932, 2014.
[56] B. C. Akdeniz, N. A. Turgut, H. B. Yilmaz, C.-B. Chae, T. Tugcu, and A. E. Pusane, "Molecular signal modeling of a partially counting absorbing spherical receiver," *IEEE Transactions on Communications,* vol. 66, no. 12, pp. 6237-6246, 2018.
[57] A. Akkaya, H. B. Yilmaz, C.-B. Chae, and T. Tugcu, "Effect of receptor density and size on signal reception in molecular communication via diffusion with an absorbing receiver," *IEEE Communications Letters,* vol. 19, no. 2, pp. 155-158, 2015.
[58] A. C. Heren, H. B. Yilmaz, C.-B. Chae, and T. Tugcu, "Effect of degradation in molecular communication: Impairment or enhancement?," *IEEE Transactions on Molecular, Biological and Multi-Scale Communications,* vol. 1, no. 2, pp. 217-229, 2015.
[59] M. Damrath, S. Korte, and P. A. Hoeher, "Equivalent Discrete-Time Channel Modeling for Molecular Communication With Emphasize on an Absorbing Receiver," *IEEE Trans Nanobioscience,* vol. 16, no. 1, pp. 60-68, 2017.
[60] C. M. Groh *et al.*, "Mathematical and computational models of drug transport in tumours," *J R Soc Interface,* vol. 11, no. 94, p. 20131173, 2014.
[61] S. S. Andrews, "Accurate particle-based simulation of adsorption, desorption and partial transmission," *Phys Biol,* vol. 6, no. 4, p. 046015, 2009.
[62] C. T. Chou, "Extended master equation models for molecular communication networks," *IEEE Trans Nanobioscience,* vol. 12, no. 2, pp. 79-92, 2013.
[63] C. T. Chou, "Impact of receiver reaction mechanisms on the performance of molecular communication networks," *IEEE Transactions on Nanotechnology,* vol. 14, no. 2, pp. 304-317, 2015.

[64] A. Ahmadzadeh, H. Arjmandi, A. Burkovski, and R. Schober, "Comprehensive Reactive Receiver Modeling for Diffusive Molecular Communication Systems: Reversible Binding, Molecule Degradation, and Finite Number of Receptors," *IEEE Trans Nanobioscience,* vol. 15, no. 7, pp. 713-727, 2016.
[65] S. Kadloor, R. S. Adve, and A. W. Eckford, "Molecular communication using brownian motion with drift," *IEEE Transactions on NanoBioscience,* vol. 11, no. 2, pp. 89-99, 2012.
[66] M. Ş. Kuran, H. B. Yilmaz, T. Tugcu, and B. Özerman, "Energy model for communication via diffusion in nanonetworks," *Nano Communication Networks,* vol. 1, no. 2, pp. 86-95, 2010.
[67] X. Bao, Y. Zhu, and W. Zhang, "Channel Characteristics for Molecular Communication via Diffusion With a Spherical Boundary," *IEEE Wireless Communications Letters,* vol. 8, no. 3, pp. 957-960, 2019.
[68] M. Zoofaghari and H. Arjmandi, "Diffusive Molecular Communication in Biological Cylindrical Environment," *IEEE Trans Nanobioscience,* vol. 18, no. 1, pp. 74-83, 2019.
[69] H. Arjmandi, M. Zoofaghari, and A. Noel, "Diffusive molecular communication in a biological spherical environment with partially absorbing boundary," *IEEE Transactions on Communications,* vol. 67 no. 10, pp. 6858-6867, 2019.
[70] F. Dinc, B. C. Akdeniz, A. E. Pusane, and T. Tugcu, "A General Analytical Approximation to Impulse Response of 3-D Microfluidic Channels in Molecular Communication," *IEEE Trans Nanobioscience,* vol. 18, no. 3, pp. 396-403, 2019.
[71] F. Dinç, B. C. Akdeniz, A. E. Pusane, and T. Tugcu, "Impulse Response of the Molecular Diffusion Channel With a Spherical Absorbing Receiver and a Spherical Reflective Boundary," *IEEE Transactions on Molecular, Biological and Multi-Scale Communications,* vol. 4, no. 2, pp. 118-122, 2018.
[72] F. Dinc *et al.*, "Analytical derivation of the impulse response for the bounded 2-D diffusion channel," *Physics Letters A,* vol. 383, no. 14, pp. 1589-1600, 2019.
[73] G. Wei and R. Marculescu, "Miniature devices in the wild: Modeling molecular communication in complex extracellular spaces," *IEEE Journal on Selected Areas in Communications,* vol. 32, no. 12, pp. 2344-2353, 2014.
[74] Y. Lu, M. D. Higgins, A. Noel, M. S. Leeson, and Y. Chen, "The Effect of Two Receivers on Broadcast Molecular Communication Systems," *IEEE Trans Nanobioscience,* vol. 15, no. 8, pp. 891-900, 2016.
[75] X. Bao, J. Lin, and W. Zhang, "Channel Modeling of Molecular Communication via Diffusion with Multiple Absorbing Receivers," *IEEE Wireless Communications Letters,* vol. 8, no. 3, pp. 809-812, 2019.
[76] P. Mukherjee, J. Berman, S. Chung, C. Hess, and R. Henry, "Diffusion tensor MR imaging and fiber tractography: theoretic underpinnings," *American journal of neuroradiology,* vol. 29, no. 4, pp. 632-641, 2008.
[77] F. Xiao, C. Nicholson, J. Hrabe, and S. Hrabetova, "Diffusion of flexible random-coil dextran polymers measured in anisotropic brain extracellular space by integrative optical imaging," *Biophys J,* vol. 95, no. 3, pp. 1382-1392, 2008.

[78] B. M. Dicheva and G. A. Koning, "Targeted thermosensitive liposomes: an attractive novel approach for increased drug delivery to solid tumors," *Expert opinion on drug delivery,* vol. 11, no. 1, pp. 83-100, 2014.
[79] D. T. McGuiness, V. Selis, and A. Marshall, "Molecular-based Nano-Communication Network: a Ring Topology Nano-bots for In-Vivo Drug Delivery Systems," *IEEE Access,* vol. 7, pp. 12901-12913, 2019.
[80] N. A. Abbasi and O. B. Akan, "An Information Theoretical Analysis of Human Insulin-Glucose System Toward the Internet of Bio-Nano Things," *IEEE Trans Nanobioscience,* vol. 16, no. 8, pp. 783-791, 2017.
[81] Y. Chahibi, "Molecular communication for drug delivery systems: A survey," *Nano Communication Networks,* vol. 11, pp. 90-102, 2017.
[82] U. A. Chude-Okonkwo, R. Malekian, B. T. Maharaj, and A. V. Vasilakos, "Molecular communication and nanonetwork for targeted drug delivery: A survey," *IEEE Communications Surveys & Tutorials,* vol. 19, no. 4, pp. 3046-3096, 2017.
[83] T. Nakano *et al.*, "Performance evaluation of leader–follower-based mobile molecular communication networks for target detection applications," *IEEE Transactions on Communications,* vol. 65, no. 2, pp. 663-676, 2017.
[84] U. A. Chude-Okonkwo, R. Malekian, and B. T. Maharaj, "Molecular Communication Model for Targeted Drug Delivery in Multiple Disease Sites With Diversely Expressed Enzymes," *IEEE Trans Nanobioscience,* vol. 15, no. 3, pp. 230-245, 2016.
[85] Z. S. Al-Ahmady, C. L. Scudamore, and K. Kostarelos, "Triggered doxorubicin release in solid tumors from thermosensitive liposome-peptide hybrids: Critical parameters and therapeutic efficacy," *International journal of cancer,* vol. 137, no. 3, pp. 731-743, 2015.
[86] J. R. Weiser and W. M. Saltzman, "Controlled release for local delivery of drugs: barriers and models," *J Control Release,* vol. 190, pp. 664-673, 2014.
[87] J. Folkman and D. M. Long, "The use of silicone rubber as a carrier for prolonged drug therapy," *Journal of Surgical Research,* vol. 4, no. 3, pp. 139-142, 1964.
[88] A. J. Sawyer *et al.*, "Convection-enhanced delivery of camptothecin-loaded polymer nanoparticles for treatment of intracranial tumors," *Drug Deliv Transl Res,* vol. 1, no. 1, pp. 34-42, 2011.
[89] B. D. Weinberg, H. Ai, E. Blanco, J. M. Anderson, and J. Gao, "Antitumor efficacy and local distribution of doxorubicin via intratumoral delivery from polymer millirods," *J Biomed Mater Res A,* vol. 81, no. 1, pp. 161-170, 2007.
[90] K. Wang *et al.*, "Development of biodegradable polymeric implants of RGD-modified PEG-PAMAM-DOX conjugates for long-term intratumoral release," *Drug Deliv,* vol. 22, no. 3, pp. 389-399, 2015.
[91] A. Kefayat and S. Vaezifar, "Biodegradable PLGA implants containing doxorubicin-loaded chitosan nanoparticles for treatment of breast tumor-bearing mice," *Int J Biol Macromol,* vol. 136, pp. 48-56, 2019.
[92] M. Milosevic *et al.*, "A Computational Model for Drug Release from PLGA Implant," *Materials (Basel),* vol. 11, no. 12, p. 2416, 2018.
[93] M. Rahimi, H. Mobedi, and A. Behnamghader, "In situ-forming PLGA implants loaded with leuprolide acetate/beta-cyclodextrin complexes: mathematical modelling and degradation," *J Microencapsul,* vol. 33, no. 4, pp. 355-364, 2016.

[94] A. N. F. Versypt, D. W. Pack, and R. D. Braatz, "Mathematical modeling of drug delivery from autocatalytically degradable PLGA microspheres—A review," *Journal of Controlled Release,* vol. 165, no. 1, pp. 29-37, 2013.
[95] W. M. Saltzman and M. L. Radomsky, "Drugs released from polymers: diffusion and elimination in brain tissue," *Chemical Engineering Science,* vol. 46, no. 10, pp. 2429-2444, 1991.
[96] L. K. Fung, M. Shin, B. Tyler, H. Brem, and W. M. Saltzman, "Chemotherapeutic drugs released from polymers: distribution of 1, 3-bis (2-chloroethyl)-l-nitrosourea in the rat brain," *Pharmaceutical Research,* vol. 13, no. 5, pp. 671-682, 1996.
[97] J. F. Strasser, L. K. Fung, S. Eller, S. A. Grossman, and W. M. Saltzman, "Distribution of 1,3-bis(2-chloroethyl)-1-nitrosourea and tracers in the rabbit brain after interstitial delivery by biodegradable polymer implants," *J Pharmacol Exp Ther,* vol. 275, no. 3, pp. 1647-1655, 1995.
[98] L. K. Fung *et al.*, "Pharmacokinetics of interstitial delivery of carmustine, 4-hydroperoxycyclophosphamide, and paclitaxel from a biodegradable polymer implant in the monkey brain," *Cancer Res,* vol. 58, no. 4, pp. 672-684, 1998.
[99] B. Reisfeld, S. Kalyanasundaram, and K. Leong, "A mathematical model of polymeric controlled drug release and transport in the brain," *Journal of Controlled Release,* vol. 36, no. 3, pp. 199-207, 1995.
[100] S. Kalyanasundaram, V. D. Calhoun, and K. W. Leong, "A finite element model for predicting the distribution of drugs delivered intracranially to the brain," *Am J Physiol,* vol. 273, no. 5, pp. R1810-R1821, 1997.
[101] C. C. Wang, J. Li, C. S. Teo, and T. Lee, "The delivery of BCNU to brain tumors," *J Control Release,* vol. 61, no. 1-2, pp. 21-41, 1999.
[102] D. Y. Arifin, K. Y. Lee, and C. H. Wang, "Chemotherapeutic drug transport to brain tumor," *J Control Release,* vol. 137, no. 3, pp. 203-210, 2009.
[103] L. Rosso *et al.*, "A new model for prediction of drug distribution in tumor and normal tissues: pharmacokinetics of temozolomide in glioma patients," *Cancer Res,* vol. 69, no. 1, pp. 120-127, 2009.
[104] A. Gopferich, "Mechanisms of polymer degradation and erosion," *Biomaterials,* vol. 17, no. 2, pp. 103-114, 1996.
[105] D. Y. Pereira, A. T. Yip, B. S. Lee, and D. T. Kamei, "Modeling mass transfer from carmustine-loaded polymeric implants for malignant gliomas," *J Lab Autom,* vol. 19, no. 1, pp. 19-34, 2014.
[106] F. Qian, G. M. Saidel, D. M. Sutton, A. Exner, and J. Gao, "Combined modeling and experimental approach for the development of dual-release polymer millirods," *J Control Release,* vol. 83, no. 3, pp. 427-435, 2002.
[107] M. Enayati, H. Mobedi, S. Hojjati-Emami, H. Mirzadeh, and M. Jafari-Nodoushan, "In situ forming PLGA implant for 90 days controlled release of leuprolide acetate for treatment of prostate cancer," *Polymers for Advanced Technologies,* vol. 28, no. 7, pp. 867-875, 2017.
[108] P. D. Fisher, P. Palomino, T. A. Milbrandt, J. Z. Hilt, and D. A. Puleo, "Improved small molecule drug release from in situ forming poly(lactic-co-glycolic acid) scaffolds incorporating poly(beta-amino ester) and hydroxyapatite microparticles," *J Biomater Sci Polym Ed,* vol. 25, no. 11, pp. 1174-1193, 2014.

[109] T. J. Vogl, N. N. Naguib, T. Lehnert, and N. E. Nour-Eldin, "Radiofrequency, microwave and laser ablation of pulmonary neoplasms: clinical studies and technical considerations--review article," *Eur J Radiol,* vol. 77, no. 2, pp. 346-357, 2011.
[110] B. Zhang, M. A. Moser, E. M. Zhang, Y. Luo, C. Liu, and W. Zhang, "A review of radiofrequency ablation: Large target tissue necrosis and mathematical modelling," *Phys Med,* vol. 32, no. 8, pp. 961-971, 2016.
[111] V. S. Vilar *et al.*, "Analysis by MRI of residual tumor after radiofrequency ablation for early stage breast cancer," *AJR Am J Roentgenol,* vol. 198, no. 3, pp. W285-W291, 2012.
[112] N. Zhang *et al.*, "Incomplete radiofrequency ablation enhances invasiveness and metastasis of residual cancer of hepatocellular carcinoma cell HCCLM3 via activating beta-catenin signaling," *PLoS One,* vol. 9, no. 12, p. e115949, 2014.
[113] H. Tajima *et al.*, "Radiofrequency ablation induces dedifferentiation of hepatocellular carcinoma," *Oncology letters,* vol. 1, no. 1, pp. 91-94, 2010.
[114] A. A. Exner *et al.*, "Quantitative computed tomography analysis of local chemotherapy in liver tissue after radiofrequency ablation1," *Academic radiology,* vol. 11, no. 12, pp. 1326-1336, 2004.
[115] F. Qian, N. Stowe, E. H. Liu, G. M. Saidel, and J. Gao, "Quantification of in vivo doxorubicin transport from PLGA millirods in thermoablated rat livers," *J Control Release,* vol. 91, no. 1-2, pp. 157-166, 2003.
[116] B. D. Weinberg, R. B. Patel, A. A. Exner, G. M. Saidel, and J. Gao, "Modeling doxorubicin transport to improve intratumoral drug delivery to RF ablated tumors," *J Control Release,* vol. 124, no. 1-2, pp. 11-19, 2007.
[117] B. D. Weinberg, E. Blanco, and J. Gao, "Polymer implants for intratumoral drug delivery and cancer therapy," *J Pharm Sci,* vol. 97, no. 5, pp. 1681-1702, 2008.
[118] B. D. Weinberg *et al.*, "Model simulation and experimental validation of intratumoral chemotherapy using multiple polymer implants," *Medical & biological engineering & computing,* vol. 46, no. 10, pp. 1039-1049, 2008.
[119] T. E. Peck and S. A. Hill, *Pharmacology for anaesthesia and intensive care*, 4 ed. Cambridge, U.K: Cambridge University Press, 2014.
[120] A. C. Guyton and J. E. Hall, *Textbook of medical physiology*, 11 ed. Philadelphia, USA: Elsevier Inc., 2006.
[121] M. Pierobon and I. F. Akyildiz, "A statistical–physical model of interference in diffusion-based molecular nanonetworks," *IEEE Transactions on communications,* vol. 62, no. 6, pp. 2085-2095, 2014.
[122] M. Burgener and R. Reedy, "Temperature distributions produced in a two-layer structure by a scanning cw laser or electron beam," *J. Appl. Phys.,* vol. 53, no. 6, pp. 4357-4363, 1982.
[123] M. U. Mahfuz, D. Makrakis, and H. T. Mouftah, "A comprehensive study of sampling-based optimum signal detection in concentration-encoded molecular communication," *IEEE Trans Nanobioscience,* vol. 13, no. 3, pp. 208-222, 2014.
[124] T. Koizumi, M. Kakemi, K. Katayama, and H. Ohtani, "A note on diffusion in finite composite media," *Chem. Pharm. Bull. ,* vol. 31, no. 3, pp. 1092-1096, 1983.

[125] M. Abramowitz and I. A. Stegun, *Handbook of mathematical functions: with formulas, graphs, and mathematical tables*. Mineola, New York: Dover Publications, 1964.
[126] G. N. Watson, *A treatise on the theory of Bessel functions*. Cambridge, UK: Cambridge University Press, 1995.
[127] A. Noel, K. C. Cheung, and R. Schober, "Using dimensional analysis to assess scalability and accuracy in molecular communication," *Proc. IEEE ICC MONACOM,* pp. 818-823, Jun. 2013.
[128] A. Jeffrey and D. Zwillinger, *Table of integrals, series, and products*, 7 ed. USA: Elsevier, 2007.
[129] R. G. Rice and D. D. Do, *Applied mathematics and modeling for chemical engineers*, 2 ed. Hoboken, NJ: John Wiley & Sons, 2012.
[130] I. Llatser, A. Cabellos-Aparicio, M. Pierobon, and E. Alarcón, "Detection techniques for diffusion-based molecular communication," *IEEE Journal on Selected Areas in Communications,* vol. 31, no. 12, pp. 726-734, 2013.
[131] S. Wilhelm *et al.*, "Analysis of nanoparticle delivery to tumours," *Nature reviews materials,* vol. 1, no. 5, p. 16014, 2016.
[132] D. B. Kirpotin *et al.*, "Antibody targeting of long-circulating lipidic nanoparticles does not increase tumor localization but does increase internalization in animal models," *Cancer research,* vol. 66, no. 13, pp. 6732-6740, 2006.
[133] M. W. Dewhirst and T. W. Secomb, "Transport of drugs from blood vessels to tumour tissue," *Nat Rev Cancer,* vol. 17, no. 12, pp. 738-750, 2017.
[134] A. L. Bredlau *et al.*, "Localized delivery of therapeutic doxorubicin dose across the canine blood–brain barrier with hyperthermia and temperature sensitive liposomes," *Drug delivery,* vol. 25, no. 1, pp. 973-984, 2018.
[135] L.-A. Armando, A. G.-V. Cindy, E. Reynaldo, and G.-Z. Roberto, "Mathematical modeling and parametrical analysis of the temperature dependency of control drug release from biodegradable nanoparticles," *The Royal Society of Chemistry,* no. 16, pp. 8728–8739, 2019.
[136] A. R. Tzafriri, E. I. Lerner, M. Flashner-Barak, M. Hinchcliffe, E. Ratner, and H. Parnas, "Mathematical modeling and optimization of drug delivery from intratumorally injected microspheres," *Clin Cancer Res,* vol. 11, no. 2, pp. 826-834, 2005.
[137] A. Hervault *et al.*, "Doxorubicin loaded dual pH- and thermo-responsive magnetic nanocarrier for combined magnetic hyperthermia and targeted controlled drug delivery applications," *Nanoscale,* vol. 8, no. 24, pp. 12152-12161, 2016.
[138] C. Burke *et al.*, "Drug release kinetics of temperature sensitive liposomes measured at high-temporal resolution with a millifluidic device," *International Journal of Hyperthermia,* vol. 34, no. 6, pp. 786-794, 2018.
[139] J. B. van Bree, A. V. Baljet, A. van Geyt, A. G. de Boer, M. Danhof, and D. D. Breimer, "The unit impulse response procedure for the pharmacokinetic evaluation of drug entry into the central nervous system," *Journal of pharmacokinetics and biopharmaceutics,* vol. 17, no. 4, pp. 441-462, 1989.
[140] "Viscosity Tables and Viscosity Charts." Anton Paar. https://wiki.anton-paar.com/en/viscosity-tables-and-viscosity-charts/ (accessed 1 Apr., 2018).

[141] N. R. Kim, A. W. Eckford, and C. B. Chae, "Symbol interval optimization for molecular communication with drift," *IEEE Trans Nanobioscience,* vol. 13, no. 3, pp. 223-229, 2014.
[142] R. A. Freitas, *Nanomedicine, volume I: basic capabilities*. Georgetown, TX: Landes Bioscience, 1999.
[143] A. R. Pries, T. W. Secomb, and P. Gaehtgens, "The endothelial surface layer," *Pflügers Archiv,* vol. 440, no. 5, pp. 653-666, 2000.
[144] A. Shemi, E. Z. Khvalevsky, R. M. Gabai, A. Domb, and Y. Barenholz, "Multistep, effective drug distribution within solid tumors," *Oncotarget,* vol. 6, no. 37, p. 39564, 2015.
[145] "ThermoDox." Celsion Corporation. https://celsion.com/thermodox/ (accessed 15 Aug., 2019).
[146] U. Bulbake, S. Doppalapudi, N. Kommineni, and W. Khan, "Liposomal formulations in clinical use: an updated review," *Pharmaceutics,* vol. 9, no. 2, p. 12, 2017.
[147] A. W. El-Kareh and T. W. Secomb, "A mathematical model for comparison of bolus injection, continuous infusion, and liposomal delivery of doxorubicin to tumor cells," *Neoplasia,* vol. 2, no. 4, pp. 325-338, 2000.
[148] H. H. Usansky and P. J. Sinko, "Computation of log BB values for compounds transported through carrier-mediated mechanisms using in vitro permeability data from brain microvessel endothelial cell (BMEC) monolayers," *Pharmaceutical research,* vol. 20, no. 3, pp. 390-396, 2003.
[149] "ChemSpider." Royal Society of Chemistry. http://www.chemspider.com/Chemical-Structure.29400.html (accessed 15 Aug., 2019).
[150] G. Kong *et al.*, "Efficacy of liposomes and hyperthermia in a human tumor xenograft model: importance of triggered drug release," *Cancer research,* vol. 60, no. 24, pp. 6950-6957, 2000.
[151] H. Namazi, V. V. Kulish, A. Wong, and S. Nazeri, "Mathematical based calculation of drug penetration depth in solid tumors," *BioMed research international,* vol. 2016, 2016.
[152] A. K. Iyer, G. Khaled, J. Fang, and H. Maeda, "Exploiting the enhanced permeability and retention effect for tumor targeting," *Drug Discov Today,* vol. 11, no. 17-18, pp. 812-818, 2006.
[153] J. Chen, S. C. Almo, and Y. Wu, "General principles of binding between cell surface receptors and multi-specific ligands: A computational study," *PLoS computational biology,* vol. 13, no. 10, p. e1005805, 2017.
[154] Y. Arinaminpathy, E. Khurana, D. M. Engelman, and M. B. Gerstein, "Computational analysis of membrane proteins: the largest class of drug targets," *Drug Discov Today,* vol. 14, no. 23-24, pp. 1130-1135, 2009.
[155] S. Basu, Y. Gerchman, C. H. Collins, F. H. Arnold, and R. Weiss, "A synthetic multicellular system for programmed pattern formation," *Nature,* vol. 434, no. 7037, pp. 1130–1134, 2005.
[156] D. Hymel and B. R. Peterson, "Synthetic cell surface receptors for delivery of therapeutics and probes," *Adv Drug Deliv Rev,* vol. 64, no. 9, pp. 797-810, 2012.
[157] D. Holcman, A. Marchewka, and Z. Schuss, "Survival probability of diffusion with trapping in cellular neurobiology," *Physical Review E,* vol. 72, no. 3, p. 031910, 2005.

[158] A. Jhaveri and V. Torchilin, "Intracellular delivery of nanocarriers and targeting to subcellular organelles," *Expert Opin Drug Deliv,* vol. 13, no. 1, pp. 49-70, 2016.
[159] N. Farsad, A. W. Eckford, S. Hiyama, and Y. Moritani, "On-chip molecular communication: analysis and design," *IEEE Trans Nanobioscience,* vol. 11, no. 3, pp. 304-314, 2012.
[160] S. Hiyama and Y. Moritani, "Molecular communication: Harnessing biochemical materials to engineer biomimetic communication systems," *Nano Communication Networks,* vol. 1, no. 1, pp. 20-30, 2010.
[161] K. Tai, S. D. Bond, H. R. MacMillan, N. A. Baker, M. J. Holst, and J. A. McCammon, "Finite element simulations of acetylcholine diffusion in neuromuscular junctions," *Biophys J,* vol. 84, no. 4, pp. 2234-2241, 2003.
[162] S. G. Krantz, *Handbook of complex variables*. NY, USA: Springer Science & Business Media, 2012.
[163] K. Schulten and I. Kosztin, *Lectures in theoretical biophysics*. Champaign, IL, USA: University of Illinois, 2000.
[164] P. Muller and A. F. Schier, "Extracellular movement of signaling molecules," *Dev Cell,* vol. 21, no. 1, pp. 145-158, 2011.
[165] E. Sykova and C. Nicholson, "Diffusion in brain extracellular space," *Physiol Rev,* vol. 88, no. 4, pp. 1277-1340, 2008.
[166] C. Nicholson and S. Hrabetova, "Brain Extracellular Space: The Final Frontier of Neuroscience," *Biophys J,* vol. 113, no. 10, pp. 2133-2142, 2017.
[167] A. L. Alexander, J. E. Lee, M. Lazar, and A. S. Field, "Diffusion tensor imaging of the brain," *Neurotherapeutics,* vol. 4, no. 3, pp. 316-329, 2007.
[168] K. A. Rejniak, V. Estrella, T. Chen, A. S. Cohen, M. C. Lloyd, and D. L. Morse, "The role of tumor tissue architecture in treatment penetration and efficacy: an integrative study," *Front Oncol,* vol. 3, p. 111, 2013.
[169] American Cancer Society, "Cancer facts & figures ", 2019.
[170] A. Kumar and J. Pillai, "Implantable drug delivery systems: An overview," in *Nanostructures for the Engineering of Cells, Tissues and Organs*: Elsevier, 2018, pp. 473-511.
[171] L. Gao *et al.*, "Enhanced antitumor efficacy of poly(D,L-lactide-co-glycolide)-based methotrexate-loaded implants on sarcoma 180 tumor-bearing mice," *Drug Des Devel Ther,* vol. 11, pp. 3065-3075, 2017.
[172] C. Carvalho *et al.*, "Doxorubicin: the good, the bad and the ugly effect," *Curr Med Chem,* vol. 16, no. 25, pp. 3267-3285, 2009.
[173] A. I. Minchinton and I. F. Tannock, "Drug penetration in solid tumours," *Nat Rev Cancer,* vol. 6, no. 8, pp. 583-592, 2006.
[174] R. Ramachandran *et al.*, "Theranostic 3-Dimensional nano brain-implant for prolonged and localized treatment of recurrent glioma," *Sci Rep,* vol. 7, p. 43271, 2017.
[175] B. D. Weinberg, E. Blanco, S. F. Lempka, J. M. Anderson, A. A. Exner, and J. Gao, "Combined radiofrequency ablation and doxorubicin-eluting polymer implants for liver cancer treatment," *J Biomed Mater Res A,* vol. 81, no. 1, pp. 205-213, 2007.

[176] J. Gao, F. Qian, A. Szymanski-Exner, N. Stowe, and J. Haaga, "In vivo drug distribution dynamics in thermoablated and normal rabbit livers from biodegradable polymers," *J Biomed Mater Res,* vol. 62, no. 2, pp. 308-314, 2002.
[177] F. Qian, N. Stowe, G. M. Saidel, and J. Gao, "Comparison of doxorubicin concentration profiles in radiofrequency-ablated rat livers from sustained-and dual-release PLGA millirods," *Pharmaceutical research,* vol. 21, no. 3, pp. 394-399, 2004.
[178] D. B. Young, J. G. Devane, and J. Butler, *In vitro-in vivo correlations*. NY, USA: Plenum Press, 1997.
[179] R. Gomeni, L. Fang, F. Bressolle-Gomeni, T. J. Spencer, S. V. Faraone, and A. Babiskin, "A General Framework for Assessing In vitro/In vivo Correlation as a Tool for Maximizing the Benefit-Risk Ratio of a Treatment Using a Convolution-Based Modeling Approach," *CPT: pharmacometrics & systems pharmacology,* vol. 8, no. 2, pp. 97-106, 2019.
[180] Y. Chahibi, M. Pierobon, and S. O. Song, "Molecular communication model of nanoparticle-body interactions in particulate drug delivery systems," in *2013 Asilomar Conference on Signals, Systems and Computers*, 2013: IEEE, pp. 1051-1055.
[181] P. Veng-Pedersen, "Noncompartmentally-based pharmacokinetic modeling," *Adv Drug Deliv Rev,* vol. 48, no. 2-3, pp. 265-300, 2001.
[182] M. Soltani and P. Chen, "Numerical modeling of fluid flow in solid tumors," *PLoS One,* vol. 6, no. 6, p. e20344, 2011.
[183] C. Nicholson, "Diffusion and related transport mechanisms in brain tissue," *Reports on progress in Physics,* vol. 64, no. 7, p. 815, 2001.
[184] K. Gustafson and T. Abe, "The third boundary condition—was it Robin's?," *The Mathematical Intelligencer,* vol. 20, no. 1, pp. 63-71, 1998.
[185] R. P. Agarwal, K. Perera, and S. Pinelas, *An introduction to complex analysis*. NY, USA: Springer Science & Business Media, 2011.
[186] W. W. Yang and E. Pierstorff, "Reservoir-based polymer drug delivery systems," *J Lab Autom,* vol. 17, no. 1, pp. 50–58, 2012.
[187] R. B. Patel, L. Solorio, H. Wu, T. Krupka, and A. A. Exner, "Effect of injection site on in situ implant formation and drug release in vivo," *J Control Release,* vol. 147, no. 3, pp. 350-358, 2010.
[188] S. S. Jensen *et al.*, "In vitro release studies of insulin from lipid implants in solution and in a hydrogel matrix mimicking the subcutis," *Eur J Pharm Sci,* vol. 81, pp. 103-112, 2016.
[189] Y. Fu and W. J. Kao, "Drug release kinetics and transport mechanisms of non-degradable and degradable polymeric delivery systems," *Expert Opin Drug Deliv,* vol. 7, no. 4, pp. 429-444, 2010.
[190] B. J. Toley, Z. G. Tropeano Lovatt, J. L. Harrington, and N. S. Forbes, "Microfluidic technique to measure intratumoral transport and calculate drug efficacy shows that binding is essential for doxorubicin and release hampers Doxil," *Integrative Biology,* vol. 5, no. 9, pp. 1184-1196, 2013.
[191] S. A. Gulec, G. Mesoloras, and M. Stabin, "Dosimetric techniques in 90Y-microsphere therapy of liver cancer: the MIRD equations for dose calculations," *Journal of Nuclear Medicine,* vol. 47, no. 7, pp. 1209-1211, 2006.

[192] K. D. Watson *et al.*, "Ultrasound increases nanoparticle delivery by reducing intratumoral pressure and increasing transport in epithelial and epithelial-mesenchymal transition (EMT) tumors," *Cancer research,* vol. 72, no. 6, pp. 1485–1493, 2012.
[193] Y. Boucher, L. T. Baxter, and R. K. Jain, "Interstitial pressure gradients in tissue-isolated and subcutaneous tumors: implications for therapy," *Cancer research,* vol. 50, no. 15, pp. 4478-4484, 1990.
[194] J. Wan, W. Wu, Y. Huang, W. Ge, and S. Liu, "Incomplete radiofrequency ablation accelerates proliferation and angiogenesis of residual lung carcinomas via HSP70/HIF-1alpha," *Oncol Rep,* vol. 36, no. 2, pp. 659-668, 2016.
[195] H. Wu, A. A. Exner, T. M. Krupka, B. D. Weinberg, R. Patel, and J. R. Haaga, "Radiofrequency ablation: post-ablation assessment using CT perfusion with pharmacological modulation in a rat subcutaneous tumor model," *Academic radiology,* vol. 16, no. 3, pp. 321-331, 2009.
[196] J. Wan, W. Wu, Y. Chen, N. Kang, and R. Zhang, "Insufficient radiofrequency ablation promotes the growth of non-small cell lung cancer cells through PI3K/Akt/HIF-1α signals," *Acta Biochim Biophys Sin,* vol. 48, no. 4, pp. 371-377, 2016.
[197] C. Phipps and M. Kohandel, "Mathematical model of the effect of interstitial fluid pressure on angiogenic behavior in solid tumors," *Computational and mathematical methods in medicine,* vol. 2011, p. 843765, 2011.
[198] L. T. Baxter and R. K. Jain, "Transport of fluid and macromolecules in tumors. I. Role of interstitial pressure and convection," *Microvascular research,* vol. 37, no. 1, pp. 77-104, 1989.
[199] Y.-M. F. Goh, H. L. Kong, and C.-H. Wang, "Simulation of the delivery of doxorubicin to hepatoma," *Pharmaceutical Research,* vol. 18, no. 6, pp. 761-770, 2001.
[200] M. Sefidgar, M. Soltani, K. Raahemifar, H. Bazmara, S. M. M. Nayinian, and M. Bazargan, "Effect of tumor shape, size, and tissue transport properties on drug delivery to solid tumors," *Journal of Biological Engineering,* vol. 8, no. 1, p. 12, 2014.
[201] W. Zhan, W. Gedroyc, and X. Y. Xu, "The effect of tumour size on drug transport and uptake in 3-D tumour models reconstructed from magnetic resonance images," *PloS one,* vol. 12, no. 2, p. e0172276, 2017.
[202] C. E. Swenson, D. Haemmerich, D. H. Maul, B. Knox, N. Ehrhart, and R. A. Reed, "Increased duration of heating boosts local drug deposition during radiofrequency ablation in combination with thermally sensitive liposomes (ThermoDox) in a porcine model," *PloS one,* vol. 10, no. 10, p. e0139752, 2015.
[203] K. Shin, B. S. Klosterhoff, and B. Han, "Characterization of cell-type-specific drug transport and resistance of breast cancers using tumor-microenvironment-on-chip," *Molecular pharmaceutics,* vol. 13, no. 7, pp. 2214-2223, 2016.
[204] C. Liu, J. Krishnan, and X. Y. Xu, "A systems-based mathematical modelling framework for investigating the effect of drugs on solid tumours," *Theor Biol Med Model,* vol. 8, no. 1, p. 45, 2011.

[205] S. Eikenberry, "A tumor cord model for doxorubicin delivery and dose optimization in solid tumors," *Theoretical Biology and Medical Modelling,* vol. 6, no. 1, p. 16, 2009.
[206] T. Nhan, A. Burgess, L. Lilge, and K. Hynynen, "Modeling localized delivery of Doxorubicin to the brain following focused ultrasound enhanced blood-brain barrier permeability," *Physics in Medicine & Biology,* vol. 59, no. 20, pp. 5987-6004, 2014.
[207] C. Liu, J. Krishnan, and X. Y. Xu, "Investigating the effects of ABC transporter-based acquired drug resistance mechanisms at the cellular and tissue scale," *Integrative Biology,* vol. 5, no. 3, pp. 555-568, 2013.
[208] R. E. Eliaz, S. Nir, C. Marty, and F. C. Szoka, "Determination and modeling of kinetics of cancer cell killing by doxorubicin and doxorubicin encapsulated in targeted liposomes," *Cancer research,* vol. 64, no. 2, pp. 711-718, 2004.
[209] E. D. Lobo and J. P. Balthasar, "Pharmacodynamic modeling of chemotherapeutic effects: application of a transit compartment model to characterize methotrexate effects in vitro," *AAPs PharmSci,* vol. 4, no. 4, pp. 212-222, 2002.
[210] A. Parmar and S. Sharma, "Engineering design and mechanistic mathematical models: Standpoint on cutting edge drug delivery," *TrAC Trends in Analytical Chemistry,* vol. 100, pp. 15-35, 2018.
[211] L. T. Baxter and R. K. Jain, "Transport of fluid and macromolecules in tumors. II. Role of heterogeneous perfusion and lymphatics," *Microvascular research,* vol. 40, no. 2, pp. 246-263, 1990.
[212] L. T. Baxter and R. K. Jain, "Transport of fluid and macromolecules in tumors: III. Role of binding and metabolism," *Microvascular research,* vol. 41, no. 1, pp. 5-23, 1991.
[213] R. K. Jain and L. T. Baxter, "Mechanisms of heterogeneous distribution of monoclonal antibodies and other macromolecules in tumors: significance of elevated interstitial pressure," *Cancer research,* vol. 48, no. 24, pp. 7022-7032, 1988.
[214] D. E. Hilmas and E. L. Gillette, "Morphometric analyses of the microvasculature of tumors during growth and after x-irradiation," *Cancer,* vol. 33, no. 1, pp. 103-110, 1974.
[215] J. Pappenheimer, E. Renkin, and L. Borrero, "Filtration, diffusion and molecular sieving through peripheral capillary membranes: a contribution to the pore theory of capillary permeability," *American Journal of Physiology-Legacy Content,* vol. 167, no. 1, pp. 13-46, 1951.
[216] R. K. Jain, "Transport of molecules in the tumor interstitium: a review," *Cancer research,* vol. 47, no. 12, pp. 3039-3051, 1987.
[217] L. J. Nugent and R. K. Jain, "Extravascular diffusion in normal and neoplastic tissues," *Cancer research,* vol. 44, no. 1, pp. 238-244, 1984.
[218] E. A. Swabb, J. Wei, and P. M. Gullino, "Diffusion and convection in normal and neoplastic tissues," *Cancer research,* vol. 34, no. 10, pp. 2814-2822, 1974.
[219] N. Z. Wu, B. Klitzman, G. Rosner, D. Needham, and M. W. Dewhirst, "Measurement of material extravasation in microvascular networks using fluorescence video-microscopy," *Microvascular research,* vol. 46, no. 2, pp. 231-253, 1993.

[220] S. Kempe and K. Mäder, "In situ forming implants—an attractive formulation principle for parenteral depot formulations," *Journal of Controlled Release,* vol. 161, no. 2, pp. 668-679, 2012.
[221] S. Ozawa, Y. Sugiyama, Y. Mitsuhashi, T. Kobayashi, and M. Inaba, "Cell killing action of cell cycle phase-non-specific antitumor agents is dependent on concentration-time product," *Cancer chemotherapy and pharmacology,* vol. 21, no. 3, pp. 185-190, 1988.
[222] L. M. Levasseur, H. K. Slocum, Y. M. Rustum, and W. R. Greco, "Modeling of the time-dependency of in vitro drug cytotoxicity and resistance," *Cancer Research,* vol. 58, no. 24, pp. 5749-5761, 1998.
[223] A. M. Cohen, *Numerical methods for Laplace transform inversion*. NY, USA: Springer Science & Business Media, 2007.